PERFORATION CAVITY EVOLUTION DURING EARLY SAND PRODUCTION

A Thesis

by

XI CHEN

Submitted to the Graduate and Professional School of

Texas A&M University

in partial fulfillment of the requirements for the degree of

MASTER OF SCIENCE

Chair of Committee,	Nobuo Morita
Committee Members,	Kan Wu
	Hiroko Kitajima
Head of Department,	Jeffery Spath

August 2021

Major Subject: Petroleum Engineering

ABSTRACT

A numerical model is developed for predicting perforation cavity evolution during the early stage of sand production. The objective of this thesis is to propose a new sand-rate-prediction model based on coupling fluid and geomechanics models with optimized parameters determined by sand rate laboratory experiments. Several parameters are determined from the sand production experiments collaborated with the SINTEF laboratory, Norway.

Sand rate experiments are conducted using semi-cylindrical cores with 20 cm in diameter and 20 cm in length with a 2-cm-diameter hole. The confining loads are applied from three directions on the core. Fourteen tri-axial experiments were performed using Castlegate sandstone. With different stress ratio (kr $= \frac{\sigma_r}{\sigma_R}$, $kz = \frac{\sigma_R}{\sigma_Z}$, σ_r : minimal horizontal stress, σ_R : maximum horizontal stress, σ_z vertical stress) and the same flow rate, the coefficients of the equation of the sand particle release rate were matched.

By running simulation program for all the SINTEF experiments with the optimized parameters, it is observed that the coefficients are dispersed. Using the average of sand-release rate coefficients determined from the SINTEF experiments, the simulation model is applied to the perforation evolution under various field conditions. The field simulation results show sand production is influenced by many factors such as well inclination, anisotropic permeability and perforation phasing.

CONTRIBUTORS AND FUNDING SOURCES

Contributors

This work was supported by a thesis (or) dissertation committee consisting of Professor Nobuo Morita and Kan Wu of the Department of petroleum engineering and Professor Hiroko Kitajima of the Department of Geology&Geophysics. The data analyzed for Chapter 3&4 was provided by SINTEF. All other work conducted for the thesis (or) dissertation was completed by the student independently.

Funding Sources

Graduate study was supported by a fellowship from Texas A&M University and a dissertation research fellowship from Dr. Morita.

TABLE OF CONTENTS

LIST OF FIGURES

Page

LIST OF TABLES

Page

CHAPTER I INTRODUCTION

1.1 Background

The sand production from oil and gas wells has been a severe problem for oil industries since it damages equipment due to erosion and it may also lower the oil productivity. There are several ways to minimize sand production. Analyzing the formation sand production would help to understand how sand is produced and it guides to the most economical way to complete wells.

Usually, in shallow, young and soft formation, the sand production occurs because the poor cementing cannot hold the sand grains together (Penberthy and Shaughnessy (1992)). Some research and estimation suggest that 70% of the oil and gas wells are not well consolidated, and sand production occurs frequently in these reservoirs during oil production. (Bianco and Halleck (2001)).

The equipment of oil industry will be eroded or destroyed by the produced sand, which lowers the productivity, increases the maintenance cost, and even breaks down the facility. Thus, several methods have been used to prevent sand production such as reducing production rate or using gravel packing.

Historically, the technologies of predicting and reducing the sand production advanced in 4 stages. Firstly, before 1980s, wireline logs technology was developed for detecting the locations of weak formation and to reduce the oil production rate according to the weakness of the formation. Between 1980 to 1998, accompanied with the development of computer, more computing intensive work came into reality. Coupling geomechanics and fluid model was used to study the early stage of sand production, which could estimate the onset of sand production in the wellbore. Since 1999, many experiments were conducted to further explore the sand

production problem, and the methods to predict sand production continued improving by the experiments and finite element models. From 2018, the poly-axial sand rate experiments were developed. The experiments mainly used to investigate anisotropic effect of stress loaded on the rock. Besides, the new numerical model improvements such as adaptive meshing and elasto-plastic model were widely used in predicting sand production. The estimation has improved via these efforts done in these years. (Papamichos (2018))

The sand production is not only enhanced by solid and fluid interaction used in the finite element model, but other factors will also have influence during production such as heterogeneity of the formation and sand arching. In some cases, sand production rate is lower than prediction due to sand arching effect, which prevents sand-release from the formation. In other cases, however, the sand production will destroy the stability of the well and cause massive sand rate causing severe accidents. (Terzaghi (1936))

Although the experiments are expensive and time-consuming, more experiments are essential to obtain information related to sand production. The numerical model can be improved and calibrated by comparing with experimental results. Based on the collaborated experiments with SINTEF, additional data are required to determine all the coefficients for sand-release-rate equation.

1.2 Objectives

The objective of this thesis is to develop a finite element model for sand production prediction from perforations based on 14 SINTEF tri-axial experiments.

Based on the SINTEF tri-axial experiments, the parameters used in sand production model are optimized. Then the sand production on the early stage of production under different factors such as well inclination and anisotropic permeability are investigated in field conditions.

1.3 Outline

Chapter 2 mainly introduces the methodology for investigating the sand production problem, including finite element method for geomechanics and flow study, adaptive meshing, and the failure model and criterion. Chapter 3 gives the results of SINTEF experiments and our calibrated simulation. The simulation results will be discussed in this chapter.

In Chapter 4, field study results are given under different conditions. Then the preliminary conclusions will be given.

CHAPTER II METHODOLOGY AND LITERATURE REVIEW

2.1 Basics of sand production

Many parameters could influence the stability of perforations, such as perforation pattern, well inclination, flow rate, reservoir depletion and in-situ stress. Thus, in order to have a good estimation of sand production via simulation, many factors need to be considered.

2.1.1 Fundamental introduction of sand production

The onset of sand production is mainly caused by the high effective in-situ stress induced by reservoir depletion. On the other hand, the sand production rate depends mainly on the fluid flow. Once the flow rate is large enough to overcome the cohesive force, the sand will detach from the perforation wall, therefore, the process will change with the stress state and flow rate, pressure, and drawdown near the wellbore.

A tri-axial experiment had been conducted with a cubic-like rock sample to simulate the in-situ stress condition underground. The result showed that if the deformation is elastic without plastic region observed (A stress state in Fig 2.1), only a high flow rate would lead to the failure of the region. When the stress continued increasing, plastic region formed and a small flow rate could bring a sand production (C-stress-state). Once rock strain reached the maximum, the shear force dominant region will expand (C and D). Then, after shutting down the well, the rock sample strain partially recovers, where some residual strain remains. The residual strength may still support the cavity, however, once the production well reopens, the sand will easily be produced even with a relatively small flow rate (B).

In conclusion, the major modes for sandstone failure are shear and tensile failures.

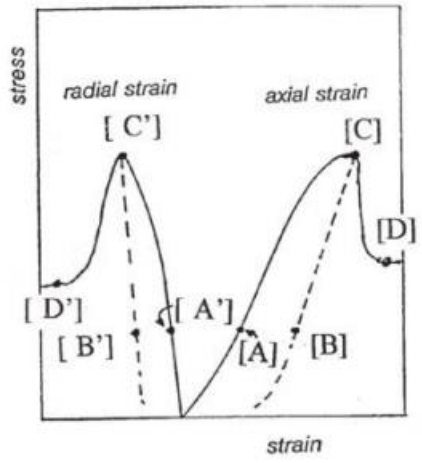

Figure 2.1 Sand Production at different stress status.

2.1.2 Different failure mechanism

Several types of failures cause sand production such as shear, and tensile failures (Veeken et al. (1991)). These failures could work alone or combined together, causing sand production.

1) Shear failure

   In the formation around the wellbore, a tangential stress and a radial stress evolve. Once the tangential stress is large enough, the shear failure will occur. When the shear stress becomes large enough, a liquid flow could cause releasing the sand from the wellbore or cavity. As mentioned above, this kind of failure often occurs when the strain reaches beyond a critical strain.

   Usually in the simulation, the rock deformation model can use elastic-brittle model or elasto-plastic model. For elasto-plastic model, several types of yield envelope could be used such as Mohr-coulomb, Drucker-Prager and Lade models. And this kind of failure

often occurs for weak rock or medium strength rock at the late stage of the reservoir development, because the reservoir depletion will increase the effective stress near the wellbore or cavity (Morita et al. (1998)). The increased stress will form a plastic region around perforation cavities resulting in sand flow.

2) Tensile failure

When the flow rate is large, the drag force exerted on the sand near the cavity will also increase, thus, the tensile stress on the surface region will also increase. The failure is dominated by pressure gradient. (Morita et al. (1989b)).

$$g_{pn}^{c} = r_c \left(\frac{\partial p}{\partial r}\right)_{r_c} \tag{2.1}$$

In the equation, g_{pn}^{c} is the critical pressure gradient to induce a tensile failure where r_c is the radius of the cavity, p is pressure and r is the radius in the polar coordinate. When a well starts producing oil and gas, the pressure gradient will increase dramatically because bottom hole pressure is reduced. Thus, the sand will be often produced in this stage (Papamichos et al. (1992)).

3) Erosion failure

The erosion failure will occur when the shear stress is large enough, then the fluid flow will overcome the cohesive force between sand grains and bring the sand to the wellbore or cavity.

4) Pore collapse failure

The erosion failure, shear failure and tensile failure are often observed. However, there is another kind of failure in the cavity. It has been observed by experiments (Haimson and Kovacich (2003); Papamichos et al. (2008)). At the beginning, the failure region initiates at the shear zone, then the failure doesn't expand to all the shear region. Instead, the failure will continue growing along the radial direction like a worm hole and the growing speed is very fast.

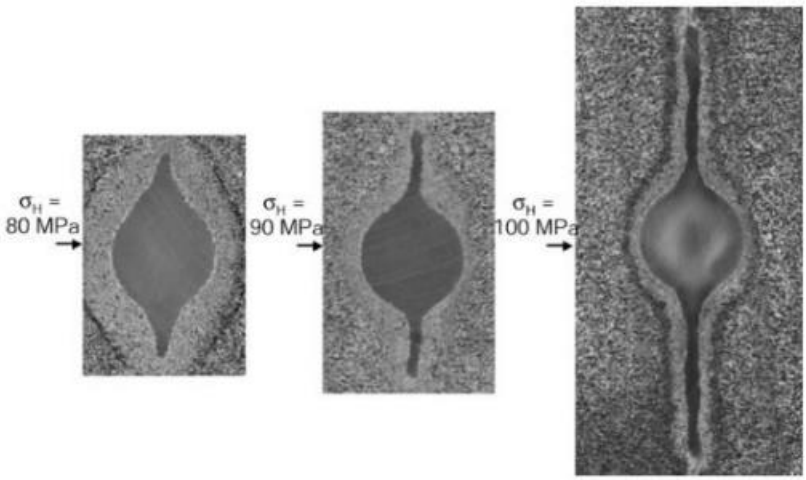

Figure 2.2 Slit-like failure showing the maximum stress influence.

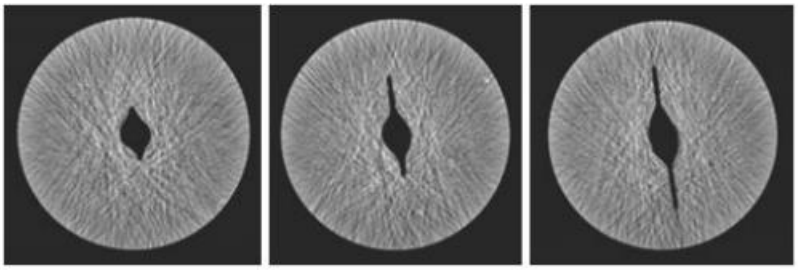

Figure 2.3 Schematic of trap door experiment.

2.1.3 Sand arching

Usually when the stress and fluid flow rate is large enough, the sand production will continue growing. However, in some condition the situation will change: the cavity become very stable and sand production stopped. The regime was firstly investigated by Terzaghi (1936) in an experiment. The experiment was done by using unconsolidated sand and a box which only had one hole in the bottom, where the sand could only flow out from the hole. At the beginning the sand continued dropping, however, after a while, the sand would form a very stable structure in the box, like an arching bridge, which increased the strength of the formation made by the unconsolidated sand.

A trap door experiment was conducted by Hall and Harrisberger (1970). The schematic of the experiments is shown figure 2.4. Flow rate was increased gradually. They observed that the stable sand arch was formed at high stress condition and the sand was packed densely. The flow rate destructed the sand arching. They did not successfully quantify the flowrate required to damage the sand arch.

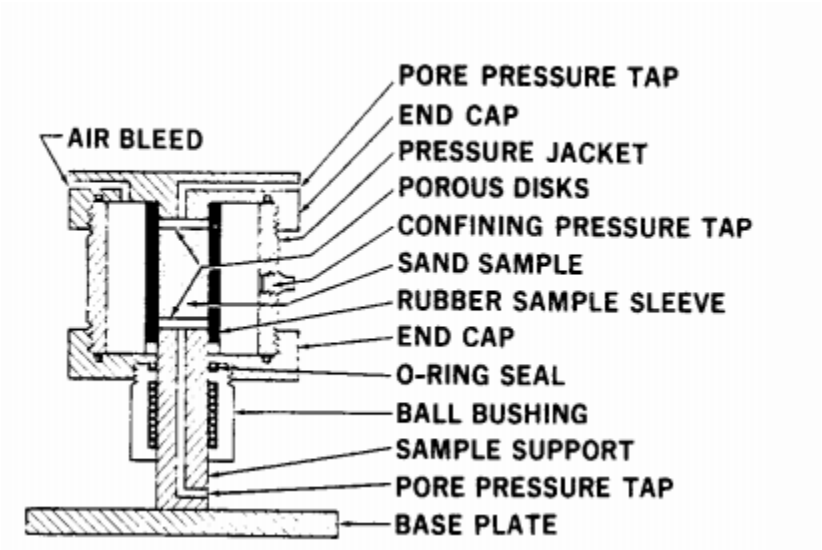

Figure 2.4 Trap door experiment device

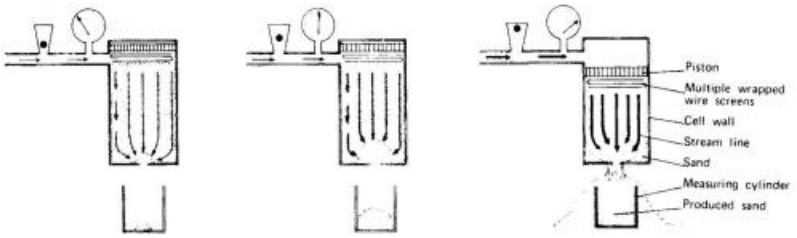

Figure 2.4 Schematic of trap door experiment (Bratli and Risnes (1981)).

After the experiment done by Hall and Harrisberger (1970), Brtli and Risnes (1981) also performed similar experiments. Their experiments gave the critical flow rate for the sand arch collapse. And they assume the sand arching is spherical. The theory well explains the mechanism of the sand arching and gives good prediction on when the sand arch could exist or destroyed at a certain flow rate.

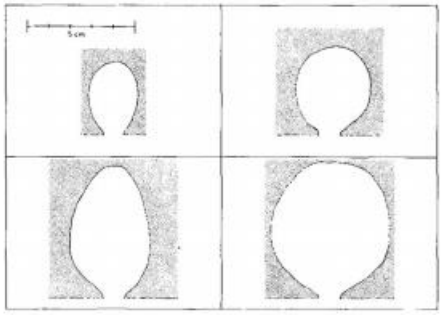

Figure 2.5 The spherical sand arching.

After these experiments, Perkins and Weingarten (1988) continued their theory and study the stability condition of spherical cavity in unconsolidated formation. They found that the porosity will also influence the result. When porosity is large enough, sand will not have enough structure strength to form arching, then collapse happened.

Bianco and Halleck (2001) continued their study to do extra experiments, aiming to find the relationship between stability and fluid properties. In the experiment, they changed the wetting phase saturation and found a minimum amount of wetting phase was need to form stable arch.

From the experiments above, we can conclude the sanding arch effect is very important in preventing sand production during well production. Thus, when considering sand production, the factors influencing sand arching should be taken into consideration.

2.2 Mathematical Model

2.2.1 Coupling relationship

The equation describes the formation can be considered into two parts, one is geomechanics part, and another is fluid part.

For the geomechanics part:

Assuming the balance of forces, equation of equilibrium is given by:

$$\sigma_{ij,j} + F_j = 0 \tag{2.2}$$

F_j is the body force in each direction. (i, j=1,2,3 in 3d situation)

Strain-displacement relationship is given by:

$$\varepsilon_{ij} = \frac{1}{2}\left(\frac{\partial u_i}{\partial x_j} + \frac{\partial u_j}{\partial x_i}\right) \tag{2.3}$$

Stress-strain relationship:

$$\varepsilon_{ij} = \frac{1+\nu}{E}\,\sigma_{ij}^{e} - \frac{1+\nu}{E}\,\sigma_{kk}^{e}\delta_{ij} - \frac{1-2\nu_m}{E_m}p\delta_{ij} + \epsilon_{ij}^{N} \tag{2.4}$$

In the equations above, p is pressure, σ is stress, E represents Young's Module (for bulk object) and E_m represents Young's Module of matrix material. ν is Possion's ratio and ν_m is Possion's ratio of matrix material. ε represents strain in each direction. ϵ^N represents initial non-linear strain. For the flow model, the relationship can be represented by Darcy's Law and mass conservation.

Mass conservation represented by differential equation:

$$\nabla[\rho u] = -\frac{\partial(\rho\varphi)}{\partial t} - q \tag{2.5}$$

Darcy's Law:

$$u = -\frac{k}{\mu}\,\beta\nabla p \tag{2.6}$$

In the equations above, u means flow rate, β represents non-darcy coefficient, which is determined by flow properties and fluid interaction with solid structure. ϕ is porosityand μ is viscosity of fluid.

With the governing equations above, combined with poro-elasto-plastic relation, we can get a couple of partial differential equations to describe solid and flow interaction in the formation.

2.2.2 Poro-Elasto-Plastic Formulation

Before introducing the formulation, several invariants need to be clarified:

$$J_1 = \sigma_{ii}$$

$$J_2 = \frac{1}{2}\sigma_{ij}\sigma_{ij}$$

$$J'_2 = \frac{1}{2}(\sigma_{ij} - \frac{1}{3}\delta_{ij}\sigma_{kk})(\sigma_{ij} - \frac{1}{3}\delta_{ij}\sigma_{kk}) \tag{2.7}$$

$$J_3 = \frac{1}{3}\sigma_{ij}\sigma_{jk}\sigma_{ki}$$

The elasto-plastic relationship can be represented by Fig 2.6. At the early stage, the relationship of stress and strain is linear. After reaching yield stress, the slope of stress-strain curve is reduced. The deformation after yield point can be separated as two parts, plastic and elastic (Fig 2.6).

$$d\epsilon = d\epsilon^e + d\epsilon^p \tag{2.8}$$

After the yield stress, a yield criterion is needed for calculating failure region. The Mohr-Coulomb, Drucker-Prager and Lade theories are applied depending on the stress strain curves obtained by triaxial tests.

A linear Drucker-Prager yield criterion can be represented as:

$$\alpha J_1 + \sqrt{J'_2} = k' \tag{2.9}$$

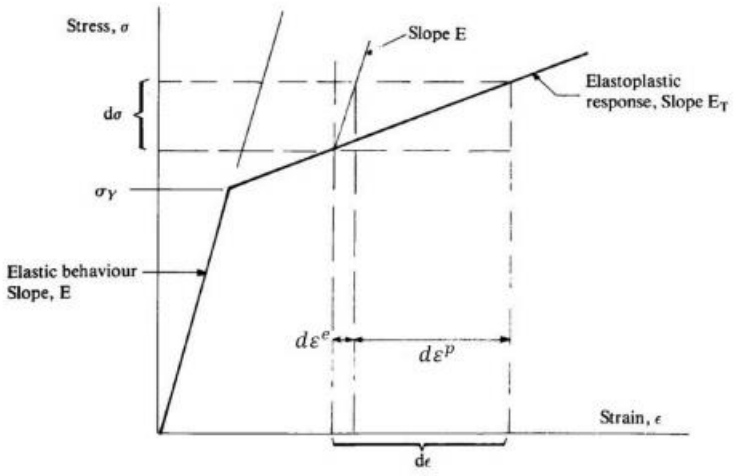

Figure 2.6 The elastoplastic response curves.

In this equation, $\alpha = \frac{2\sin(\phi)}{\sqrt{3}(3-\sin(\phi))}$, $k' = \frac{6c\cos(\phi)}{\sqrt{3}(3-\sin\phi)}$, c is cohesion and ϕ is internal friction angle.

The Drucker-Prager criterion is related to octahedral shear stress and shear strain energy is proportional to it.

$$\tau_{oct} = \sqrt{(\frac{2J_2'}{3})} \tag{2.10}$$

The octahedral stress can be explained by the equation below, where the σ_1, σ_2 and σ_3 are principal stresses of the stress state.

Then tangent stress can be calculated by:

$$\begin{aligned}\tau_{oct} &= \sqrt{T_{i(oct)}^{(n)} T_{i(oct)}^{(n)} - s_{oct}^2} \\ &= \frac{1}{3}\left[(s_{11}-s_{22})^2 + (s_{22}-s_{33})^2 + (s_{33}-s_{11})^2\right]^{\frac{1}{2}} \\ &= \frac{1}{3}\sqrt{2I_1^2 - 6I_2} = \sqrt{\frac{2}{3}J'_2}\end{aligned} \tag{2.11}$$

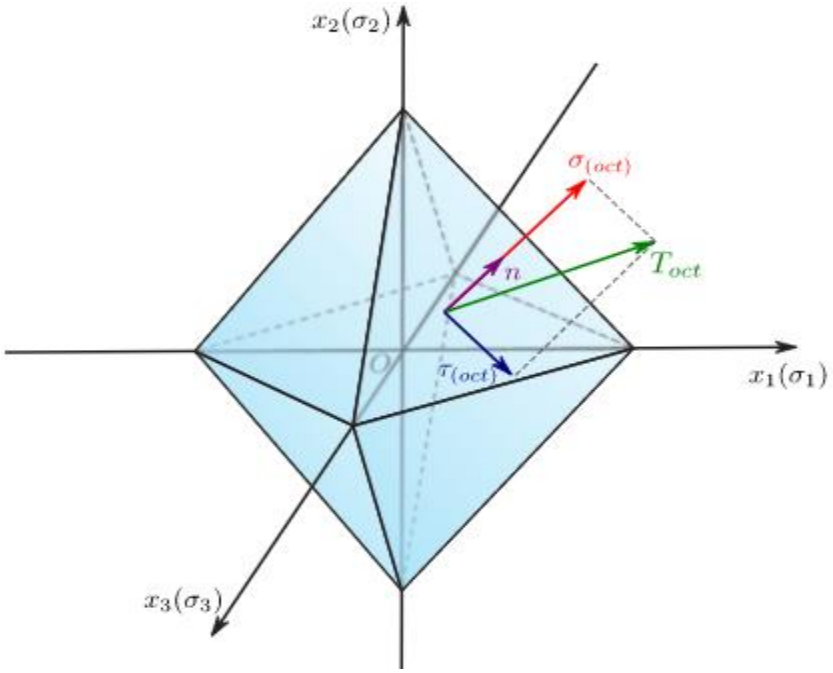

Figure 2.7 octahedral stress

The criterion represented in $\sigma_1, \sigma_2, \sigma_3$ is shown in the graph below. According to the definition of Drucker-Prager criterion, the envelope should have a cone shape.

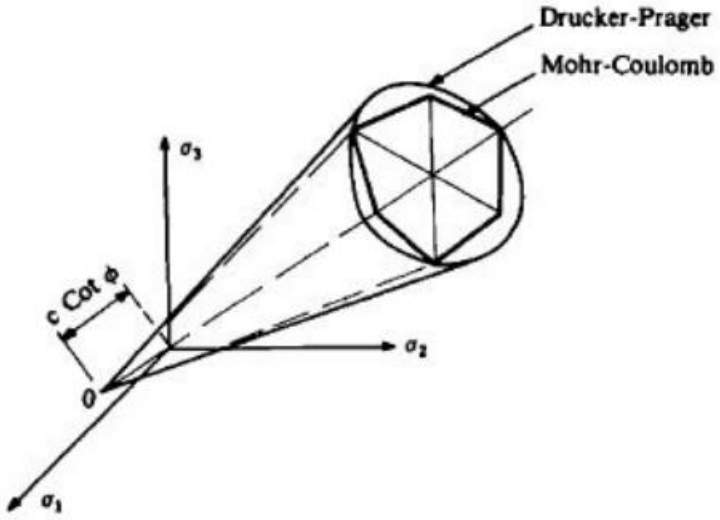

Figure 2.8 The envelope of Drucker-Prager and Mohr-Coulomb in 3-axial stress state, note $\sigma_1, \sigma_2, \sigma_3$ is principal stress.

According to the stress-strain curve, after yielding, the slope of the material will change. The current stress state will influence next time step. To determine the ductile flow direction, we assume associative flow rule so that the ductile flow direction is perpendicular to the yielding surface.

$$d\varepsilon_{ij}^{p} = d\lambda \frac{\partial f}{\partial \sigma_{ij}^{e}} \tag{2.12}$$

The direction of ductile flow can be calculated using the equation above, where f is the loading function and $d\lambda$ is a scaler parameter related to the plastic deformation.

In the formation, we assume the yield function is:

$$f = \sqrt{S_{ij}S_{ij}} - g(J_1) \tag{2.13}$$

Then the equation can be rewritten as follow:

$$d\varepsilon_{ij}^{p} = d\lambda \frac{\partial f}{\partial \sigma_{ij}^{e}} = d\lambda \left(\frac{S_{ij}}{\sqrt{S_{ij}S_{ij}}} - g'(J_1)d_{ij} \right) = \frac{d\lambda\, S_{ij}}{\sqrt{S_{ij}S_{ij}}} \tag{2.14}$$

Integrating the equation above, we can get the plastic deformation. As the ductile flow progresses, the formation strength will increase, thus the strain hardening for the plastic strain is given by:

$$e^{p} = \int \sqrt{\frac{2}{3} d\epsilon_{ij}^{p} d\epsilon_{ij}^{p}} \tag{2.15}$$

Then the equation for the rock constitutive relationship can be rewritten as:

$$\epsilon_{ij} = \frac{1+v}{E}\sigma_{ij}^{e} - \frac{1+v}{E}\sigma_{kk}^{e}\delta_{ij} - \frac{1-2v_m}{E_m} p\delta_{ij} + \epsilon_{ij}^{N} + \epsilon_{ij}^{p} \tag{2.16}$$

2.2.3 Finite element representation

After deriving a differential equation with respect to the displacement, the equation must be discretized for calculating the numerical value. This is done by using the finite element method, which has good performance in getting the approximate solution in geomechanics problems (physical meaning of Virtual Work Principle exists, thus the estimation is good, but this method should not be used to fluid part).

Organize the equations and we can get the finite element equation for geomechanics:

$$\int_{\Omega} B^{T} D B d\Omega [u^{\epsilon}] = \int_{\Gamma} N^{T} t d\Gamma + \int_{\Omega} B^{T} D \varepsilon^{o} d\Omega + \int_{\Omega} B^{T} D \sigma^{o} d\Omega + \int_{\Omega} B^{T} D H_{p} d\Omega \tag{2.17}$$

In the equation above,

B is the derivative matrix of shape function.

N is shape function matrix.

D is deformation matrix containing material elastic and plastic properties.

ε^o is residual deformation.

σ_o is residual stress.

t is external face load applied to element.

H^p is a matrix used to describe pore pressure influence.

Using the weighting residual method to get the weak form for fluid part, the weak equation can be obtained as Eq 2.18.

$$\int_\Omega (\nabla N)^T T (\nabla N) d\Omega [P^{n+1}] - \frac{C(P^n)}{\Delta T} \int_\Omega N^T N d\Omega [P^{n+1}] = -\frac{C(P^n)}{\Delta T} \int_\Omega N^T N d\Omega [P^n] - \int_\Gamma N^T q d\Gamma \qquad (2.18)$$

In this equation,

P^n is pressure at previous time step, P^{n+1} is pore pressure for next time step.

q is fluid flow rate.

T is transmissibility matrix for fluid.

ΔT is time step increment.

2.2.4 Sand production model

When considering sand production during the well operation, we only focus the plastic region because it's the most possible location to release sand. Then calculate the flow rate in this region. The sand production rate is calculated based on the flow rate, viscosity, porosity and other rock and flow properties.

The main flow chart is showed below.

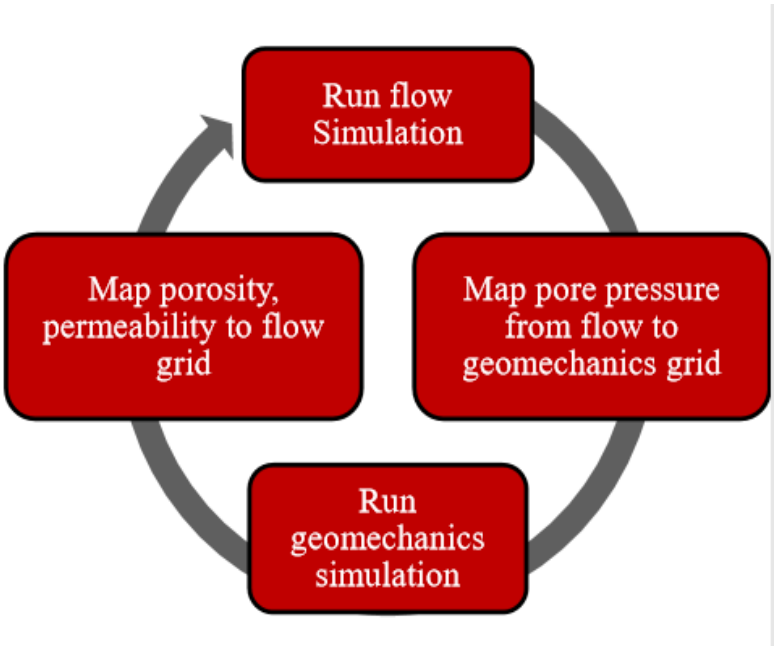

Figure 2.9 Workflow of simulation procedure.

2.2.5 Sand cavity growth mesh

Cavity grows with sand production. The mesh around cavities also evolves with the growth of the cavity. Both meshes for SINTEF cylindrical model and field sand production model for perforation use the same mesh evolution scheme, although the cavity shape is different.

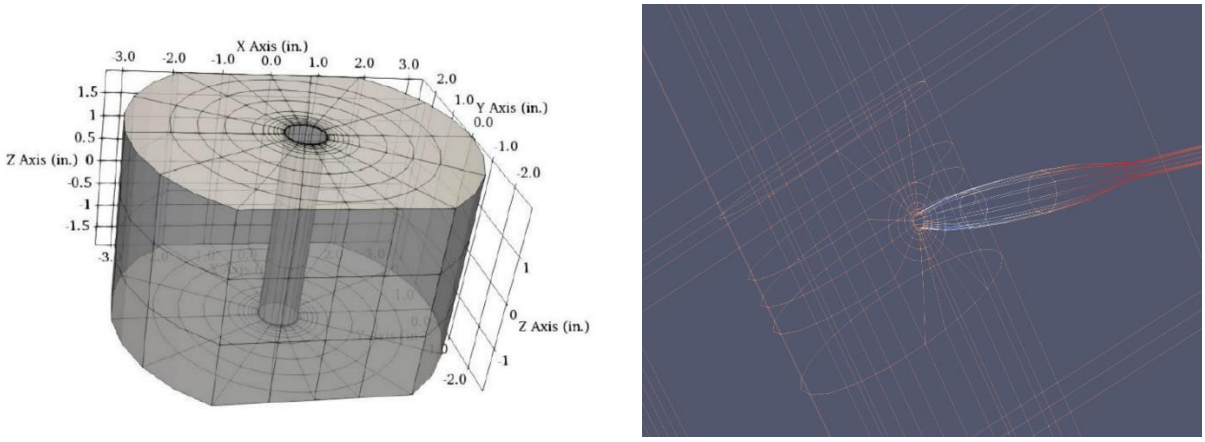

Figure 2.10 The cavity meshing and dimensions (meshes for lab model and field model)

SINTEF experiments uses a circular borehole while the field model uses an ellipsoidal mesh expressed by

$$\left(\frac{x-l}{a}\right)^2+\left(\frac{y}{b}\right)^2+\left(\frac{z}{c}\right)^2=1$$

a, b and c are the radii of ellipsoid.

The inner most layer of element is showed in Fig.2.11. The local nodal numbering is the same for both SINTEF and field models.

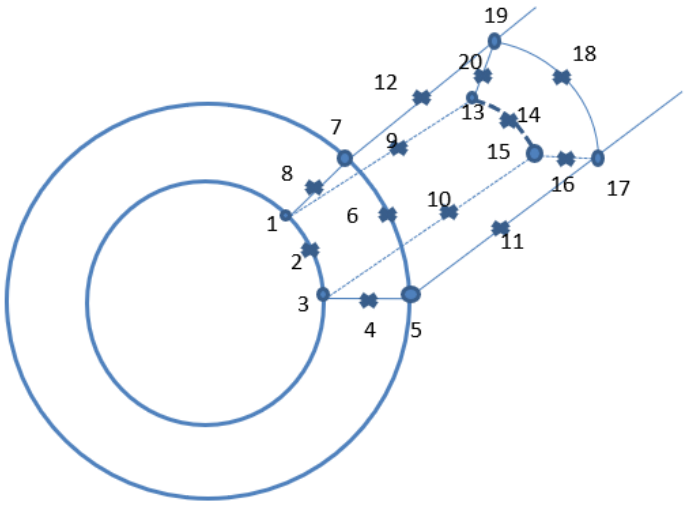

Figure 2.11 Inner most element and numbering

Around the cavity or bottom hole, there are 6 layers of elements in the radial direction. The inner 6 layers of elements will move its boundary due to the sand production.

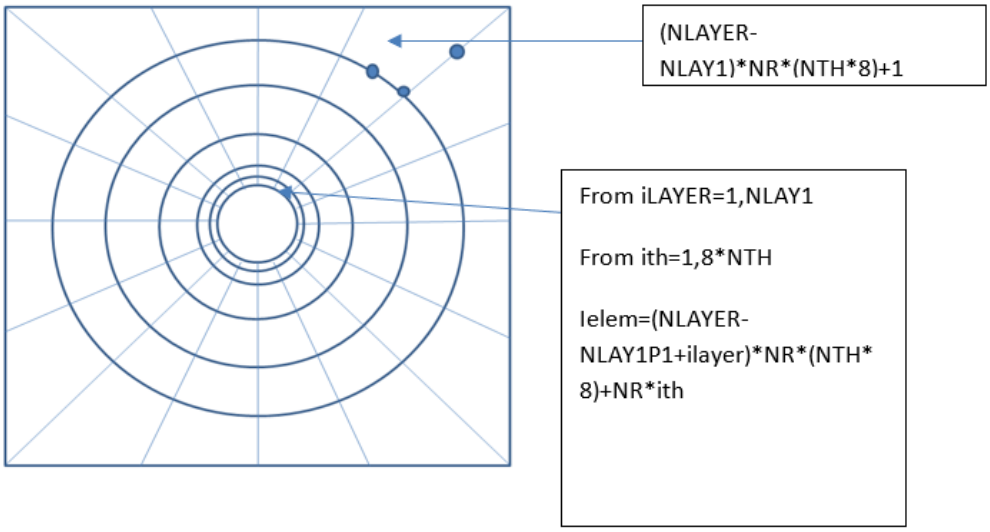

Figure 2.12 Inner layers of mesh.

During the sand production, the sand attached on the wellbore or cavity will be released, and the inner boundary will be enlarged. In order to simulate the growth of the inner boundary, the sand production rate needs to be calculated. According to the sand production volume and the retreat distance of each gaussian points, the boundary movement can be determined.

The pictures below show the gaussian points along the perforation surface.

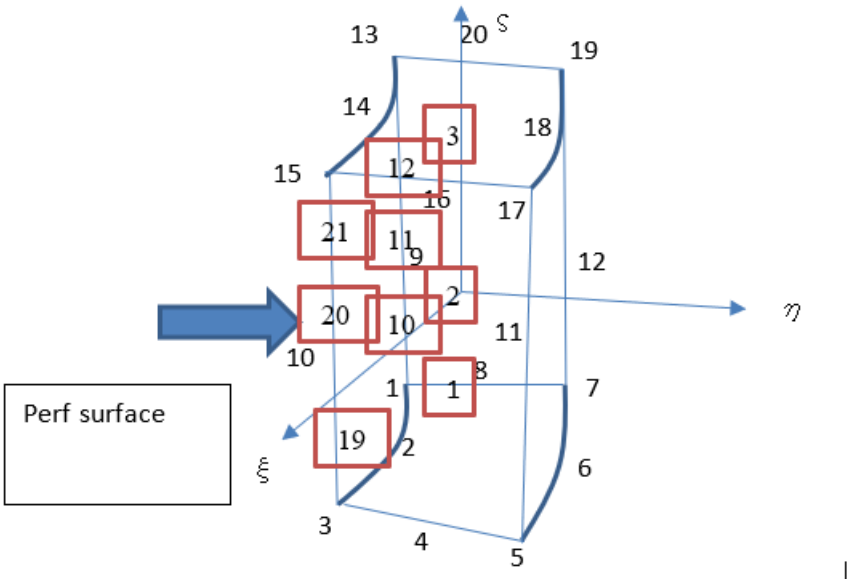

Figure 2.13 Perforation surface nodal and gaussian points numbering.

For each node, the movement is determined by the failure of adjacent gaussian points. For example, the outward-growth of 15th nodal point is calculated by the gaussian point 21 and other gaussian points in other elements surrounding the node 15th .

The detailed steps are shown below for the remeshing scheme.

Step 1: The perforation is initially an ellipsoidal shape (radii a, b, and c and location of the center l remains constant until the plastic strain exceeds a critical strain).

Step 2:

a. Search for the Gauss points with the plastic strain exceeding the critical plastic strain initiating failure: Step N+1
b. Determine curvature Step N+1
c. Determine flow rate Step N+1
d. Q>Qc

No: Keep the cavity surface location at previous location.

Yes: Calculate sand rate Step N+1

Calculate erosion volume Step N+1

Move the cavity surface according to the sand release rate.

Re-calculate all the variables at new mesh coordinate using the N step values

(Note: the coordinate of the new Gauss point is close between Step N+1 and N so that all the variables calculated at N step are used to calculate the variables at N+1. After removing the sand-released region, the plastic strain is reduced below the critical plastic strain)

2.2.6 sand production volume calculation

During oil production, the effective stress near the wellbore increases dramatically resulting in shear failure. After the failure of the region, the failed sand fragments are still adhered to the cavity wall. The sand fragment release rate is determined by the flowrate, density, saturation and viscosity etc. The following equation is used for the sand-mass flow rate, which is constructed by observing laboratory sand rate experiments.

$$\frac{dM_s}{dt} = A_1 \rho_s u_{res} \left[\frac{M_{ref}}{M_w + M_o + M_g}\right]^{A_2} \left(\frac{1-\phi}{\phi}\right) \left[\frac{UCS_{ref}}{UCS}\right]^{A_3} \varphi(\epsilon^p) S_f dS \qquad (2.19)$$

where,

$\frac{dM_s}{dt}$: Sand production rate in gm/sec.

A_1: Loading factor to be determined using experiments and field data.

A_2: Mobility exponent to be determined using experiments and field data.

ρ_s: Solid mass density (gm/cc).

u_{res}: Fluid velocity at reservoir conditions (cm/sec).

M_i: In-situ mobility (i = water(w), oil(o), gas(g)) in md/cp.

M_{ref} : Reference mobility from experiment/field in md/cp.

ϕ: Porosity.

S_f: Fraction of failure area.

A_4: A coefficient used to adjust the decline rate for plastic failure.

UCS: Uniaxial compressive strength.

$\left[\frac{UCS_{ref}}{UCS}\right]^{A_3}$: The coefficient used to adjust the sand removal rate respect to reference UCS.

$\varphi(\epsilon^p)$: The difference of plastic strain and critical value.

ϵ^p: The critical value, which means the sand could be produced at this point.

Eq. 2.19 is derived with the following steps. It is assumed that the release rate of particles from cavity surface or velocity of solid removed from cavity surface is proportional to the fluid velocity flowing through pore.

$$\frac{dM_s}{dt} \propto \rho_s u_{res}\left(\frac{1-\phi}{\phi}\right) \tag{2.20}$$

Since the release rate is higher for a high mobility fluid, we have

$$\frac{dM_s}{dt} \propto \rho_s u_{res} \left(\frac{1-\phi}{\phi}\right) \rho_s u_{res} \left[\frac{M_{ref}}{M_w + M_o + M_g}\right]^{A_2} \tag{2.21}$$

where M_{ref} is the reference-mobility which is used for the experiments to determine the coefficients used in the empirical equation. Note that if $A_2 = 1$, the sand rate becomes proportional to the pressure gradient at the cavity surface. Since the sand erosion rate may depend on both the pressure gradient and mobility, A_2 should be determined by experiments.

The sand particle release rate is considered here as a transient process. If the confining stress is increased, the plastic strain exceeds the critical failure strain. The particles in the failure zone where the plastic strain exceeding the critical strain is released with exponential decline with respect to time.

The transient particle release rate is given by:

$$\varphi(\epsilon^p) = \sum_i (\epsilon_i^p - \epsilon_c^p) e^{-A_4(t-\tau)} \tag{2.22}$$

Thus the $\varphi(\epsilon^p)$ can be represented as:

$$\int_0^t \varphi(\epsilon^p)\, dt = (\epsilon_i^p - \epsilon_c^p) \int_0^t e^{-A_4(t-\tau)} d\tau = \frac{(\epsilon_i^p - \epsilon_c^p)}{A_4} (1 - e^{-A_4 t}) \tag{2.23}$$

Or, for each time step, we have

$$\Delta M_s \propto \rho_s u_{res} \left(\frac{1-\phi}{\phi}\right) \rho_s u_{res} \left[\frac{M_{ref}}{M_w + M_o + M_g}\right]^{A_2} \frac{(\epsilon_i^p - \epsilon_c^p)}{A_4} (1 - e^{-A_4 t}) \Delta t \tag{2.24}$$

For laboratory model, the measurement is short so that $1 - e^{-A_4(t-\tau)} \sim A_4 \Delta t$ or

$$\varphi(\epsilon^p) = \sum_i (\epsilon_i^p - \epsilon_c^p)$$

$$\Delta M_s \propto \rho_s u_{res} \left(\frac{1-\phi}{\phi}\right) \rho_s u_{res} \left[\frac{M_{ref}}{M_w + M_o + M_g}\right]^{A_2} (\epsilon_i^p - \epsilon_c^p)\Delta t \tag{2.25}$$

On the other hand, for field model, the sand release rate remains affecting at ∞. However, if the incremental time step is more than several days, it is approximated by

$$\Delta M_s \propto \rho_s u_{res} \left(\frac{1-\phi}{\phi}\right) \rho_s u_{res} \left[\frac{M_{ref}}{M_w + M_o + M_g}\right]^{A_2} \frac{(\epsilon_i^p - \epsilon_c^p)}{A_4} (1 - e^{-A_4 \Delta t})\Delta t \tag{2.26}$$

, neglecting the sand rate for $\Delta t < t < \infty$.

A weak sandstone disintegrates into sand grains if the plastic strain exceeds the critical plastic strain while a strong rock disintegrates into rock fragments consisting of bonded grains. Therefore, the sand mass release rate may depend on $\left[\frac{UCS_{ref}}{UCS}\right]^{A_3}$. Then, the final sand mass release rate is expressed by

$$\frac{dM_s}{dt} = A_1 \rho_s u_{res} \left[\frac{M_{ref}}{M_w + M_o + M_g}\right]^{A_2} \left(\frac{1-\phi}{\phi}\right) \left[\frac{UCS_{ref}}{UCS}\right]^{A_3} (\epsilon_i^p - \epsilon_c^p) e^{-A_4 t} S_f dS \tag{2.27}$$

The description of sand production given by this model can be summarized as follows:

(A) Sand is mostly produced as transient. The sand production continues for several hours to several days if the effective stress is not increased. The sand production continues if the stress around cavities increases with reservoir pressure depletion.

(B) The average sand production rate increases with increasing flow rate.

(C) The average sand production rate increases with a higher-pressure gradient at cavity surface.

(D) The average sand rate increases with a lower rock strength.

Even if the rock stress exceeds the failure stress, the sand particles are not released from the cavity surface due to the sand arch effect. Based on sand-arch experiments, the following equation is used to induce sand from failed perforation cavity.

The minimum flow rate required to remove sand particles from cavity surface

Sand particles are not released from the perforation cavity surface even after formation failure if the curvature of the cavity is small and the capillary pressure is large enough. Previous experiments derived the following equations for sand particles to be detached from failed cavity surface. For half spherical cavity, the critical flow rate can be calculated and estimated via equations 2.28, 2.29 and 2.30.

1) Fluid is pure oil

$$q(bbl/\text{ day / perf }) = 0.59[k(\text{ darcy })/\mu(cp)]R(inch) \times \left[p_c(psi)\beta_f + 2\tau_f(psi)\right] \tag{2.28}$$

$$p_c = \phi S_w p_{cap}$$

$$\beta_f = 2\tan^2\ \alpha_p - 2 = 2\tan^2\ 60^\circ - 2 \approx 4$$

$$\tau_f(psi) = 8 \times 10^{13}\left(D_{50}/D_{\text{cavity}}\right)^{14.52}$$

$\alpha_p = (\phi_0 + \pi/2)/2$ where ϕ_0 is the internal friction angle.

Then we can get the critical flow rate per unit area:

$$q/(2\pi R^2) = 0.59R(\text{ inch})/(2\pi R^2) \times \left[p_c\beta_f + 2\tau_f\right]$$

$$\hat{q}_c = 0.59k/\mu/2\pi R \times \left[C_{correction}p_c\beta_f + 2\tau_f\right] \quad (2.29)$$

The unit of q is $bbl/$ day $/$ perf, for $\hat{q}_c$ is $bbl/day/in^2$, R is inch, $p_c\ and\ \tau_f$ is psi.

2) Fluid is pure gas

$$q/(2\pi R^2) = 3.313[k/\mu]R/(2\pi R^2) \times (p_c\beta_f + 2\tau_f)$$

$$\hat{q}_c = 3.313[k/\mu]/(2\pi R) \times (C_{\text{correction}} \times p_c\beta_f + 2\tau_f) \quad (2.30)$$

The unit of q is $f^3/day/$perf and $\hat{q}_c$ is $ft^3/day/in^2$.

In the equations above, the parameters meaning are listed below.

R: sand arch radius (in.)

$\bar{p}_c = \phi S_w p_{capillary}$ ϕ=porosity, S_w=water saturation, $p_{capillary}$=capillary pressure

$C_{correction} = 0.14$

D_{50}, D_{Cavity}=median sand diameter, cavity radius

$\beta_f = 2\tan^2(\phi_{friction}/2 + \frac{\pi}{4}) - 2 \approx 4:\ \phi_{friction=}30^o$

$$\tau_f(psi) = 78753e^{-1.227(D_{cavity}/D_{50})} \text{ or, } \tau_f(psi) = 8\times10^{13}(D_{50}/D_{cavity})^{14.52}$$

Sand arch strength estimation

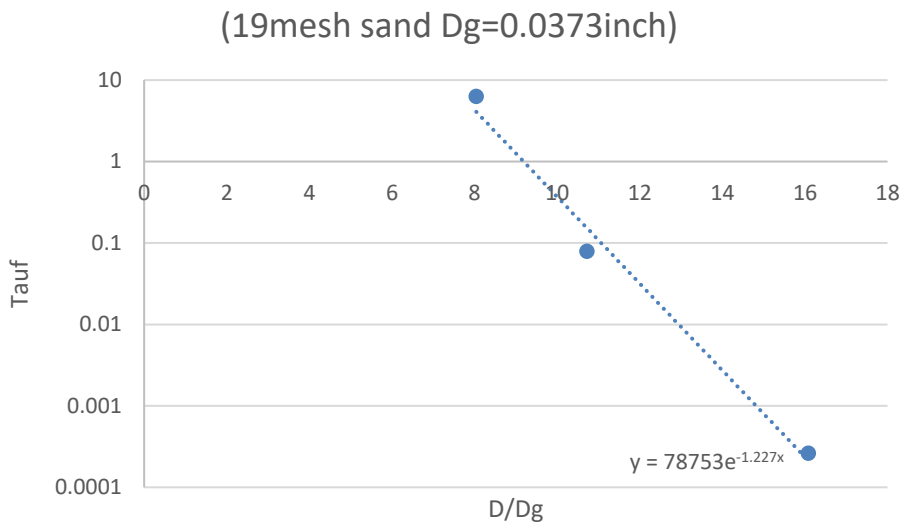

Figure 2.14 Interpolation with an exponential function for sand arch strength (Dg=Median diameter of grain size, D=diameter of cavity)

From cavity strength test with fluid flow, we have the following experimental data

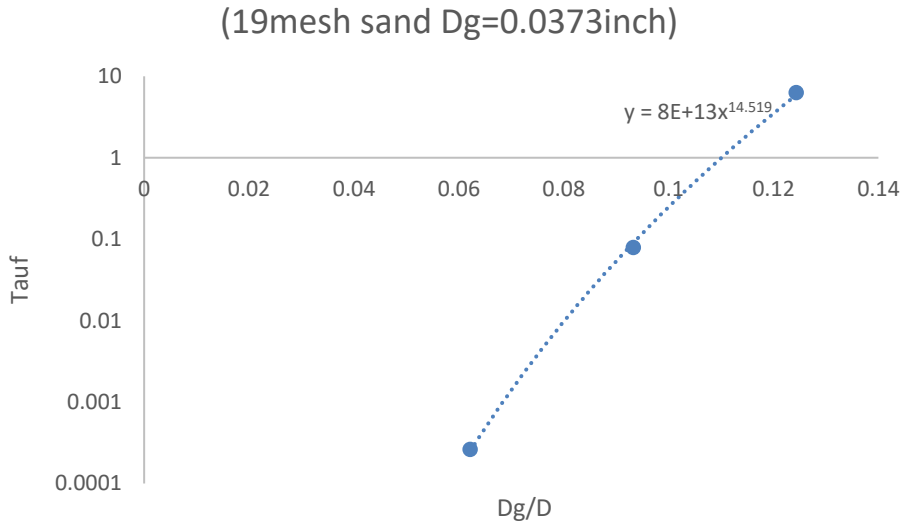

Figure 2.15 Interpolation with a power function for sand arch strength (Dg=Median diameter of grain size, D=diameter of cavity)

CHAPTER III DETERMINATION OF SAND-RELEASE RATE COEFFICIENT USING SINTEF EXPERIMENTS

3.1 Mechanical properties for Castlegate sandstone used for the triaxial sand rate measurement tests.

Castlegate sandstone used for the experiments have medium strength with UCS=2056 psi. The porosity is between 26-27%. The permeabilities between the samples vary between 490 md to 820 md. Lade yield model is used for constructing the constitutive equation.

Lade yield model

Lade model can be easily fitted to empirical yield values by introducing k, where the equation becomes identical to Drucker-Prager for k=1 (Figure 3.1). The loading function t is given by the following equation.

$$S_{ij} = \sigma_{ij} - \sigma_m \delta_{ij}$$

$$\tau = \sqrt{\frac{1}{2} S_{ij} S_{ij}} \qquad (3.1)$$

$$r = \left(\frac{27}{2} J_3\right)^{1/3}$$

$$J_3 = S_{11}S_{22}S_{33} + 2S_{12}S_{23}S_{31} - S_{11}S_{23}^2 - S_{22}S_{13}^2 - S_{33}S_{12}^2$$

$$t = \frac{1}{2}\tau\left[1 + \frac{1}{k} - \left(1 - \frac{1}{k}\right)\left(\frac{r}{\sqrt{3}\tau}\right)^3\right] \qquad (3.2)$$

$$t = g(\sigma_m),\ 0 < k < 1 \tag{3.3}$$

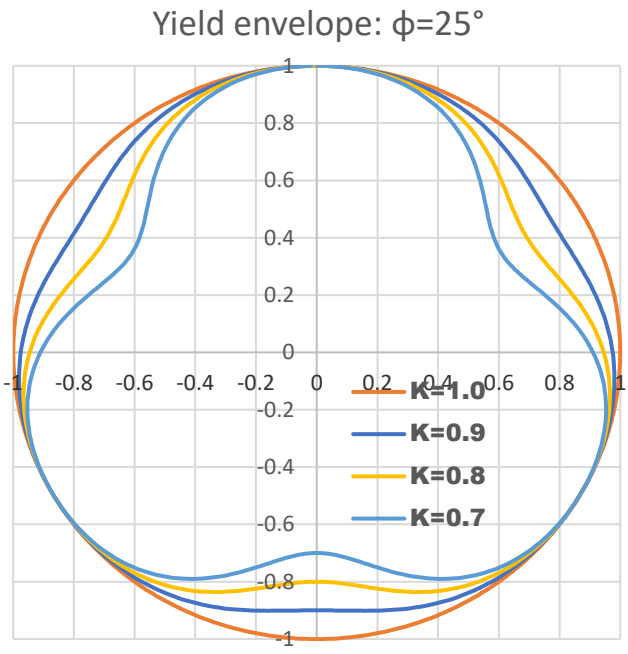

Figure 3.1 yield envelope for different type of failure criterion.

k=1 for Drucker-Prager. Strain hardening constitutive relation based on the Lade yield model is used.

$$t + G(\bar{J}1) = S_o^y + \int \exp(B_1 + B_2 K + B_3 K^2 + ...) dK \tag{3.4}$$

K is given by the following relation for strain hardening problems.

$$K = \varepsilon^p \tag{3.4}$$

The unknown coefficients in $G(J_1)$ and B_1, B_2, B_3 ... are determined from the triaxial stress strain curves of the Castlegate sandstone. For the experiments below, we choose k=0.8 to

match the final sand production volume for more accurate estimation, and the result with k=0.84 is attached in the appendix II.

Castlegate triaxial stress strain data

Triaxial stress-strain relation is obtained at different confining pressures as shown in Fig.3.2. Figure 3.3 shows the theoretical constitutive relation with parameters of Eq.3.3 fitted to the measured stress strain curves. Fig.3.4 shows the yield envelope and Figures 3.5 and 3.6 show the failure envelope. The determined coefficients for various yield envelope and failure envelopes are given in appendix table C-1.

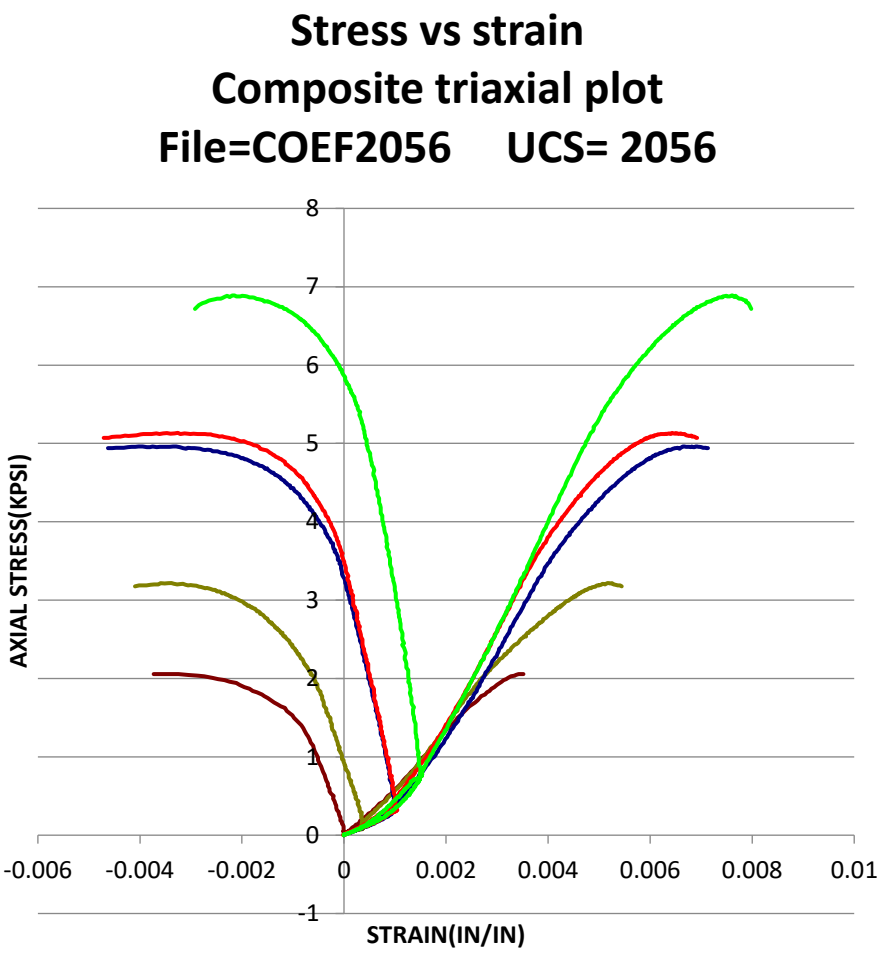

Figure 3.2 Triaxial stress strain curves measured for the Castlegate sandstone used for the sand rate experiments (axial strain on the right and radial strain on the left at 4 different confining pressures)

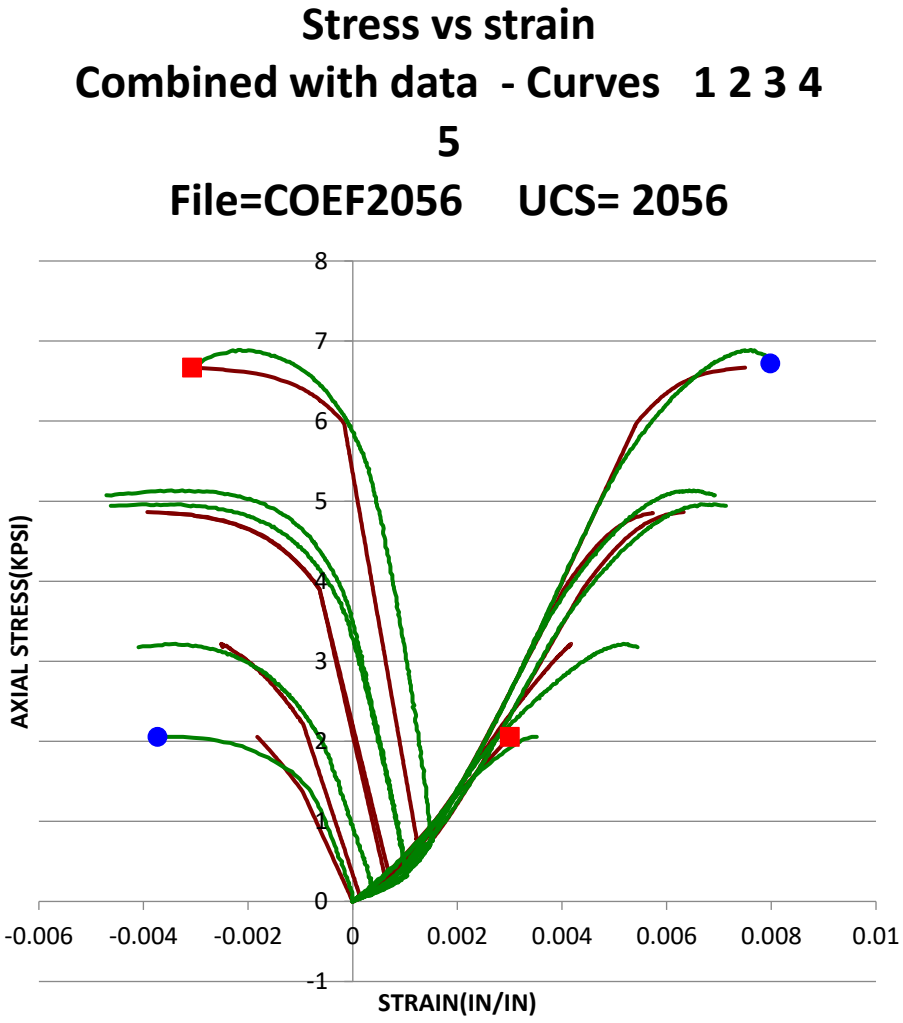

Figure 3.3 Theoretical constitutive relation with parameters of Eq.3.3 fitted to the measured stress strain curves

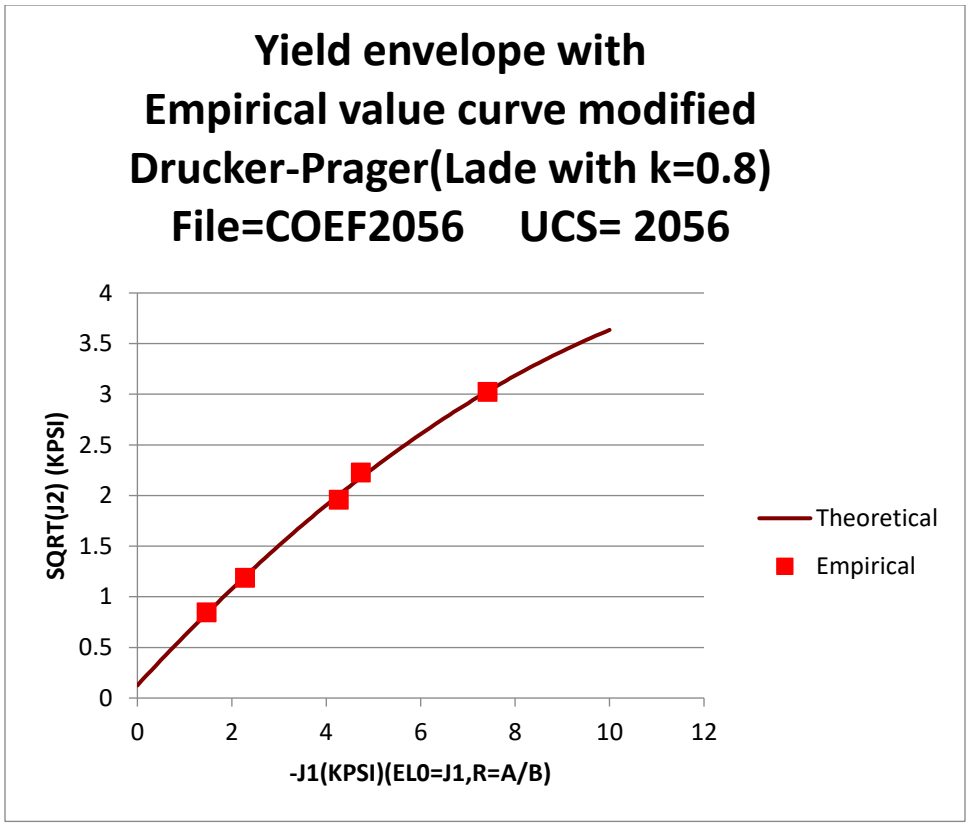

Figure 3.4 Yield envelope

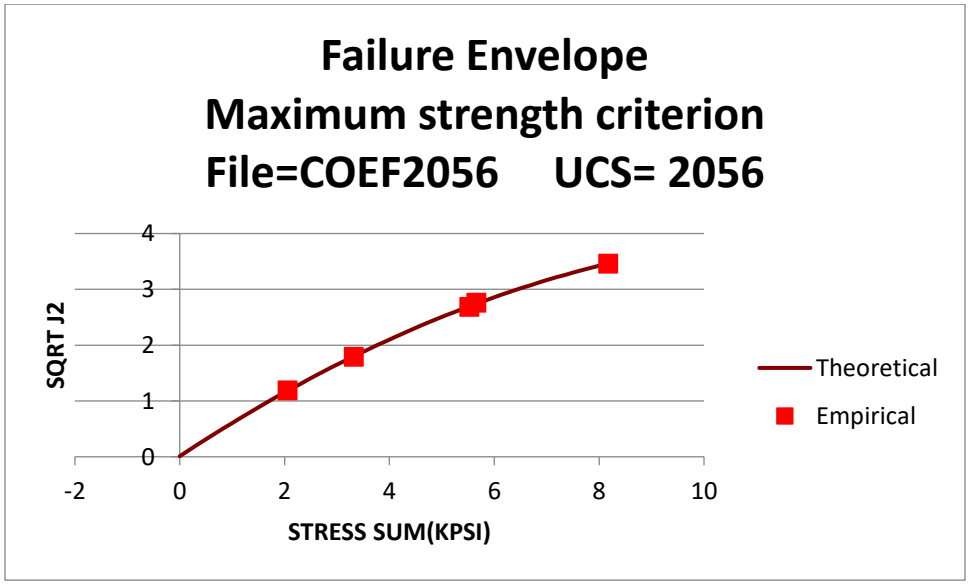

Figure 3.5 Failure envelope based on the maximum strength criterion

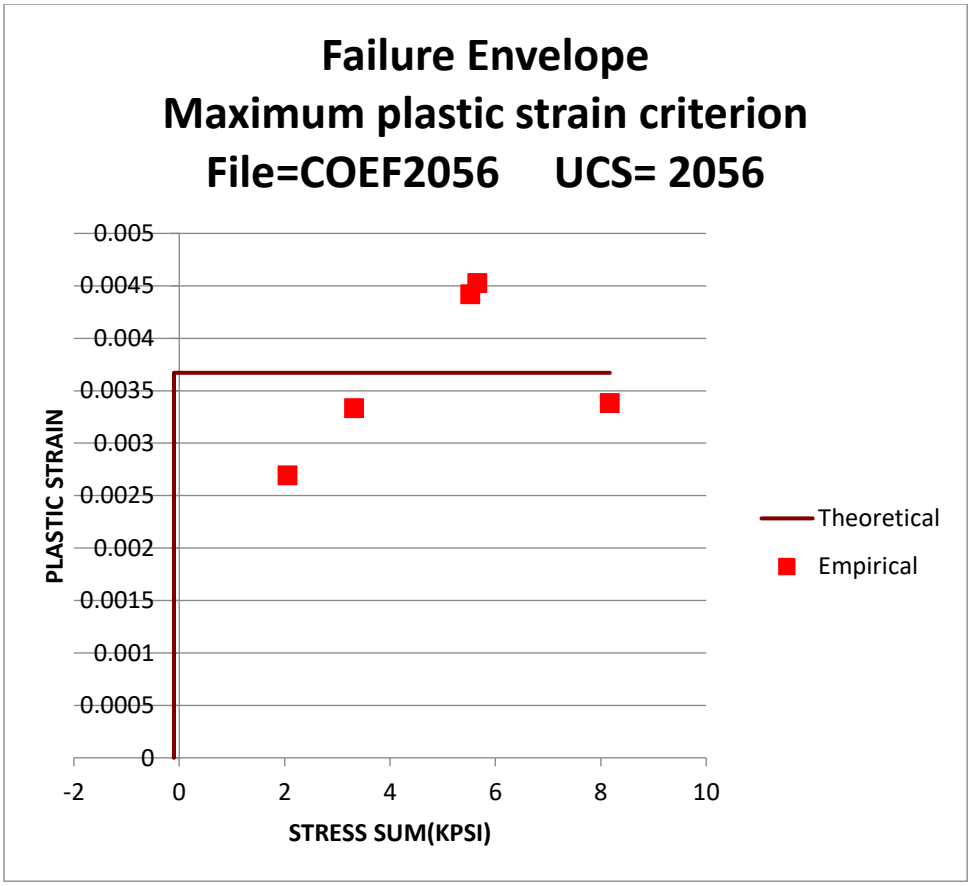

Figure 3.6 Failure envelope based on the critical plastic strain.

3.2 Determination of sand-release rate coefficient using SINTEF triaxial sand-rate tests

According to the stress state of the onset of sand production and triaxial stress strain curves of Castlegate sandstone, k = 0.8 has been chosen for the Lade yield model. For each experiment, sand production onset time, final sand volume or trend are matched. All the experiments will be discussed in details in each section.

Table 3.1 Summary table of experimental conditions to determine A1.

		Sr(kpsi)	SR	Sz	porosity	K(darcy)	dP(psi)	DT(Day)	Sr/SR	Sz/SR	A1(k=0.8)	A1(k=0.8)
Case1	303	2.83	7.96	8.07	0.264	0.82	0.00964	0.132	0.355528	1.013819	5.50E-03	5.50E-03
Case2	302b	6.644	9.894	9.96	0.264	0.49	0.01615	0.311	0.671518	1.006671	3.00E-03	3.00E-03
Case3	304	4.825	7.192	12.81	0.266	0.6	0.01318	0.1231	0.670884	1.781146	6.00E-03	6.00E-03
Case4	305	4.642	6.927	4.667	0.266	0.5	0.01582	0.1575	0.670131	0.67374	8.40E-03	8.40E-03
Case5	306	5.936	8.7138	7.256	0.264	0.8	0.009889	0.147	0.681218	0.832702	5.00E-03	5.00E-03
Case6	308	5.3098	5.3098	5.3098	0.267	0.72	0.01098	0.15585	1	1	1.30E-02	
Case7	311	2.95239	8.7646	2.94716	0.261	0.6	0.013185	0.144	0.336854	0.336257	4.10E-03	4.10E-03
Case8	312	5.3526	7.9872	11.283	0.265	0.6	0.013185	0.13	0.670147	1.412635	1.00E-02	1.00E-02
Case9	314	2.789	8.2831	5.8856	0.265	0.53	0.014926	0.136	0.33671	0.710555	4.00E-03	4.00E-03
Case10	315	4.74	4.75	10.01	0.261	0.49	0.01615	0.138	0.997895	2.107368	1.70E-02	
Case11	316	5.3707	5.4287	5.3867	0.266	0.66	0.011986	0.1318	0.989316	0.992263	1.50E-02	
Case12	317	3.0907	4.6122	9.9278	0.267	0.6	0.01318	0.1354	0.670114	2.152509	1.80E-02	
Case13	318	2.8804	8.1018	8.2163	0.268	0.82	0.00964	0.158	0.355526	1.014133	8.50E-03	8.50E-03
Case14	302	6.529	6.529	6.529	0.268	0.9	0.00879	0.132	1	1	1.50E-02	
0											9.46E-03	6.06E-03

For the post-processing of the simulation result, we assume the symmetry along the longitudinal direction. The length of the core is 20 cm so that we use 10 cm assuming the symmetry in the longitudinal direction. The flow rate for the experiment is 1.6 L/min so that for the model study, 0.8 L/min is used. The numerical model calculates the volume reduction by Jacobian so that the sand mass calculation is given by $M = (1-\phi) \times \rho_{quartz} \times \Delta V_{vol\_loss} \times 2$. In this equation, ϕ is porosity, x2 represents half model for the calculation.

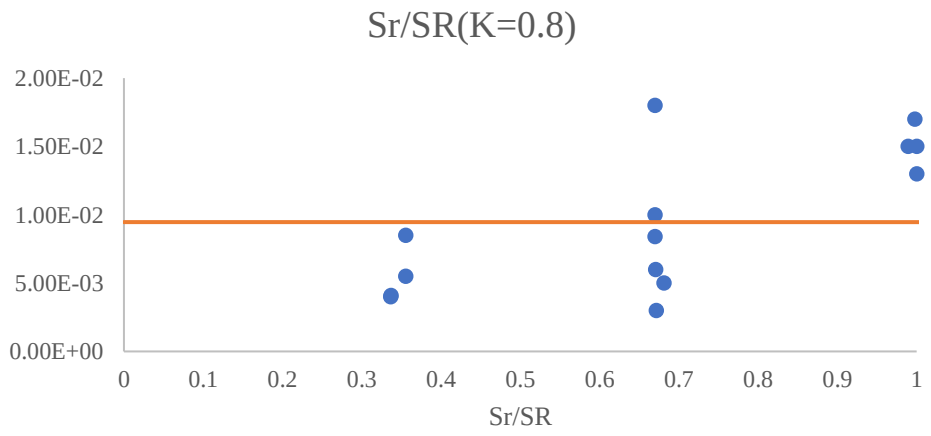

Figure 3.7 Coefficient A1 vs Kr (= Sr/SR) data for each experiment

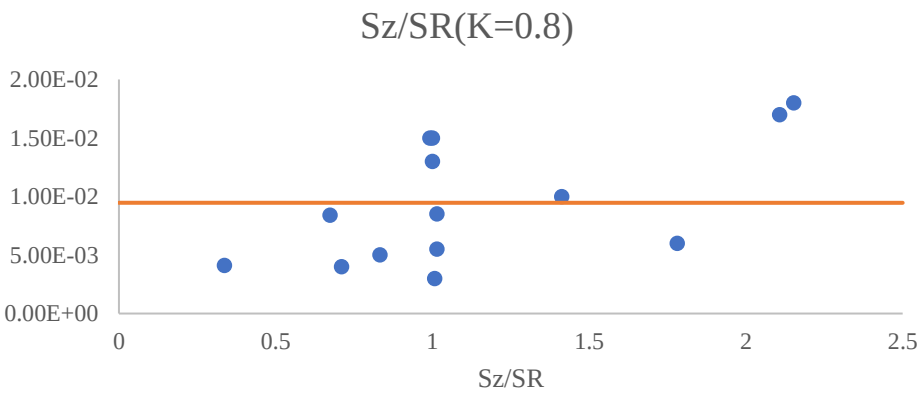

Figure 3.8 Coefficient A1 vs Kz(=Sz/SR) data for each experiment

Figures 3.7 and 3.8 show that if the stress is uniform in tangential direction around the borehole with $\frac{\sigma_r}{\sigma_R} = 1$, the value A_1 becomes high. Examining the failure shape for $\frac{\sigma_r}{\sigma_R} = 1$, all the experimental results show that the failure is induced at a local location and progress in a triangular shape. Based on the failure shape and the location of the failure, it is judged that the heterogeneity of the Castlegate sandstone used for the experiments controls the failure. The local heterogeneity of permeability of Castlegate sandstone is significant and the high channel flow through a high permeability location initiates failure and progresses into a triangular failure shape.

Coefficient A_1 matching the empirical sand rate after removing the cavity evolutions due to heterogeneity is given in Figures 3.9 and 3.10.

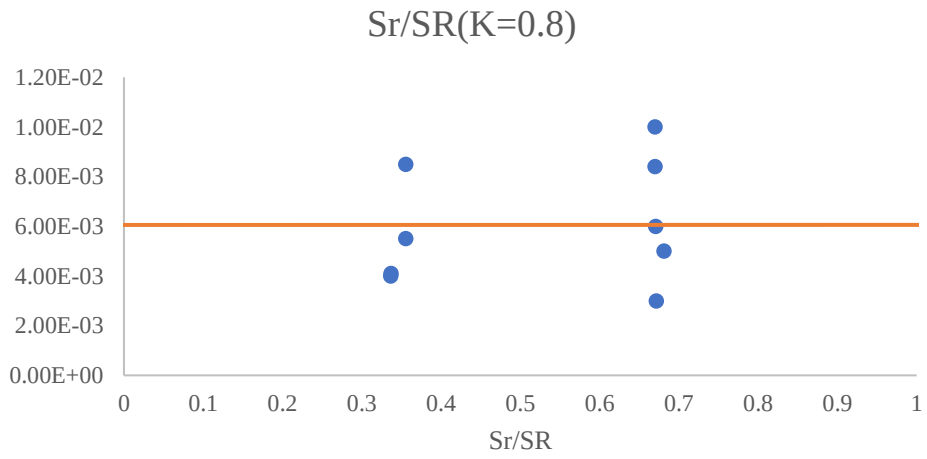

Figure 3.9 Coefficient A1 vs Kr(=Sr/SR) data for each experiment after removing cavity evolutions due to heterogeneity

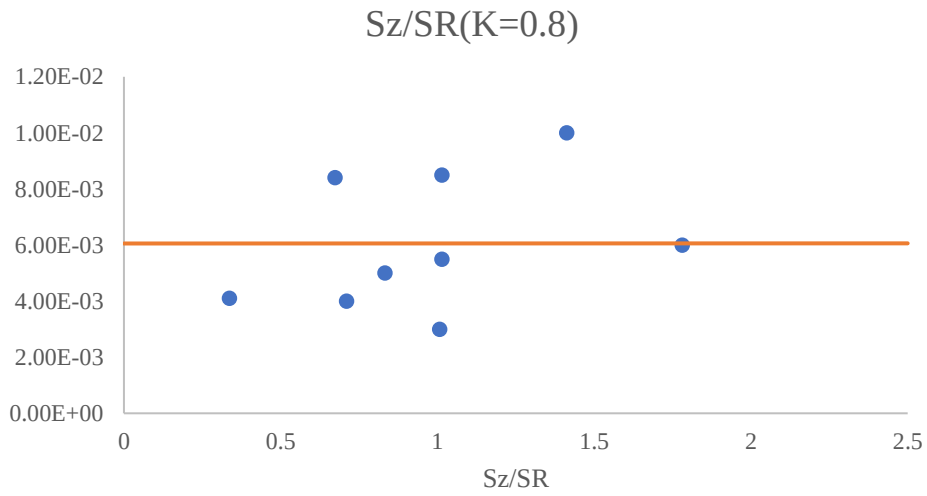

Figure 3.10 Coefficient A1 vs Kz(=Sz/SR) data for each experiment after removing cavity evolutions due to heterogeneity

Case-1 303 kr = 1/3 kz = 1

The simulation conditions for Case-1 are shown in Table 3.2. The stress condition in the vertical direction is isotropic, but for the horizontal direction, the stress is directional with kr = 1/3.

Table 3.2 Fluid and rock properties for kr=1/3 and kz=1.

Height	200 mm
internal diameter of borehole	20 mm
external diameter of sample	200 mm
Permeability	0.82 Darcy
Porosity	0.264
Fluid Type	3.5% NaCl solution and kerosene oil
Fluid density	0.78 g/cm^3
Fluid viscosity	1.4 cp
Quartz density	2.65 g/cm^3
Differential pressure	0.00964 kpsi
Running time	0.132 day
Lade yield coefficient	0.8

Case 1 experiment was performed under the confining stress as recorded in Figs.3.11 and 3.12, where a small confining load is applied during the flow initiation. Thus, when we calculate the simulation time, an offset of start time needs to be reduced. For this experiment, the offset time is about 960s.

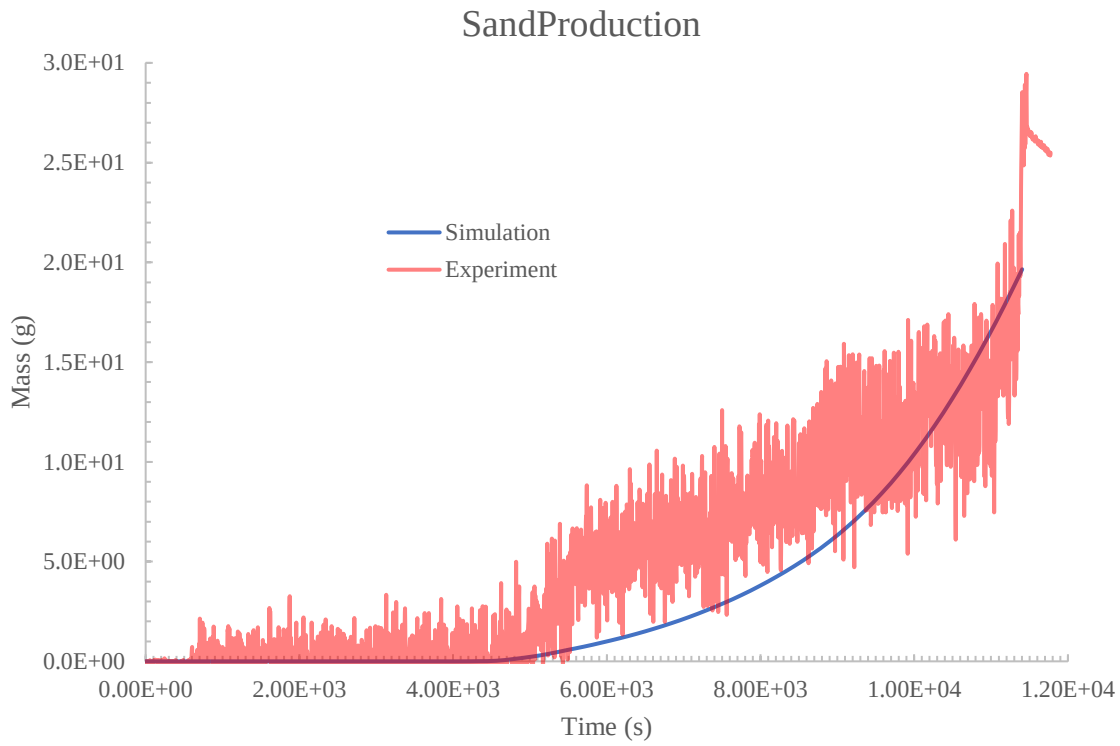

Figure 3.11 Simulation result vs experiment result with kr = 1/3, kz =1.

As shown in Figures 3.11 and 3.12, although the experiments data fluctuate, the stress initiating sand production is about 3100 psi. The model prediction shows about the same sand production initiation time. The empirical sand rate significantly fluctuates, since it is measured under fluid flow with a calibrated digital scale. The scale goes up and down with fluid force. The simulation curve should match the trend of the empirical sand production rather than the final sand mass. According to the data above, the simulation result matches well with the experiment data, however, at the beginning of the sand-production process, there is a sudden increase in sand volume. That may be caused by the sand fragments at the beginning, then the sand-production rate becomes stable.

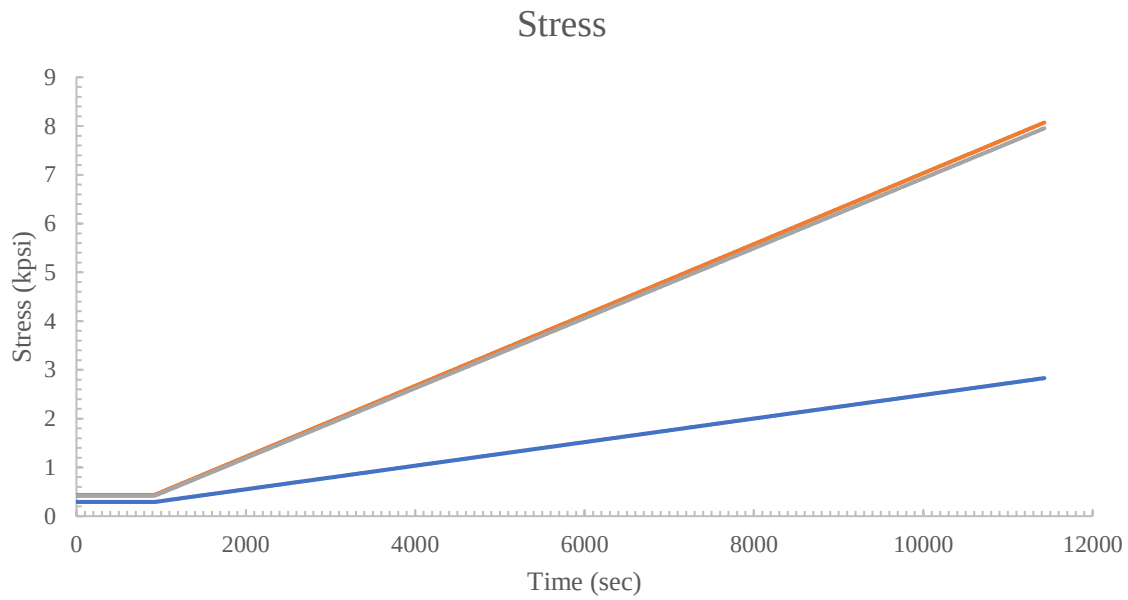

Figure 3.12 Stress load curve

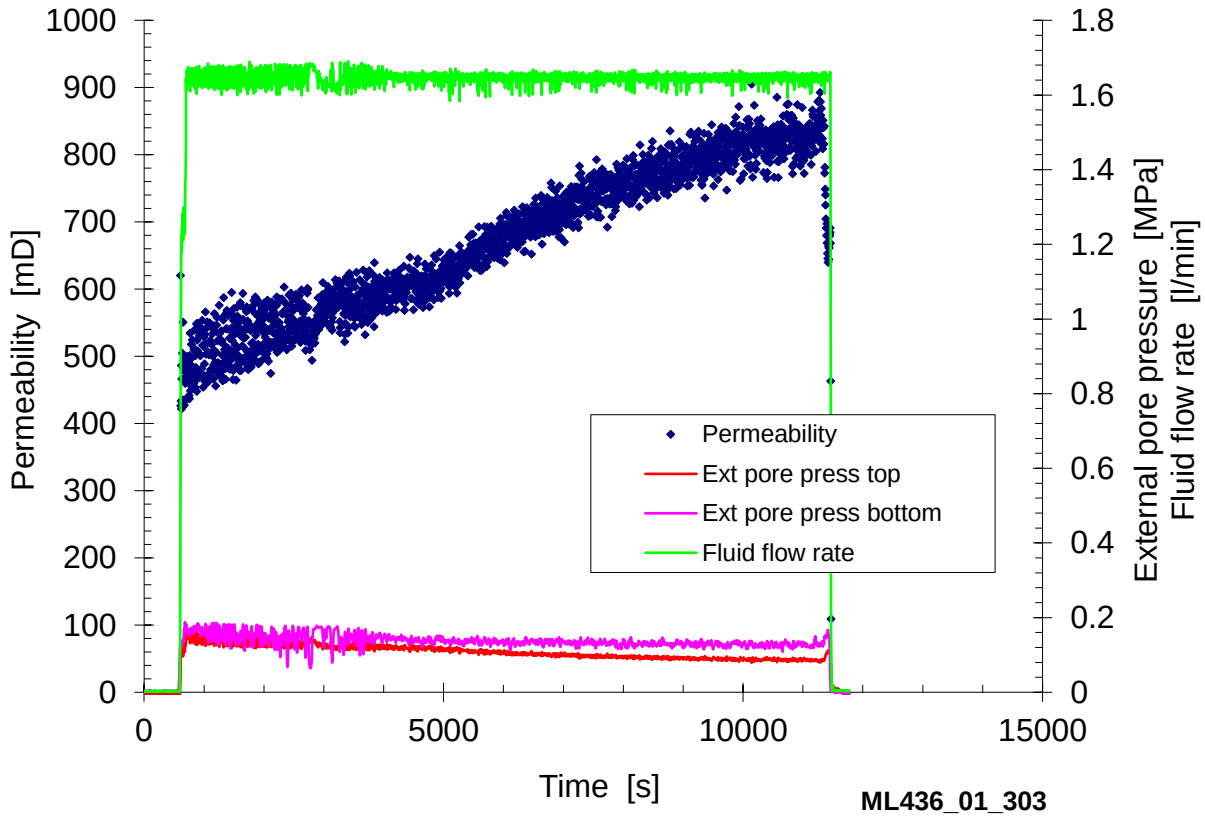

Figure 3.13 Fluid flow rate and pore pressure during experiment with kr=1/3, kz=1

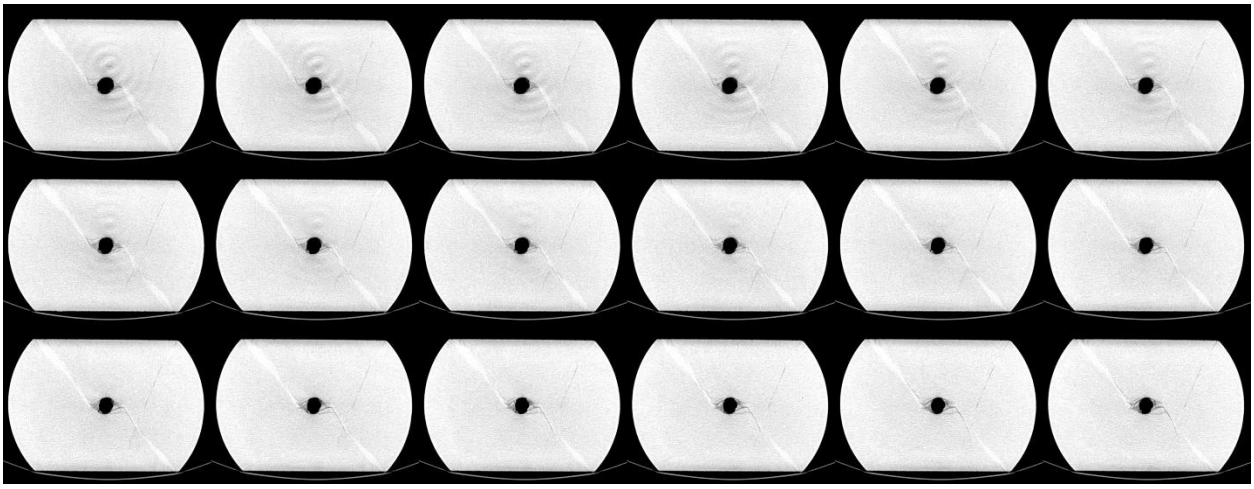

Figure 3.14 rock scanning for each layer with kr=1/3, kz=1

From the rock scanning picture and after-experiment pictures (figure 3.14 and 3.15), the failure shape around inner cavity is not uniform, which can be also proved by bottom pictures below taken after experiment. The hole shape varies a lot with different layer, and the direction of the failure is perpendicular to the minor horizontal stress.

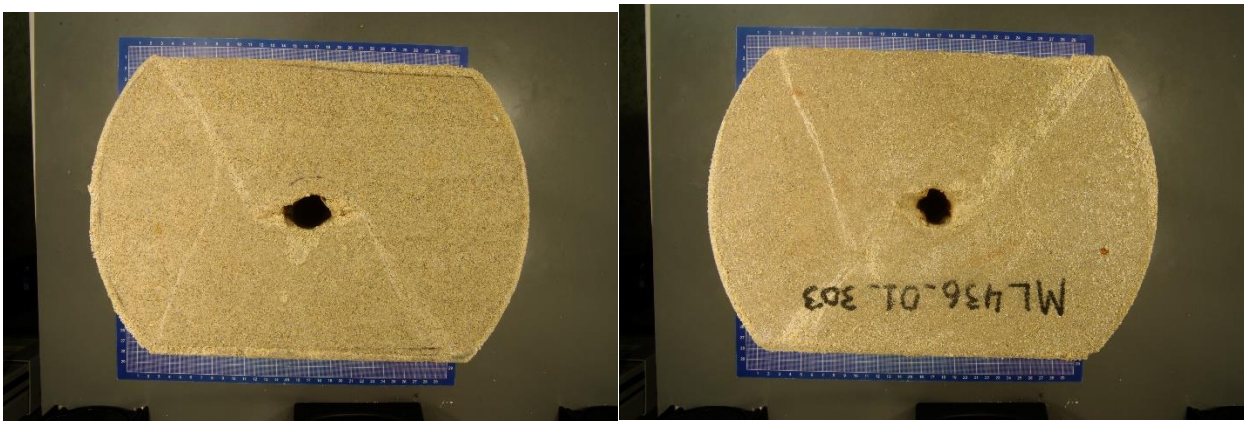

Figure 3.15 Experiment result from bottom and surface with kr=1/3, kz=1

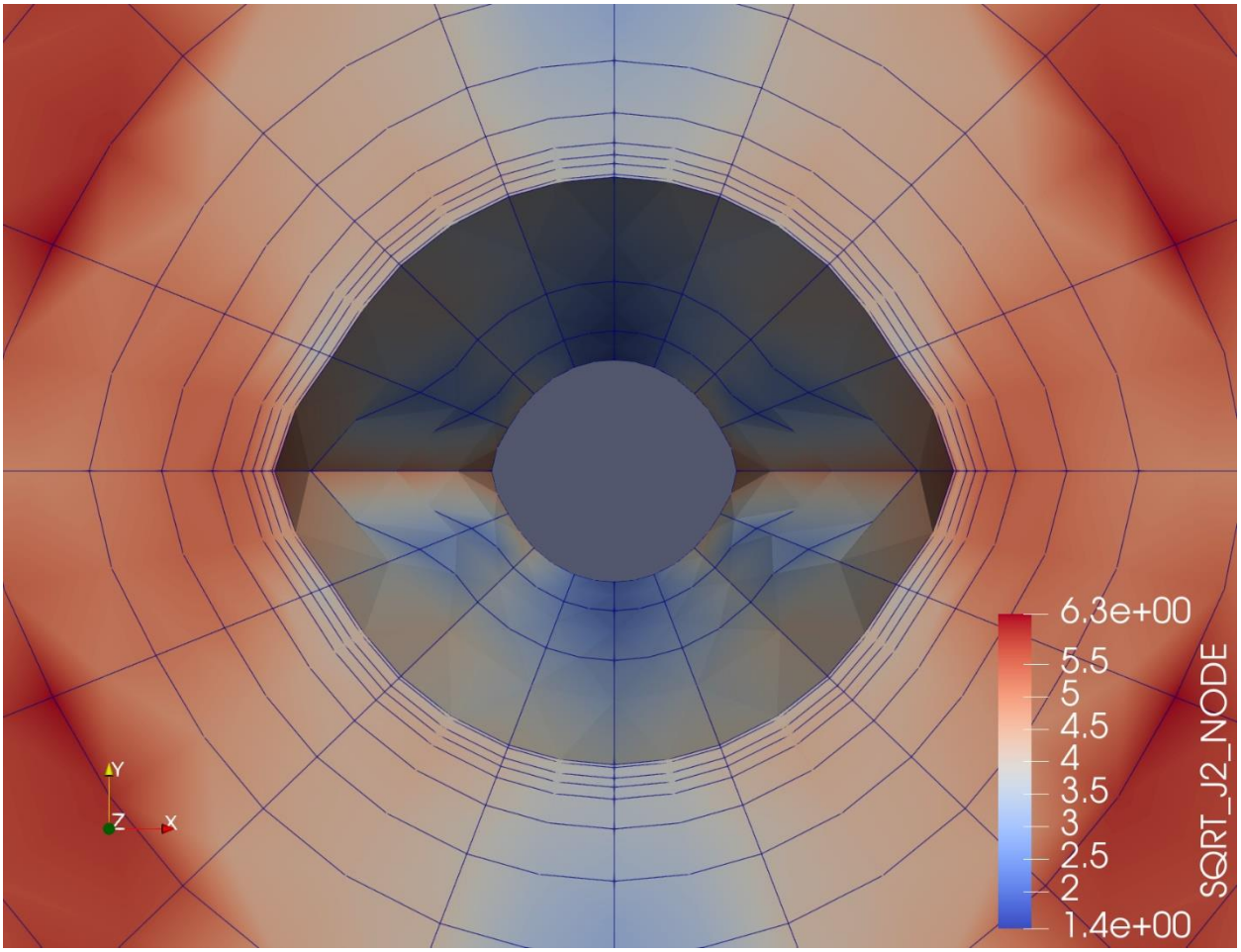

Figure 3.16 Cavity evolution with kr=1/3, kz=1

The simulation result matches experimental result (blue line is in the shadow is the deformation of the original circle).

Case-2 302b kr = 2/3 kz = 1

The simulation conditions for Case-2 are shown in Table 3.3. The stress condition for the vertical direction is isotropic, but, for the horizontal direction, it is anisotropic, kr = 2/3.

Table 3.3 Fluid and rock properties with kr=2/3 and kz=1.

Height	200 mm
internal diameter	20 mm
external diameter	200 mm
Permeability	0.49 Darcy
Porosity	0.264
Fluid Type	3.5% NaCl solution and kerosene oil
Fluid density	0.78 g/cm^3
Fluid viscosity	1.4 cp
Quartz density	2.65 g/cm^3
Differential pressure	0.01615 psi
Running time	0.3110 day
Failure model	0.8
σ_r	6.644
σ_R	9.894
σ_z	9.96

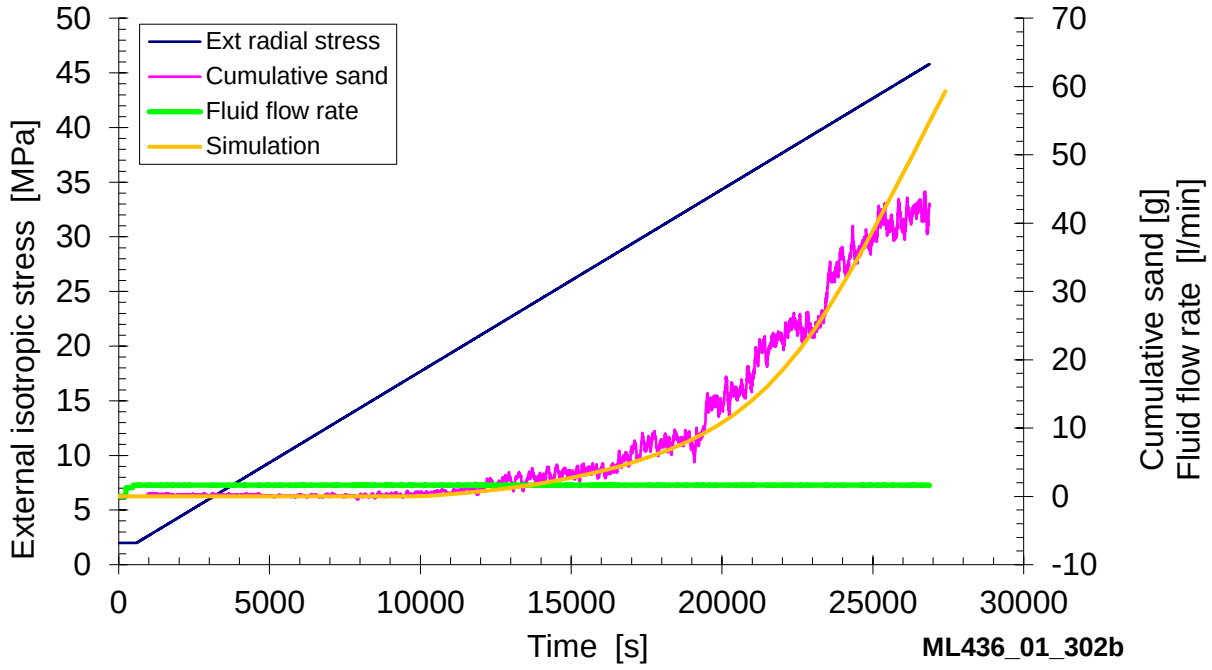

Figure 3.17 Simulation result vs experiment result with kr=2/3 and kz=1.

From Figure 3.17, the experimental sand-production data are more stable, and the total mass production is about 2 times than the first case. Thus, we have the chance to get a clear view of the solid production rule. Using the conditions shown in Table 3.3 to simulate the sand-production, the trend of the experiment curve is matched. Compared with simulation data, the onset time is almost the same, however, sand-production is below our prediction at the early stage after sand production initiation. The main reason is the permeability variation. For simplification of the simulation, we use the average permeability near the end of the experiment. From the permeability vs time plotting, when t>20000 seconds, the change of permeability reaches 500 millidarcy (mD), thus at the beginning, the sand production volume is limited, then the sand production rate increases locally, and goes over our estimation rate.

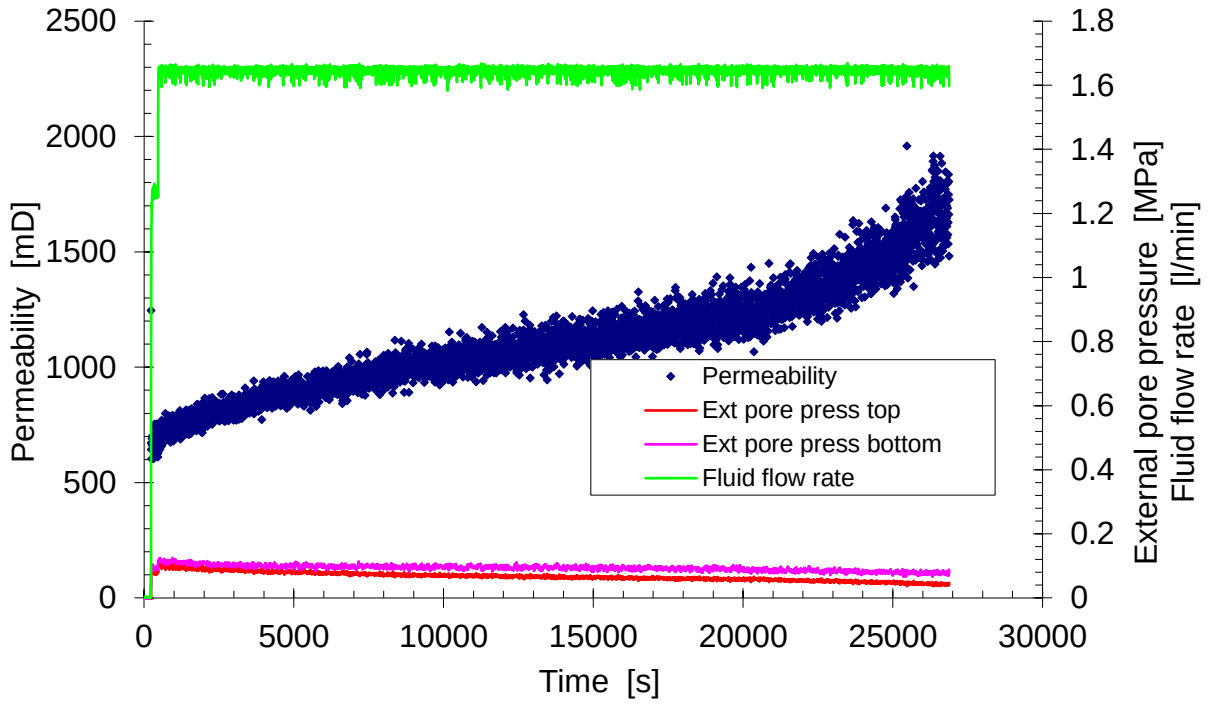

Figure 3.18 Fluid flow rate and pore pressure during experiment with kr=2/3 and kz=1.

The permeability changed a lot during the experiment, especially after the sand production initiation.

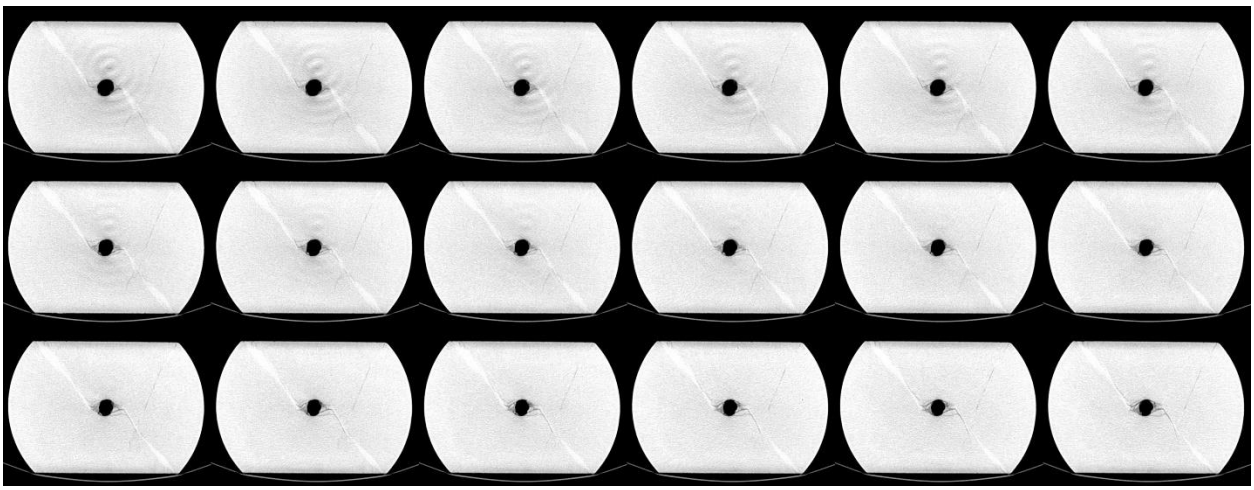

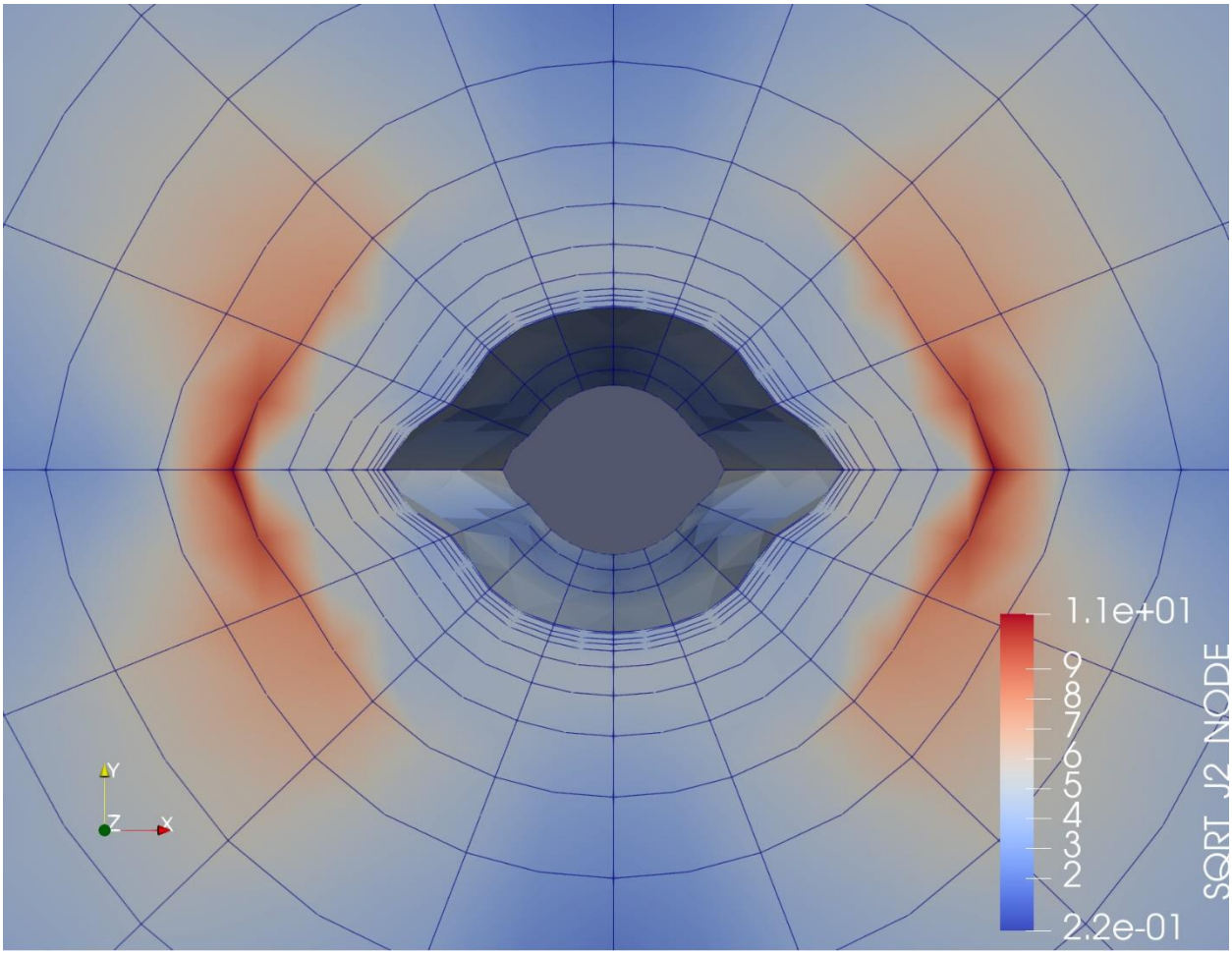

Figure 3.19 Cavity evolution with kr=2/3 and kz=1.

Case-3 304 kr = 2/3 kz = 5/3

The simulation conditions for Case-3 are shown in Table 3.4. The stress condition for the vertical and horizontal direction are both anisotropic.

Table 3.4 Fluid and rock properties with kr=2/3 and kz=5/3.

Height	200 mm
internal diameter	20 mm

external diameter	200 mm
Permeability	0.49 Darcy
Porosity	0.264
Fluid Type	3.5% NaCl solution and kerosene oil
Fluid density	0.78 g/cm^3
Fluid viscosity	1.4 cp
Quartz density	2.65 g/cm^3
Differential pressure	0.01318 psi
Running time	0.1231 day
Failure model	0.8
σ_r	4.825 kpsi
σ_R	7.192 kpsi
σ_z	12.81 kpsi

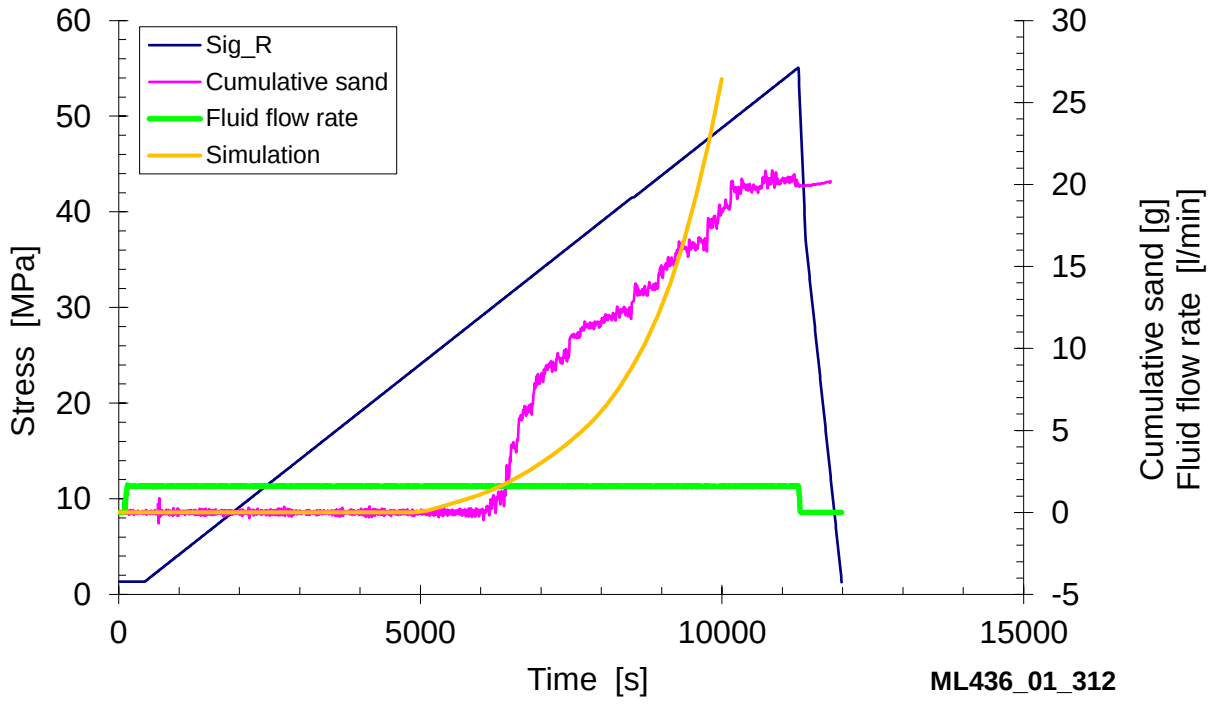

Figure 3.20 Simulation result vs experiment result with kr=2/3 and kz=5/3.

The calculation and experiment data cannot be matched well. The onset of the sand production occurs too sudden for the experiment. The difference is about 1000 seconds between simulation and experiment. After the onset, the sand-production increased quickly, however, the sand-production slowed down shortly after sand onset, and the produced sand-mass did not change anymore in the end. The simulation shows gradual cavity enlargement in the radial diction, while the experiment shows a local failure following cavity enlargement in a triangular shape. The experiment is controlled by the heterogeneity of rock rather than the stress state. If we assume the permeability is heterogeneous along the tangential direction around the borehole, the onset and progress of the sand production can be matched.

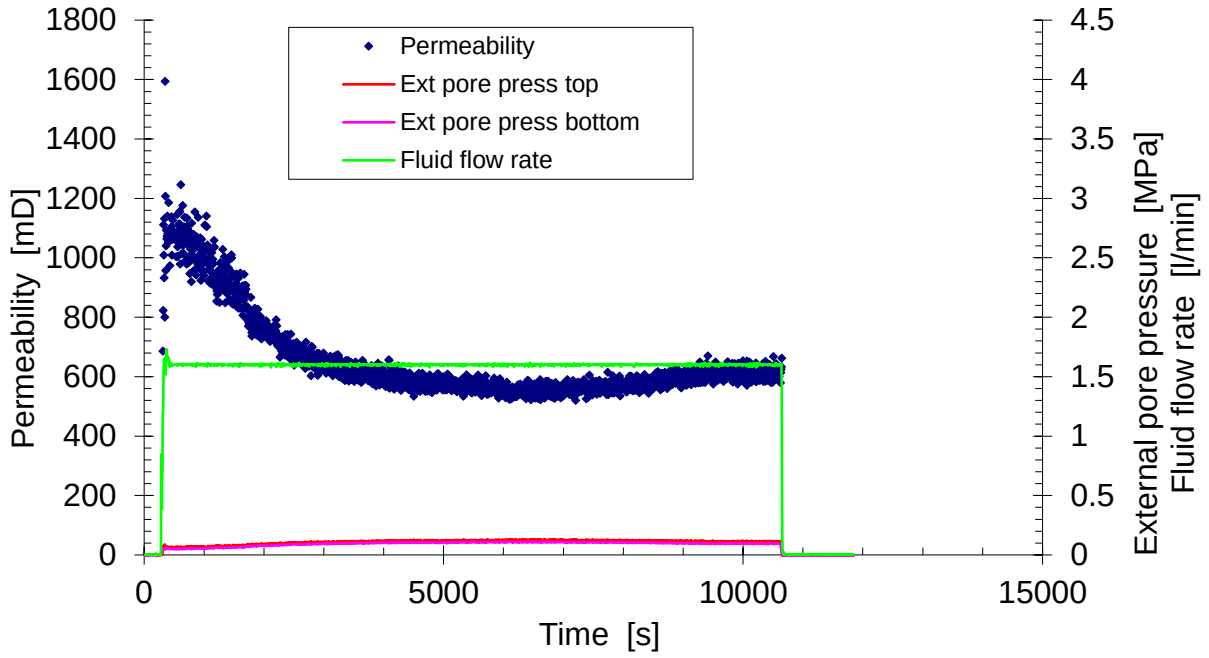

Figure 3.21 Fluid flow rate and pore pressure during experiment with kr=2/3 and kz=5/3.

From the chart, the permeability change is not obvious during sand production.

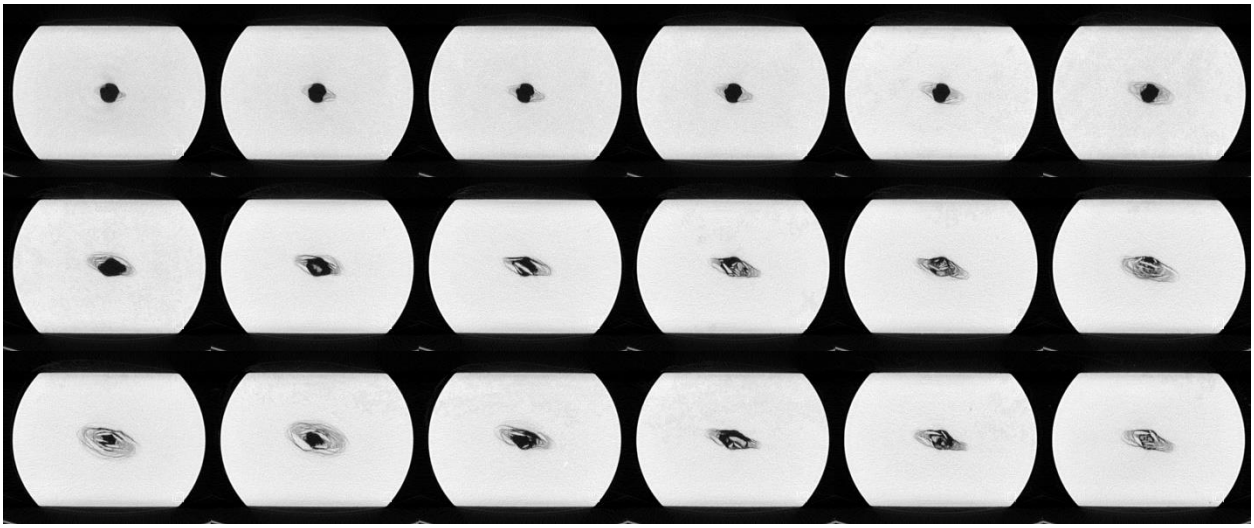

Figure 3.22 rock scanning for each layer with kr=2/3 and kz=5/3.

The scanning pictures in Figure 3.22 show the variety of the cavity shape along the cavity. On the top, the cavity still keeps its original shape and we can see non-uniform failure region on the bottom picture. At the bottom of the sample, the cavity failure region is very large. That is because the scanning is to measure the density near the cavity. Although the sand had been produced, the structure was not destroyed.

Figure 3.23 Experiment result from bottom and surface with kr=2/3 and kz=5/3.

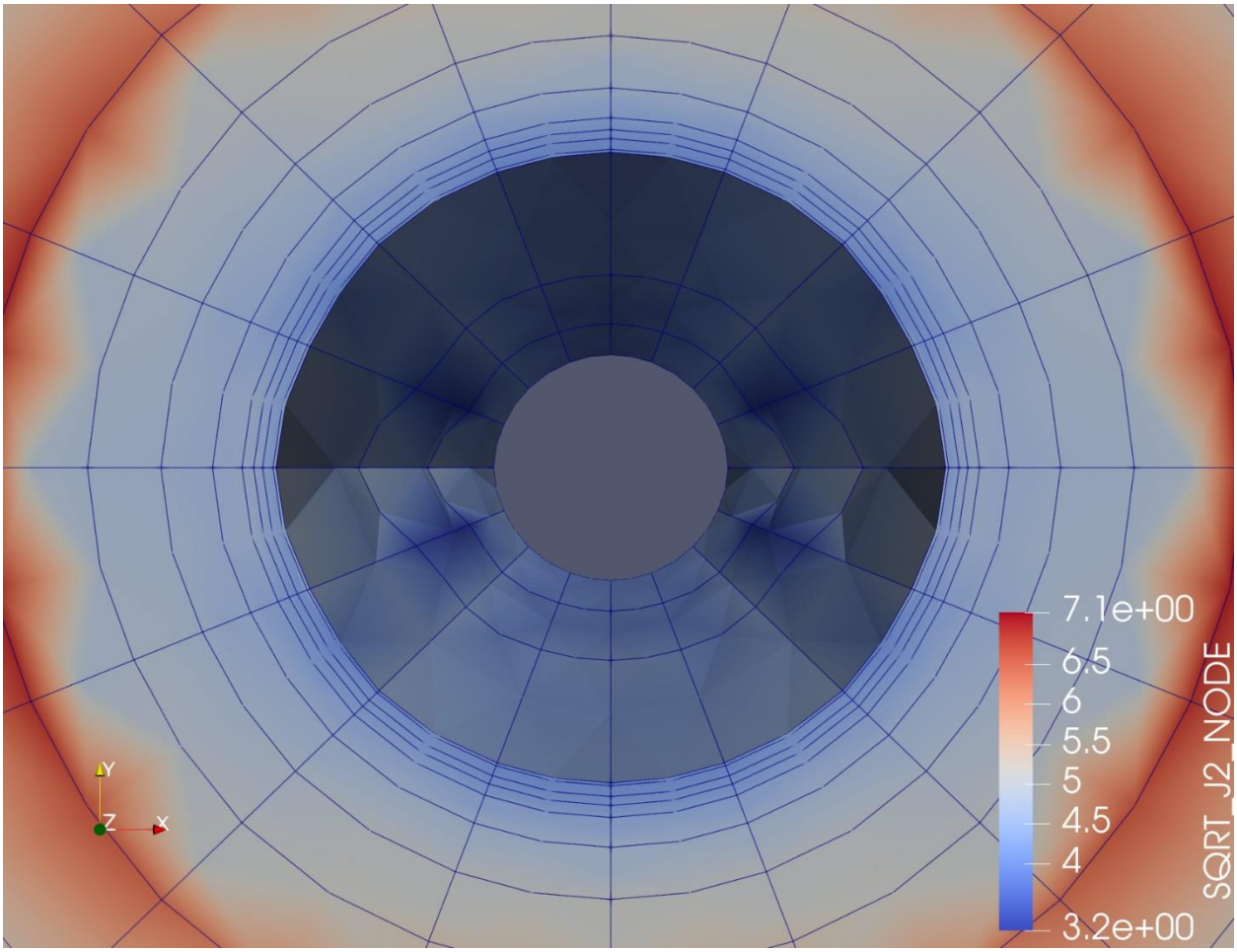

Figure 3.24 Cavity evolution with kr=2/3 and kz=5/3

The shape of the experiment did not match the simulation result, which is likely caused by the heterogeneous of the rock material.

Case-4 305 kr = 2/3 kz = 2/3

The simulation conditions for Case-4 are shown in Table 3.5. The stress condition for the vertical and horizontal direction are both anisotropic.

Table 3.5 Fluid and rock properties for kr=2/3 and kz=2/3.

Height	200 mm
internal diameter	20 mm
external diameter	200 mm
Permeability	0.49 Darcy
Porosity	0.266
Fluid Type	3.5% NaCl solution and kerosene oil
Fluid density	0.78 g/cm^3
Fluid viscosity	1.4 cp
Quartz density	2.65 g/cm^3
Differential pressure	0.01582 psi
Running time	0.1575 day
Failure model	0.8
σ_r	4.642 kpsi
σ_R	6.927 kpsi
σ_z	4.667 kpsi

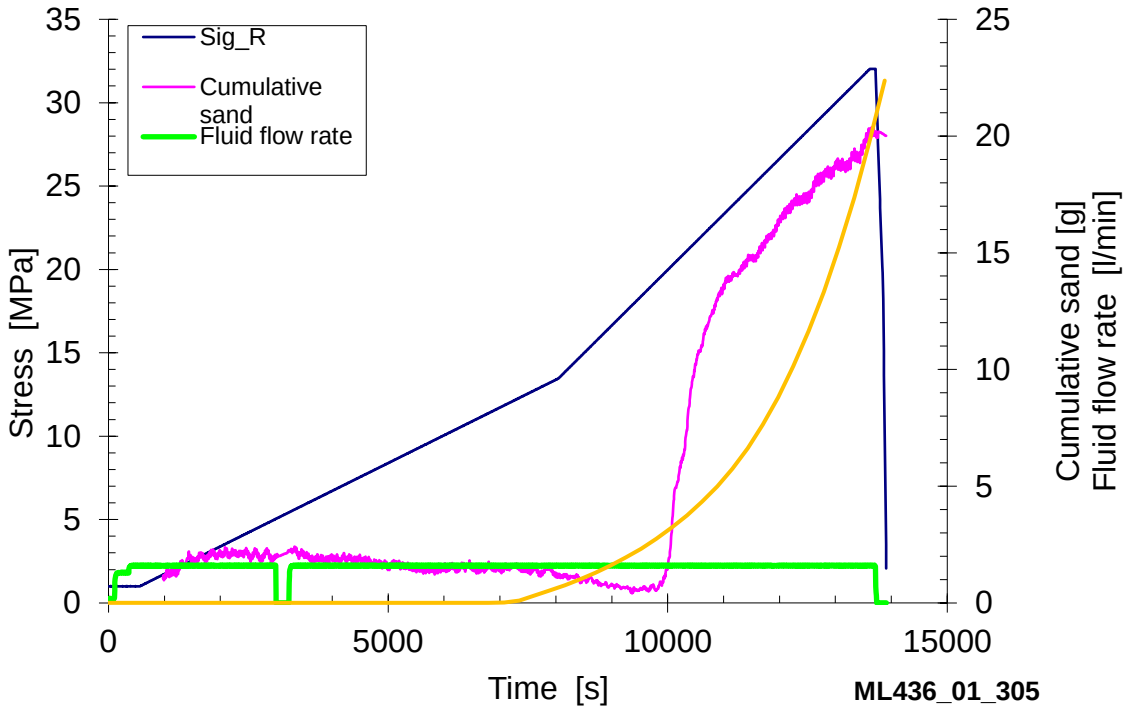

Figure 3.25 Simulation result vs experiment result with kr=2/3, kz=5/3

In this experiment, sand is suddenly produced and then, sand production becomes gradual. It is hard to find the exact onset time of sand production. But we can confirm the sand-production-onset time is largely different from simulation result. Then at the end of the experiment, sand-production rate decreased. According to the scan-photos, a triangular failure region is observed around the borehole with a slit-like cavity extension. It seems that a sudden failure occurs around a borehole. Then, it follows a progressive cavity failure like a worm-hole. The permeability change is very stable during the experiment at about 500 mD.

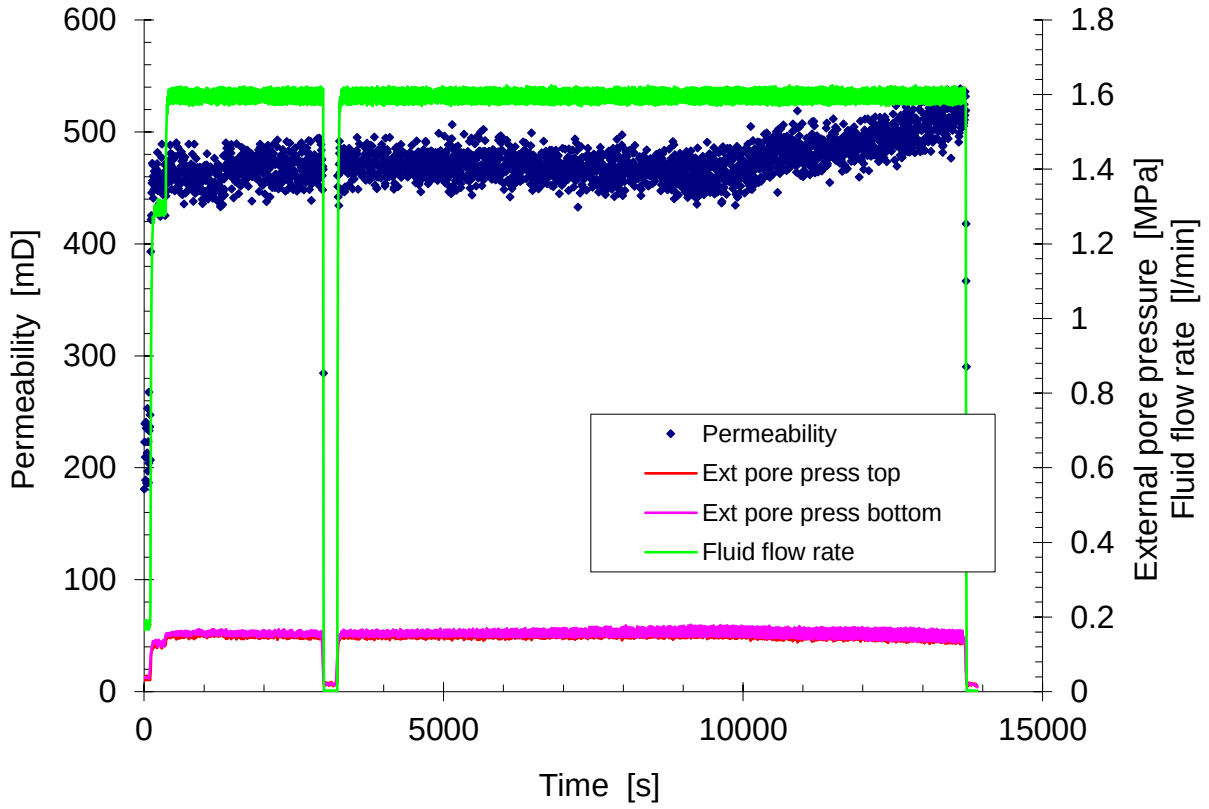

Figure 3.26 Fluid flow rate and pore pressure during experiment with kr=2/3, kz=5/3

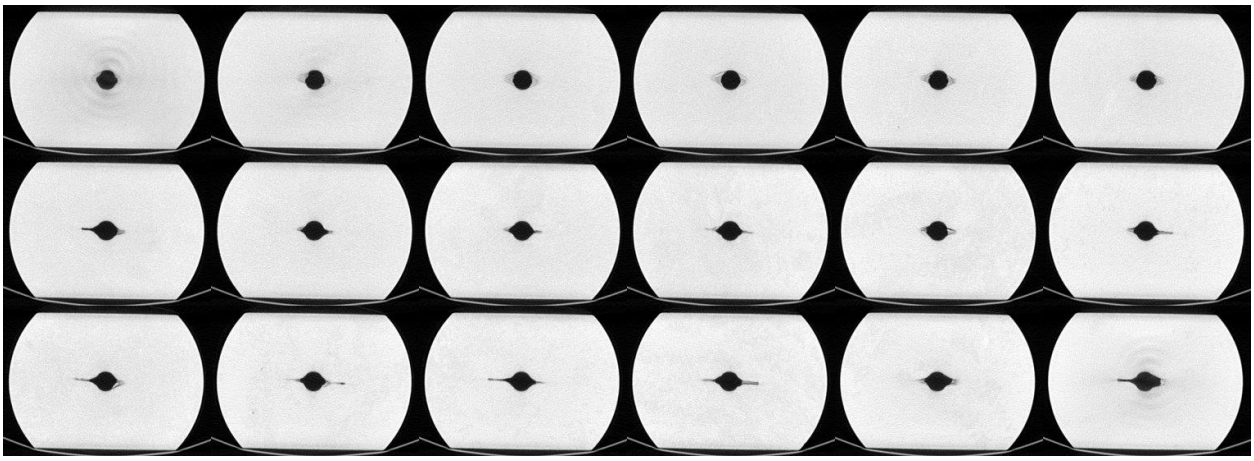

Figure 3.27 rock scanning for each layer with kr=2/3, kz=5/3

Figure 3.28 Experiment result from bottom and surface with kr=2/3, kz=5/3

The scanning pictures in Figure 3.27 show the deformation or failure is narrow, which is perpendicular to the maximum stress direction. On the other hand, no slit-like cavity is observed in the rock photo taken after experiment. It indicates that the rock failure progressed in a slit-like cavity but sand production is prevented due to the narrow slit. Therefore, the rock picture after experiment does not show the slit-like cavity, although the density has changed as shown in the scan-photos. The simulation result shows that the over-all calculation of produced sand mass matches the experiment.

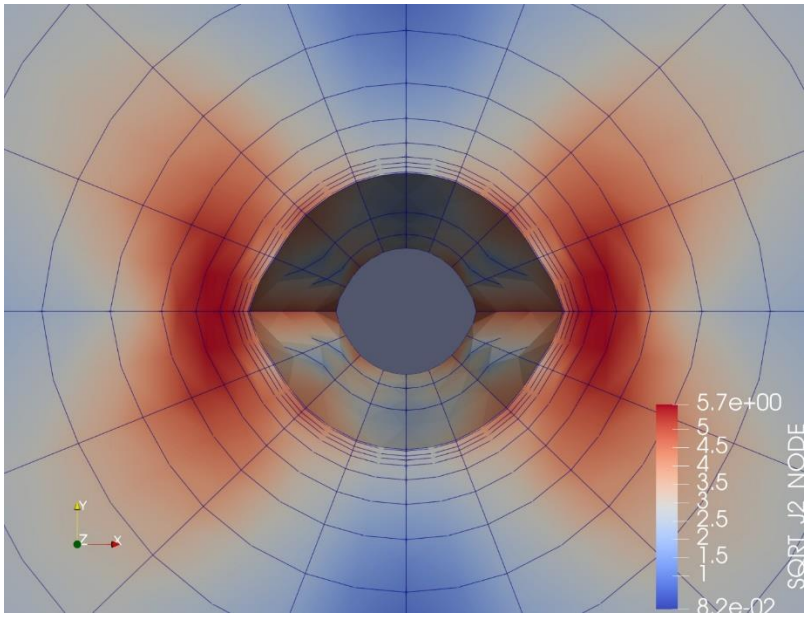

Figure 3.29 Cavity evolution with kr=2/3, kz=5/3

Case-5 306 kr = 2/3 kz = 4/5

The simulation conditions for Case-4 are shown in Table 3.6. The stress condition for the vertical and horizontal direction are both anisotropic.

Table 3.6 Fluid and rock properties with kr=2/3 and kz=4/5.

Height	200 mm
internal diameter	20 mm
external diameter	200 mm
Permeability	0.8 Darcy
Porosity	0.264

Fluid Type	3.5% NaCl solution and kerosene oil
Fluid density	0.78 g/cm^3
Fluid viscosity	1.4 cp
Quartz density	2.65 g/cm^3
Differential pressure	0.00989 psi
Running time	0.147 day
Failure model	0.8
σ_r	5.936 kpsi
σ_R	8.714 kpsi
σ_z	7.256 kpsi

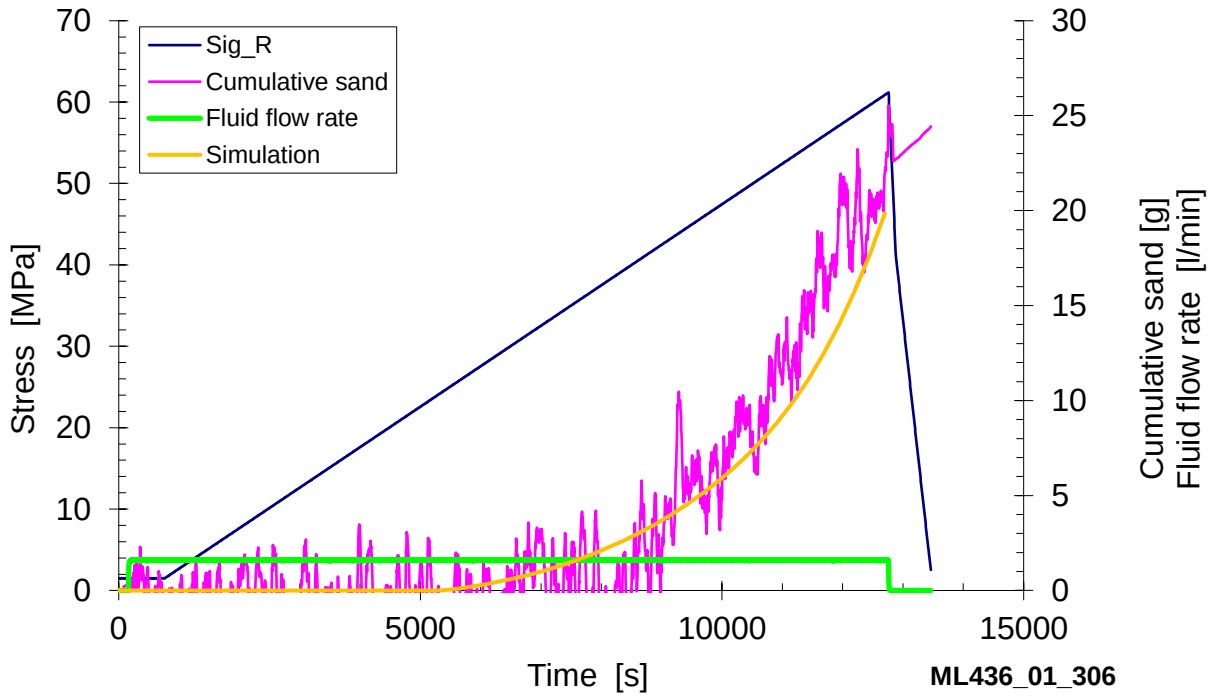

Figure 3.30 Simulation result vs experiment result with kr=2/3 and kz=4/5

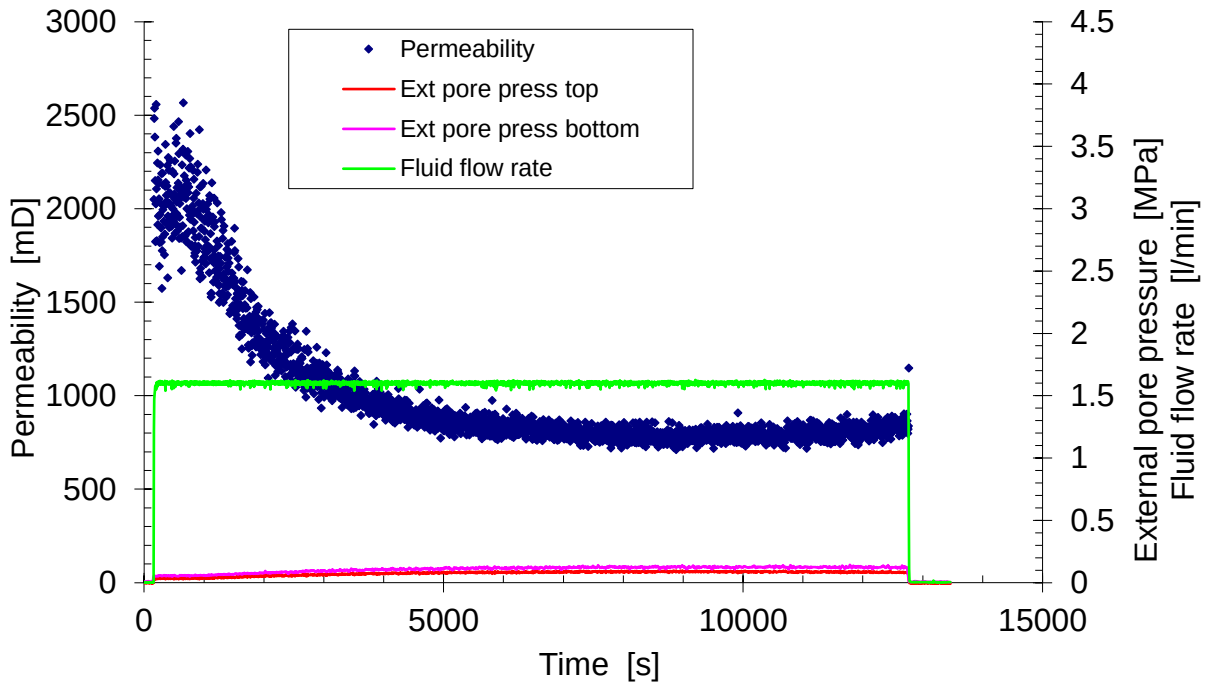

Figure 3.31 Fluid flow rate and pore pressure during experiment with kr=2/3 and kz=4/5

During the experiment, the permeability did not vary a lot.

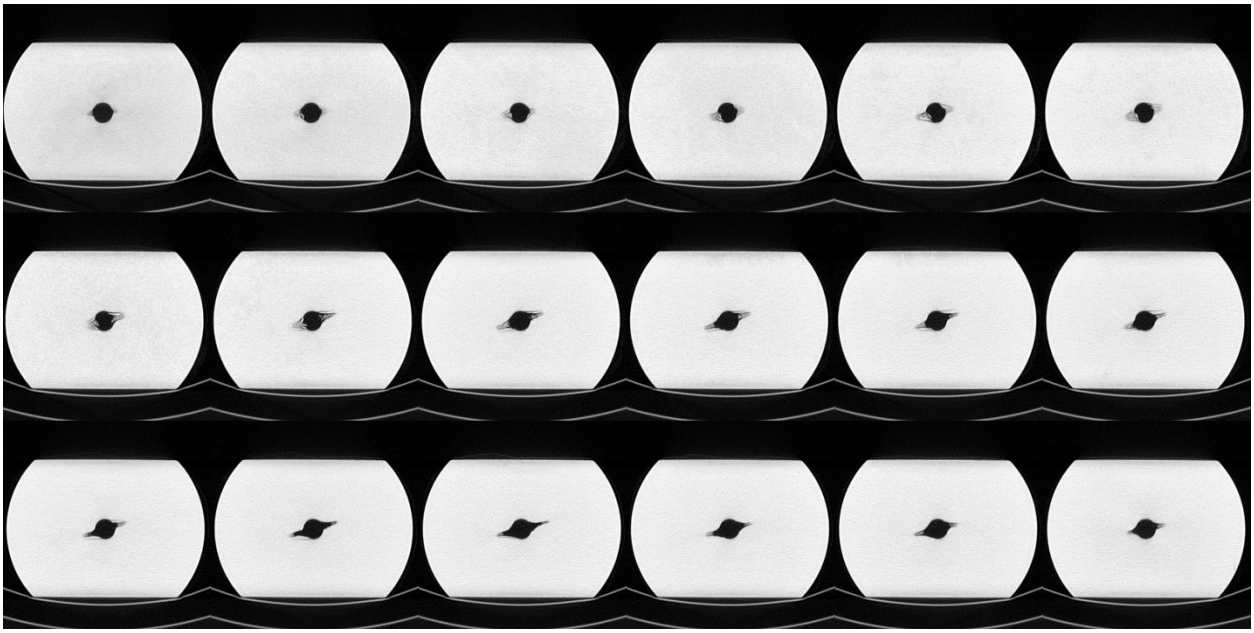

Figure 3.32 rock scanning for each layer with kr=2/3 and kz=4/5

Because the scanning pictures (Figure 3.32) show the density of the rock, the lower density region can be identified in the pictures, which is conflict with the photos of the sample after-experiment (Figure 3.33, the top and bottom pictures). The direction of failure is slightly offset from the stress concentrated direction. The reason is the heterogeneous of the rock material.

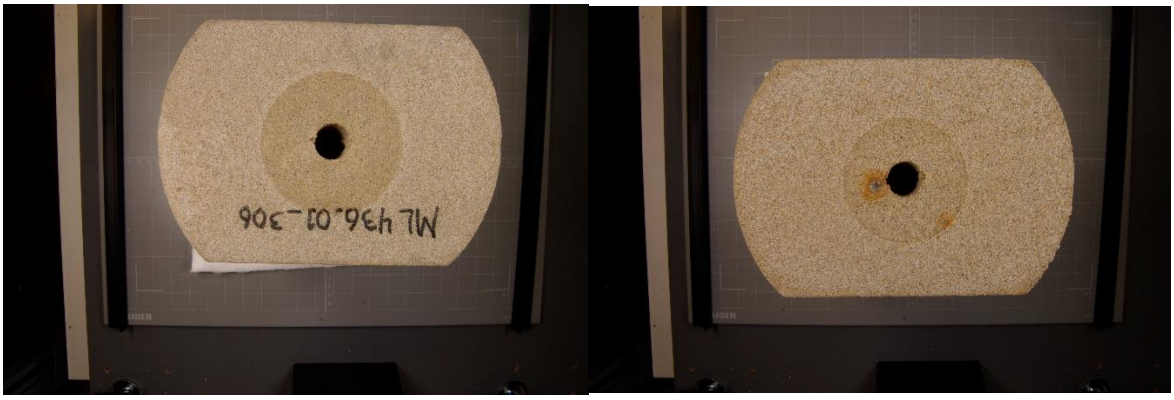

Figure 3.33 Experiment result from bottom and surface with kr=2/3 and kz=4/5

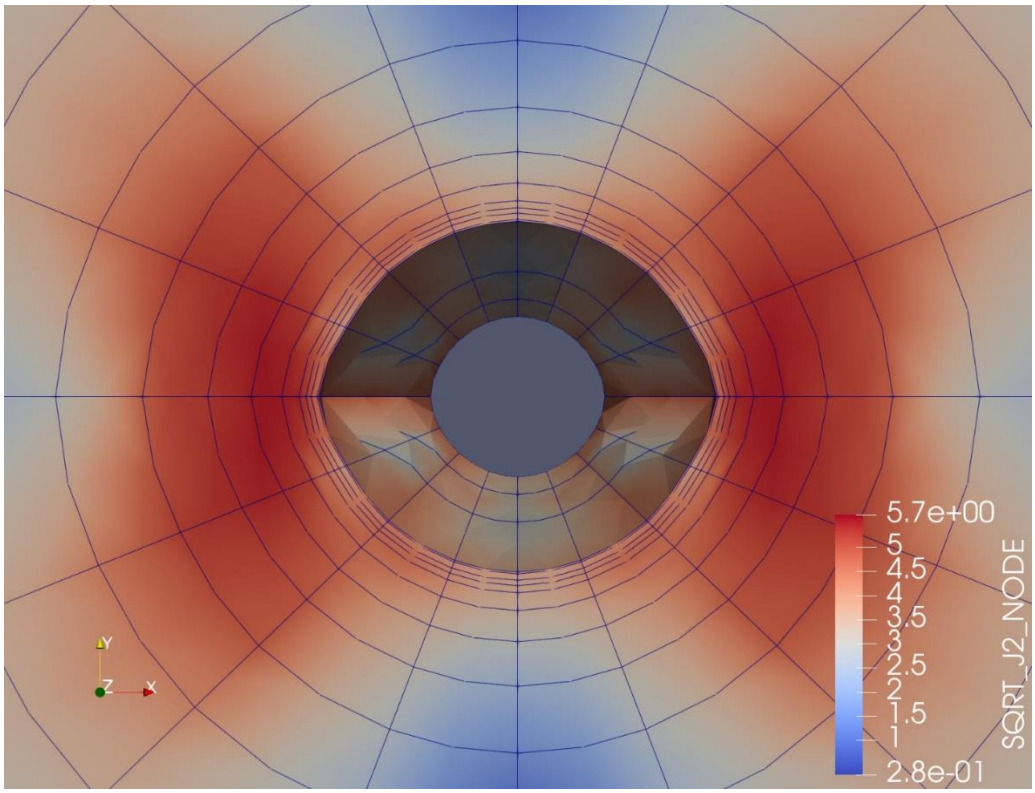

Figure 3.34 Cavity evolution with kr=2/3 and kz=4/5

Case-6 308 kr = 1 kz = 1

The simulation conditions for Case-6 are shown in Table 3.7. The stress condition for the vertical and horizontal direction are both isotropic.

Table 3.7 Fluid and rock properties with kr=1 and kz=1.

Height	200 mm
internal diameter	20 mm
external diameter	200 mm
Permeability	0.72 Darcy
Porosity	0.267
Fluid Type	3.5% NaCl solution and kerosene oil
Fluid density	0.78 g/cm^3
Fluid viscosity	1.4 cp
Quartz density	2.65 g/cm^3
Differential pressure	0.01098 psi
Running time	0.1559 day
Failure model	0.8
σ_r	5.31 kpsi
σ_R	5.31 kpsi
σ_z	5.31 kpsi

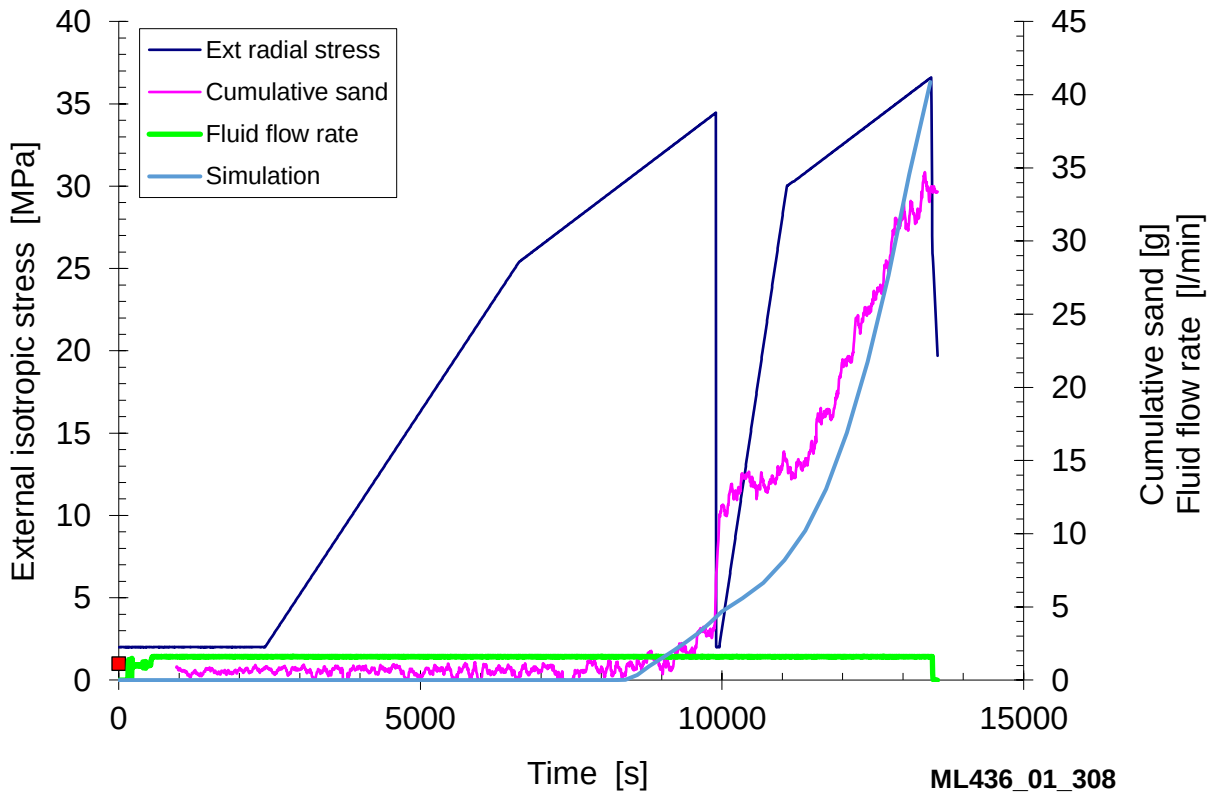

Figure 3.35 Stress increase and sand production during experiment with kr=1 and kz=1.

The experiment is a little different from others: there are 2 main stage loading. We have to match 2 set of curves as much as possible. Compared with the simulation result, the empirical data had a very different behavior after the first unloading stage. At that time, the pressure dropped a lot but a sudden sand production was observed. During the procedure, the permeability did not change a lot, remained at 0.8 darcy.

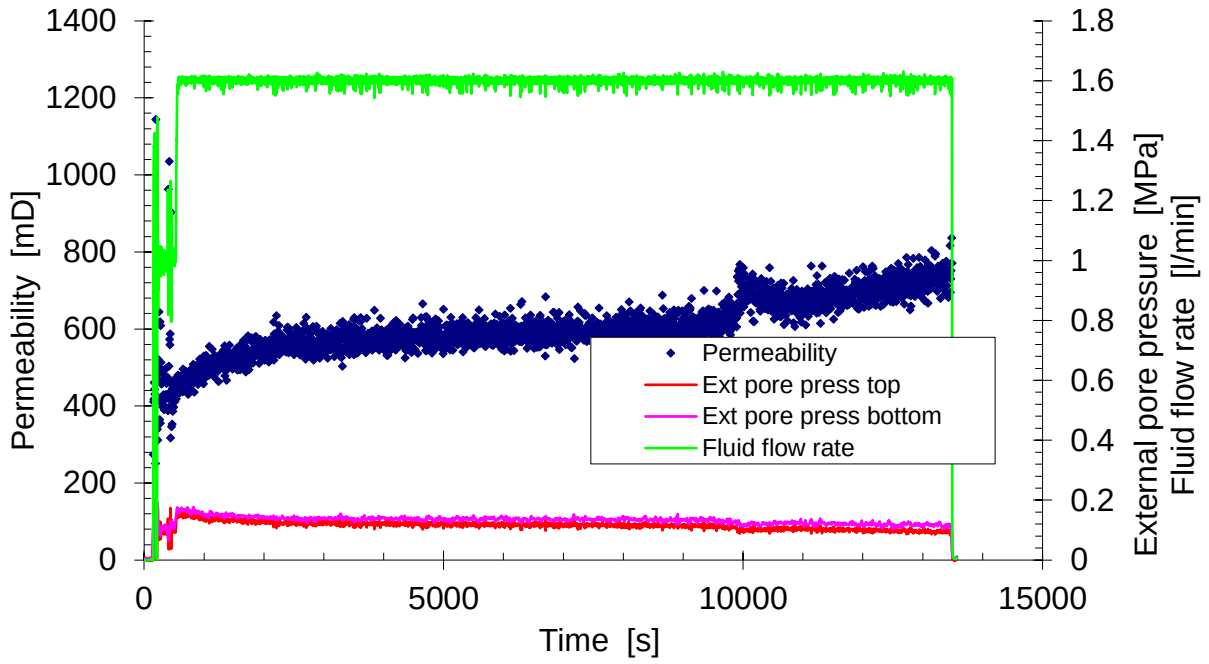

Figure 3.36 Fluid flow rate and pore pressure during experiment with kr=1 and kz=1.

After the onset of sand production, the permeability increased a little.

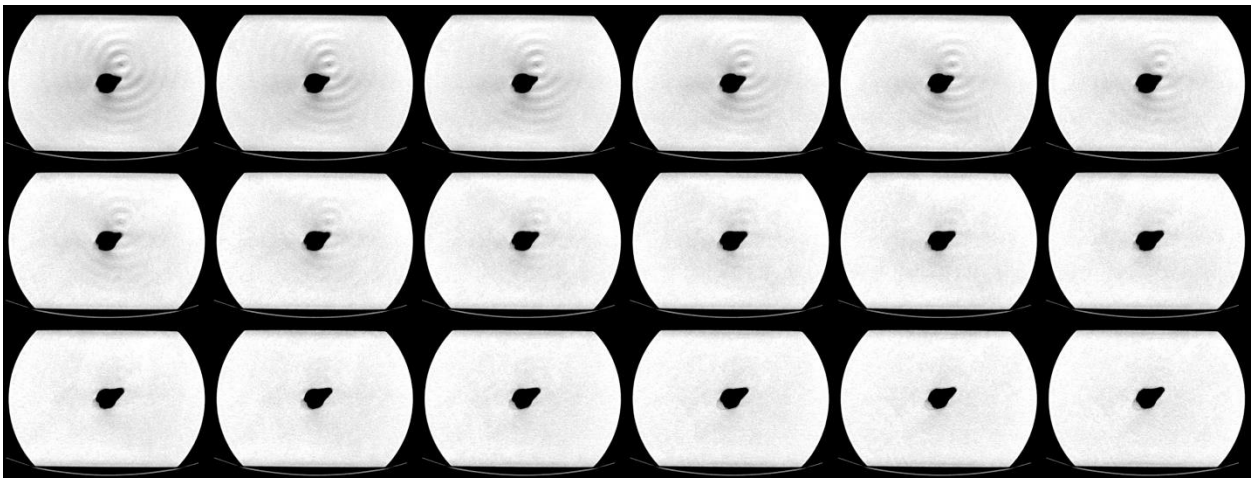

Figure 3.37 rock scanning for each layer with kr=1 and kz=1.

The scanning pictures show the failure profiles are almost the same in each layer. But the shape is not symmetric nor radial. Because in this experiment kr = kz =1, so there should not be major or minor stress direction specified. The failure progress must be radial as the simulation result shows. The failure must be more dominated by the local heterogeneity of rock. Note that the permeability is very heterogeneous for the Castlegate sandstone.

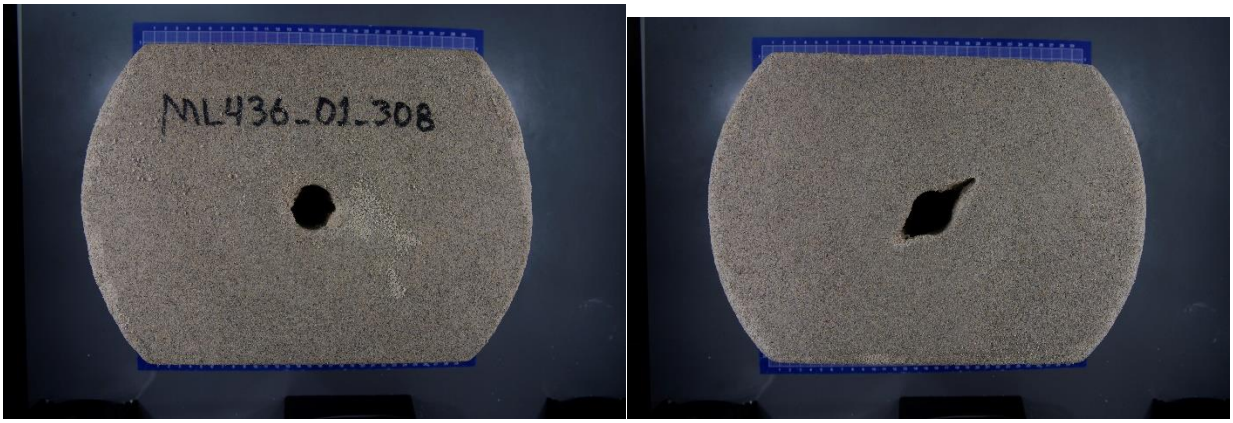

Figure 3.38 Experiment result from bottom and surface with kr=1 and kz=1.

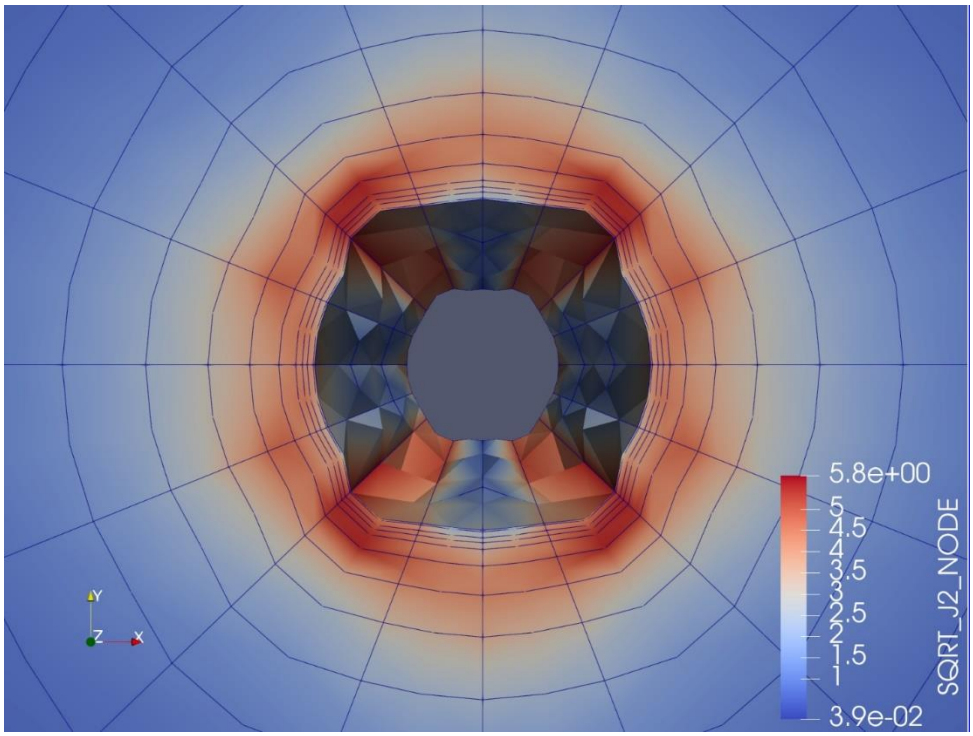

Figure 3.39 Cavity evolution with kr=1 and kz=1.

The cavity evolution simulation result is far away from the shape observed from the experiment, thus we need to consider the heterogeneous properties of the permeability. Increasing the permeability to twice in 45-degree direction and re-run the simulation, the failure shapes match between the simulation and experiment.

Assume a high permeability area at meshes at 45° angle, then, the cavity develops in the direction, which is similar to the cavity development in the experiment.

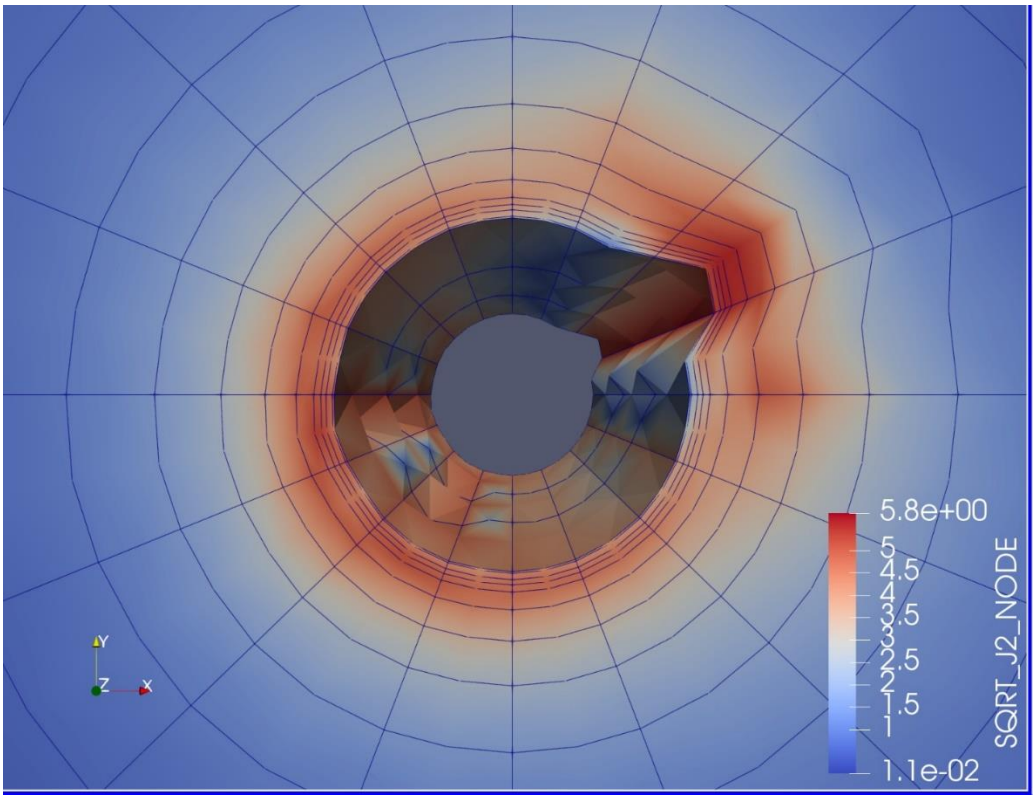

Figure 3.40 Cavity evolution with twice permeability at 45 degree with kr=1 and kz=1.

Case-7 311 kr = 1/3 kz = 1/3

The simulation conditions for Case 7are shown in Table 3.8. The stress condition for the vertical and horizontal direction are both anisotropic.

Table 3.8 Fluid and rock properties with kr=1/3 and kz=1/3.

Height	200 mm
internal diameter	20 mm
external diameter	200 mm
Permeability	0.6 Darcy
Porosity	0.261
Fluid Type	3.5% NaCl solution and kerosene oil
Fluid density	0.78 g/cm^3
Fluid viscosity	1.4 cp
Quartz density	2.65 g/cm^3
Differential pressure	0.0131 psi
Running time	0.144 day
Failure model	0.8
σ_r	2.952 kpsi
σ_R	8.764 kpsi
σ_z	2.947 kpsi

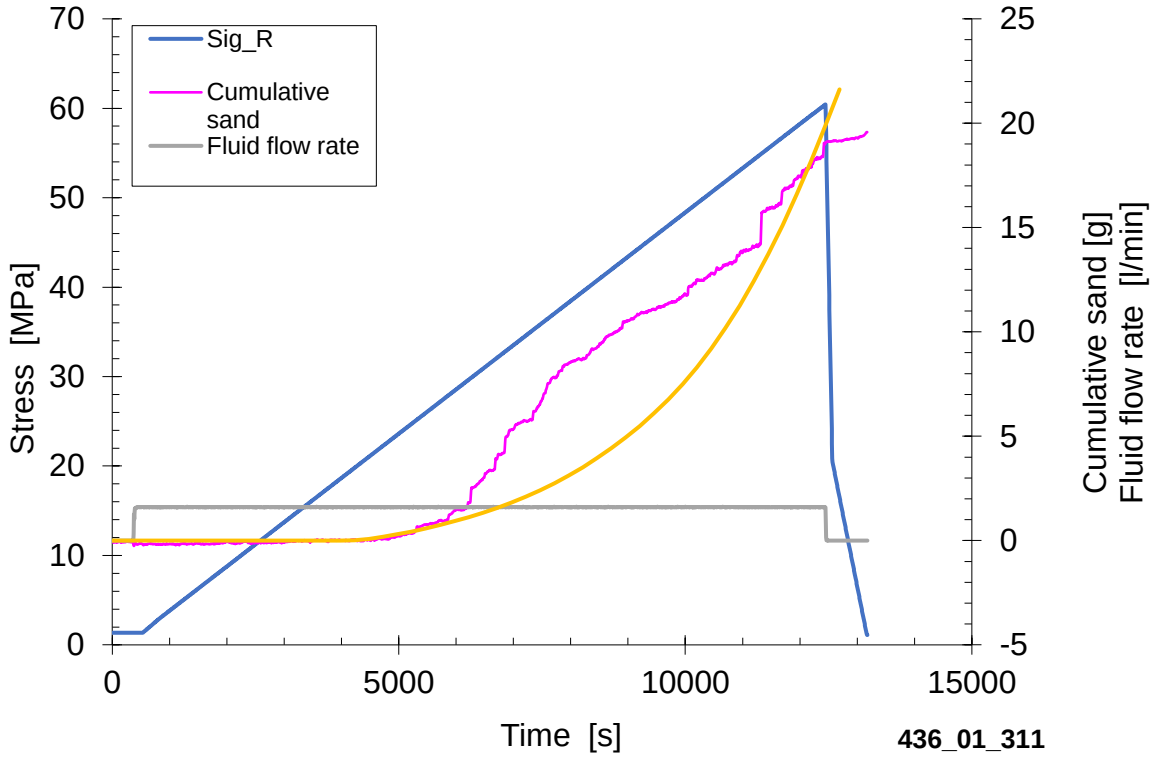

Figure 3.41 Simulation result vs experiment result with kr=1/3 and kz=1/3.

The onset times of the sand production for the experiment and simulation are very close, about 4000 s. During the sand-production, the permeability remains stable, with slight decline, but we could simplify it as 0.6 darcy. Then, the coefficient A_1 is calculated to match the experiment data. The onset and profile matching are good in this case.

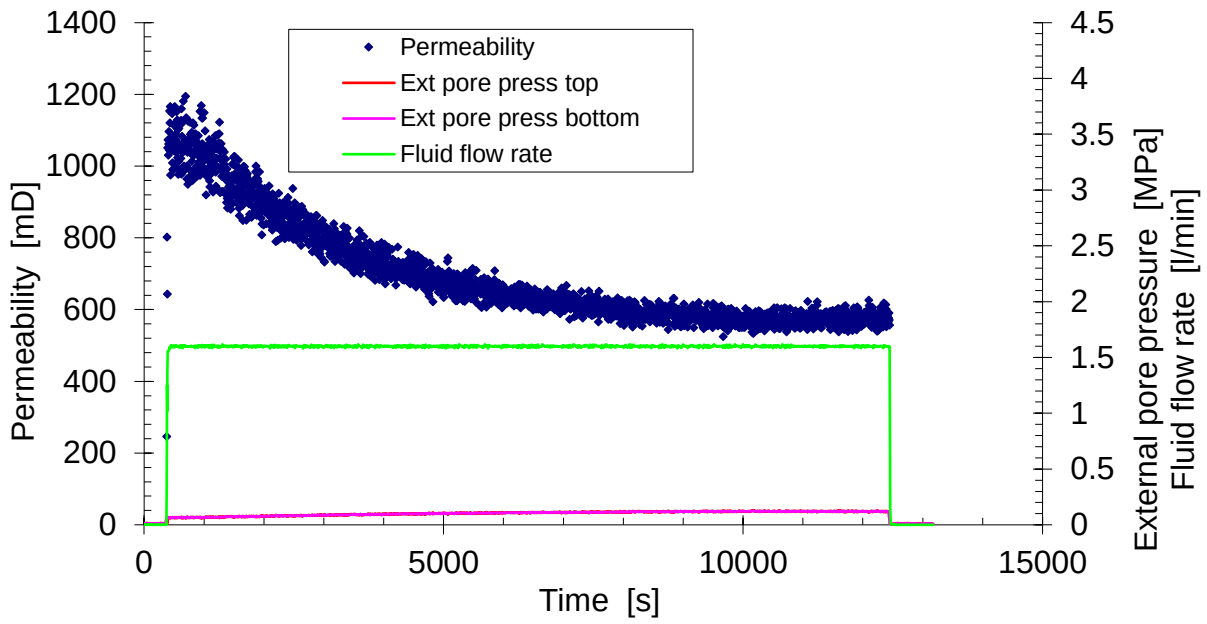

Figure 3.42 Fluid flow rate and pore pressure during experiment with kr=1/3 and kz=1/3.

During the experiment, the permeability stays stable around 600 mD.

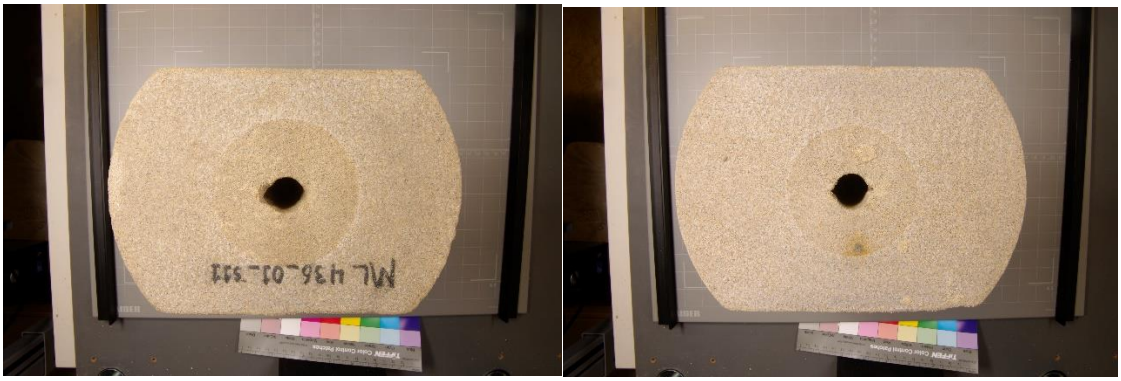

Figure 3.43 Experiment result from bottom and surface with kr=1/3 and kz=1/3.

Simulation result showed the cavity looks like an ellipse. Although no scanning data was obtained for this experiment, we still have after-experiment pictures for the top and bottom, where the shape of the failure proves our hypothesis.

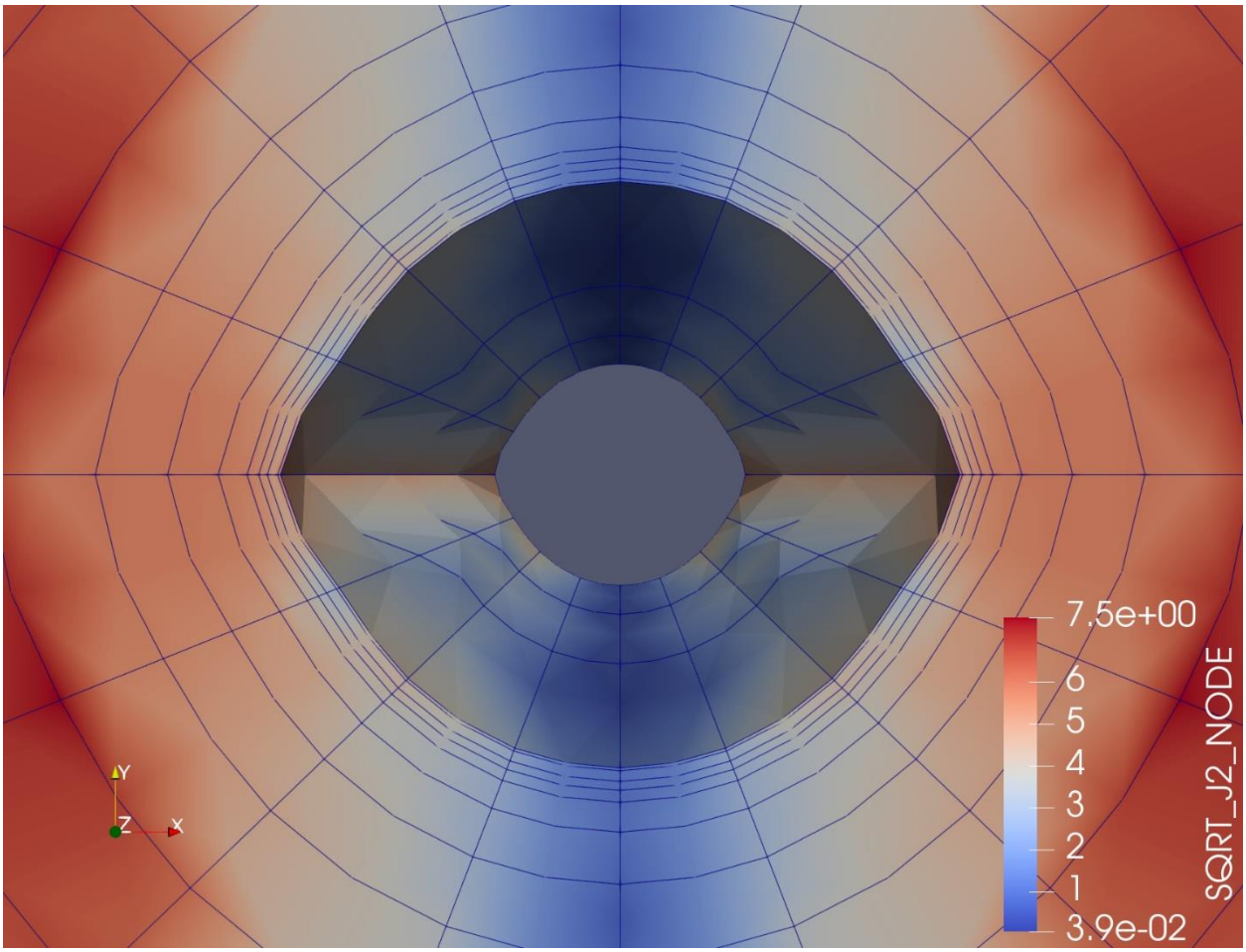

Figure 3.44 Cavity evolution with kr=1/3 and kz=1/3.

Case-8 312 kr = 2/3 kz = 4/3

The simulation conditions for Case 8 are shown in Table 3.9. The stress condition for the vertical and horizontal direction are anisotropic.

Table 3.9 Fluid and rock properties with kr=2/3 and kz=4/3.

Height	200 mm
internal diameter	20 mm
external diameter	200 mm
Permeability	0.6 Darcy
Porosity	0.265
Fluid Type	3.5% NaCl solution and kerosene oil
Fluid density	0.78 g/cm^3
Fluid viscosity	1.4 cp
Quartz density	2.65 g/cm^3
Differential pressure	0.0131 psi
Running time	0.13 day
Failure model	0.8
σ_r	5.352 kpsi
σ_R	7.987 kpsi
σ_z	11.28 kpsi

Comparing the empirical data and simulation, the sand production onset time is 6000 seconds for both experiment and simulation. After the onset of sand production, the experimental

data show the sand rate becomes suddenly very large, however, it slows down gradually. The scan-photo reveals fragments of failed rock. Considering the sand-arch effect, it is reasonable to guess that the sand-arch due to rock fragments is forming during sand-production in this experiment. A_1 is estimated by trying to match the amount of sand in the end.

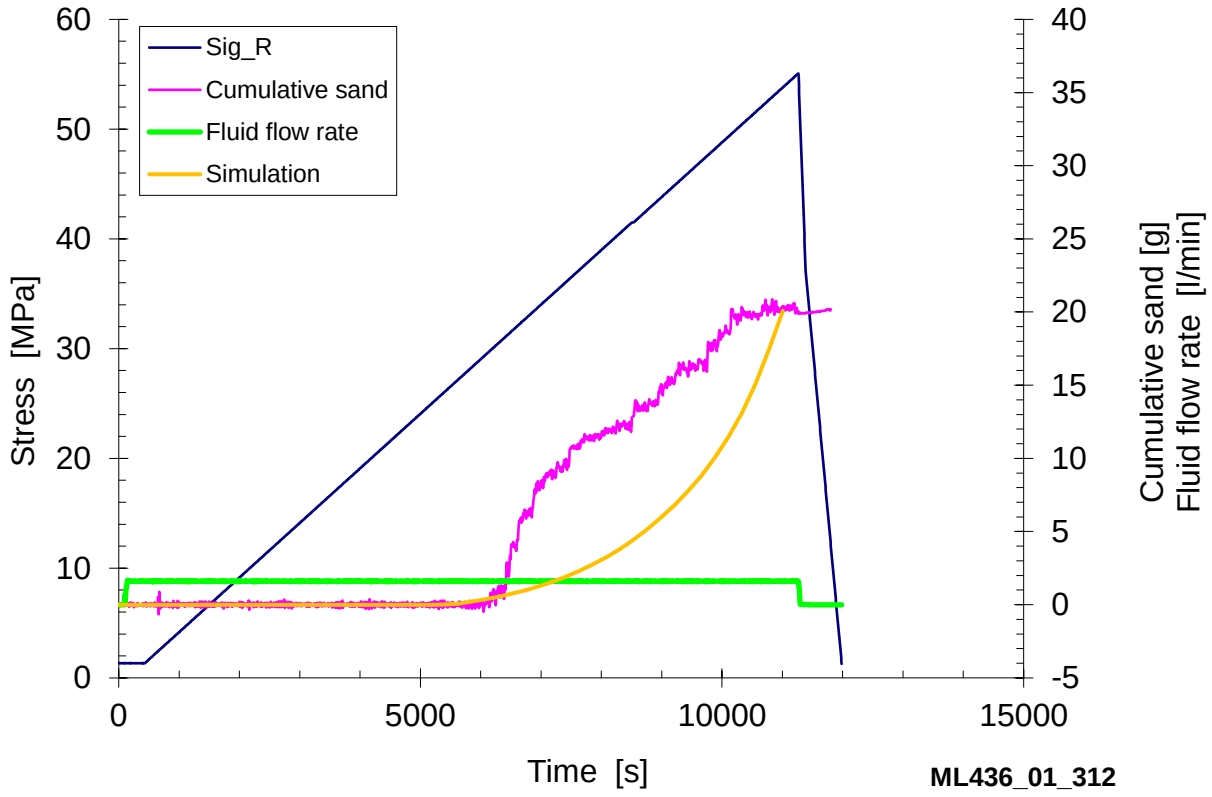

Figure 3.45 Simulation result vs experiment result with kr=2/3 and kz=4/3.

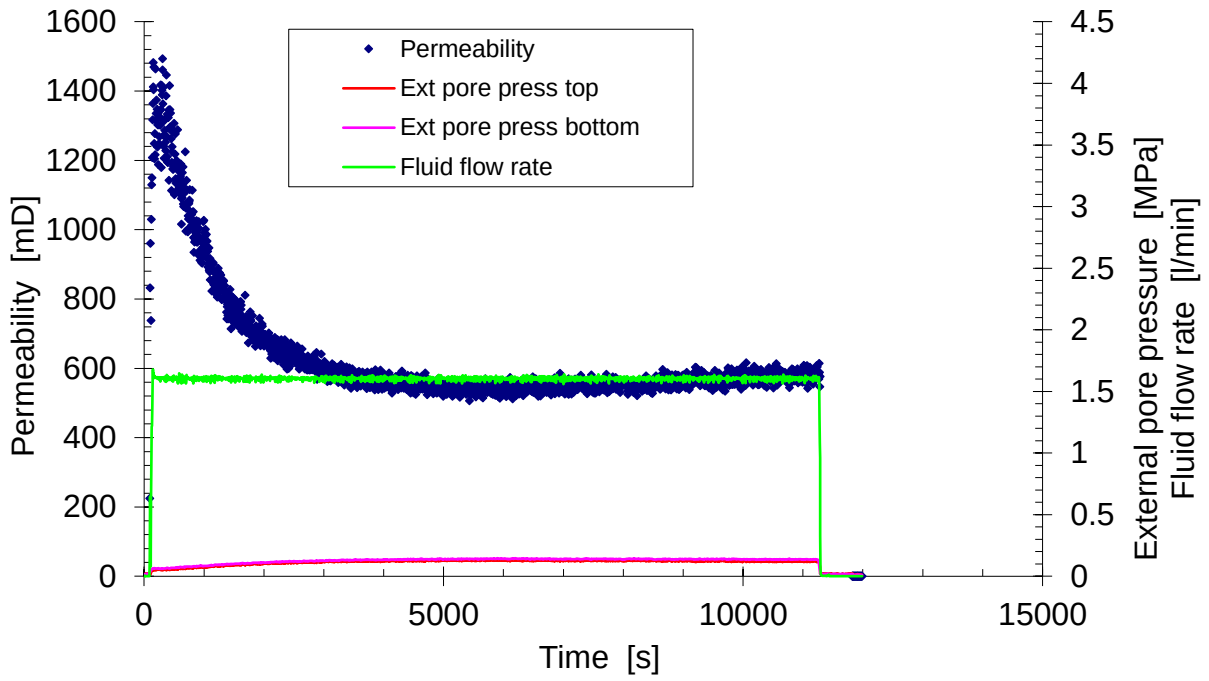

Figure 3.46 Fluid flow rate and pore pressure during experiment with kr=2/3 and kz=4/3.

During experiment, the permeability declines a lot, from 1400 mD to 600 mD. However, it maintains the value (600 mD) after the onset of sand production.

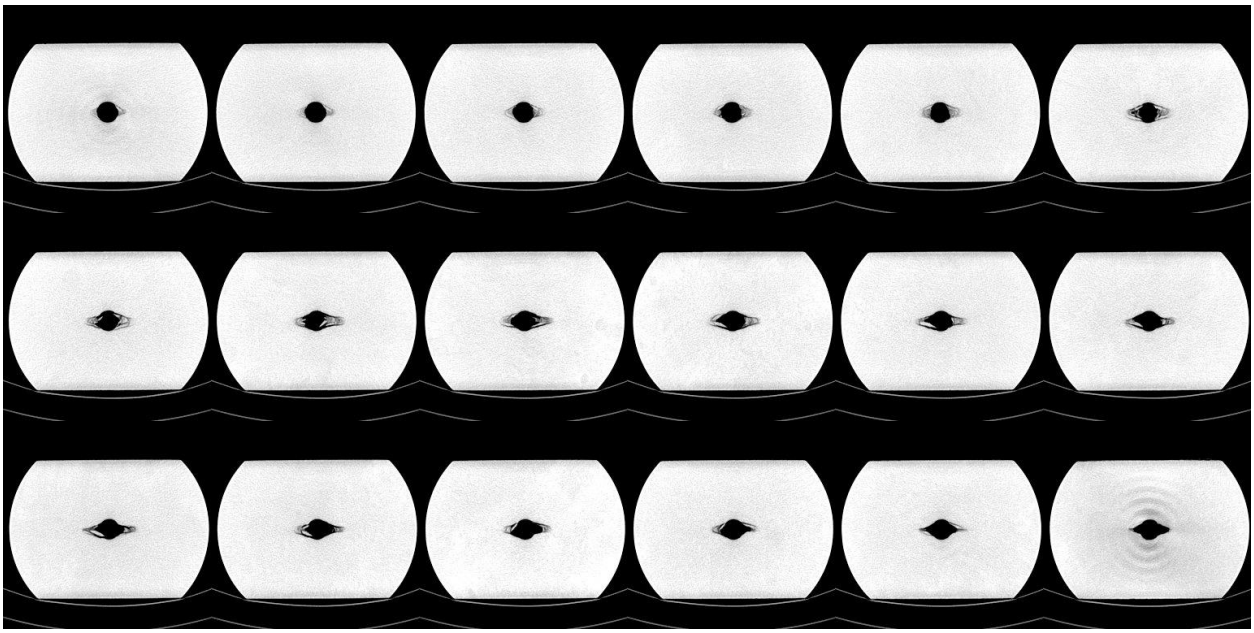

Figure 3.47 rock scanning for each layer with kr=2/3 and kz=4/3.

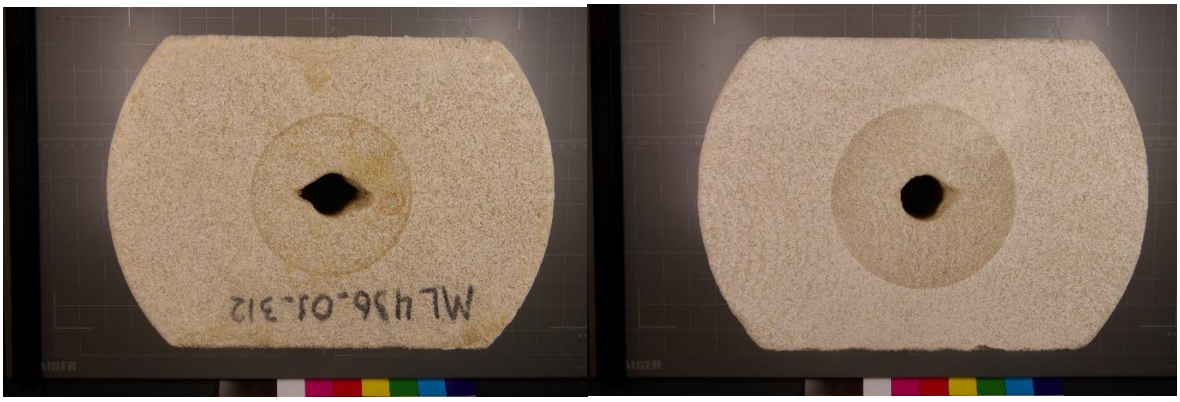

Figure 3.48 Experiment result from bottom and surface with kr=2/3 and kz=4/3.

In the scanning pictures (Figure 3.47), from top to bottom, the failure region gradually expands, and the growth shape is in the lateral direction, which matches the photos of the specimen top and bottom surfaces. Besides, the simulation result could also predict well the two spikes shape failure regions. (Figure 3.49)

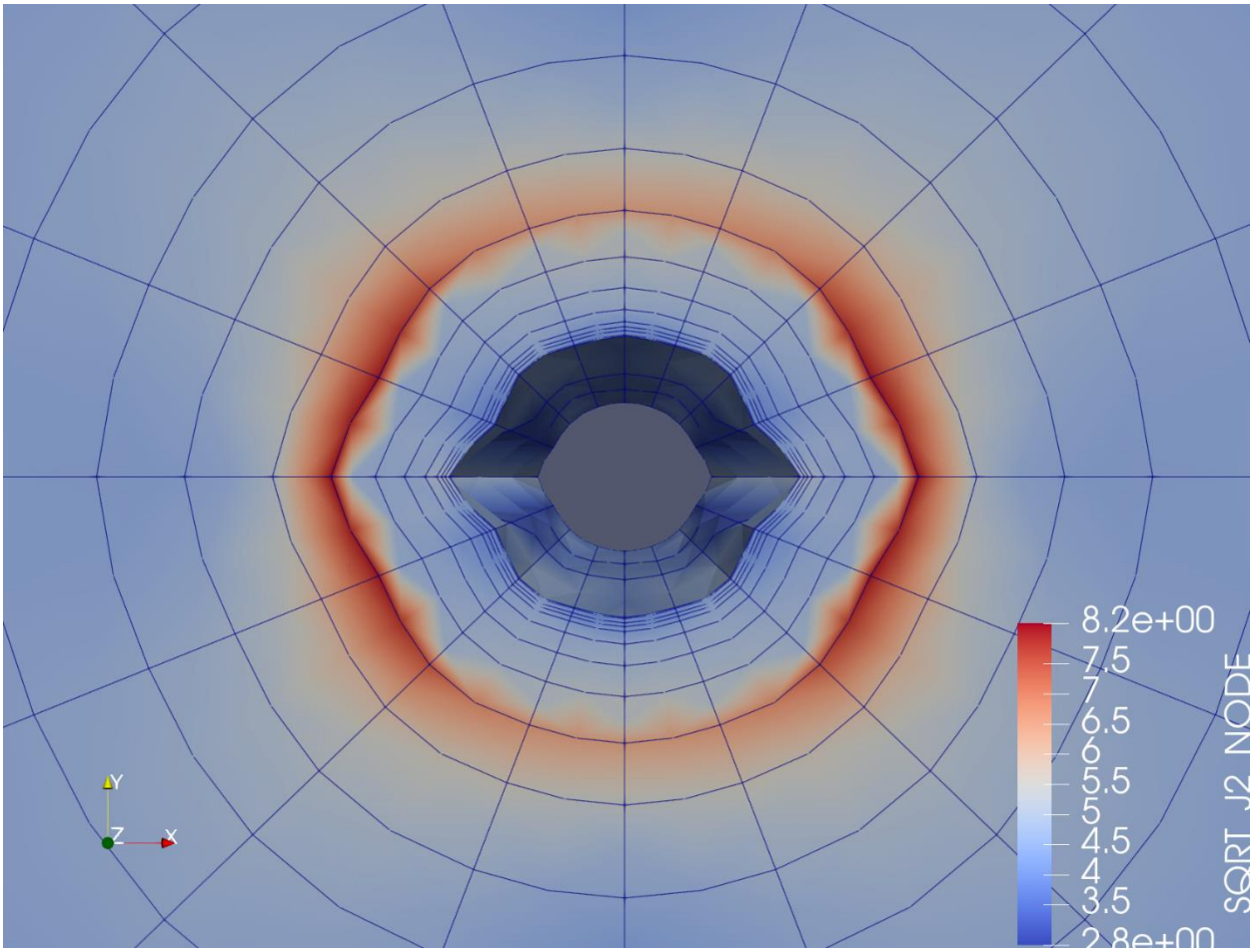

Figure 3.49 Cavity evolution with kr=2/3 and kz=4/3.

Case-9 314 kr = 1/3 kz = 2/3

The simulation conditions for Case 9 are shown in Table 3.10. The stress conditions for the vertical and horizontal direction are both anisotropic.

Table 3.10 Fluid and rock properties with kr=1/3 and kz=2/3.

Height	200 mm
internal diameter	20 mm
external diameter	200 mm
Permeability	0.53 Darcy
Porosity	0.265
Fluid Type	3.5% NaCl solution and kerosene oil
Fluid density	0.78 g/cm^3
Fluid viscosity	1.4 cp
Quartz density	2.65 g/cm^3
Differential pressure	0.0149 psi
Running time	0.136 day
Failure model	0.8
σ_r	2.789 kpsi
σ_R	8.283 kpsi
σ_z	5.886 kpsi

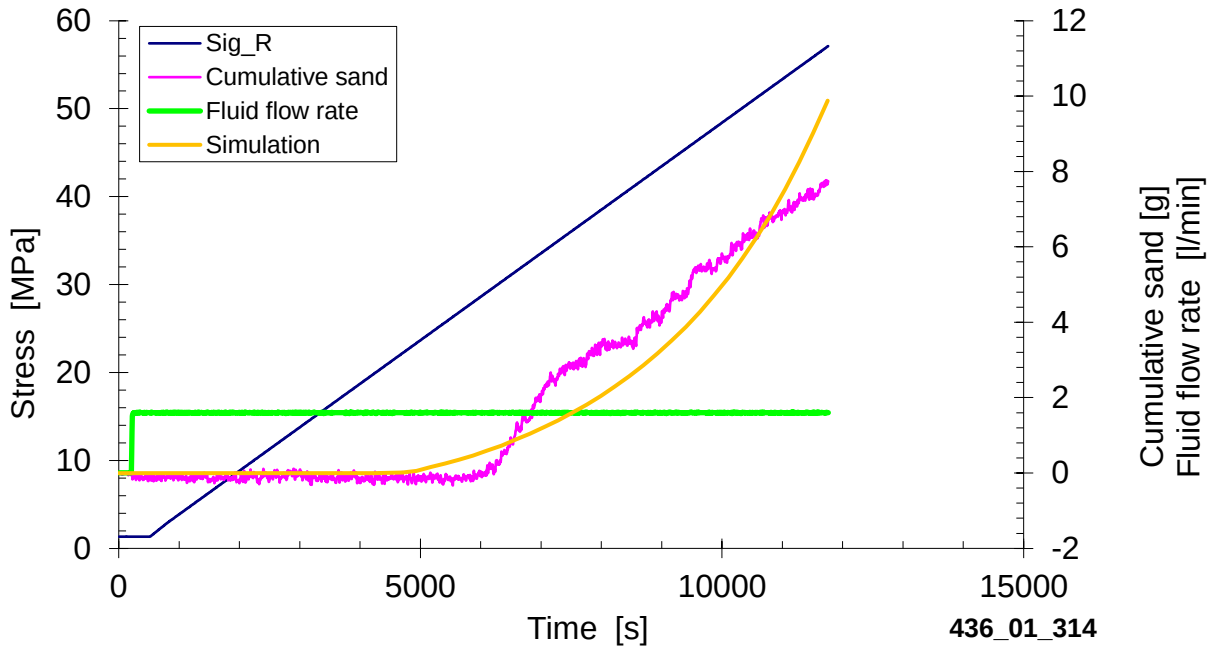

Figure 3.50 Simulation result vs experiment result with kr=1/3 and kz=2/3.

The experiment sand production curve shows that the sand-arching effect due to rock fragments still exists in this case, thus, in the simulation we need to match the final sand volume. The sand volume for the simulation is matched to the final volume of produced sand. However, the onset time gap between the real data and prediction is large. For the simulation, it is about 4500 s, whereas, for experiment data, it is about 6000s.

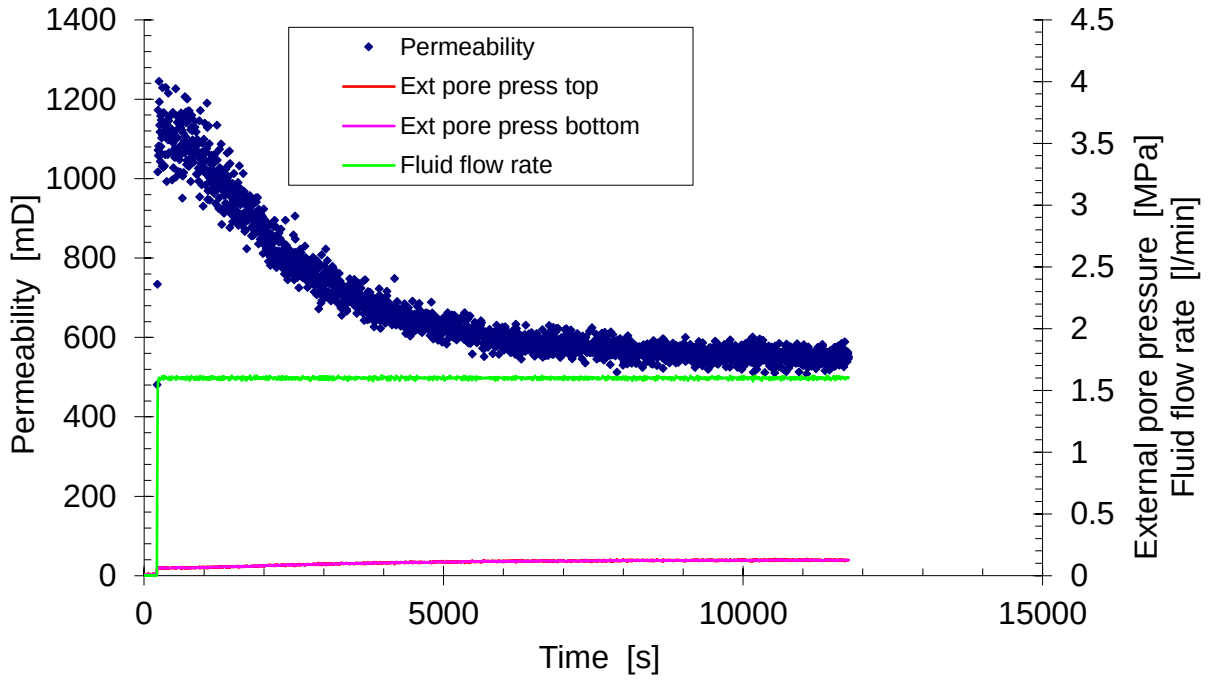

Figure 3.51 Fluid flow rate and pore pressure during experiment with kr=1/3 and kz=2/3.

After 5000 s, the permeability approaches to 600 mD and did not change anymore. Thus, we choose 600 mD as the permeability for the simulation.

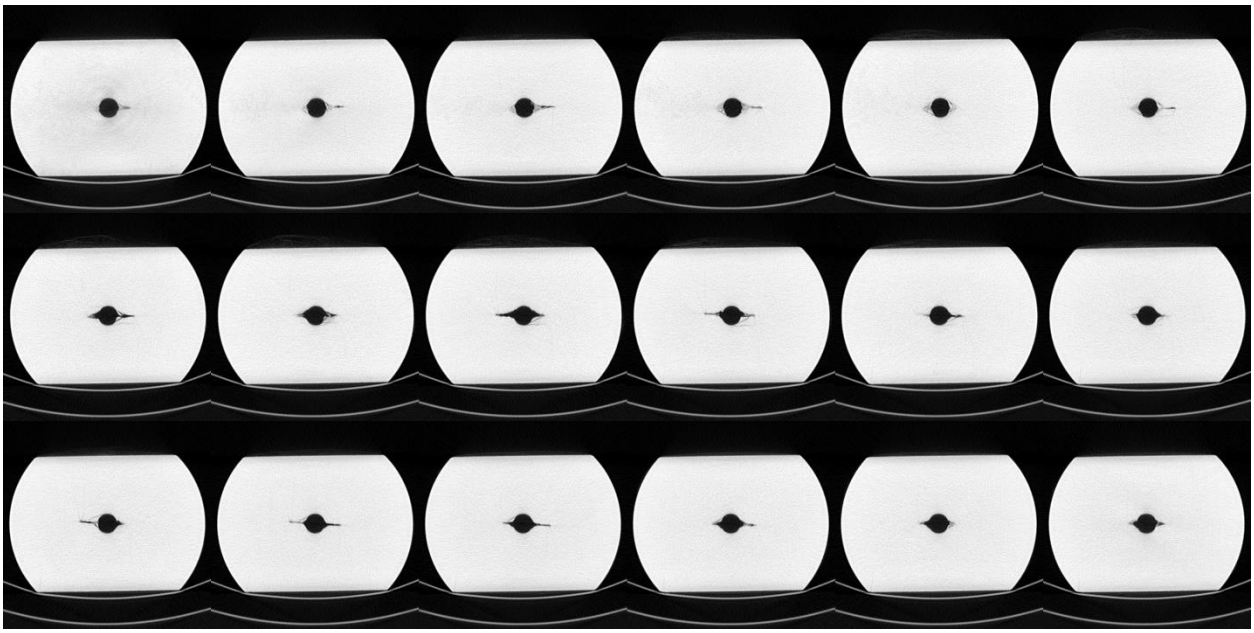

Figure 3.52 rock scanning for each layer with kr=1/3 and kz=2/3.

From the scanning pictures, a slot-like cavity is observed. It developed in the stress concentrate direction. Compared to the simulation result, the direction and shape are correct. However, in the experiment, the cavity is narrower. The reason is that the grid density is not enough for the mesh created.

Comparing the scanning pictures with top and bottom surfaces after experiment, the profile of the failure region is not as narrow as scanned pictures. It indicates that the shape of the failed region is a slit-like cavity while the shape created by produced sand is more like a triangular.

Figure 3.53 Experiment result from bottom and surface with kr=1/3 and kz=2/3.

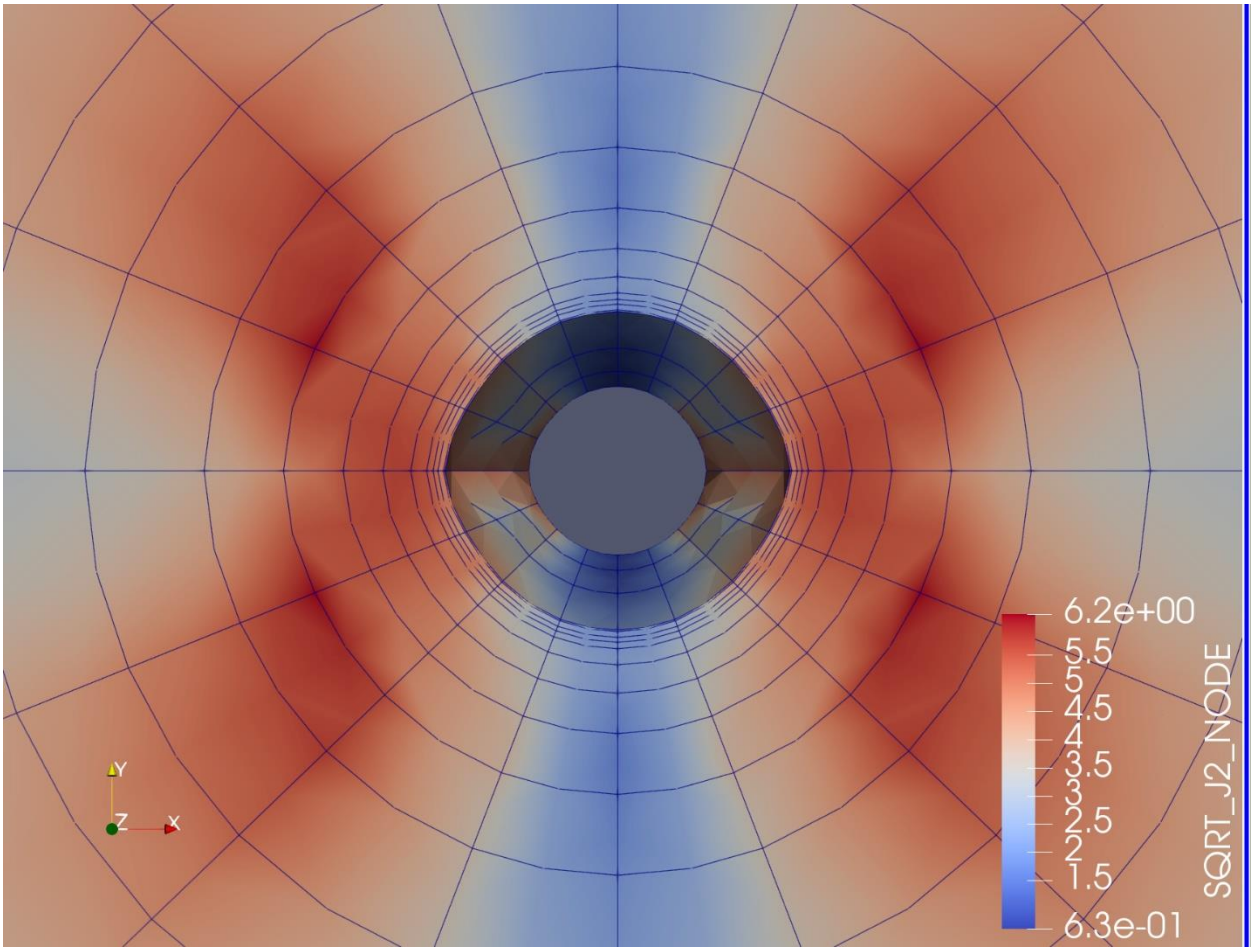

Figure 3.54 Cavity evolution with kr=1/3 and kz=2/3.

Case-10 315 kr = 1 kz = 2

The simulation conditions for Case-10 are shown in Table 3.11. The stress in the vertical direction is twice the radial direction and the radial stress is not directional.

Simulation parameters are listed below.

Table 3.11 Fluid and rock properties with kr=1 and kz=2.

Height	200 mm
internal diameter	20 mm
external diameter	200 mm
Permeability	0.49 Darcy
Porosity	0.261
Fluid Type	3.5% NaCl solution and kerosene oil
Fluid density	0.78 g/cm^3
Fluid viscosity	1.4 cp
Quartz density	2.65 g/cm^3
Differential pressure	0.0161 psi
Running time	0.138 day
Failure model	0.8
σ_r	4.548 kpsi
σ_R	4.548 kpsi
σ_z	9.82 kpsi

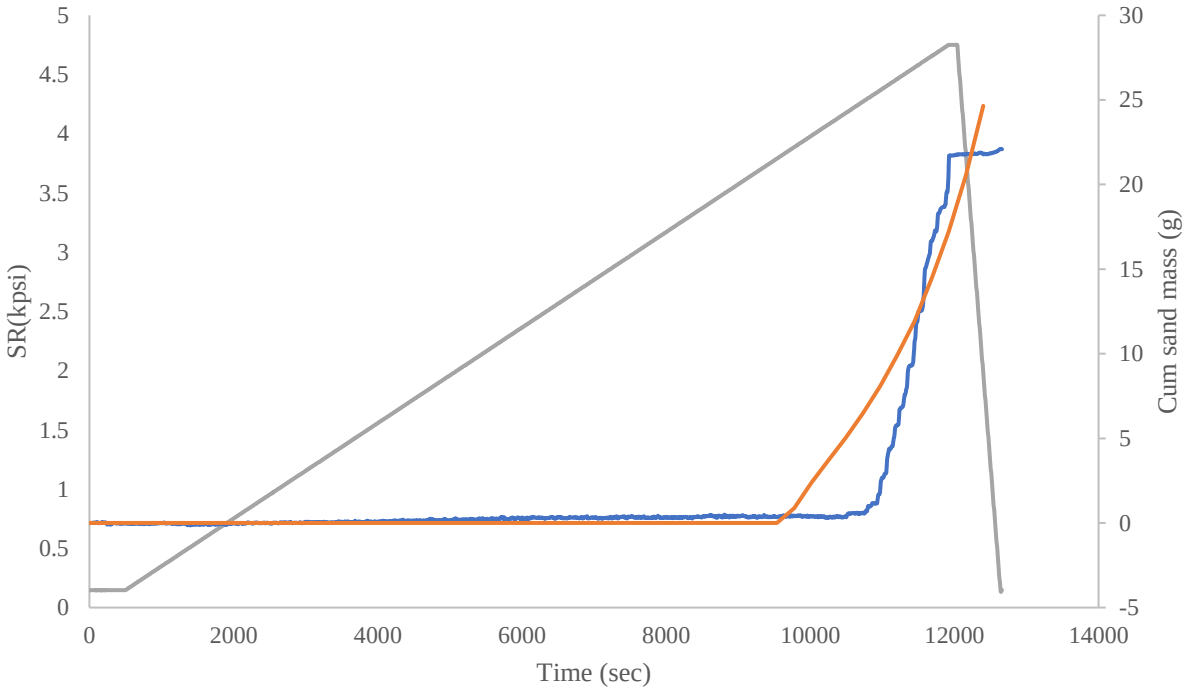

Figure 3.55 Simulation result vs experiment result with kr=1 and kz=2.

The stress in the horizontal direction is uniform so that the progress of sand production should be also uniform around the borehole. However, the experiment shows a local failure in 45° direction followed by a triangular shape cavity evolution. Based on the experimental data, initially the sand production rate increases, followed by declines in the end. This phenomenon also shows the possibility of sand-arching effect due to rock fragments. The onset time of the sand production prediction is far earlier than the experimental data; that means the rock is not as weak as we thought. Besides, according to the time vs stress curve, the simulation and real sand-production rate are at first almost similar, then the real sand rate declined.

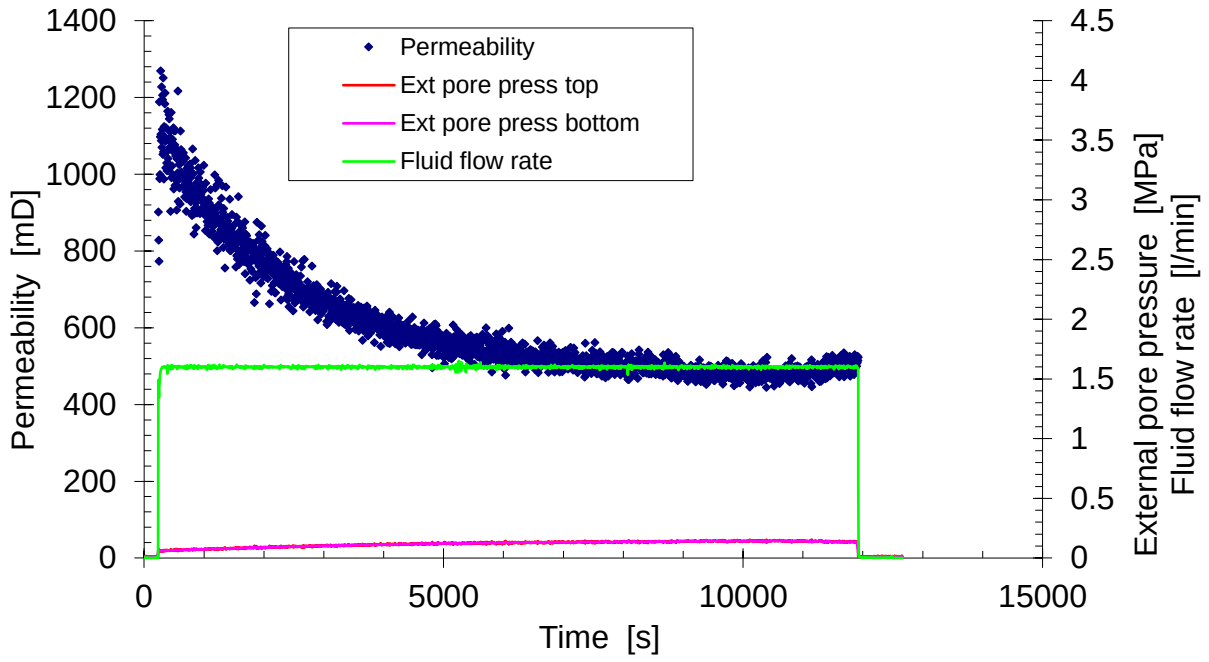

Figure 3.56 Fluid flow rate and pore pressure during experiment with kr=1 and kz=2.

After the onset of the sand-production, the permeability is about 0.6 D.

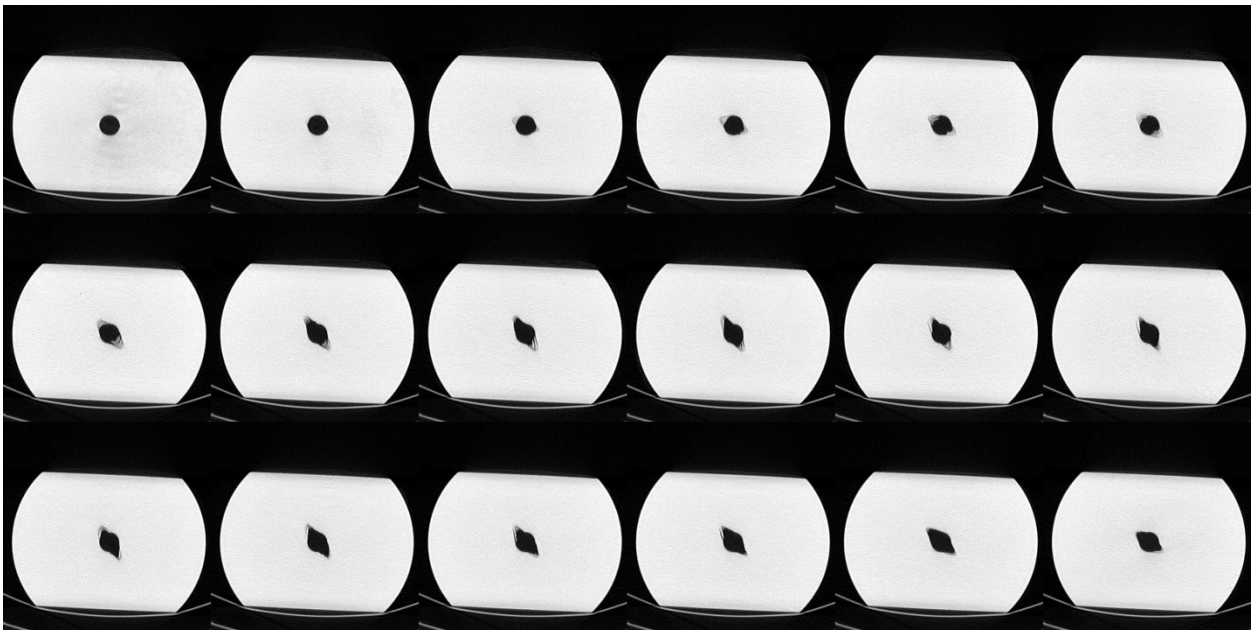

Figure 3.57 rock scanning for each layer with kr=1 and kz=2.

From the scanning pictures (Figure 3.57), we know how the sand is produced and how the failure region looks like. Compared to the top and bottom surfaces after experiment, the results did not match. Besides, the simulation result shape is different from the scanning photos. The scanning image shows the variation of density while the real photos show the real cavity.

Figure 3.58 Experiment result from bottom and surface with kr=1 and kz=2.

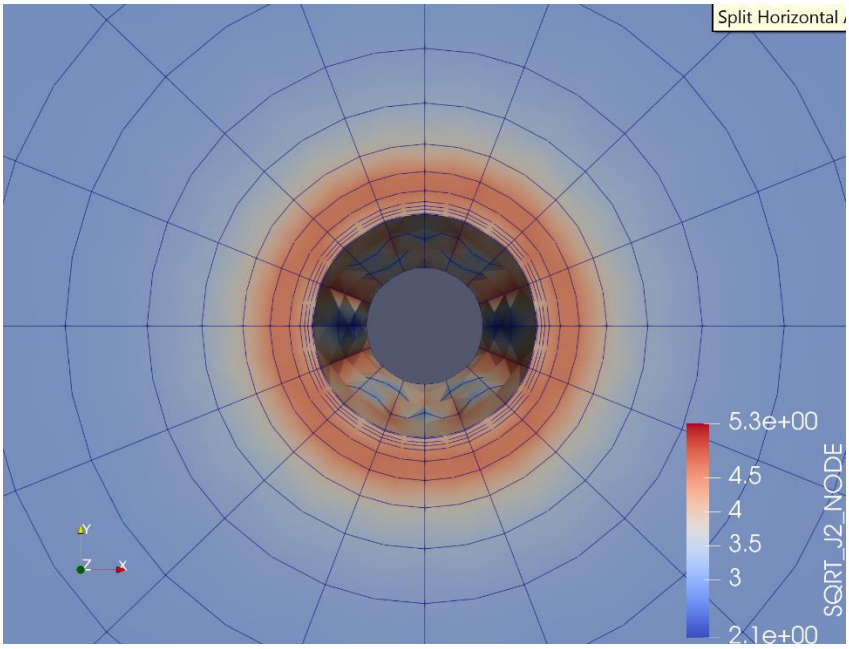

Figure 3.59 Cavity evolution with kr=1 and kz=2.

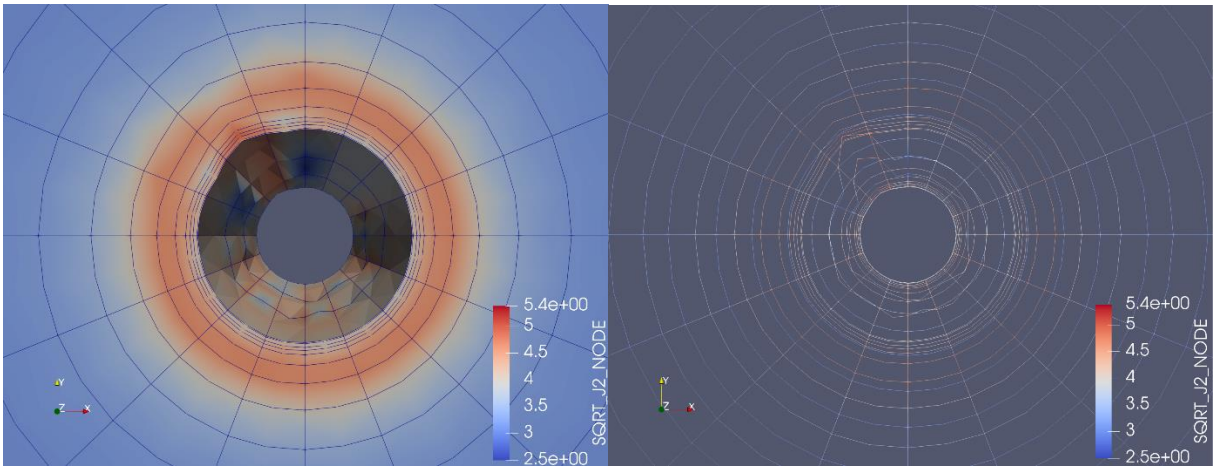

Figure 3.60 Cavity evolution with Permeability streak at element 135° with 1 Darcy permeability with kr=1 and kz=2.

Another simulation calculation was done for investigating the heterogenous permeability effect on the cavity shape. If the permeability is increased twice in 45° direction for the simulation, the shapes of sand produced zone match between the simulation and experiment

Case-11 316 kr = 1 kz = 1

The simulation conditions for Case 11 are shown in Table 3.12. The stress conditions for the vertical and horizontal direction are both isotropic.

Table 3.12 Fluid and rock properties with kr=1 and kz=1.

Height	200 mm
internal diameter	20 mm
external diameter	200 mm
Permeability	0.66 Darcy

Porosity	0.261
Fluid Type	3.5% NaCl solution and kerosene oil
Fluid density	0.78 g/cm^3
Fluid viscosity	1.4 cp
Quartz density	2.65 g/cm^3
Differential pressure	0.0120 psi
Running time	0.132 day
Failure model	0.8
σ_r	5.37 kpsi
σ_R	5.429 kpsi
σ_z	5.386 kpsi

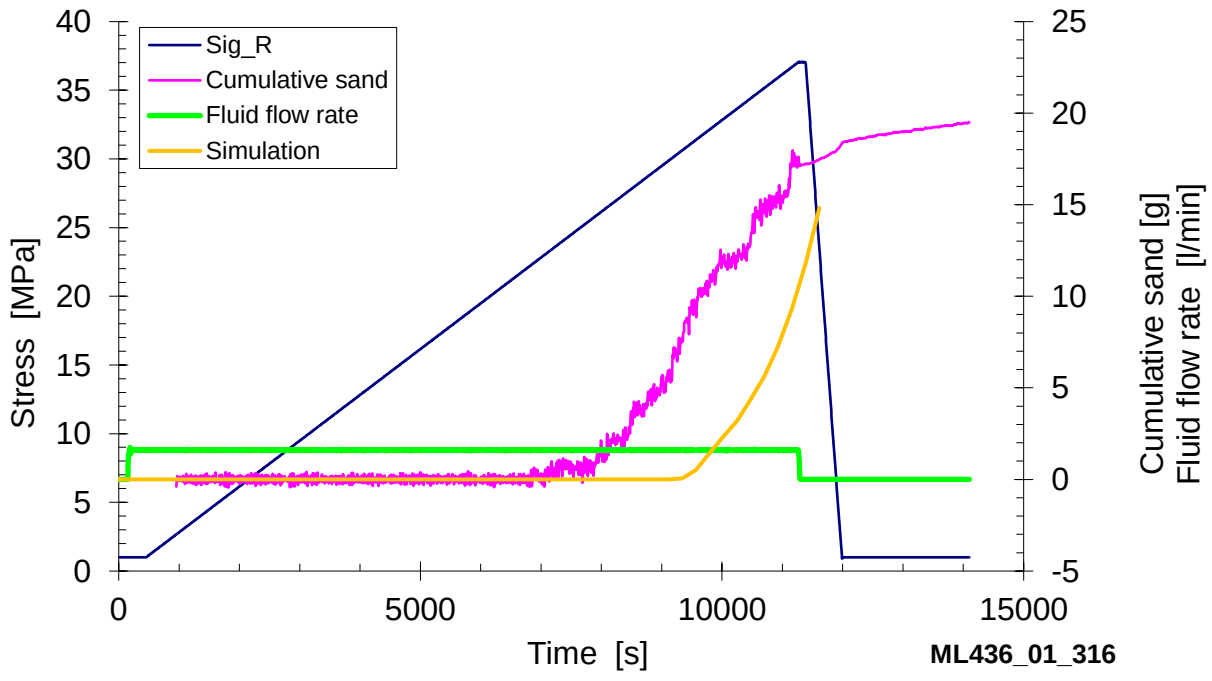

Figure 3.61 Simulation result vs experiment result with kr=1 and kz=1.

Since the stress in the tangential direction is constant, the cavity evolution must be radial and a circular cavity must be formed. However, the experiment shows that a slit-like cavity is formed. According to the experiment data, at first the sand production rate increased, however, it decreased in the end. This phenomenon also showed the possibility of sand-arching effect where sand fragments block narrow cavity. The onset time of the prediction is far behind the real data, suggesting the rock is not as strong as we thought.

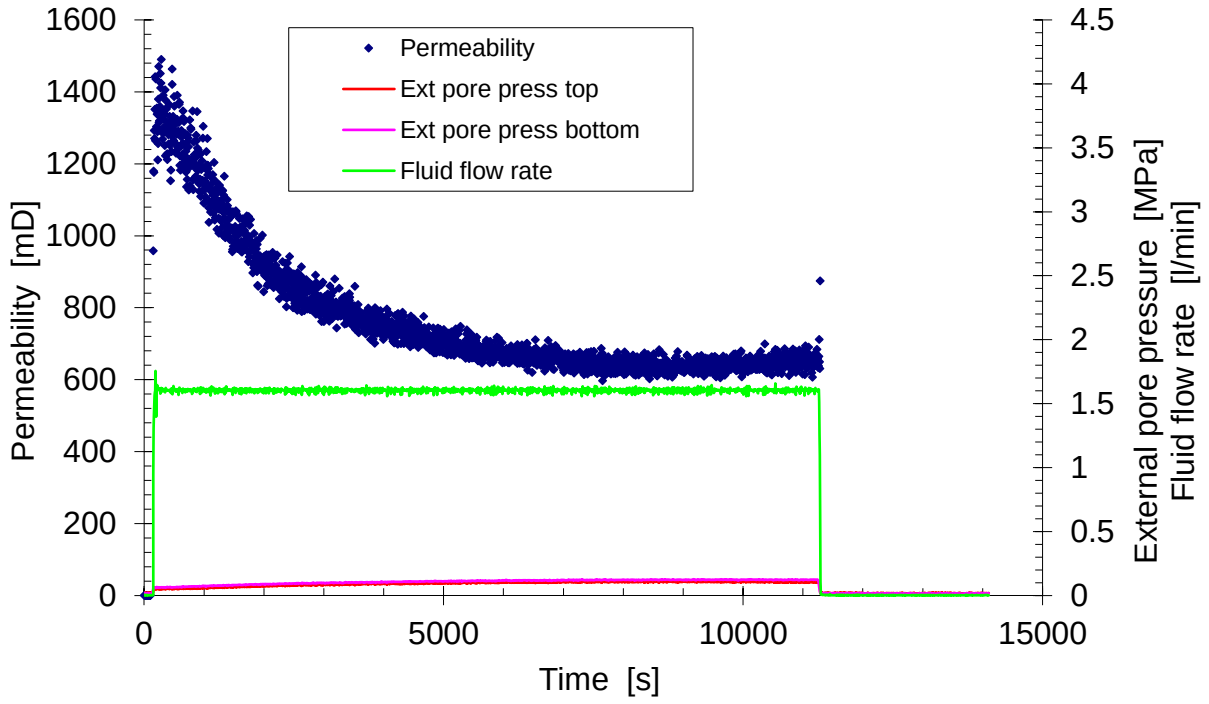

Figure 3.62 Fluid flow rate and pore pressure during experiments with kr=1 and kz=1.

After the sand-production onset, the permeability fluctuation is small, we can consider it as 620 mD.

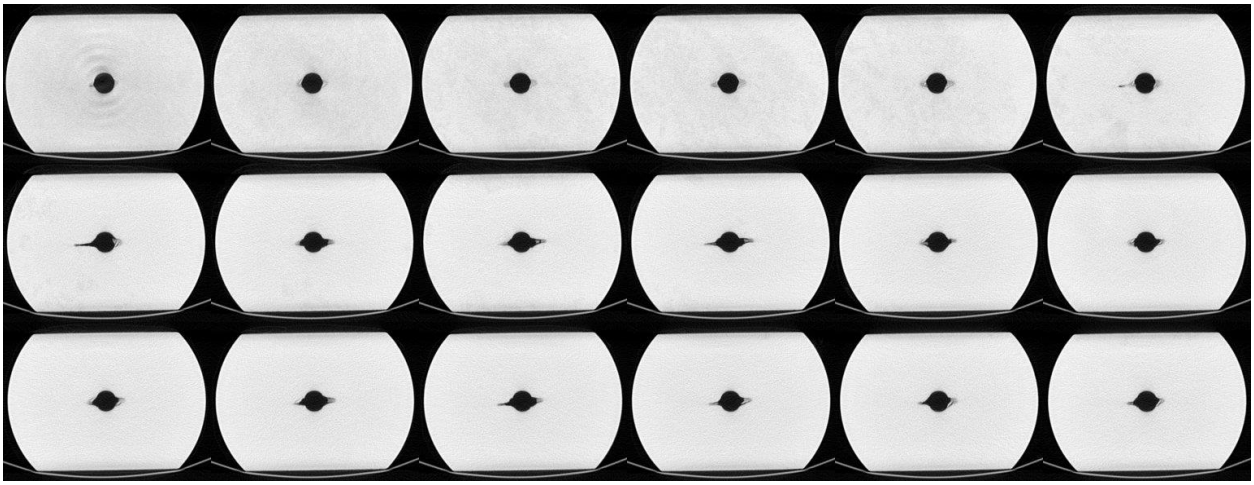

Figure 3.63 rock scanning for each layer with kr=1 and kz=1.

The scanning data show there are two very narrow failed zones around cavity. But the shape did not match between the images and the top and surface pictures or simulation result.

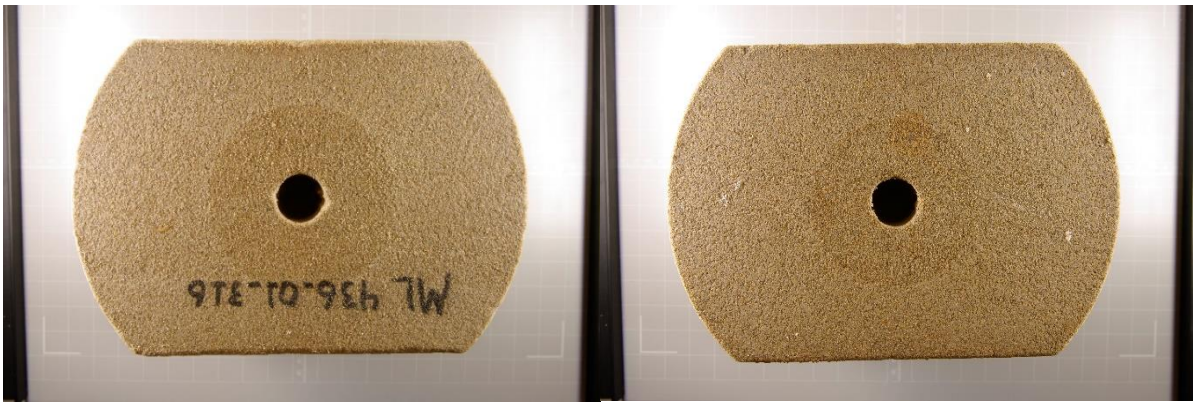

Figure 3.64 Experiment result from bottom and surface with kr=1 and kz=1.

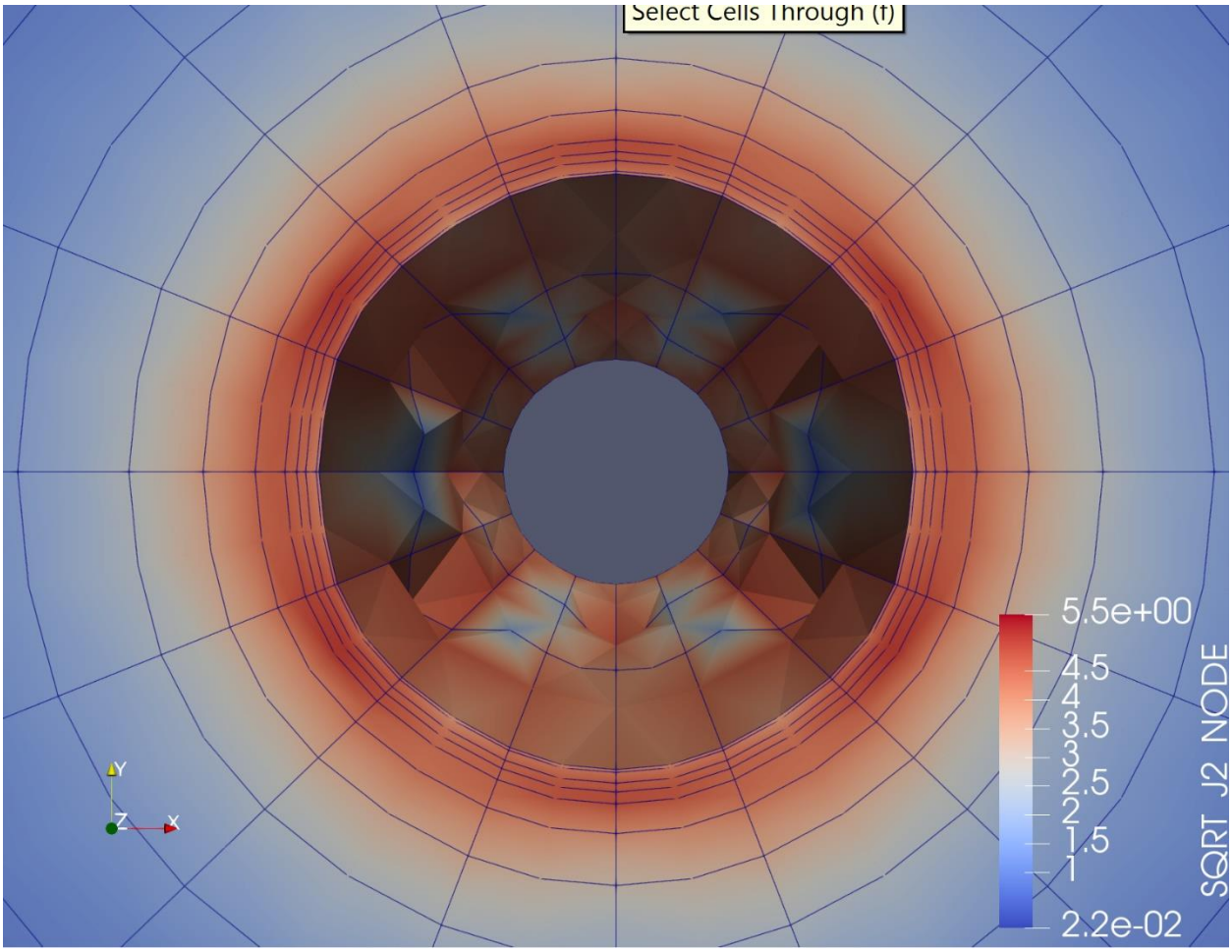

Figure 3.65 Cavity evolution with kr=1 and kz=1.

Case-12 317 kr = 2/3 kz = 2

The simulation conditions for Case-12 are shown in Table 3.13. The stress condition for the vertical and horizontal direction are both anisotropic.

Table 3.13 Fluid and rock properties with kr=2/3 and kz=2.

Height	200 mm
internal diameter	20 mm
external diameter	200 mm
Permeability	0.6 Darcy
Porosity	0.267
Fluid Type	3.5% NaCl solution and kerosene oil
Fluid density	0.78 g/cm^3
Fluid viscosity	1.4 cp
Quartz density	2.65 g/cm^3
Differential pressure	0.0131 psi
Running time	0.135 day
Failure model	0.8
σ_r	3.09 kpsi
σ_R	4.61 kpsi
σ_z	9.927 kpsi

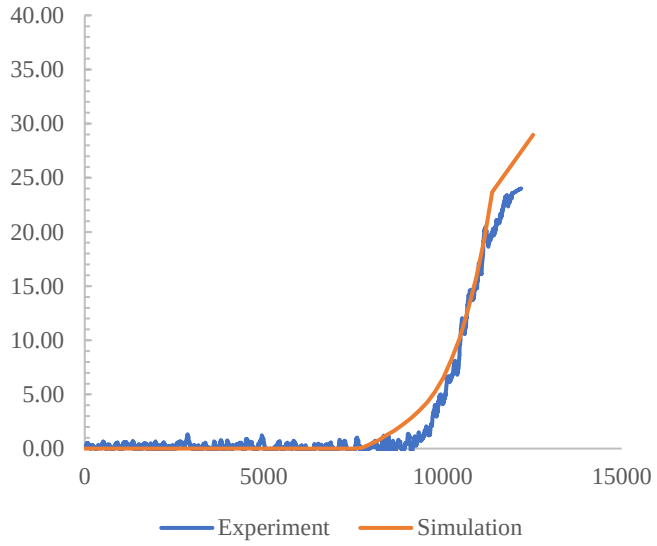

Figure 3.66 Simulation result vs experiment result with kr=2/3 and kz=2.

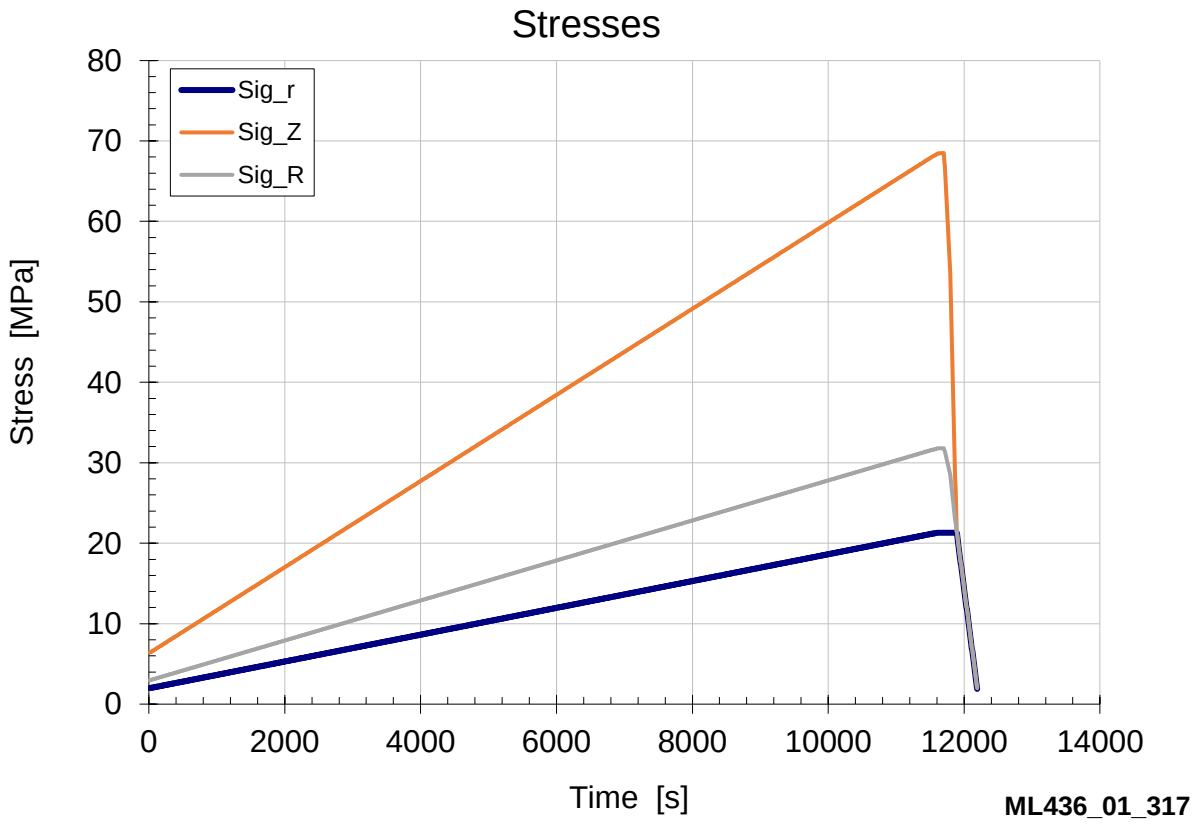

Figure 3.67 Stress conditions used in simulation with kr=2/3 and kz=2.

The onset time of sand production in the simulation is 8000s, while that in real experiment is about 9000s. Thus, we choose matching the final sand volume. From the graph above, the sanding rate is higher for simulation data, while the production rate for experimental data also increases very quickly.

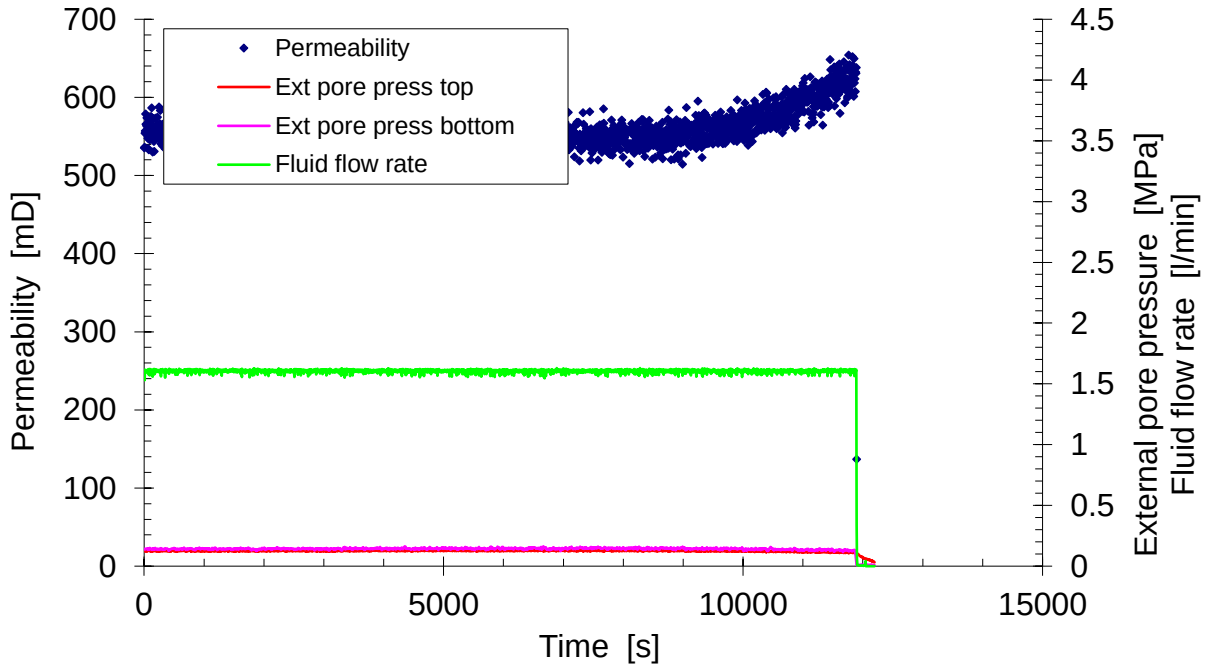

Figure 3.68 Fluid flow rate and pore pressure during experiment with kr=2/3 and kz=2.

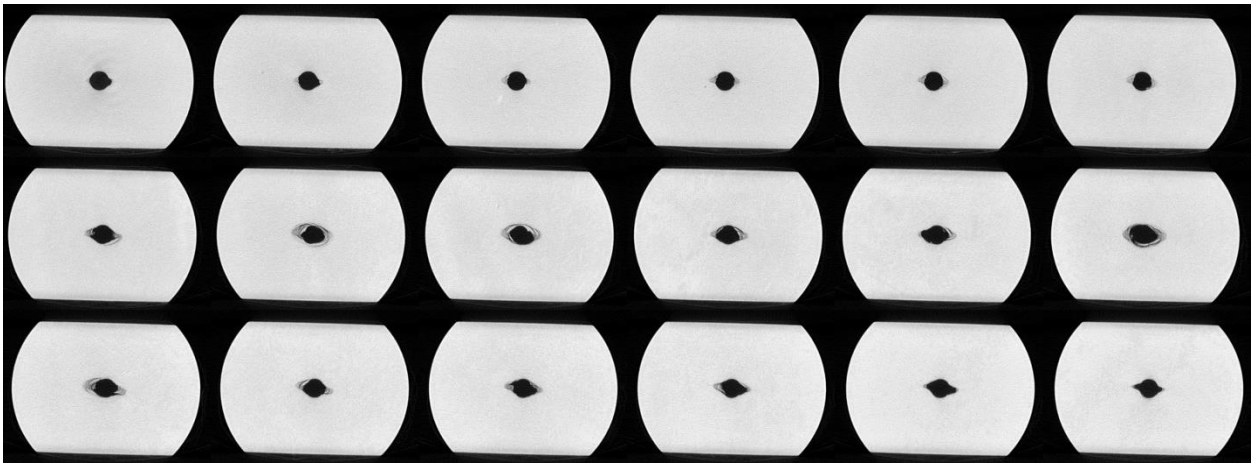

Figure 3.69 rock scanning for each layer with kr=2/3 and kz=2.

The scanning data show that the failure region is in the lateral direction and have two triangle cavities, however, in the top and bottom surfaces, we can just see the failure in right side, where the failure at the other side is not obvious. It indicates that the failure region density decreased in both right and left directions, while the cavity progressed in one direction. Compared to simulation result, the scanning data match well with the numerical sand production model.

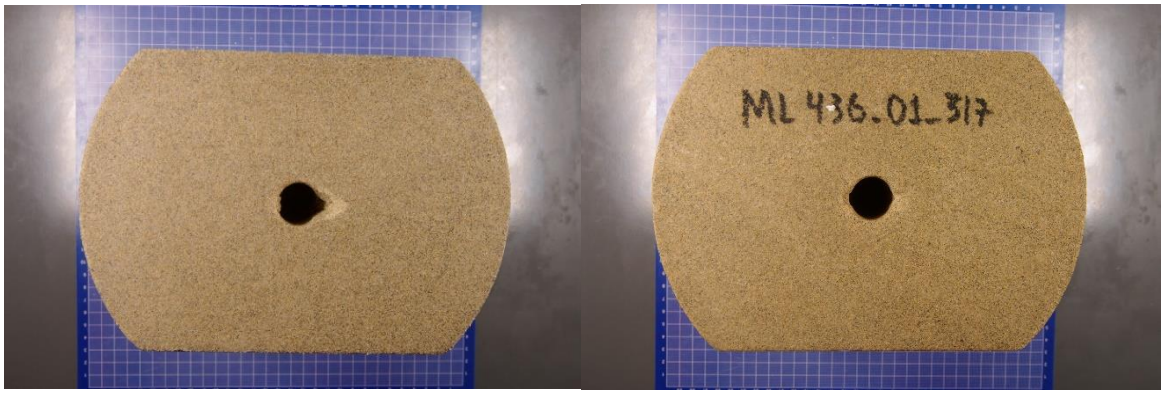

Figure 3.70 Experiment result from bottom and surface with kr=2/3 and kz=2.

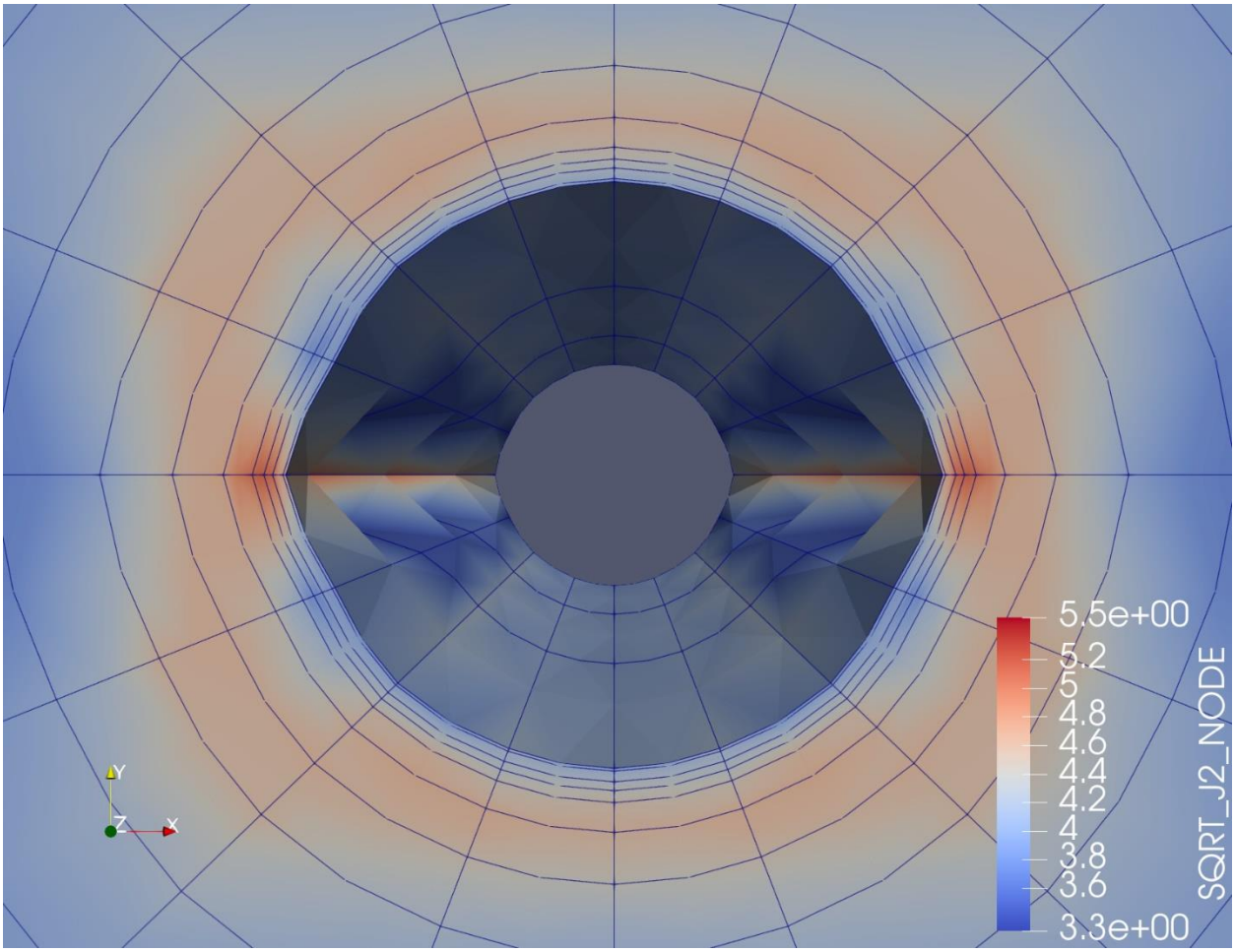

Figure 3.71 Cavity evolution with kr=2/3 and kz=2.

Case-13 318 kr = 1/3 kz = 1

The simulation conditions for Case-13 are shown in Table 3.14. The stress conditions for the vertical and horizontal direction are both anisotropic.

Table 3.14 Fluid and rock properties with kr=1/3 and kz=1.

Height	200 mm
internal diameter	20 mm
external diameter	200 mm
Permeability	0.82 Darcy
Porosity	0.268
Fluid Type	3.5% NaCl solution and kerosene oil
Fluid density	0.78 g/cm^3
Fluid viscosity	1.4 cp
Quartz density	2.65 g/cm^3
Differential pressure	0.00964 psi
Running time	0.158 day
Failure model	0.8
σ_r	2.88 kpsi
σ_R	8.10 kpsi
σ_z	8.216 kpsi

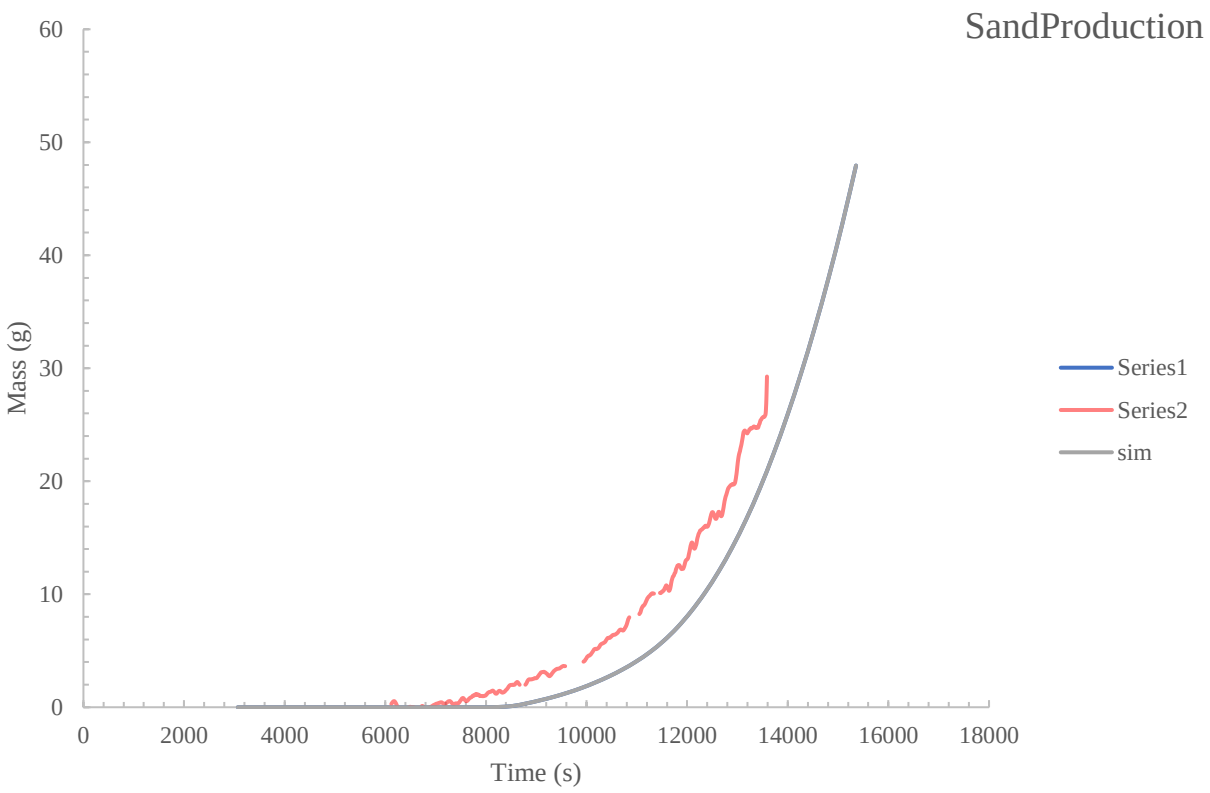

Figure 3.72 Simulation result vs experiment result with kr=1/3 and kz=1.

The onset of sand production for the simulation is at about 8000 seconds, while the onset of real experiment is at about 7000 seconds. Besides, the sand production rate increases very quickly during the experiment. We tried to match the sand production volume at the end of the experiment.

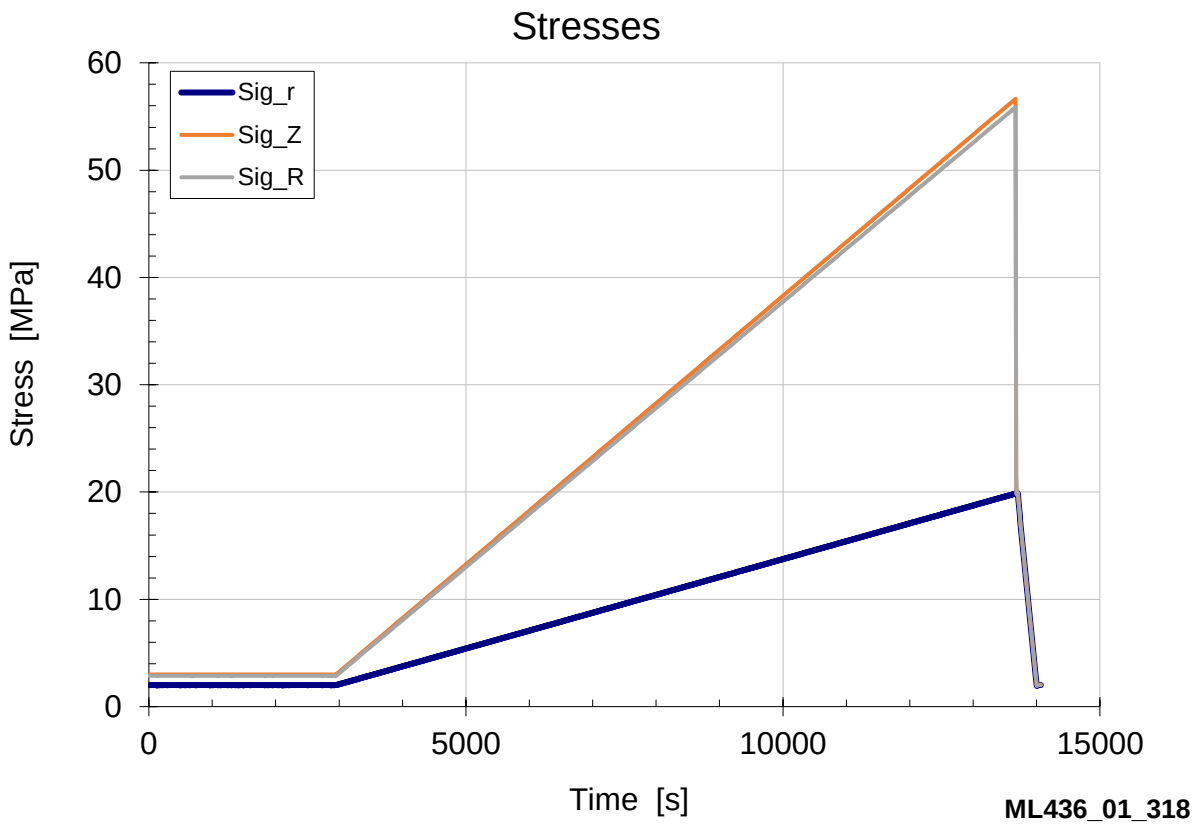

Figure 3.73 Stress load curve with kr=1/3 and kz=1.

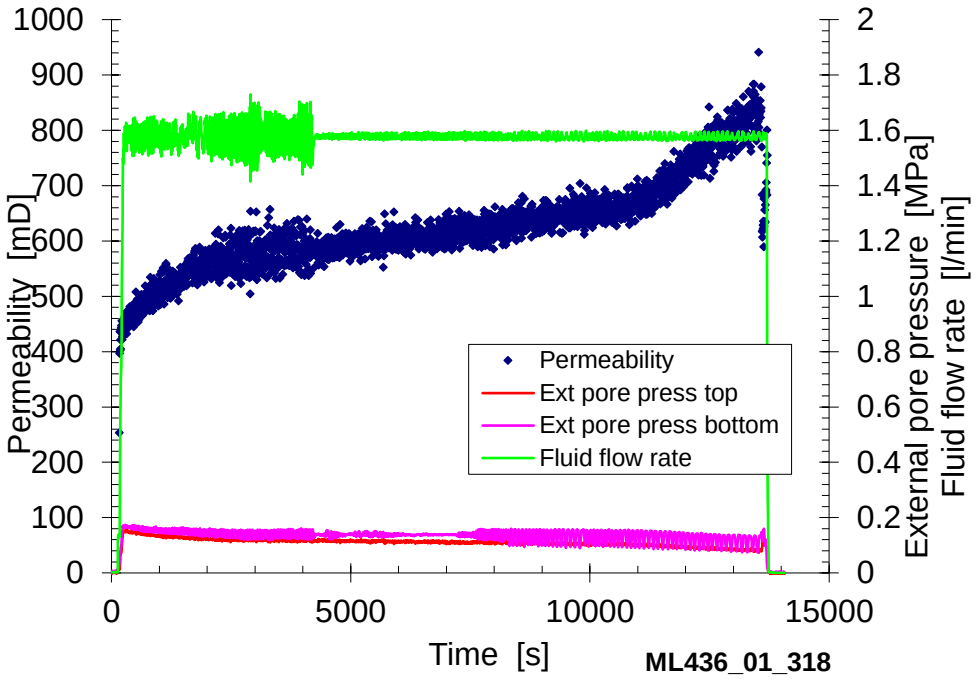

Figure 3.74 Fluid flow rate and pore pressure during experiment with kr=1/3 and kz=1.

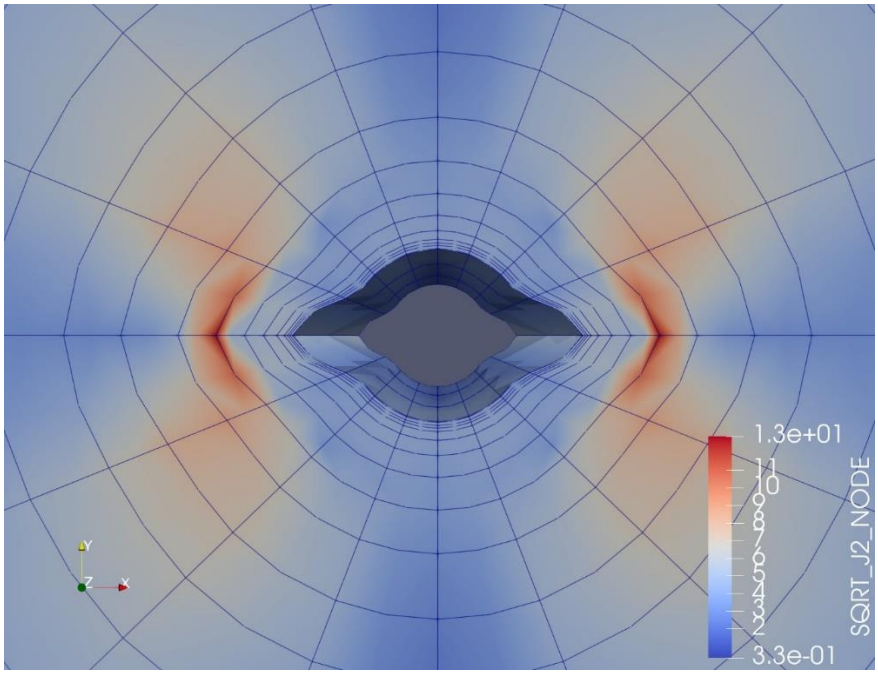

Figure 3.75 Cavity evolution with kr=1/3 and kz=1.

From the simulation prediction, the cavity shape looks to extend along the least stress direction. However, there is no core photos for the experiment, so we do not know how the cavity evolved in the experiment.

Case-14 302 kr = 1 kz = 1

The simulation conditions for Case 14 are shown in Table 3.15. The stress condition for the vertical and horizontal direction are both isotropic.

Table 3.15 Fluid and rock properties with kr=1 and kz=1.

Height	200 mm
internal diameter	20 mm
external diameter	200 mm
Permeability	0.9 Darcy
Porosity	0.268
Fluid Type	3.5% NaCl solution and kerosene oil
Fluid density	0.78 g/cm^3
Fluid viscosity	1.4 cp
Quartz density	2.65g/cm^3
Differential pressure	0.00879 psi
Running time	0.132 day
Failure model	0.8
σ_r	6.529 kpsi
σ_R	6.529 kpsi
σ_z	6.529 kpsi

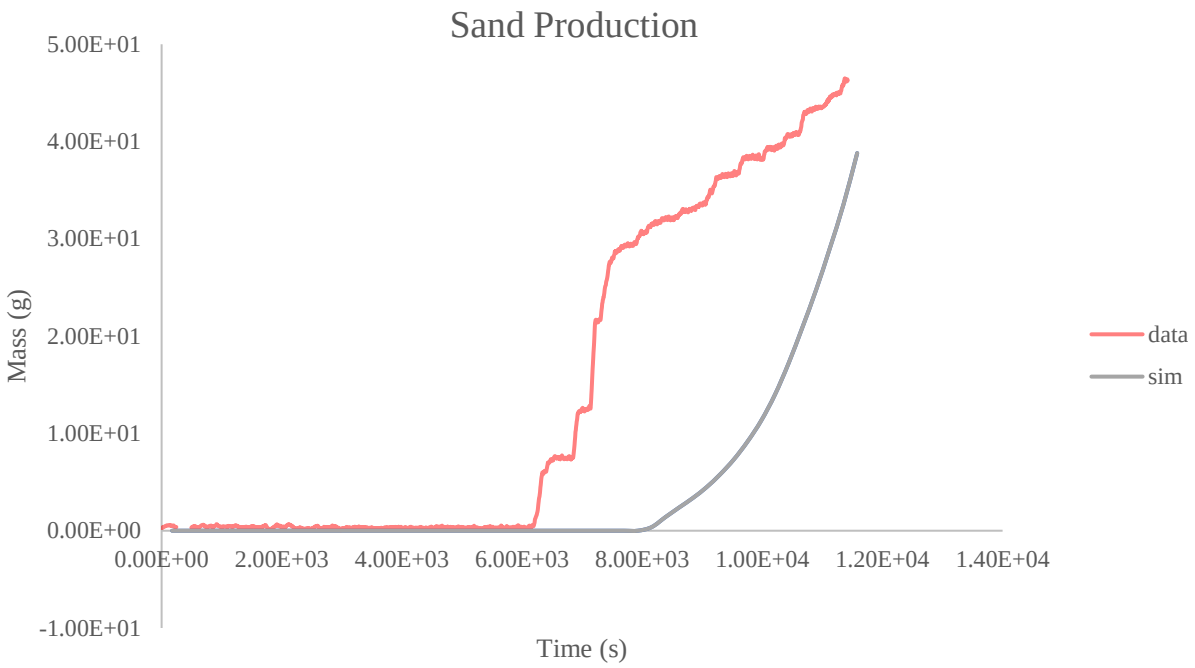

Figure 3.76 Simulation result vs experiment result with kr=1 and kz=1.

The onset time for sand production for the experiment is more than 6000 seconds, while, for simulation, it is about 8000 seconds. From the result, we could guess, the strength of this piece of sample is not as strong as others. If $\sigma_r = \sigma_R$, the cavity progress must be radial. However, the earlier onset of production shows that the failure starts at one local point with a higher permeability and with weak rock strength.

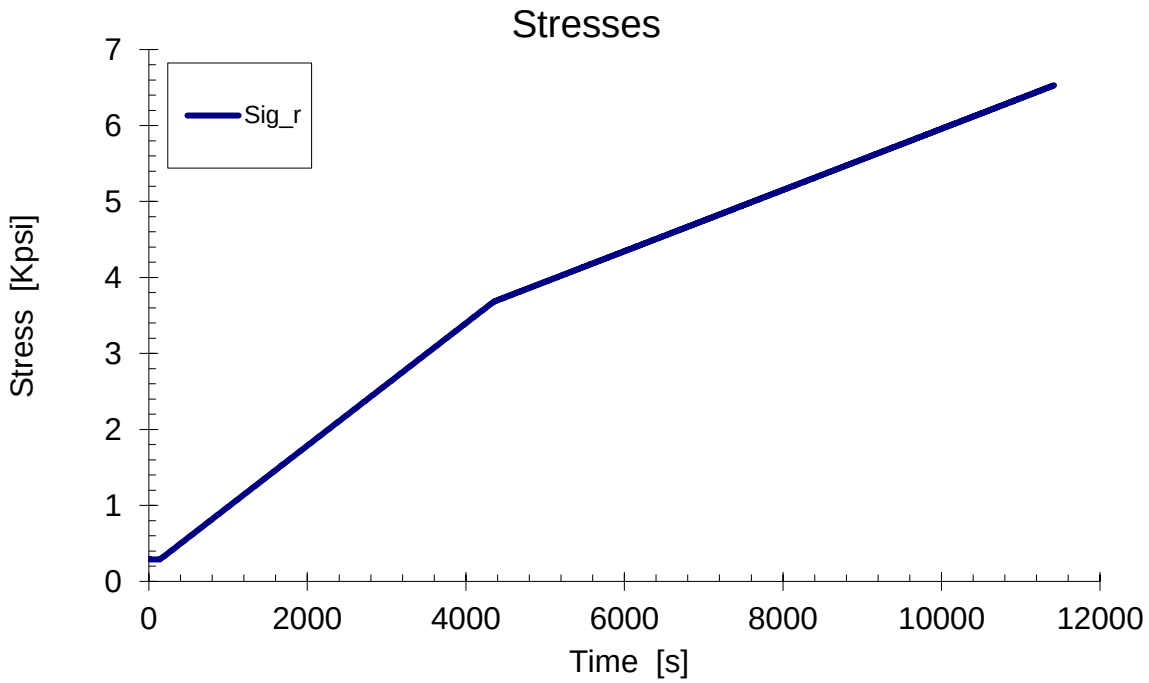

Figure 3.77 Stress load curve with kr=1 and kz=1.

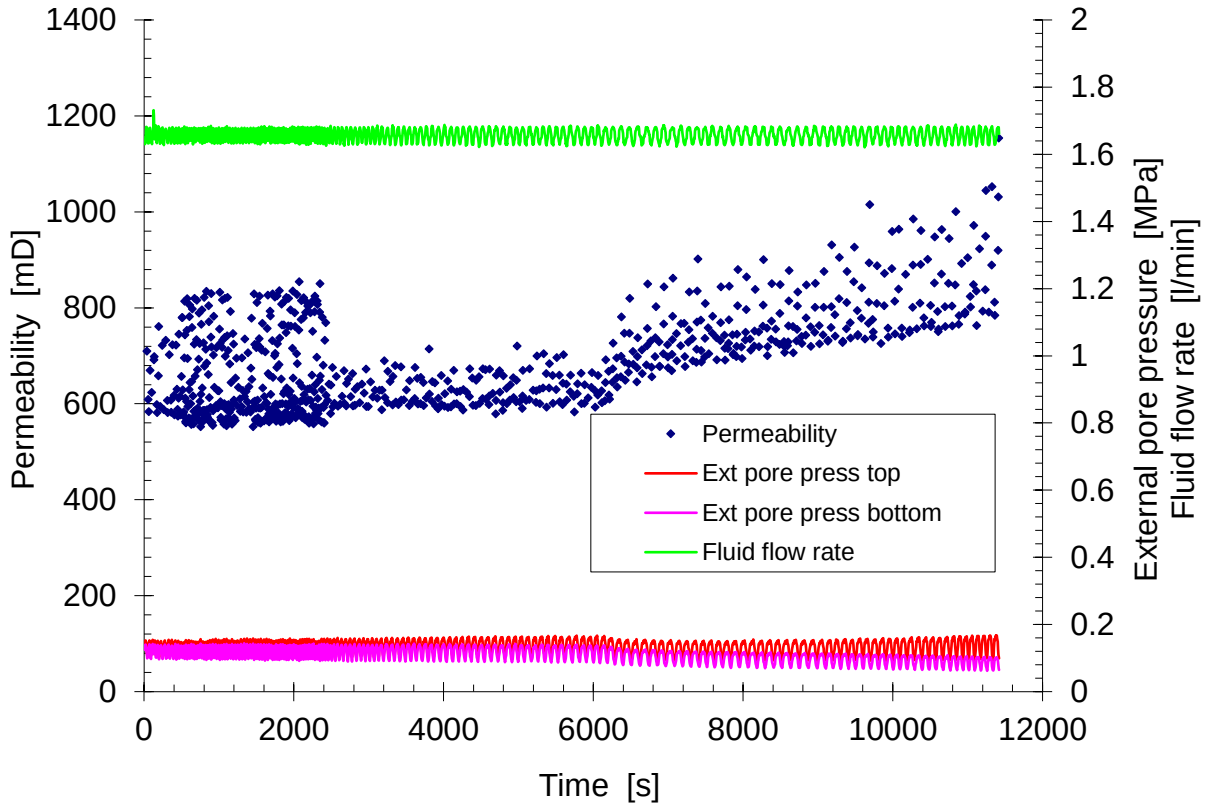

Figure 3.78 Fluid flow rate and pore pressure during experiment with kr=1 and kz=1.

In this experiment, there is no scanning data and after-experiment top & bottom surfaces.

CHAPTER IV SAND RATE SIMULATION FOR FIELD CONDITIONS

4.1 Field conditions

The Castlegate sandstone used in the experiments has a UCS of 2056 psi, with approximately 600 md permeability and 0.265 porosity, although these values vary between samples. The reservoir rock with the similar strength, permeability and porosity is often found in the North Sea oil reservoirs where sand production problems are not severe but should be mitigated. The following conditions are used as a filed simulation condition.

Table 16 Reservoir conditions

Depth of the reservoir = 10000 ft
Vertical stress gradient = 0.9 psi/ft (9000 psi at 10000 ft)
$\sigma_{h1} = 7500\,psi$, $\sigma_{h2} = 7500\,psi$
The initial reservoir pressure = 6000 psi
Formation: Rock similar to the Castlegate sandstone (UCS = 2056 psi, porosity = 0.26, k = 600md)
One phase flow above bubble point, viscosity = 1.4cp
1kpsi depletion per year with $\sigma_h^e / \sigma_v^e = 0.4$
200 psi drawdown (k=600md, zero skin factor) (19.257 bbl/day/perf)
Eight shots per foot spiral pattern with 60-degree phasing.

4.2 Effect of different factors

Sand production is controlled by many factors including in-situ stress, pressure, depletion rate and drawdown.

4.2.1 Effect of sand production decline coefficient

Field sand production step rate tests show the sand production increases with an increase in drawdown but the rate declines with time after changing in the drawdown. Laboratory tests also have shown that the sand rate does not stop when the confining pressure on rock sample is kept constant but it declines exponentially with time. The transient sand release equation is described in Eqs. 2.19-2.27.

Fig.4.1 shows the step rate tests performed in Gulfaks reservoir. (Massie, Ian, Nygaard, Morita (1987)) The sand rate increases if the drawdown is increased stepwise. But the sand rate immediately declines within 1 hour. Figure 4.2 shows a laboratory step rate experiment for sand rate measurement. Each time, the confining stress is increased, the sand rate increases. Even if the confining stress is maintained constant, the produced sand keeps increasing for a while.

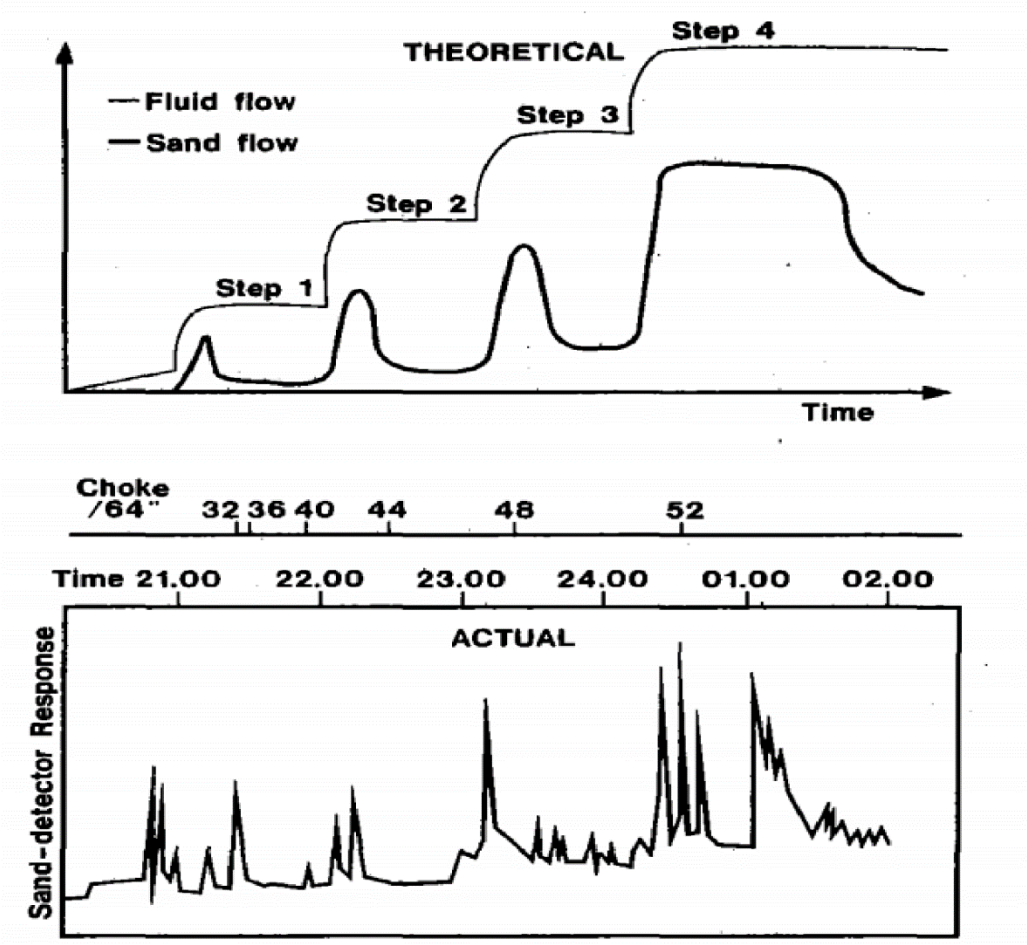

Figure 4.1 Theoretical and actual sand rate response during step rate tests in Gulfacks (Massie, Ian, Nygaard, Morita (1987))

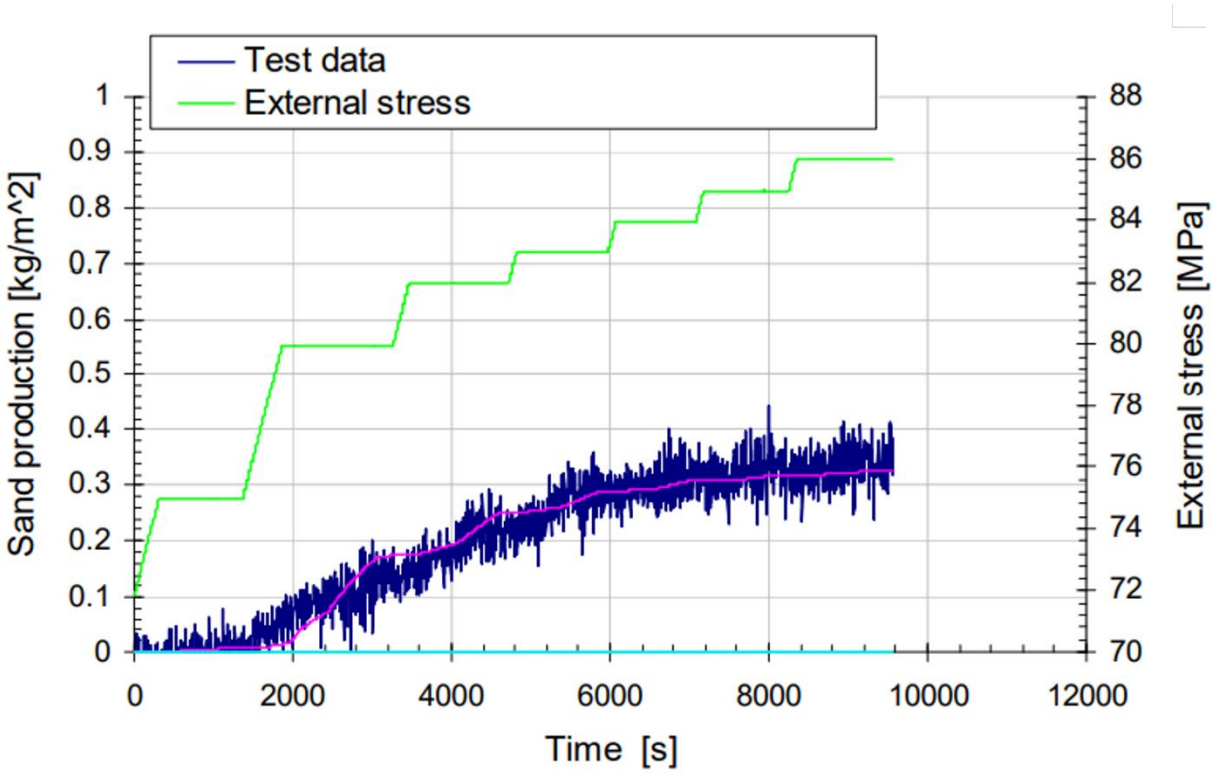

Figure 4.2 Laboratory measurement of sand rate

The decline rate may depend on the strength of rock and the stress state. From Figs.4.1 and 4.2, we assume the decline rate = $e^{-A_4 t}$ $(A_4 = 2.5 \sim 7.5,\ t = days)$. Then, simulation is performed with A_4 =2.5, 3.75 and 7.5, for a vertical well.

We assume the production initiates at time = 0 with 1 kpsi/365 days reservoir pressure depletion rate. Note that the initial reservoir condition is shown in Table 4.1. Cavities evolve in the horizontal direction where the stress concentration is the highest. The cavity evolution initiates at 280 days after production. However, since the cavities evolve into slit-like cavities, the evolution is slow until 380-420 days production. A_4 is the transient sand release rate

coefficient. According to the sand release rate equation, if $A_4 = 7.5$, the sand rate declines to 1/10th within 0.3 days if the stress increase is stopped while if $A_4 = 2.5$, it declines to 1/10th within 0.92 days. If the transient effect is limited to a shorter period (if $A_4 = 7.5$), the cavity evolution is slow and steady waiting for the stress increase induced by reservoir depletion while if it is longer ($A_4 = 2.5$), the cavity evolution is quick. The cavity evolves with an increase in the in-situ stress due to the reservoir depletion if the transient effect is smaller while it evolves quickly if the transient effect is larger. The field observation shows that although the cavity growth is slow during the early sand production, 10 to 20 gram of sand is produced from each cavity within 20-30 days once the onset of sand production initiates. Therefore, A_4=2.5 is used for field simulation. Note that field simulations with $A_4 = 7.5$ are shown in Appendix B for comparison.

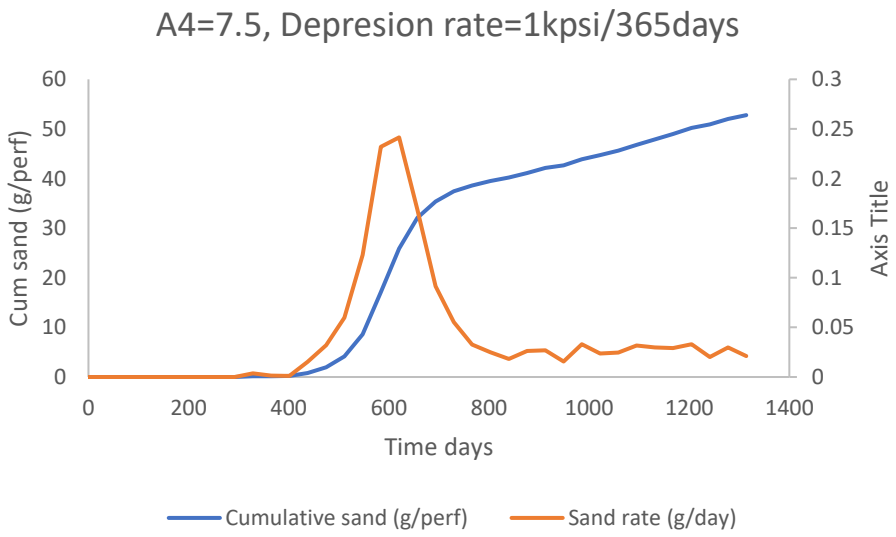

Figure 4.3 Vertical well sand production rate and accumulation with A_4=7.5 and depression rate=1kpsi/365days

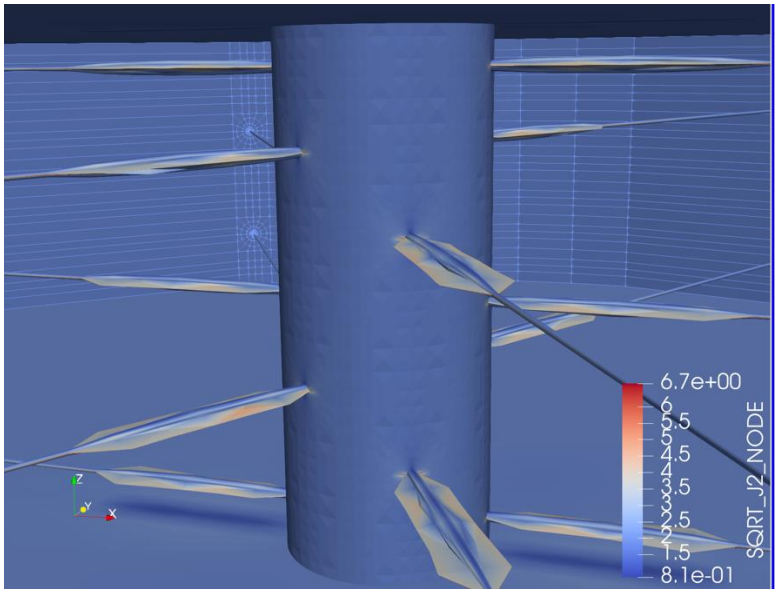

Figure 4.4 Visual result after failure with A_4=7.5 and depression rate=1 kpsi/365 days

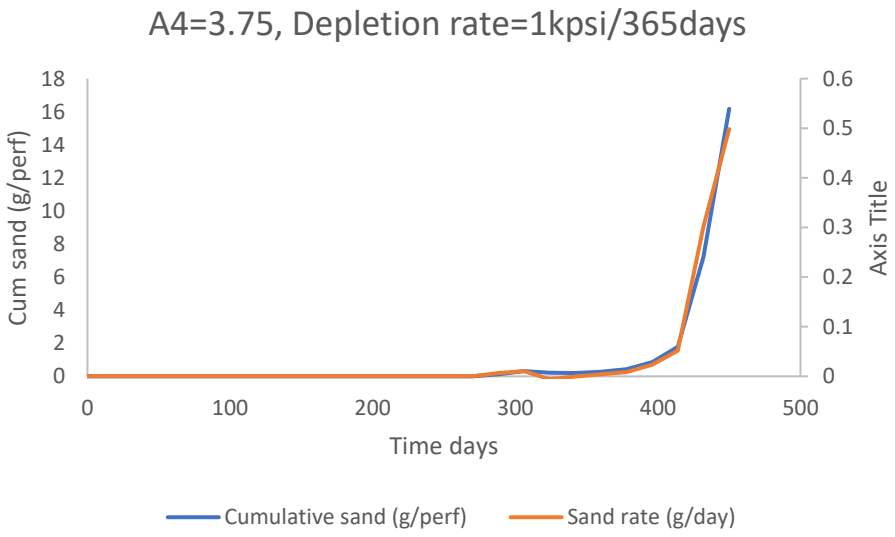

Figure 4.5 Vertical well sand production rate and accumulation with A_4=3.75 and depression rate=1 kpsi/365 days

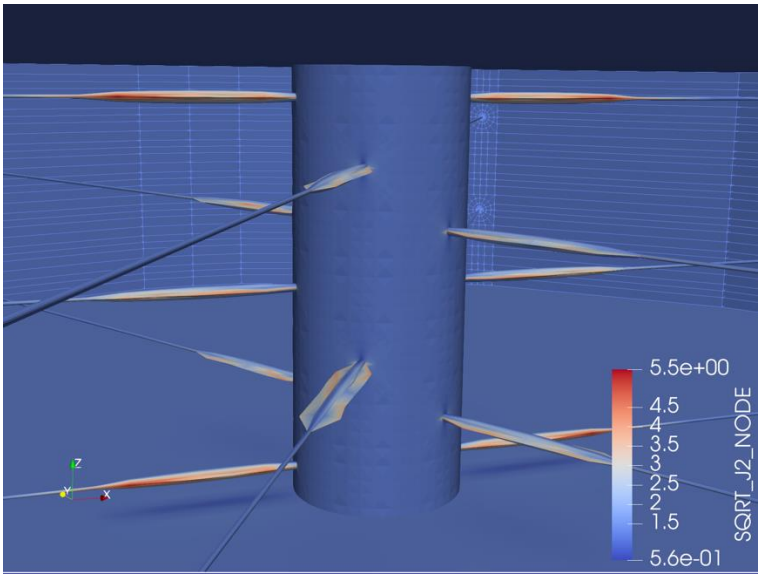

Figure4.6 Visual result after failure with A_4=3.75 and depression rate=1 kpsi/365 days

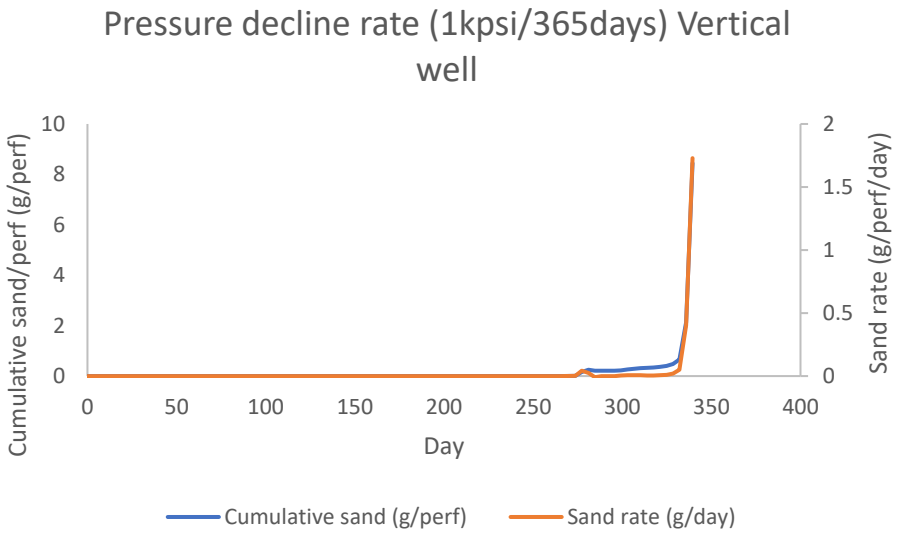

Figure 4.7 Vertical well sand production rate and accumulation with A_4=2.5 and depression rate=1 kpsi/365 days

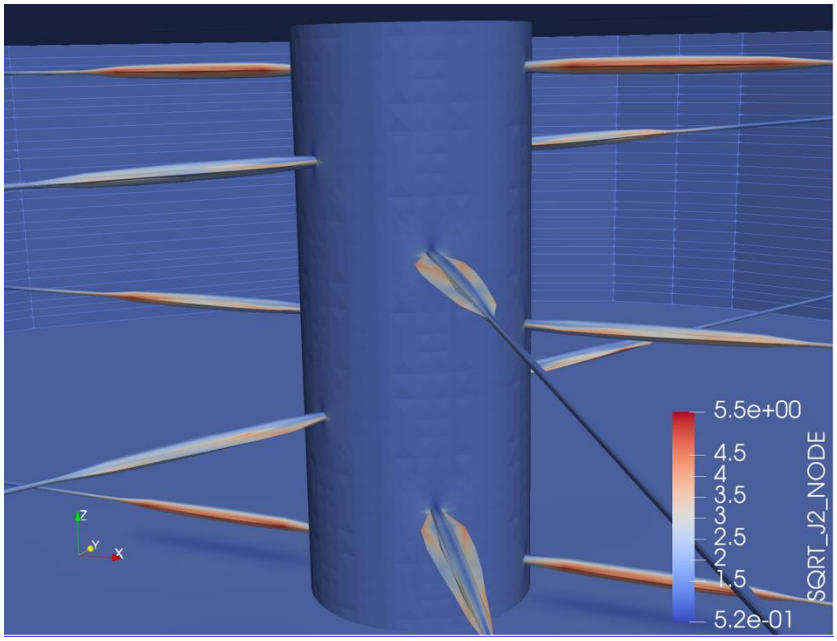

Figure 4.8 Visual result after failure with A_4=2.5 and depression rate=1 kpsi/365 days

4.2.2 Effect of depletion rate on sand rate

Figs.4.9, 4.10 and 4.11 compare the sand productions for the reservoir pressure depletion rate with 1 kpsi/365 days, 1 kpsi/182.5 days and 1 kpsi/91.25 days, respectively. The days from the production initiation to sand production on-set date are proportionally shorter as the depletion rate is higher. The cavity initially evolves into a stable slit-like cavity, then, sand rate suddenly increases after a while.

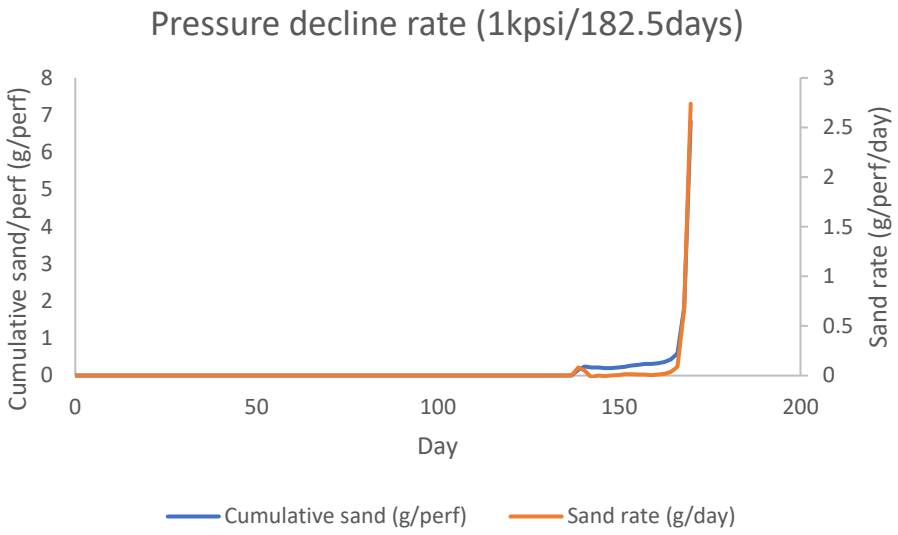

Figure 4.9 Vertical well sand production rate and accumulation with A_4=2.5 and depletion rate=1kpsi/182.5days

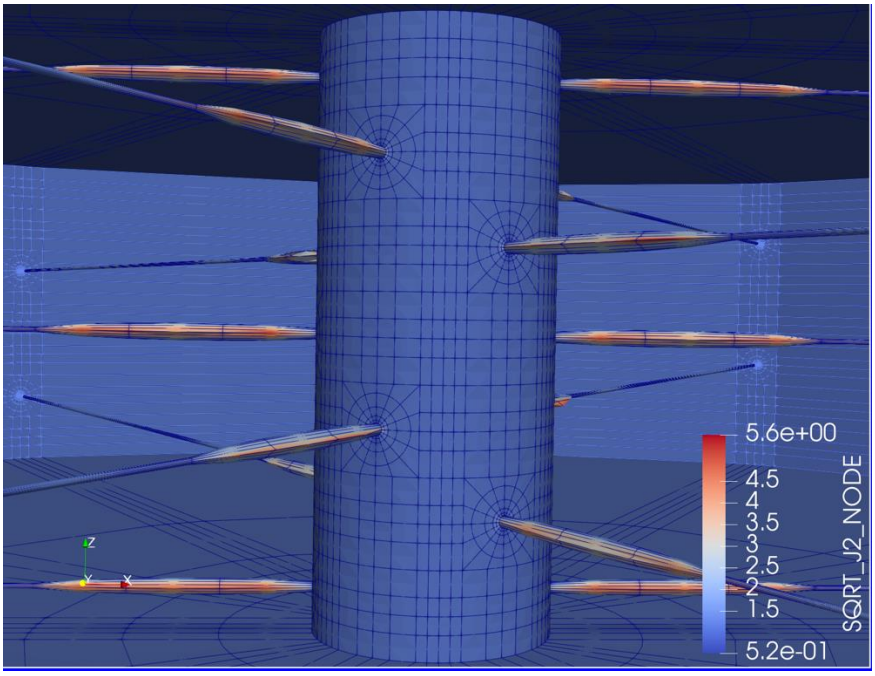

Figure 4.10 Visual simulation result with A_4=2.5 and depletion rate=1 kpsi/182.5 days

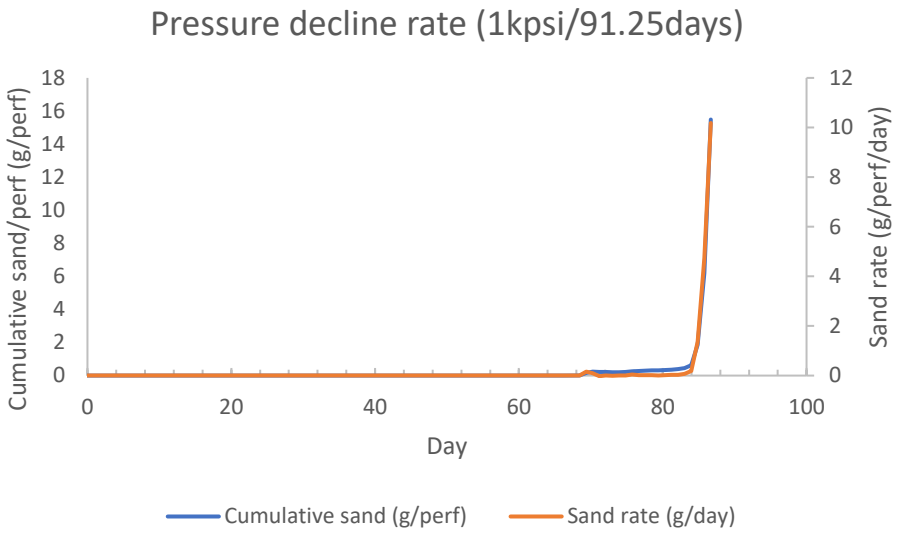

Figure 4.11 Vertical well sand production rate and accumulation with A_4=2.5 and depletion rate=1kpsi/91.25days

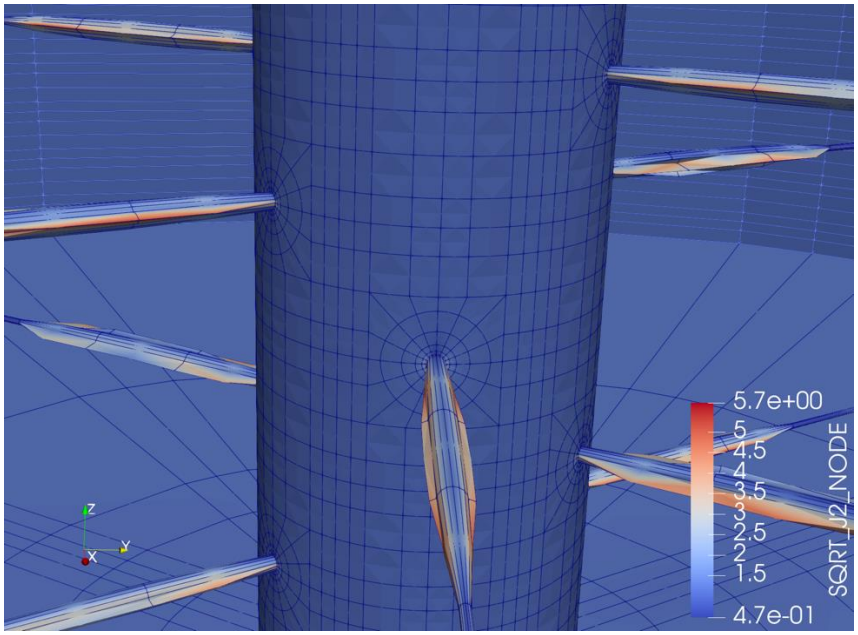

Figure 4.12 Visual simulation result with A_4=2.5 and depletion rate=1kpsi/91.25days

4.2.3 Effect of flow rate

Compared to the simulation experiment under 9.6285 bbl/day/perf flow rate (Fig.4.13), it can be observed that when the flow rate is 19.257 bbl/day/perf (Figure 4.15), the growth of cavity is quick. And for the result with 50 psi drawdown, the sand production is less than other two flow rates. The cavity growth is also more stable with a smaller drawdown. The results show that pressure drawdown could influence the sand production in both ways; if the drawdown is large, then the sand rate is high and cavity growth is not stable whereas if the drawdown is small, the stress increase is the constraint of the sand production.

Flow rate 9.6285bbl/day/perf (DP=100psi)

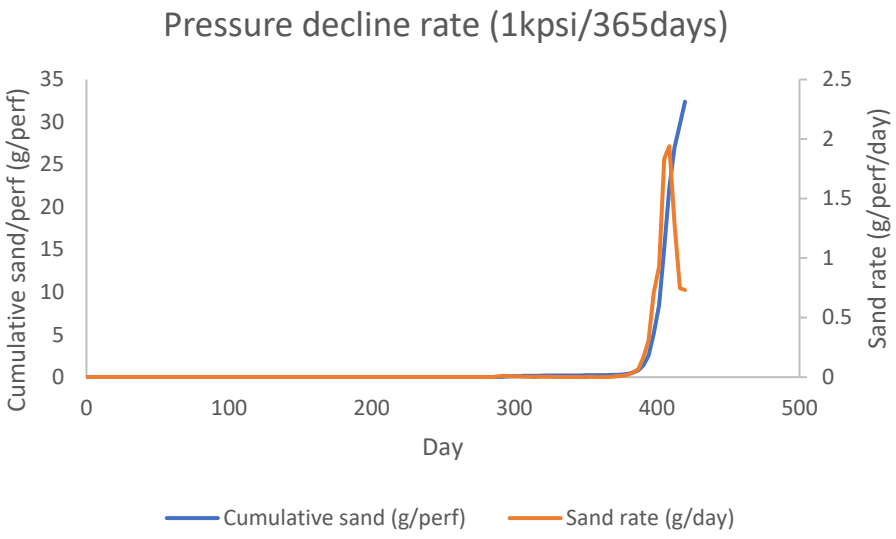

Figure 4.13 Simulation result with dp = 100psi

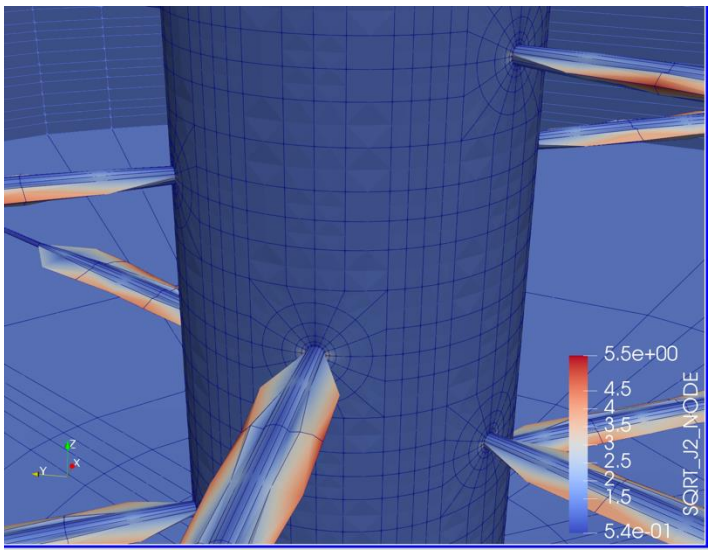

Figure 4.14 Visual simulation result with dp = 100psi

Flow rate 4.814 bbl/day/perf (DP=50psi)

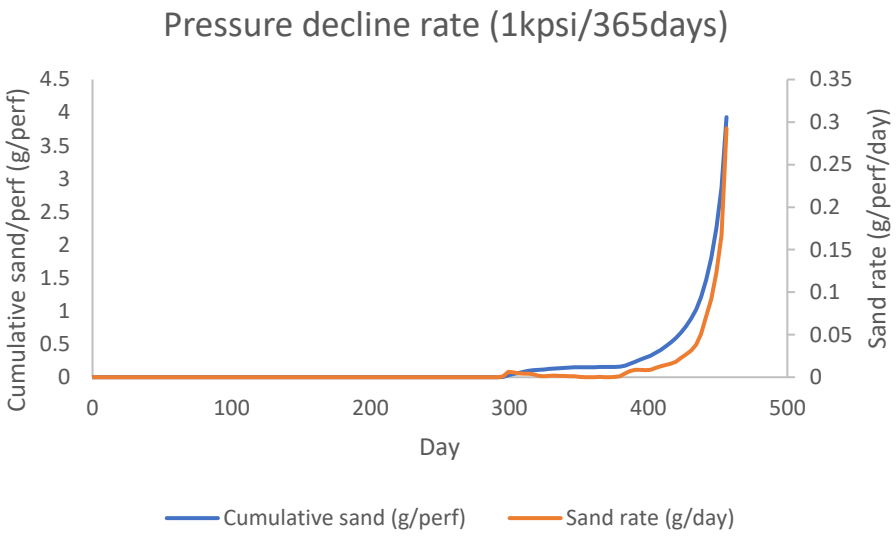

Figure 4.15 Simulation result with dp = 50psi

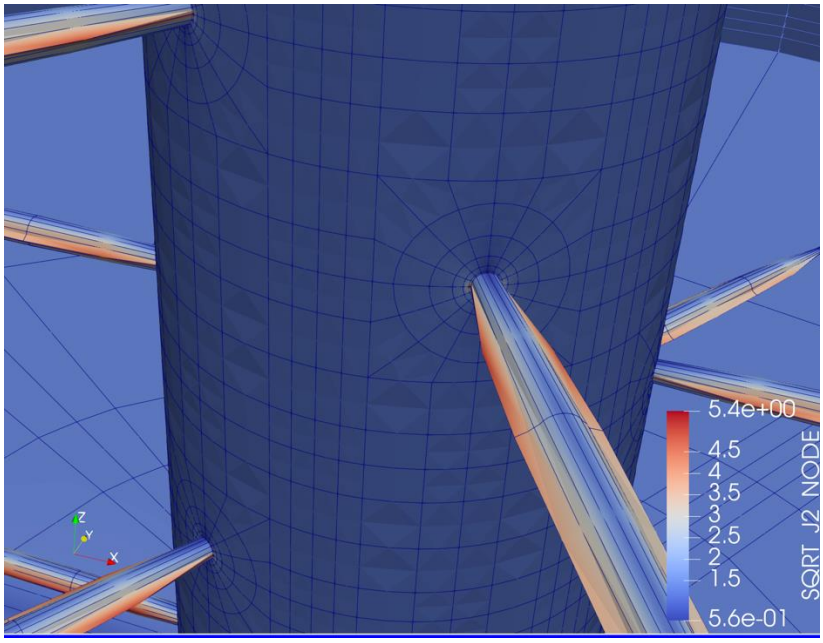

Figure 4.16 Visual simulation result with dp = 50psi

4.2.4 Effect of well inclination, isotropic permeability (permeability kx=ky=kz=600 mD)

Simulations are performed changing the well inclination assuming the permeability is isotropic. The perforations are stable for vertical wells. The stability depends on rock strength. If the rock strength is as strong as 2056 psi like the Castlegate sandstone, the cavity evolves into a slit-like shape if the vertical stress is significantly higher than the horizontal stress. Fig.4.17 shows that the sand production initiates at 270 days but the sand rate does not increase until 340 days. As Figures 3.51 in Chapter 3 shows that the cavity develops in horizontal direction into a slit-like cavity. Sand cannot be produced from the narrow cavity. Figure 4.18 shows the perforation cavities developed for a vertical well. Thin cavities develop in the horizontal directions where the stress concentration is very high. Figure 4.19 shows the enlarged pictures of cavity initiation between 270-300 days. A localized cavity appears on the horizontal direction when the cavity starts developing.

Figures 4.20 and 4.22 show the sand rate for 30° and 45° well inclination angle. The sand production starts around 270 days. However, if the well is inclined, the sand rate sharply increases after initiation.

If the well angle increases more than 55° (Figure 4.24), the cavity stability depends on which direction the perforations are shot. The perforation shot in the horizontal direction has the least stability while the perforation shot in the vertical direction has the highest stability. For 8 shots with 60° phasing spiral perforation, if one is shot in the vertical direction, then, other two are shot in 60° and 120°. On the other hand, if the perforation gun is rotated by 30°, the perforation directions are 30°, 90° and 150° from the vertical direction.

Generally speaking, sand production starts around 270 days for the spiral perforation. However, the perforation oriented in the horizontal direction does not increase the sand rate until the production is continued for 340 days.

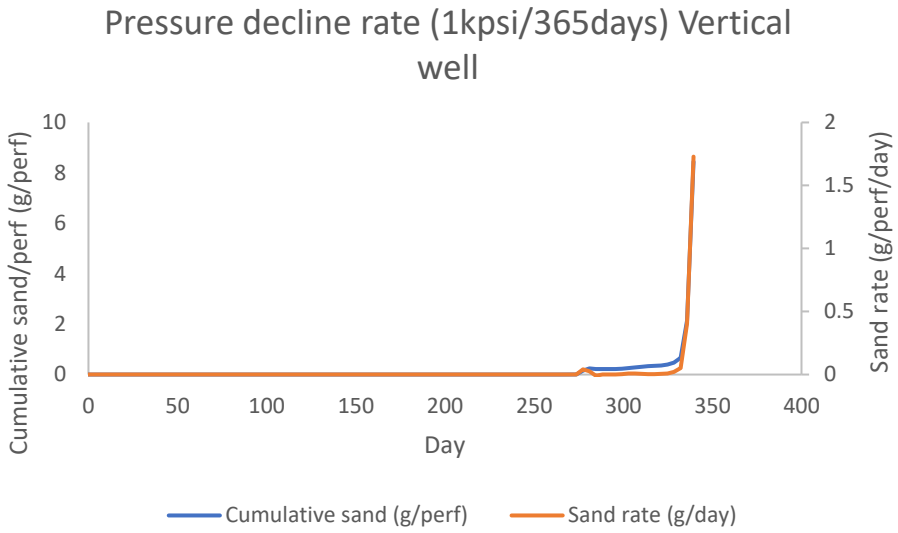

Figure 4.17 Vertical well sand production rate and accumulation with A_4=2.5 and depression rate= 1 kpsi/365 days, angle=90°

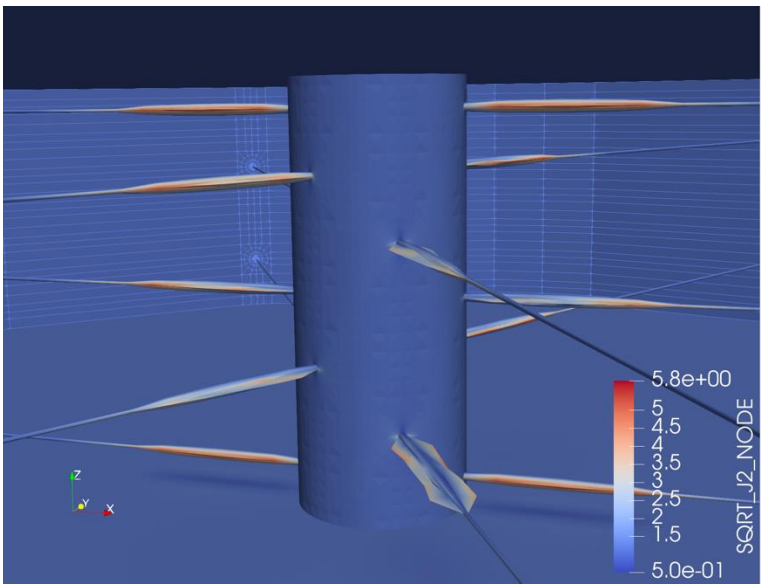

Figure 4.18 Visual simulation result with A_4=2.5 and depression rate=1 kpsi/365 days, angle=90°

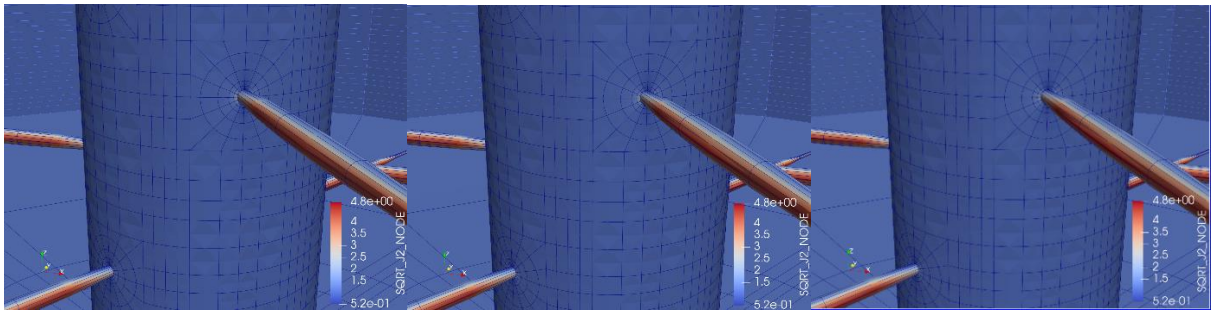

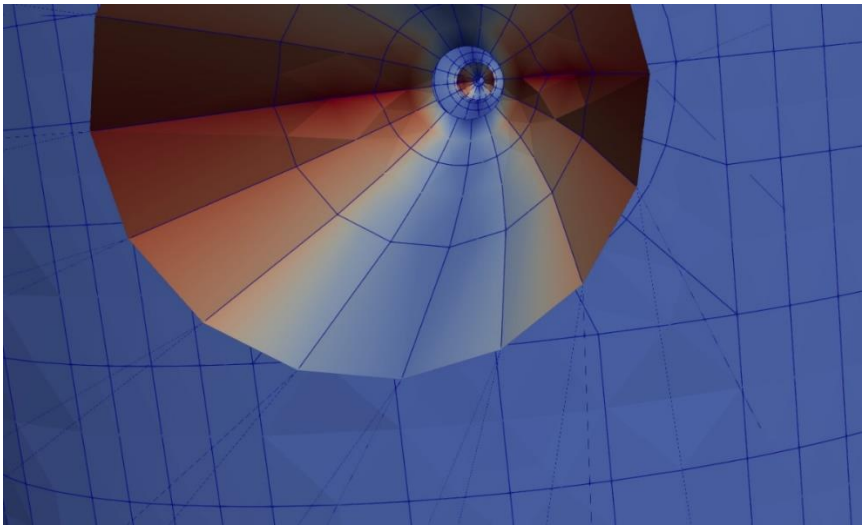

Figure 4.19 Visual simulation details with A_4=2.5 and depression rate=1 kpsi/365 days, angle=0°

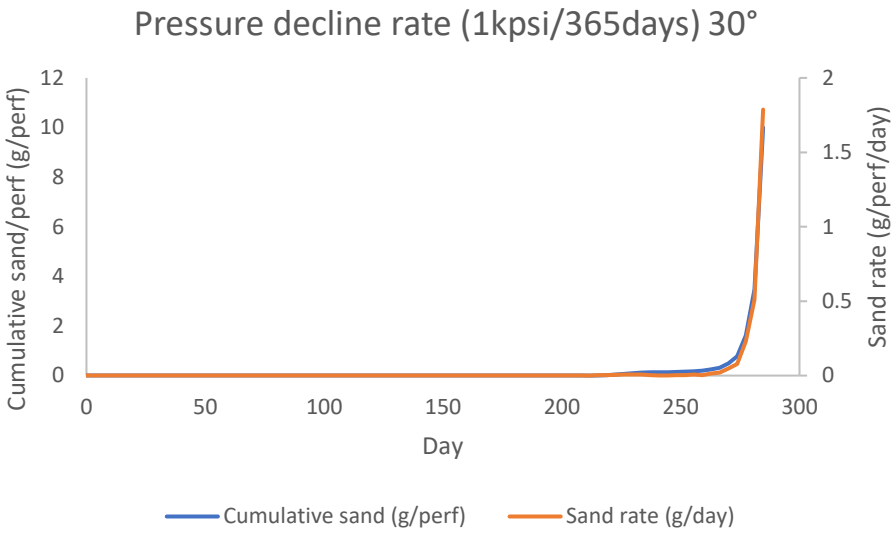

Figure 4.20 Vertical well sand production rate and accumulation with A_4=2.5 and depression rate=1 kpsi/365 days, angle=30

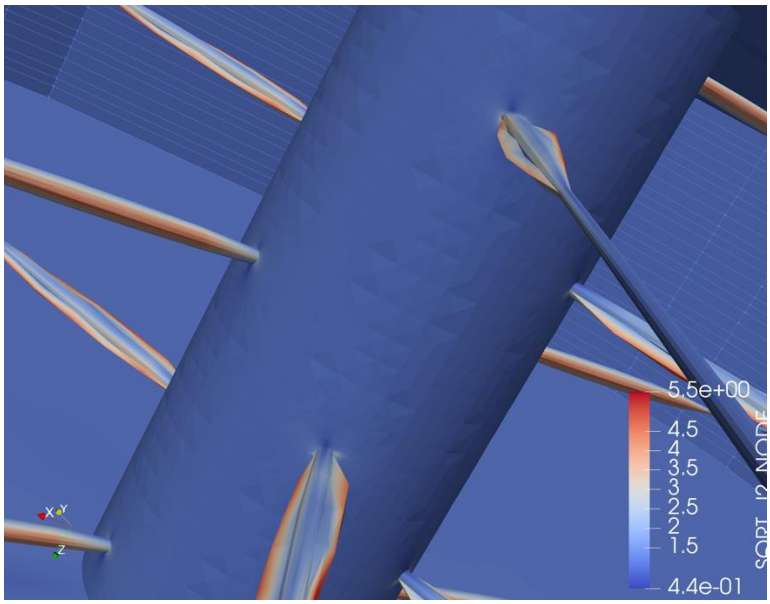

Figure 4.21 Visual simulation result with A_4=2.5 and depression rate=1 kpsi/365 days, angle=30°

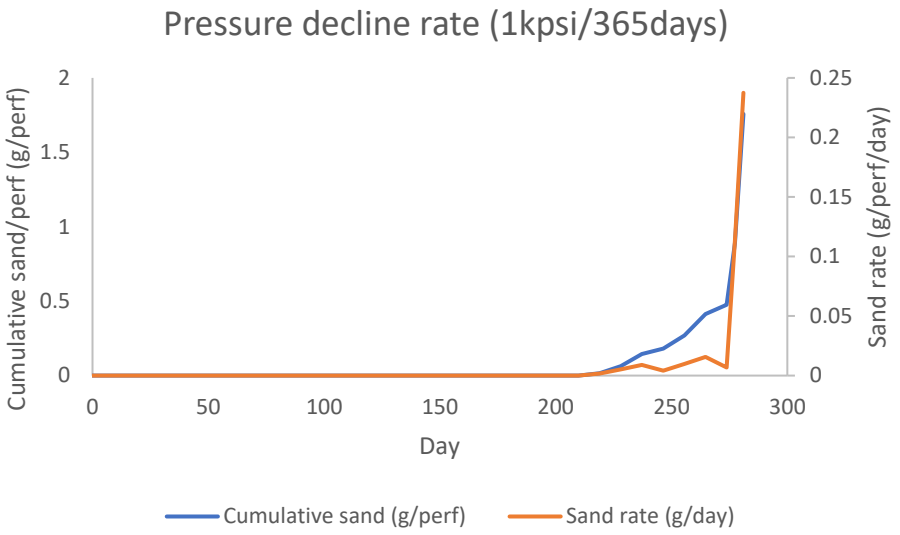

Figure 4.22 Vertical well sand production rate and accumulation with A_4=2.5 and depression rate=1 kpsi/365 days, angle=45°

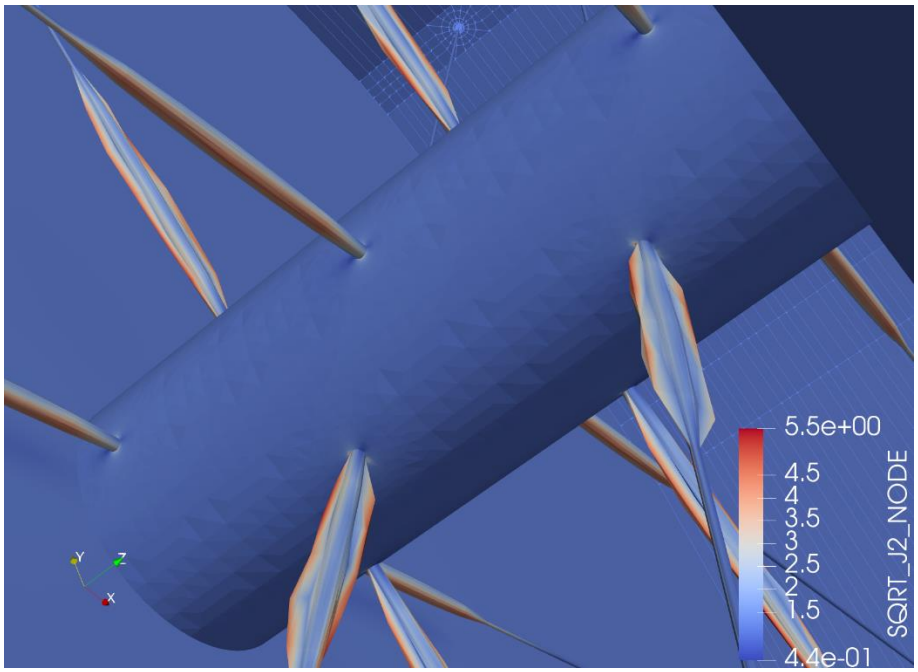

Figure 4.23 Visual simulation result with A_4=2.5 and depression rate=1 kpsi/365 days, angle=45°

55°

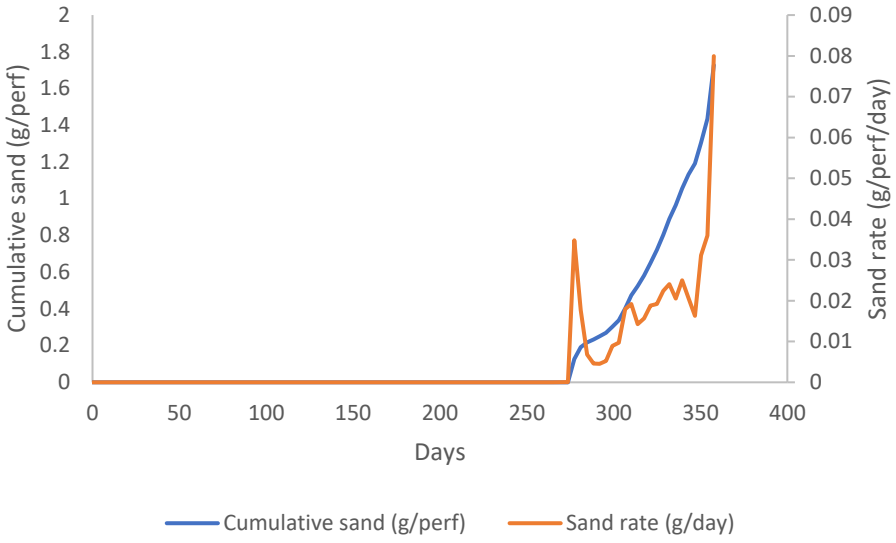

Figure 4.24 Visual simulation result with A_4=2.5 and depression rate=1 kpsi/365 days, angle=55°

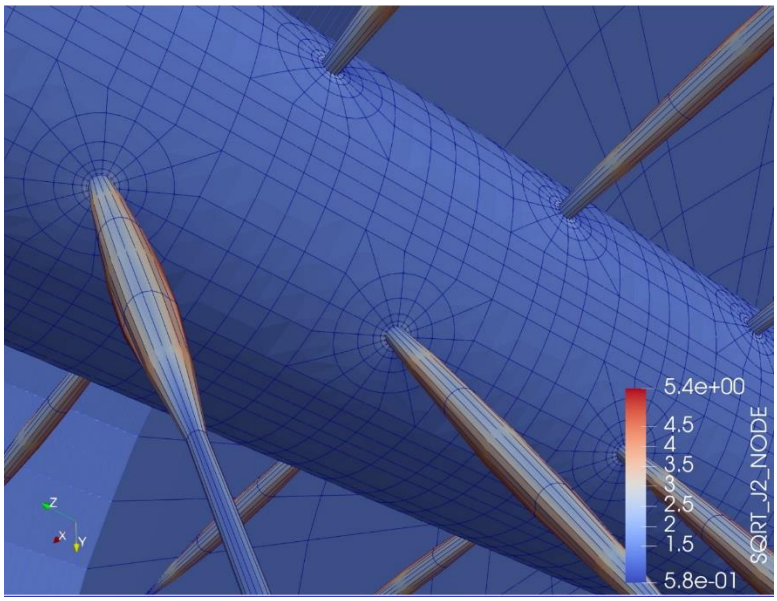

Figure 4.25 Vertical well sand production rate and accumulation with A_4=2.5 and depression rate=1kpsi/182.5days, angle=55

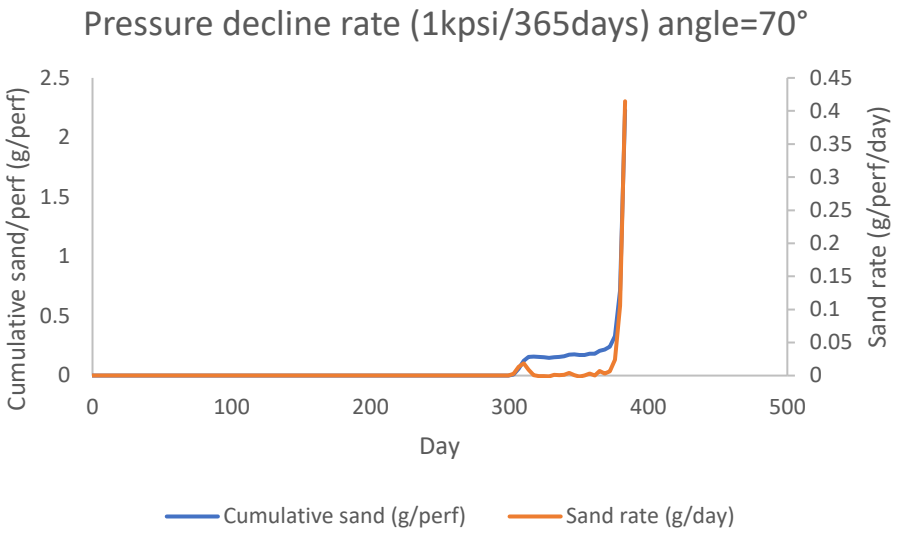

Figure 4.26 Vertical well sand production rate and accumulation with A_4=2.5 and depression rate=1kpsi/182.5days, angle=70

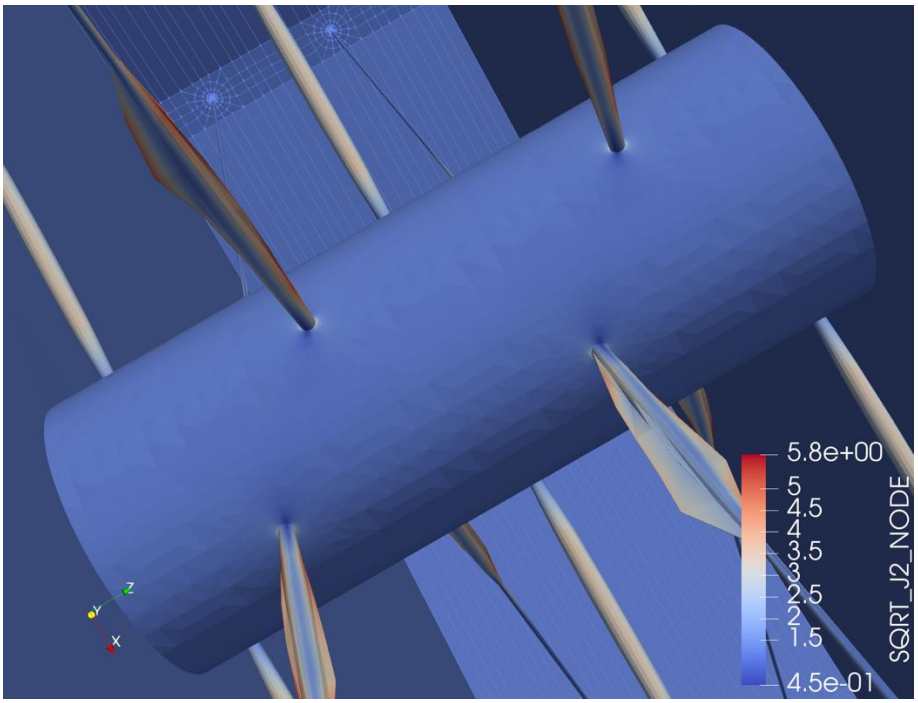

Figure 4.27 Visual simulation result with A_4=2.5 and depression rate=1 kpsi/365 days, angle=70°

DE=30° (rotated 30° so that one set of perforations are oriented in the horizontal direction)

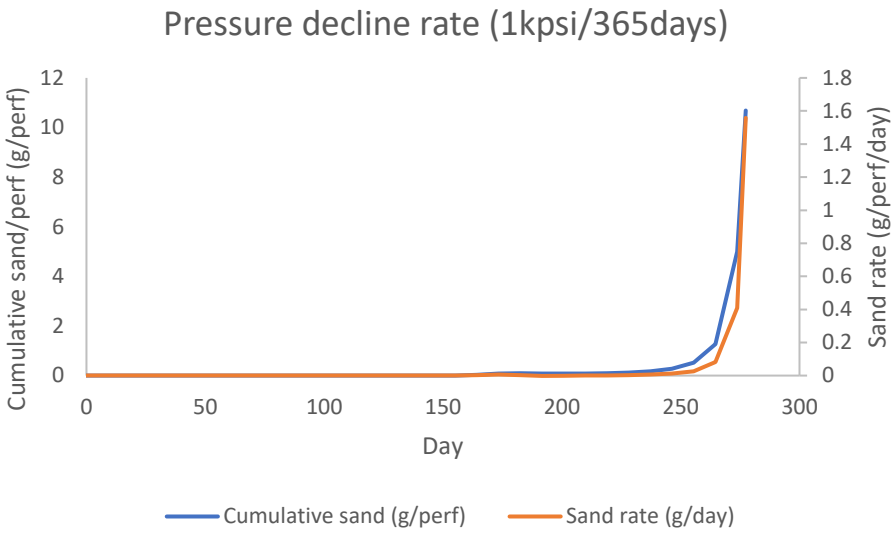

Figure 4.28 Vertical well sand production rate and accumulation with A_4=2.5 and depression rate=1kpsi/182.5days, angle=70, DE = 30

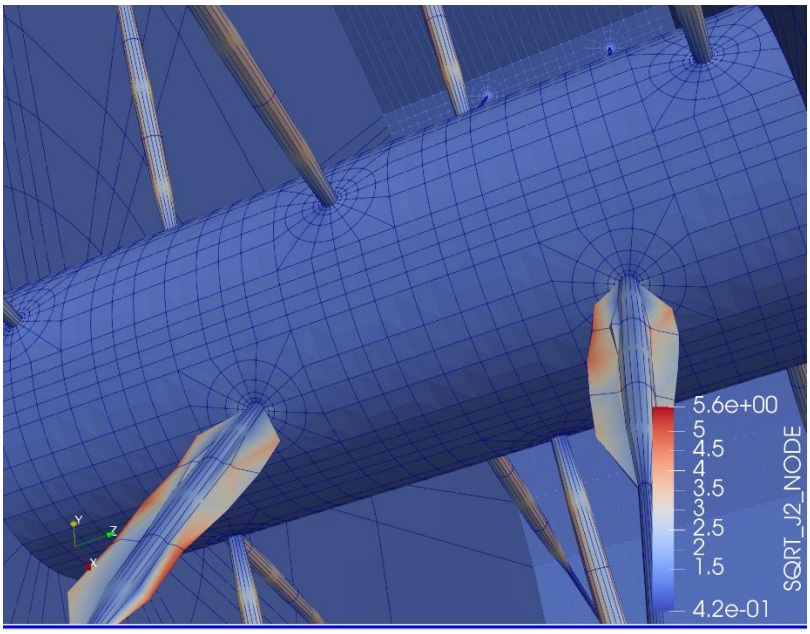

Figure 4.29 Visual simulation result with A_4=2.5 and depression rate=1kpsi/182.5days, angle=70°, DE=30°

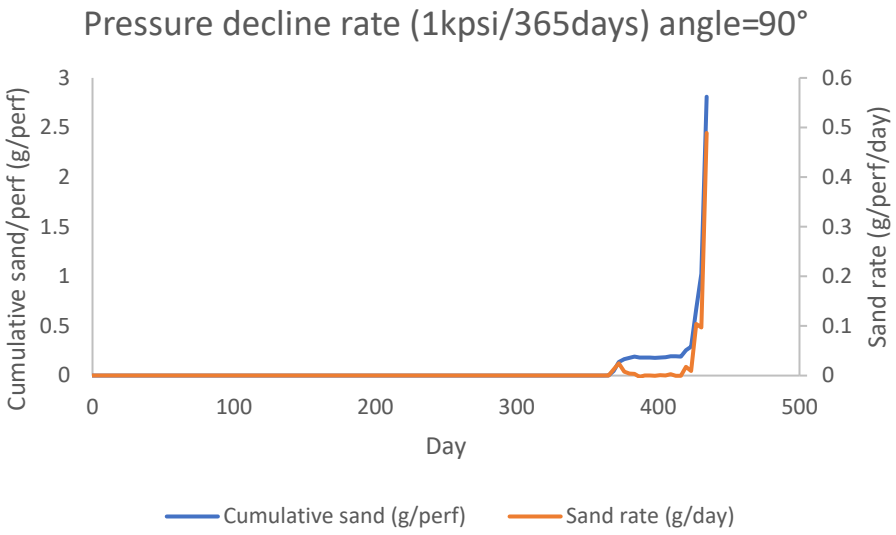

Figure 4.30 Vertical well sand production rate and accumulation with A_4=2.5 and depression rate=1kpsi/182.5days, angle=90°

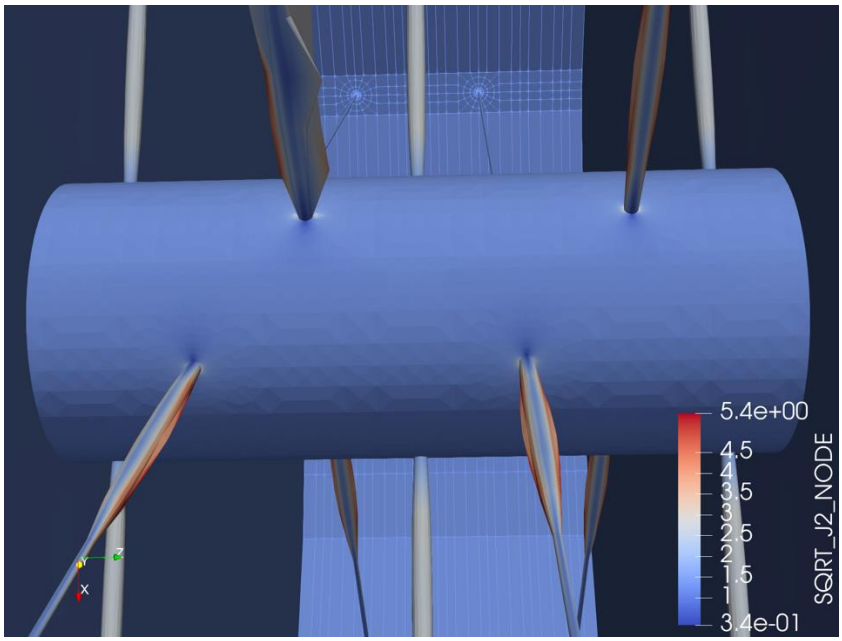

Figure 4.31 Visual simulation results with A_4=2.5 and depression rate=1kpsi/182.5days, angle=90°

Horizontal, DE=30°(rotated 30° so that one set of perforations are oriented in the horizontal direction)

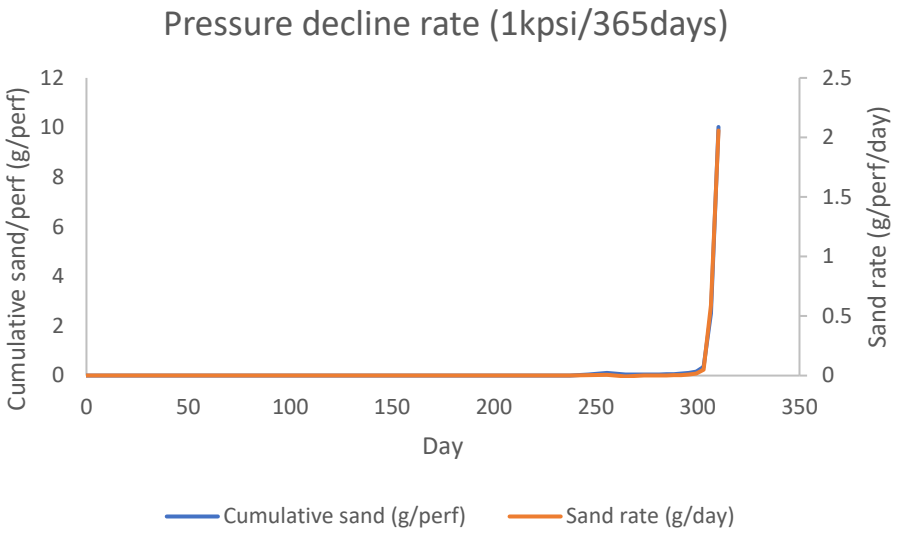

Figure 4.32 Vertical well sand production rate and accumulation with A_4=2.5 and depression rate=1kpsi/182.5days, angle=70°, DE = 30°

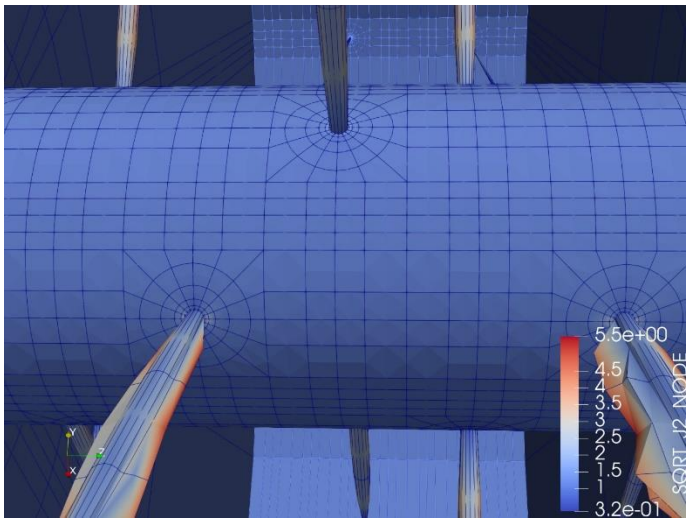

Figure 4.33 Visual simulation result with A_4=.5 and depression rate=1kpsi/182.5days, angle=70°, DE=30°

4.2.5 Well inclination effect for depletion rate (1 kpsi/365 days) with anisotropic permeability (permeability kx=600 mD, ky=600 mD, kz=60 mD)

Generally, the vertical permeability is 1/10-1/100 of the horizontal permeability if the average value from top to bottom reservoir is used. The reason is that the formation is laminated with low permeability layer. However, around each perforation, the permeability ratio K_v/K_h may be 1 to 1/10. If the vertical permeability is smaller, the flow patterns become very complex around each perforation. Overall, the flow rate becomes smaller if the vertical permeability is 60 mD and the horizontal permeability is 600 mD for a given drawdown. In this section, perforation stability is evaluated for a reservoir with anisotropic permeability.

The simulation shows that if the well is vertical, slit-like cavities develop and sand production initiates at 270 days and the sand rate sharply increases after 340 days as shown in Fig.4.34. The simulation also shows that if the well inclination is less than 45°, the sand production begins 270 days and increases sharply after initiation as shown in Figures 4.36 and 4.38. However, if the well angle is more than 70°, the perforations become stable after sharp increase of sand rate as shown in Figure 4.40 and 4.42 if the spiral perforations are oriented towards 0°, 60°, and 120° from the vertical direction. The reason is that the flow rate is significantly reduced for 60°, and 120° perforations due to the anisotropic permeability. The low flow rate significantly stabilizes the perforations.

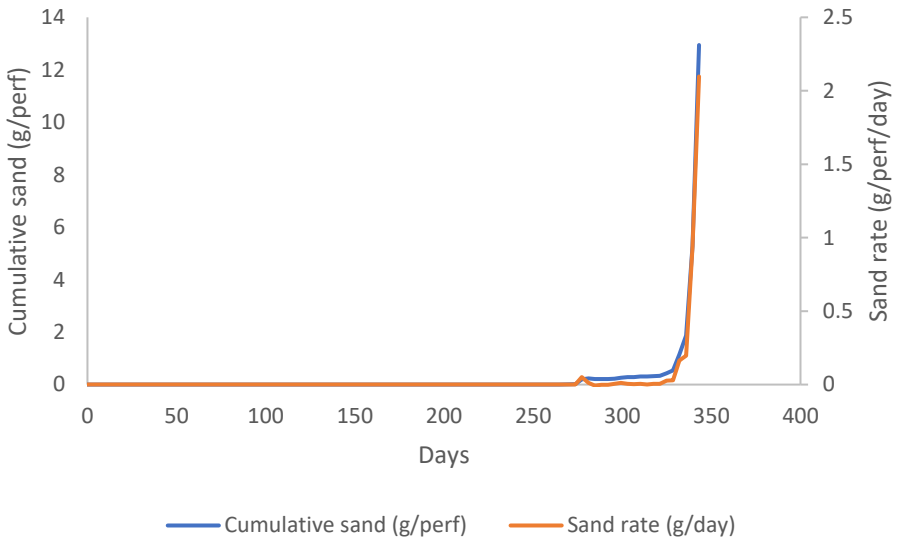

Figure 4.34 Vertical well sand production rate and accumulation with anisotropic formation, angle=0°

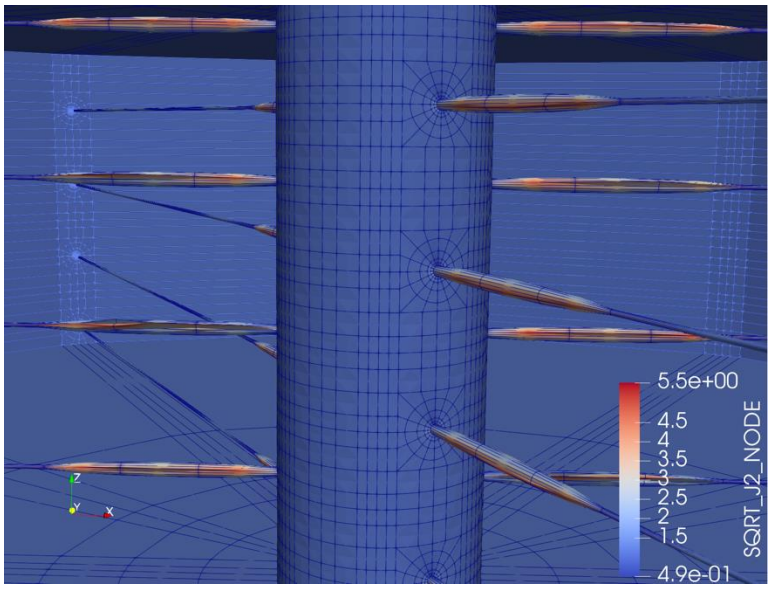

Figure 4.35 Visual simulation result with anisotropic formation, angle=0°

Well inclination 30°

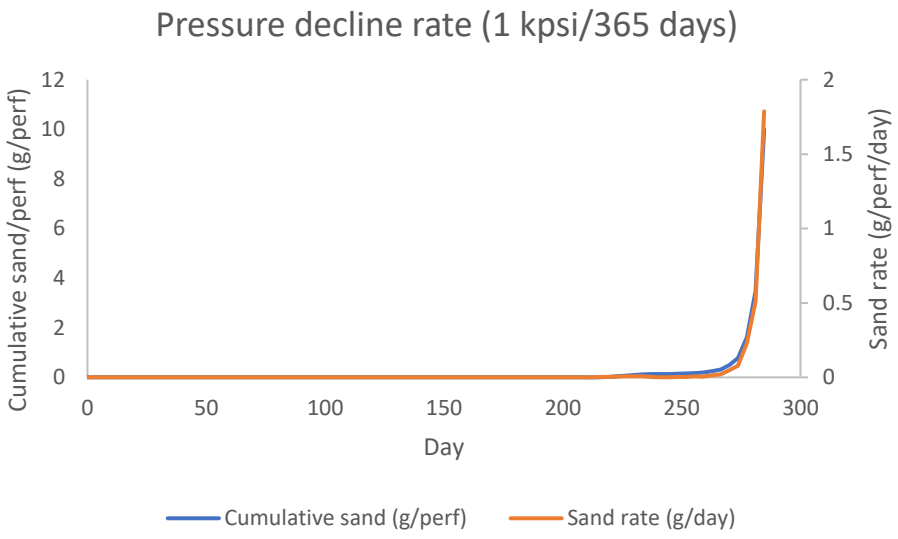

Figure 4.36 Vertical well sand production rate and accumulation with anisotropic formation, angle=30°

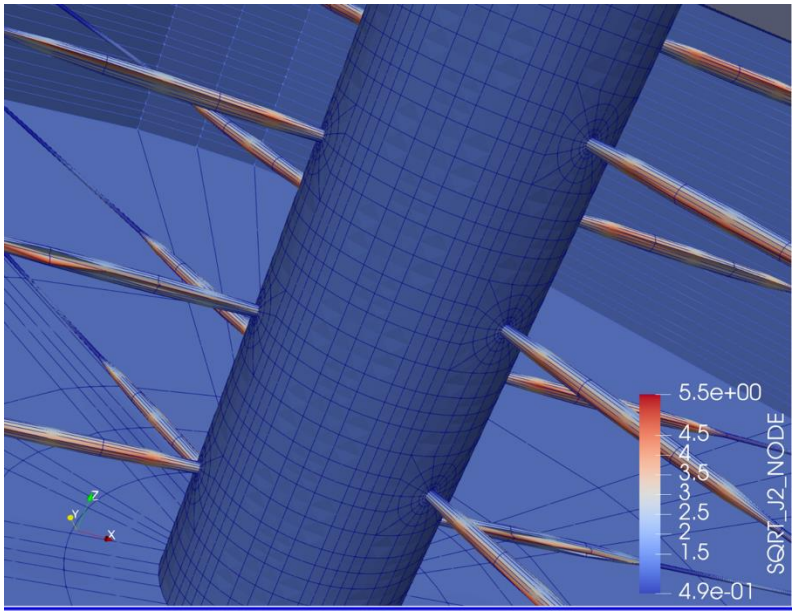

Figure 4.37 Visual simulation result with anisotropic formation, angle=30°

Well inclination 45°

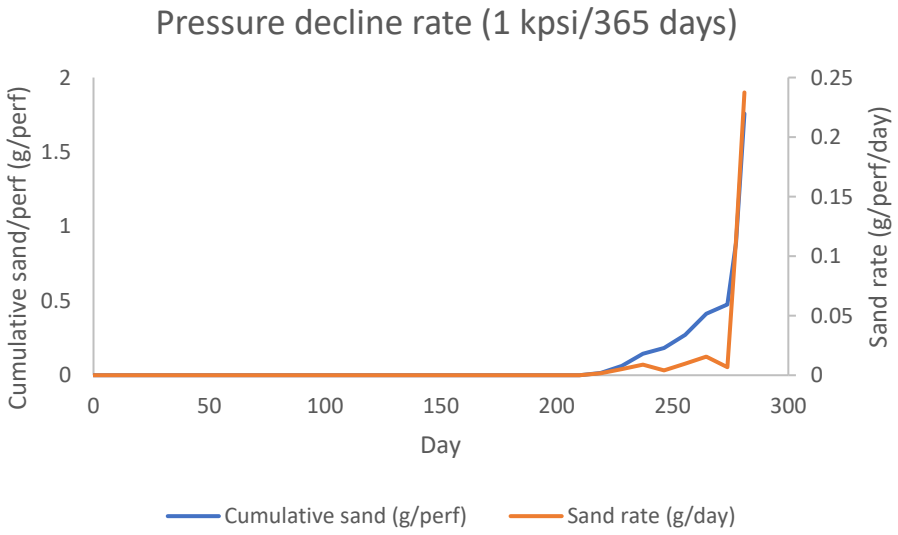

Figure 4.38 Vertical well sand production rate and accumulation with anisotropic formation, angle=45°

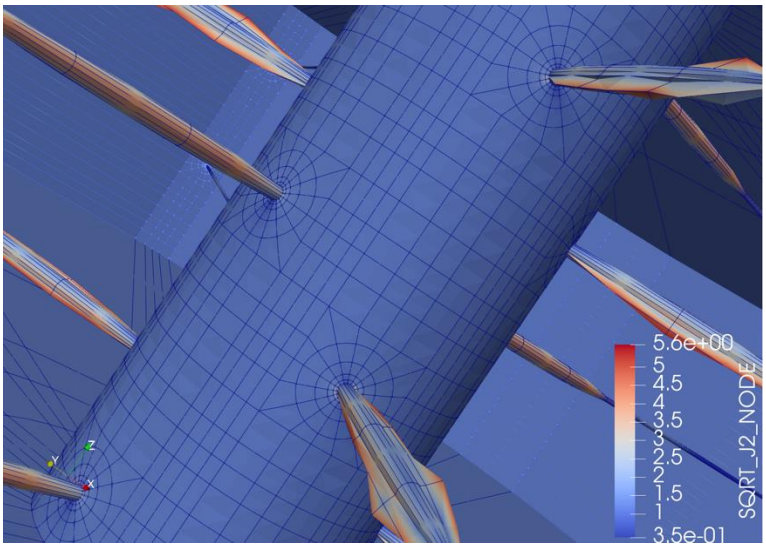

Figure 4.39 Visual simulation result with anisotropic formation, angle=45°

Well inclination 70°

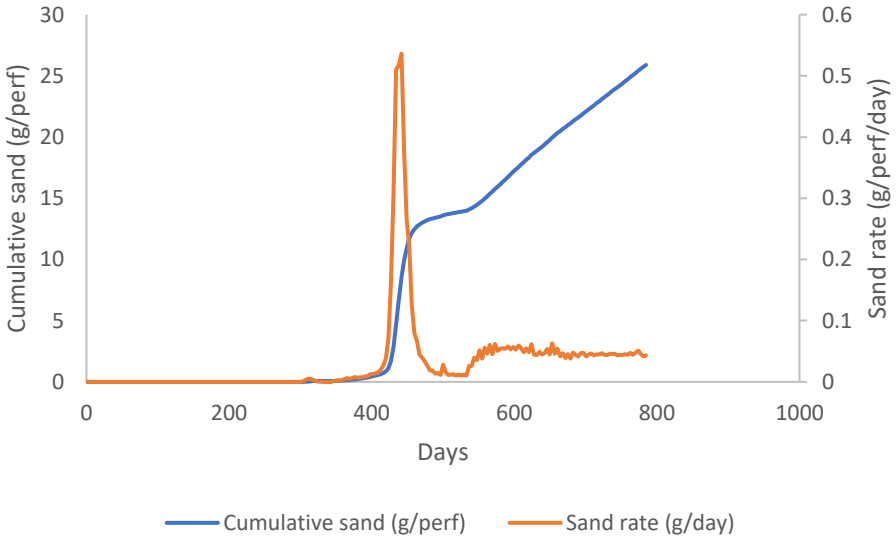

Figure 4.40 Vertical well sand production rate and accumulation with anisotropic formation, angle=70°

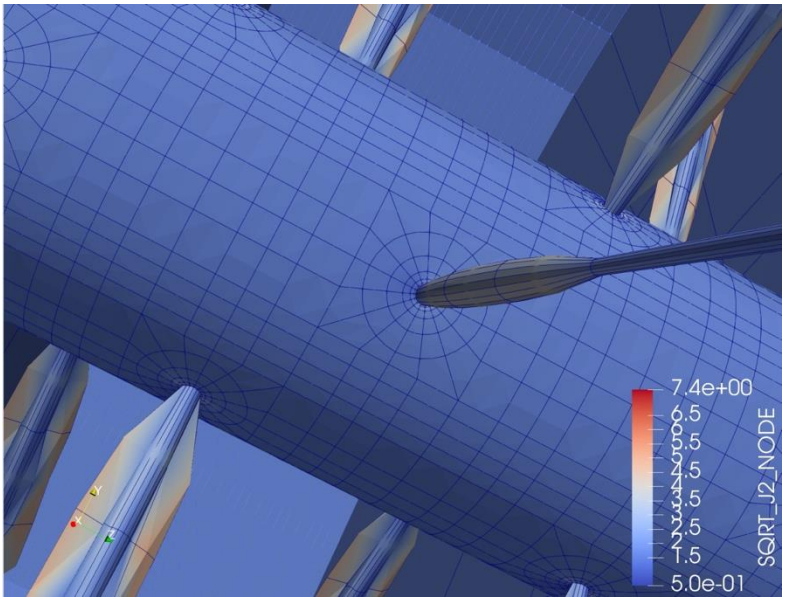

Figure 4.41 Visual simulation result with anisotropic formation, angle=70°

Well inclination 90° (horizontal well)

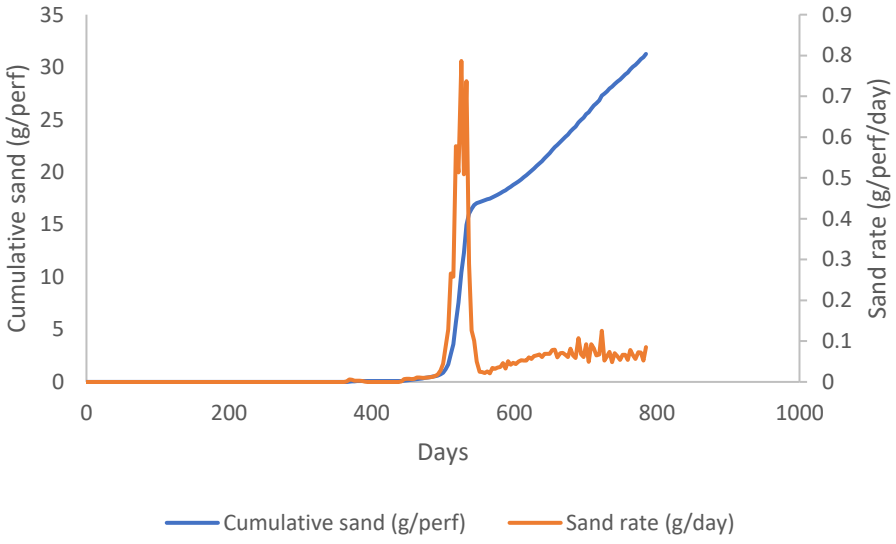

Figure 4.42 Vertical well sand production rate and accumulation with anisotropic formation, angle=90°

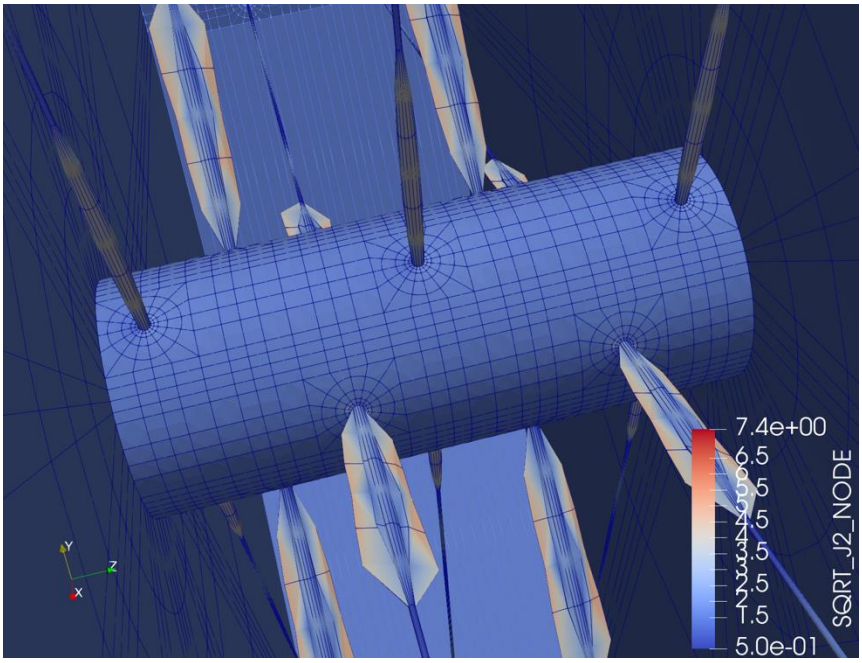

Figure 4.43 Visual simulation result with anisotropic formation, angle=90°

4.2.6 X-shape oriented perforation

As shown for inclined wells, the perforation stability depends on which direction a perforation is oriented with respect to the maximum in-situ stress. For normal faulting stress regime, the vertical stress is the highest. Therefore, the perforation oriented in the vertical direction is very stable while the perforation oriented in the horizontal direction is generally least stable. If the perforation is oriented only towards top and bottom of the casing for inclined wells, the perforations are stable. However, too many perforations cannot be shot in one direction due to the spacing. In addition, if shot direction is 180° or 360°-phasing, the productivity index becomes low. The best method may be x-shape oriented perforation where the perforations are oriented 20-30° from vertical direction as shown in Figure 4.45. The well angle is changed for oriented perforations. The calculations show that if the well angle is less than 45°, the stability is not significantly different from the standard non-oriented spiral pattern. The stability starts increasing with 55° well angle as shown in Figure 4.48. If the well inclination is more than 70°, the onset of sand production is significantly delayed as shown in Figures.4.50 and 4.52.

30°

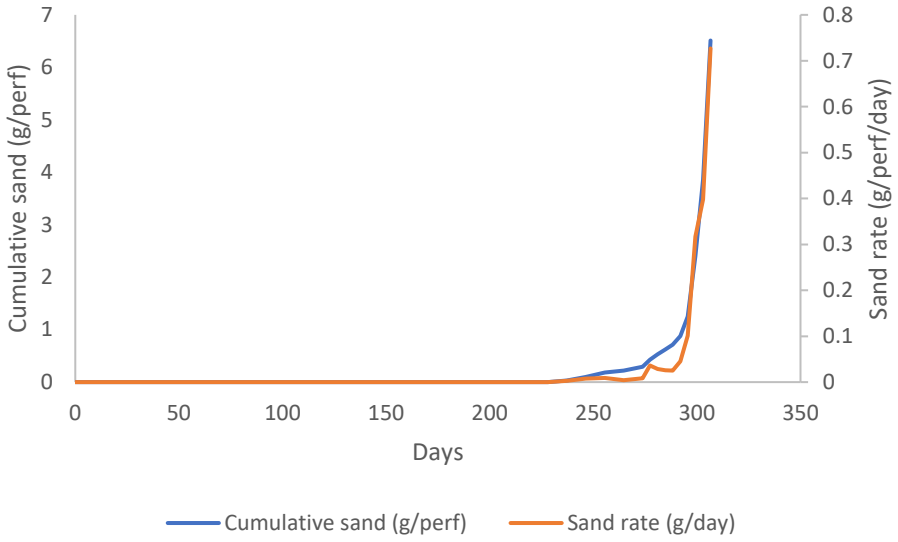

Figure 4.44 Vertical well sand production rate and accumulation with X-shape orientation perforation, angle=30°

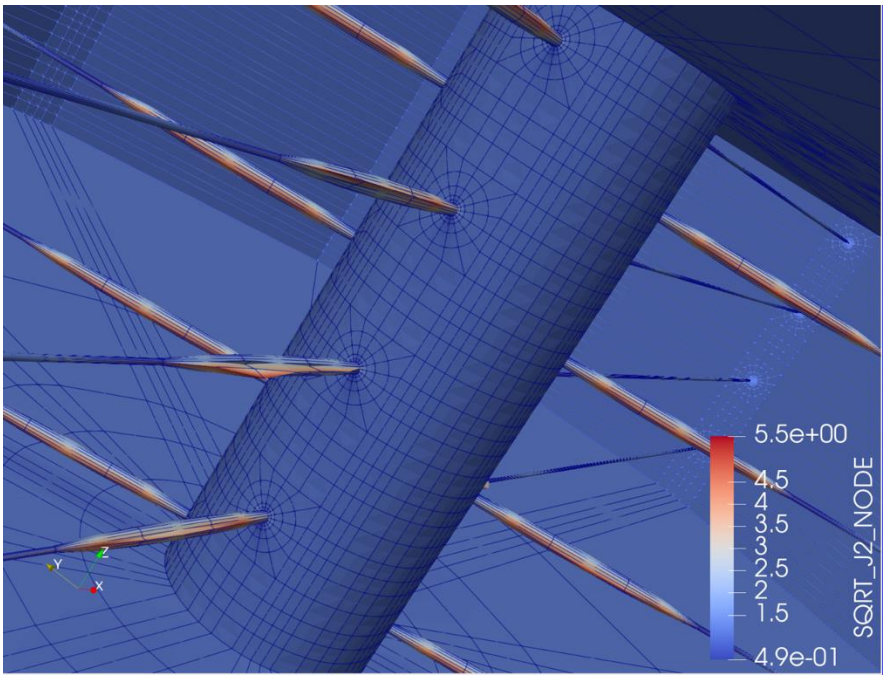

Figure 4.45 Visual simulation result with X-shape orientation perforation, angle=30°

45°

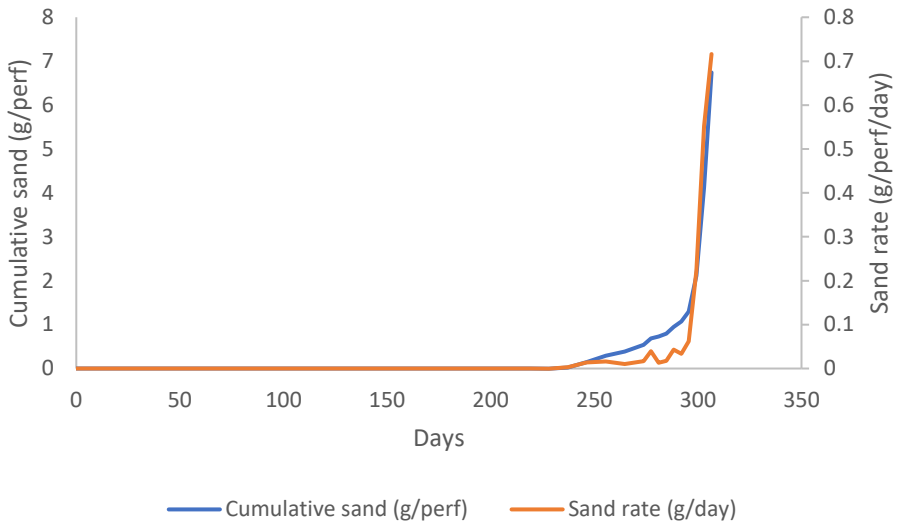

Figure 4.46 Vertical well sand production rate and accumulation with X-shape orientation perforation, angle=45°

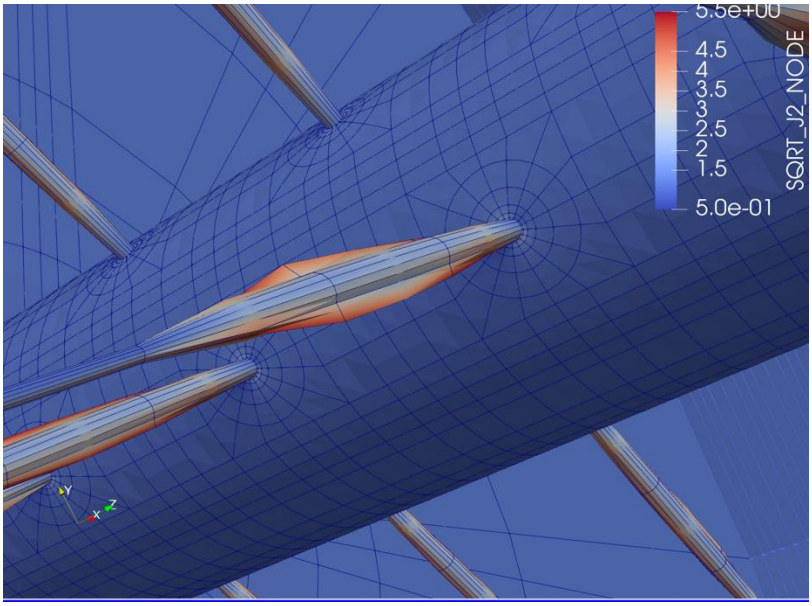

Figure 4.47 Visual simulation result with X-shape orientation perforation, angle=45

55°

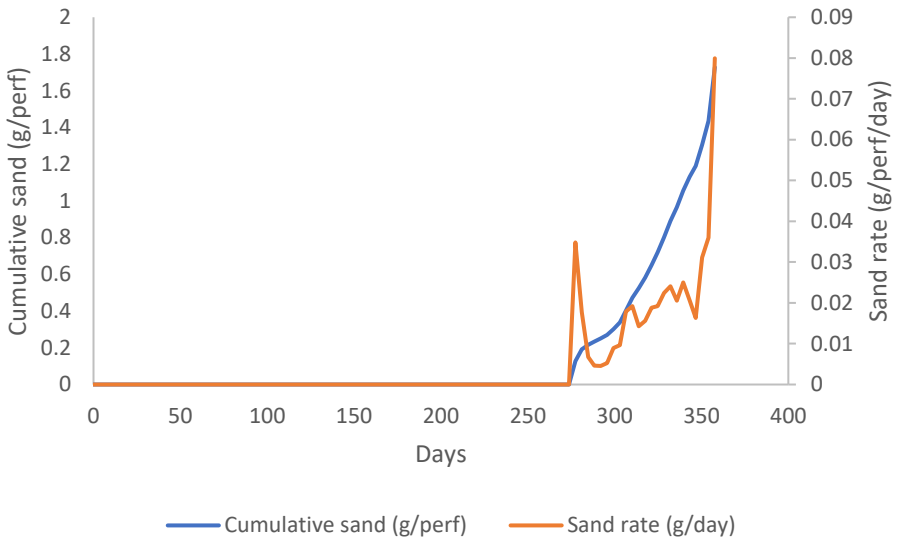

Figure 4.48 Vertical well sand production rate and accumulation with X-shape orientation perforation, angle=55°

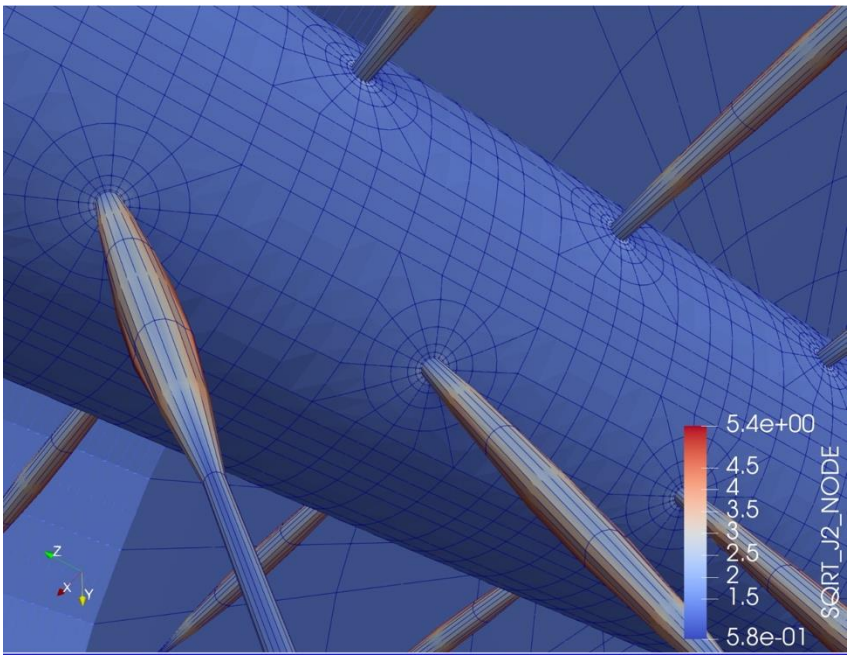

Figure 4.49 Visual simulation result with X-shape orientation perforation, angle=55°

70°

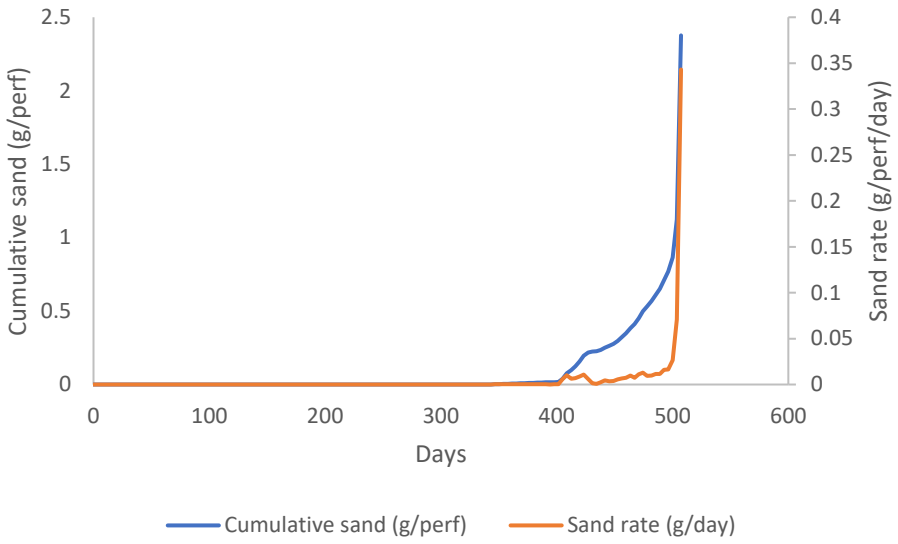

Figure 4.50 Vertical well sand production rate and accumulation with X-shape orientation perforation, angle=70°

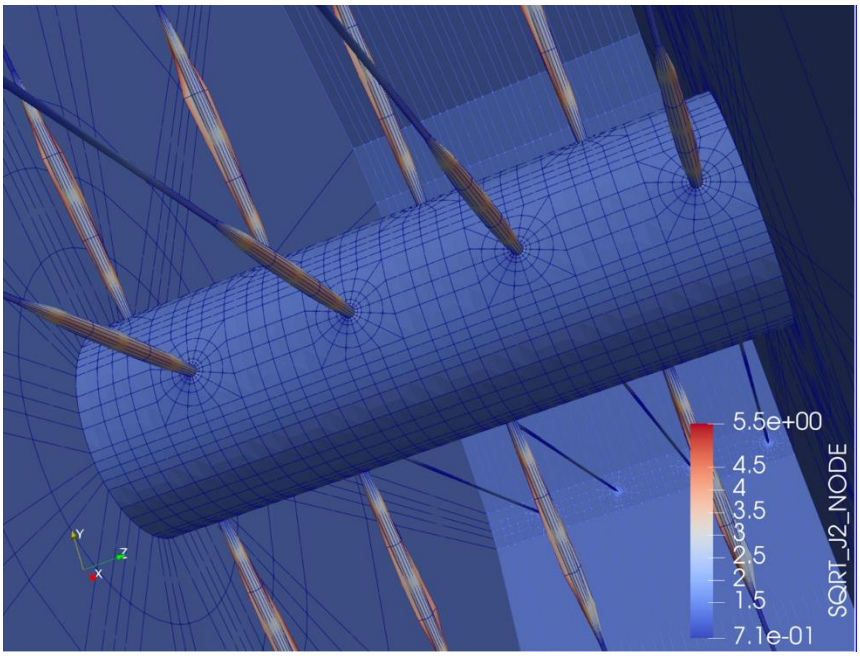

Figure 4.51 Visual simulation result with X-shape orientation perforation, angle=70°

90°

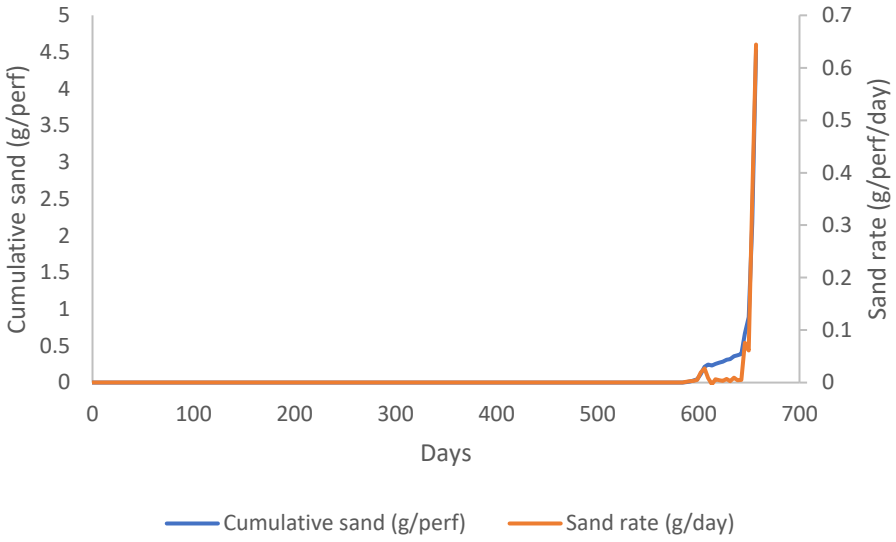

Figure 4.52 Vertical well sand production rate and accumulation with X-shape orientation perforation, angle=90°

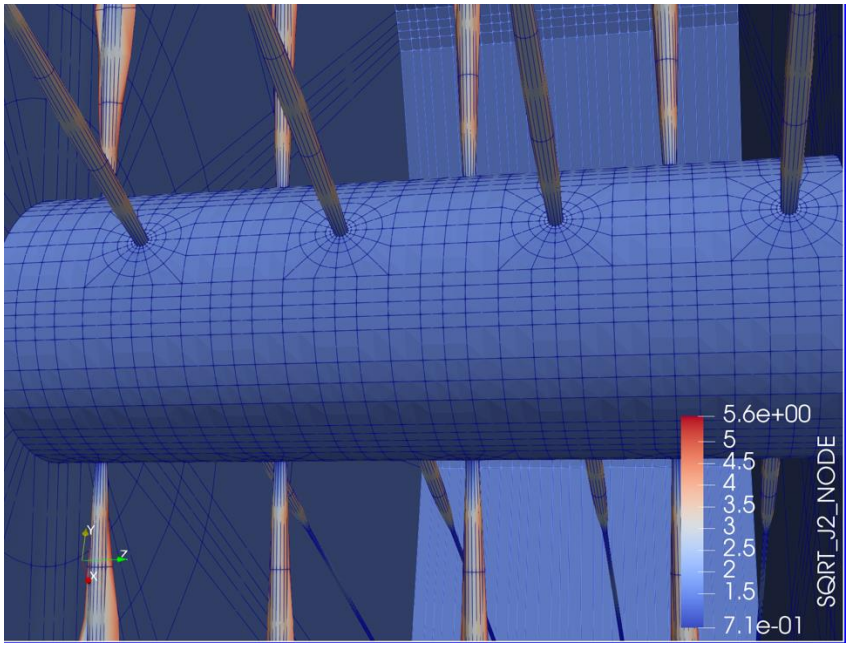

Figure 4.53 Visual simulation result with X-shape orientation perforation, angle=90°

CHAPTER V DISCUSSION AND CONCLUSIONS

In this thesis, I have developed a sand production prediction model on early stage of well production. The parameters for sand production model were calculated by fourteen SINTEF experiments using the Castlegate sandstone. It can be observed that the yield criterion is dominant by Lade model not Drucker-Prager model. And most of sand production curve can match experimental data, however, for several cases such as kr=kz=1 or kr=1and kz=2, the shape of simulation failure region does not match the experiment data. The reason may be the heterogeneity of the Castlegate sandstone. If the permeability is assumed to be heterogeneous, the simulation matches the experimental results.

For the field study, after every pressure step during the step-rate sand production test, it is assumed that the sand production rate declined in an exponential rate. Considering the actual production condition, the perforation cavity evolves in a very short time (10-20 days), thus, the coefficient $A_4 = 2.5$ is an appropriate value matching field sand rate.

Sand production simulating a field condition shows

(A) The sand production starts slow while cavities evolve around the original perforations but will jump very high after a certain time.

(B) Several factors could influence the sand production volume. The simulation results show that the depletion rate influences the sand rate.

(C) With the increase of flow rate, the sand production volume will increase.

(D) The well inclination effect has been tested on isotropic permeability. The well inclination does not affect the sand rate since perforations are normally oriented in all directions uniformly. However, if one set of perforations are intentionally oriented in the vertical direction and the other sets are oriented towards 60° and 120° for 60°-phasing

spiral pattern, the stability is high while if one set of perforations are oriented in the horizontal directions and the other sets are oriented in 30° and 150°, the stability is low if the well inclination is more than 70°.

(E) For inclined rock, the perforation stability does not significantly different between isotropic and anisotropic permeability. However, if one set of perforations are oriented in the vertical direction with two other sets in 60° and 120°, the flow rate through the vertical perforations is significantly higher, resulting a higher stability for the less table perforations oriented in 60° and 120°.

(F) The oriented X-shape perforation is helpful to maintain the stability of perforations when the well inclination angle is more than 55° because of the perforation orientations are closer to the vertical direction.

REFERENCES

Nobuo Morita. Field and laboratory verification of sand-production prediction models. SPE Drilling & Completion, 9(04):227–235, 1994. ISSN 1064-6671. doi: 10.2118/27341-PA. URL https://doi.org/10.2118/27341-PA.

Nobuo Morita and K. E. Gray. A constitutive equation for nonlinear stress-strain curves in rocks and its application to stress analysis around a borehole during drilling, 1980/1/1/ 1980. URL https://doi.org/10.2118/9328-MS.

Nobuo Morita, R. C. Burton, and Eric Davis. Fracturing, frac packing, and formation failure control: Can screenless completions prevent sand production? SPE Drilling & Completion, 13 (03):157–162, 1998. ISSN 1064-6671. doi: 10.2118/51187-PA. URL https://doi.org/ 10.2118/51187-PA.

Nobuo Morita, Giin-Fa Fuh, and Robert C. Burton. Field and laboratory observations of post failure stabilizations during sand production, 2006/1/1/ 2006. URL https://doi.org/ 10.2118/102802-MS.

Karl V. Terzaghi. Stress distribution in dry and in saturated sand above a yielding trap door. Proc., First Intl. Conf. on Soil Mechanics and Foundation Engineering, pages 307–311, 1936.

Jr. Hall, C. D. and W. H. Harrisberger. Stability of sand arches: A key to sand control. Journal of Petroleum Technology, 22(07):821–829, 1970. ISSN 0149-2136. doi: 10.2118/2399-PA. URL https://doi.org/10.2118/2399-PA.

E. Papamichos. Sand production in isotropic and anisotropic stress tests, 2018/8/21/ 2018.

E. Papamichos, A. Skjærstein, and J. Tronvoll. A volumetric sand production experiment, 2000/1/1/ 2000. URL https://doi.org/.

Rolf K. Bratli and Rasmus Risnes. Stability and failure of sand arches. Society of Petroleum Engineers Journal, 21(02):236–248, 1981. ISSN 0197-7520. doi: 10.2118/8427-PA. URL https://doi.org/10.2118/8427-PA.

D. R. J. Owen and E. Hinton. Finite elements in plasticity : theory and practice. D.R.J. Owen, E. Hinton. Pineridge Press, 1980.

D. C. Drucker and W. Prager. Soil mechanics and plastic analysis or limit design. Quart. Appl. Math. 10 (1952), 157-165, 1952. doi: https://doi.org/10.1090/qam/48291.

D. Antheunis, P. B. Vriezen, B. A. Schipper, and A. C. van der Vlis. Perforation collapse: Failure of perforated friable sandstones, 1976/1/1/ 1976. URL https://doi.org/10.2118/ 5750-MS

W. L. Penberthy and C. M. Shaughnessy. Sand control. W. L. Penberthy, C. M. Shaughnessy. SPE series on special topics Henry L. Doherty series: v. 1. Richardson, TX : Henry L. Doherty Memorial Fund of AIME : Society of Petroleum Engineers, 1992., 1992. ISBN 1555630413 9781555630416.

L. C. B. Bianco and P. M. Halleck. Mechanisms of arch instability and sand production in two phase saturated poorly consolidated sandstones, 2001/1/1/ 2001. URL https://doi.org/ 10.2118/68932-MS.

Bezalel Haimson and Joseph Kovacich. Borehole instability in high-porosity berea sandstone and factors affecting dimensions and shape of fracture-like breakouts. Engineering Geology, 69(3):219–231, 2003. ISSN 0013-7952. doi: https://doi.org/10. 1016/S0013-7952(02)00283-1. URL http://www.sciencedirect.com/science/ article/pii/S0013795202002831.

T. K. Perkins and J. S. Weingarten. Stability and failure of spherical cavities in unconsolidated sand and weakly consolidated rock, 1988/1/1/ 1988. URL https://doi.org/10.2118/ 18244-MS.

APPENDIX A

Table A-1 Summary Table of Experiments conditions for k = 0.84 (Drucker-Prager Model)

Experiment No.	Sr (kpsi)	SR (kpsi)	Sz (kpsi)	K (Darcy)	Dt (day)	Dp (psi)	A_1
1	2.83	7.96	8.07	0.82	0.1320	0.00964	0.235E-04
2	6.644	9.894	9.96	0.49	0.3110	0.01615	0.22E-04
3	4.825	7.192	12.81	0.60	0.1231	0.01318	0.52E-04
4	4.642	6.927	4.667	0.50	0.1575	0.01512	0.35E-04
5	5.936	8.7138	7.256	0.80	0.1470	0.009889	0.246E-04
6	5.3098	5.3098	5.3098	0.72	0.1559	0.01098	0.1785E-04
7	2.95239	8.7646	2.947	0.60	0.1440	0.01319	0.203E-04
8	5.3526	7.9872	11.28	0.60	0.1300	0.01319	0.3E-04
9	2.789	8.2831	5.8856	0.53	0.1360	0.01492	0.083E-04
10	4.545	4.548	9.82	0.49	0.1380	0.01615	0.215E-04
11	5.3707	5.4287	5.3867	0.66	0.1318	0.011986	0.35E-04
12	3.0907	4.6122	9.9278	0.60	0.1354	0.01318	0.65E-04

13	2.8804	8.1018	8.2163	0.82	0.1580	0.00964	0.527E-04
14	6.529	6.529	6.529	0.9	0.1320	0.00879	0.40E-04

APPENDIX B FIELD SIMULATION RESULT WITH 4=7.5

Field simulation is performed in Chapter 5. The decline rate may depend on the strength of rock and the stress state. From Fig.5.1.1, we assume the decline rate is given by $e^{-A_4 t}$ $(A_4 = 2.5 \sim 7.5,\ t = days)$. In this appendix, the field simulation results for A=7.5 are shown.

Table B-1 Reservoir conditions

Depth of the reservoir=10000 ft

Vertical stress gradient=0.9 psi/ft (9000 psi at 10000ft)

$\sigma_{h1} = 7500\,psi$, $\sigma_{h2} = 7500\,psi$

The initial reservoir pressure = 6000psi

Formation: Rock similar to the Castlegate sandstone (UCS = 2056psi, porosity = 0.26, k =6 00md)

One phase flow above bubble point, viscosity = 1.4cp

1kpsi depletion per year with $\sigma_h^e / \sigma_v^e = 0.4$

200 psi drawdown (k = 600md, zero skin factor) (19.257 bbl/day/perf)

Eight shots per foot spiral pattern with 60 degrees phasing

B-1 Effect of depletion rate on sand rate

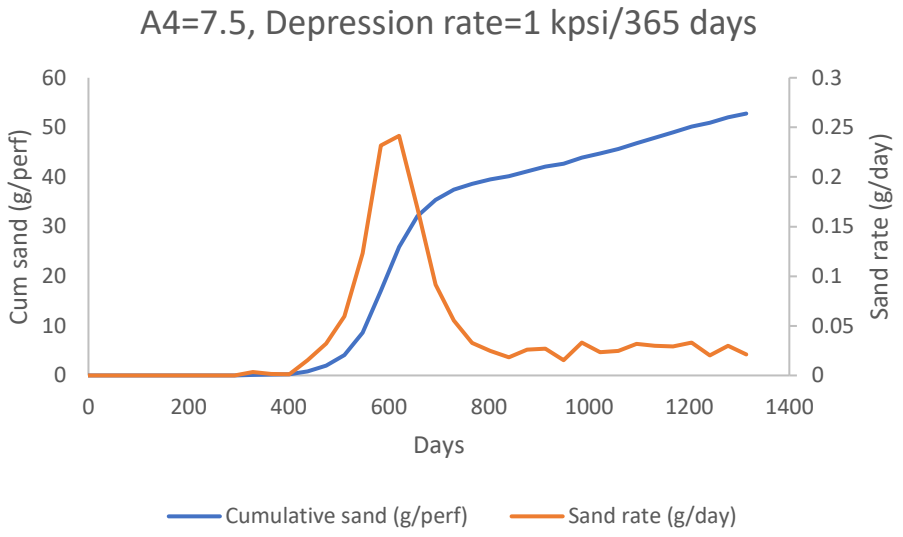

Figure 6.1 Cumulative sand production and sand rate (simulation result with A4=7.5, depletion duration is 365 days)

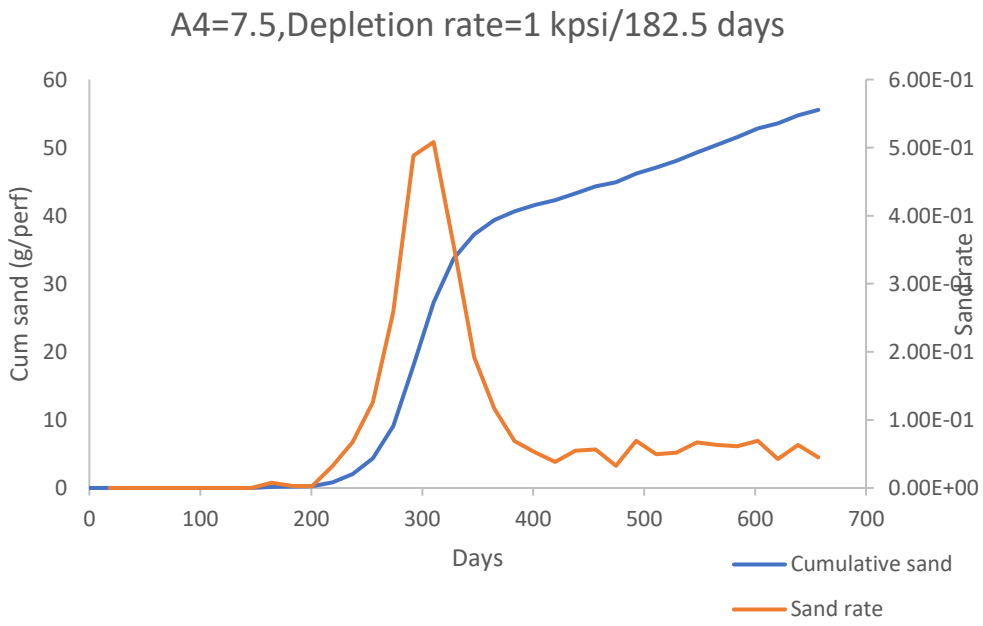

Figure 6.2 Cumulative produced sand and sand rate (simulation result with A4=7.5, and depletion duration is 182.5 days)

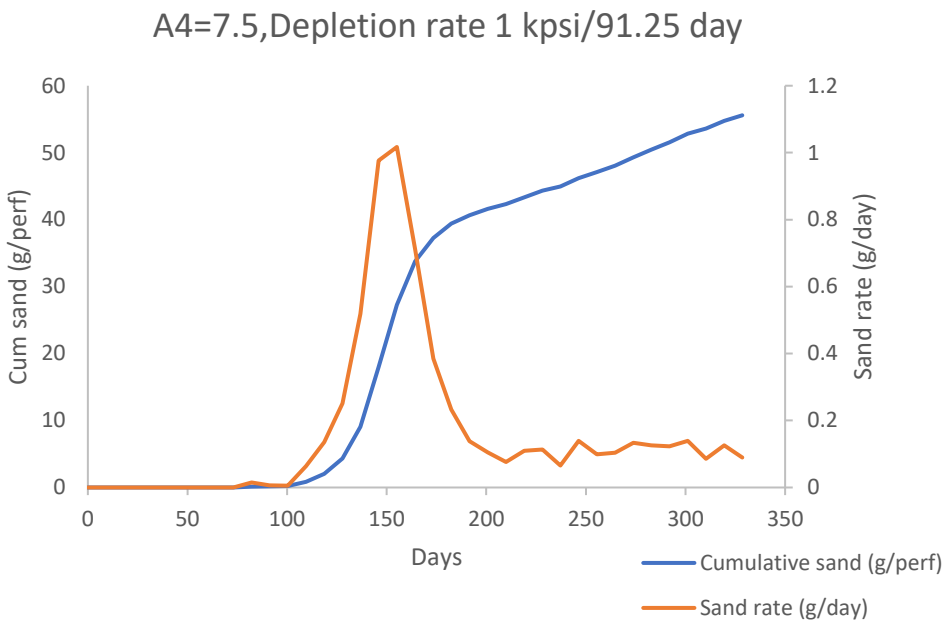

Figure 6.3 Cumulative produced sand and sand rate (simulation result with A4=7.5, and depletion duration is 182.5 days)

B-2 Effect of flow rate

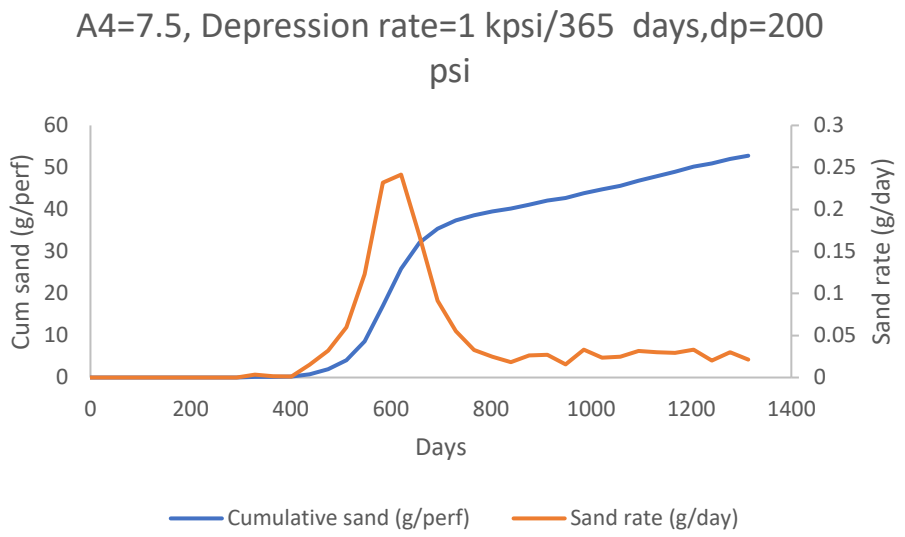

Figure 6.4 Cumulative produced sand and sand rate (simulation result with A4=7.5, dp=200psi)

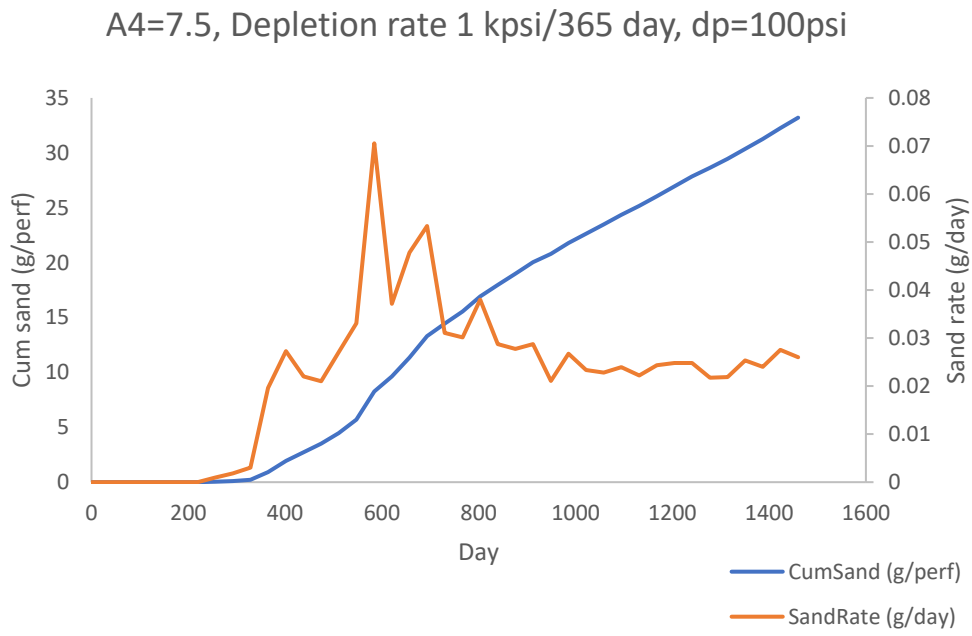

Figure 6.5 Cumulative produced sand and sand rate (simulation result with A4=7.5, dp = 100psi)

B-3 Effect of well inclination, isotropic permeability (permeability kx=ky=kz=600md)

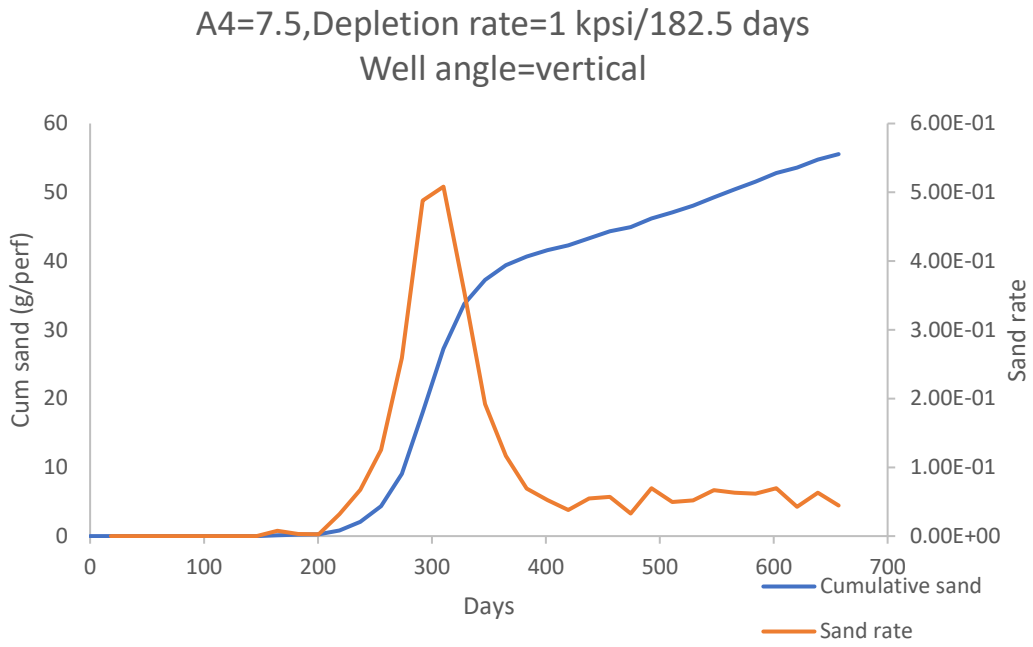

Figure 6.6 Cumulative produced sand and sand rate (simulation result with A4=7.5, vertical well)

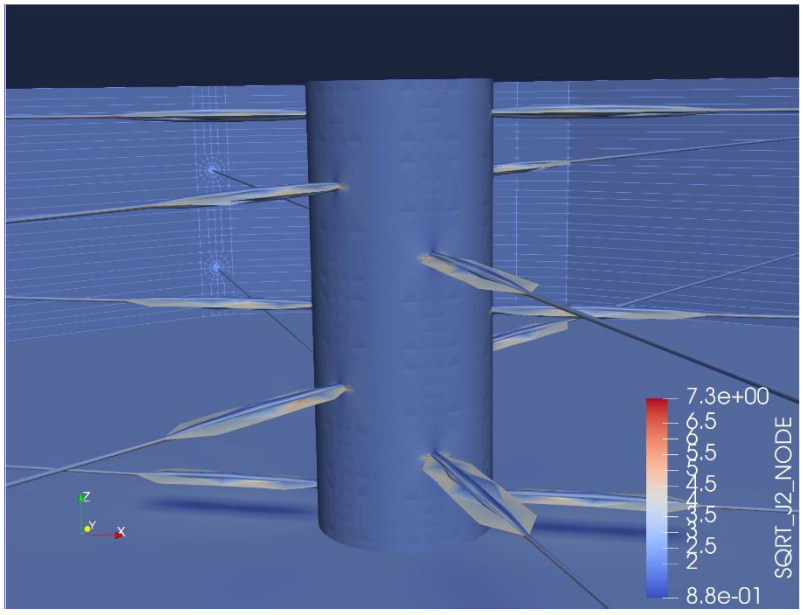

Figure 6.7 Visual result of perforation cavity evolution for vertical well

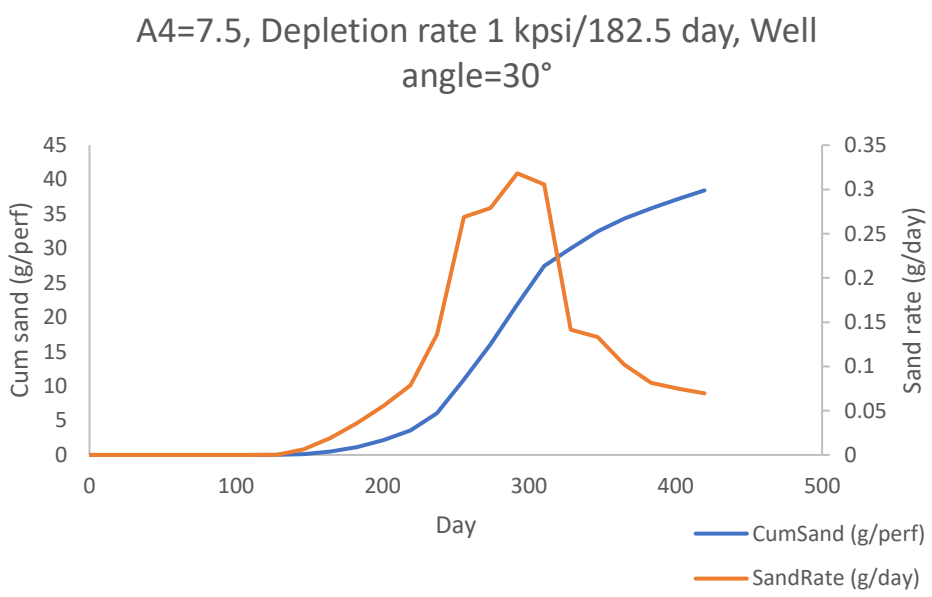

Figure 6.8 Cumulative produced sand and sand rate (simulation result with A4=7.5, angle = 30°)

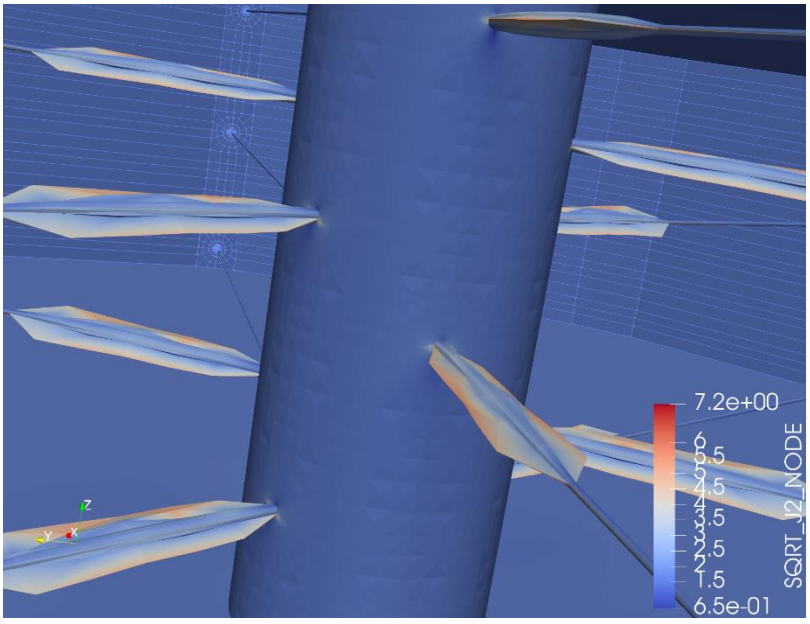

Figure 6.9 Visual result for well angle =30°

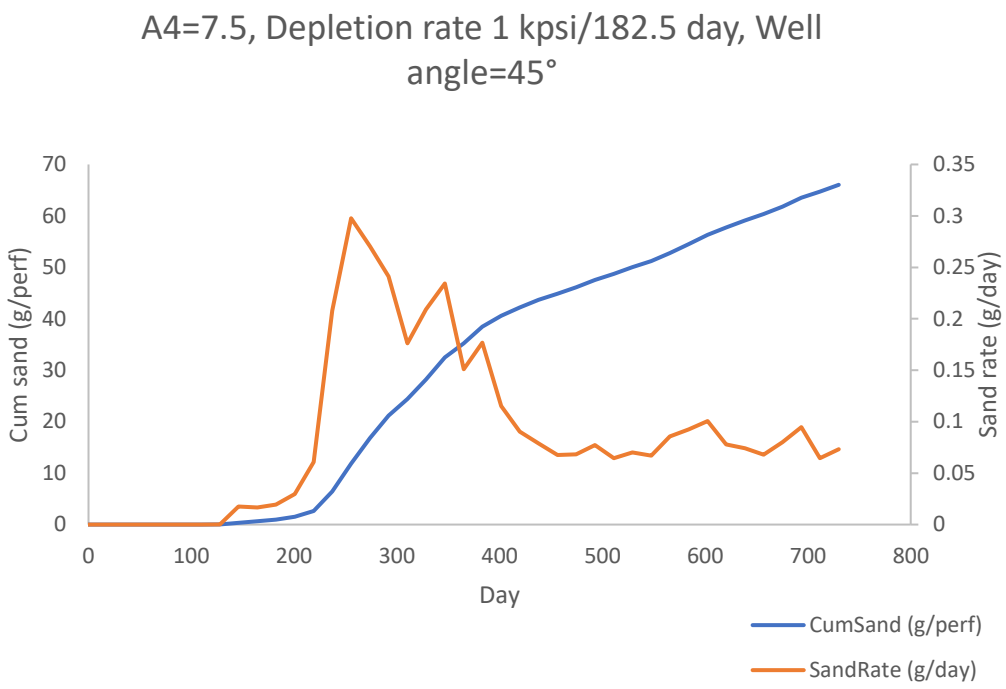

Figure 6.10 Cumulative produced sand and sand rate (simulation result with angle =45°)

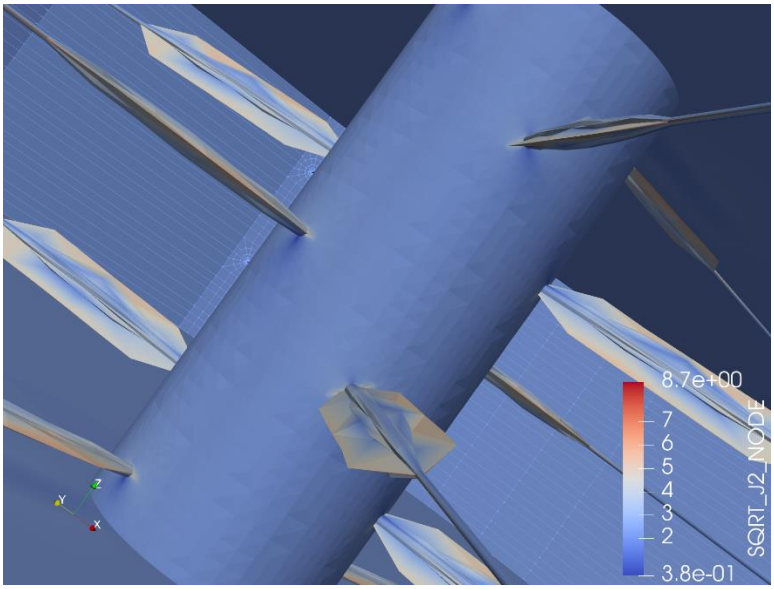

Figure 6.11 Visual result with angle =45

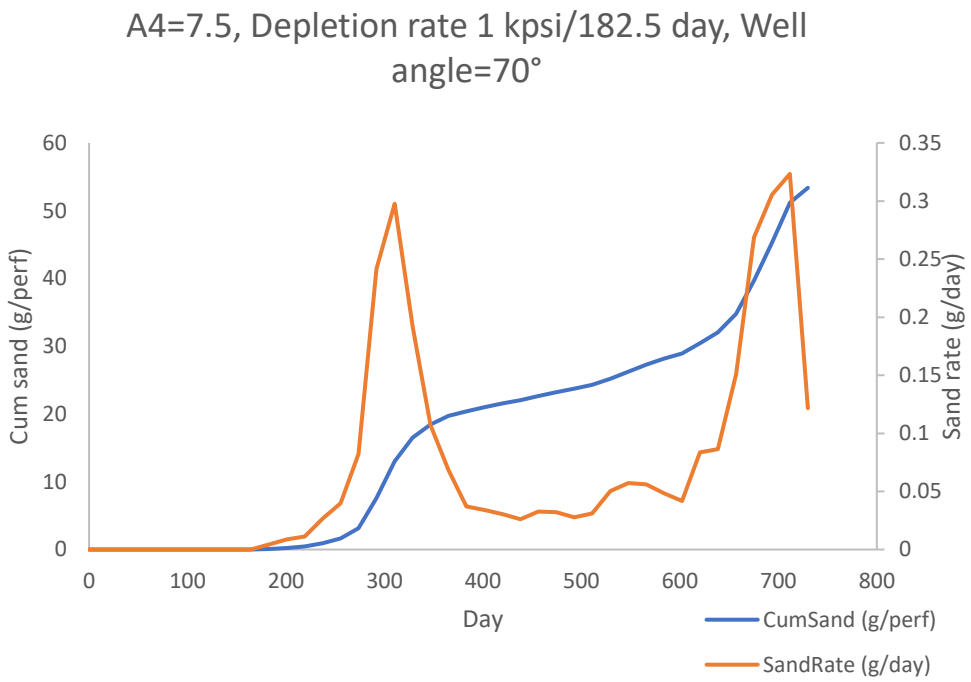

Figure 6.12 Cumulative produced sand and sand rate (simulation result with well angle = 70°)

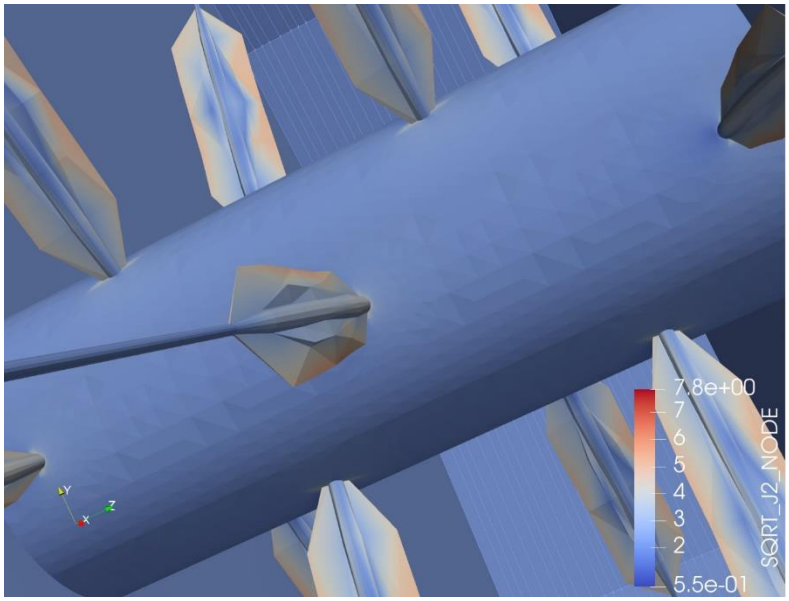

Figure 6.13 Visual result with angle =70

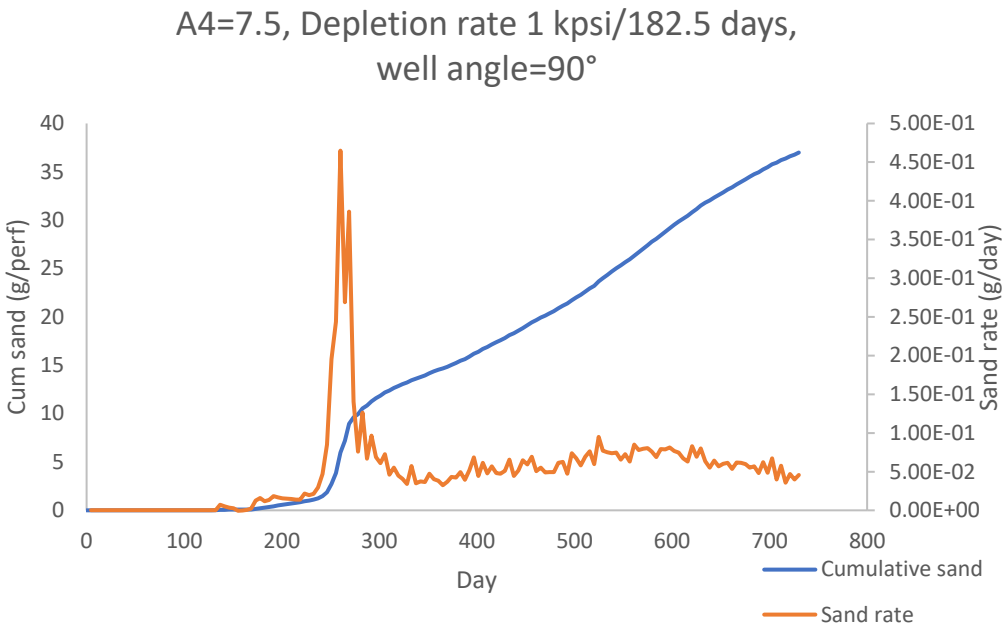

Figure 6.14 Cumulative produced sand and sand rate (simulation result for horizontal well)

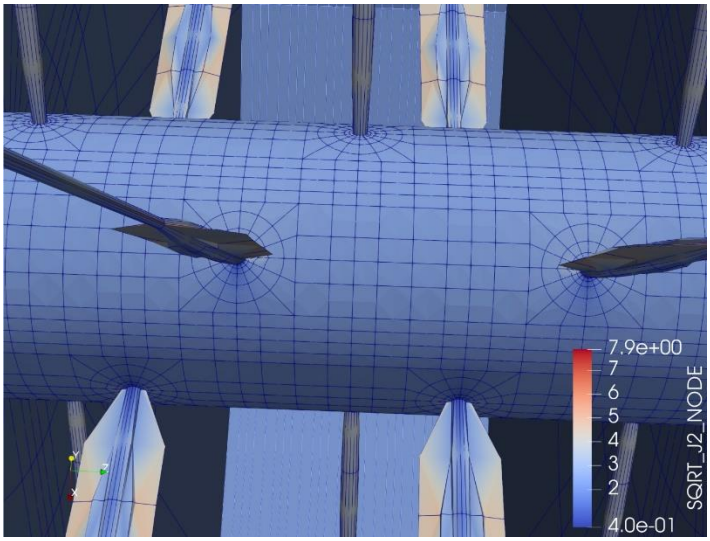

Figure 6.15 Visual result for horizontal well

B-4 Well inclination effect for A4=7.5, Depletion rate=1kpsi/182.5day, anisotropic permeability (permeability kx=600md,ky=600md, kz=60md)

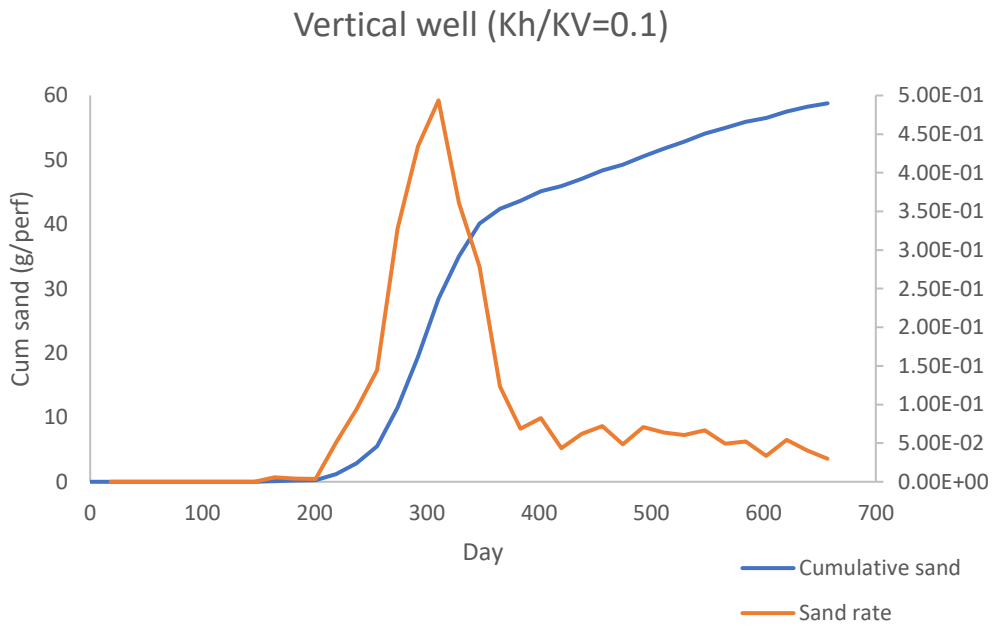

Figure 6.16 Cumulative produced sand and sand rate (simulation result for vertical well with anisotropic condition)

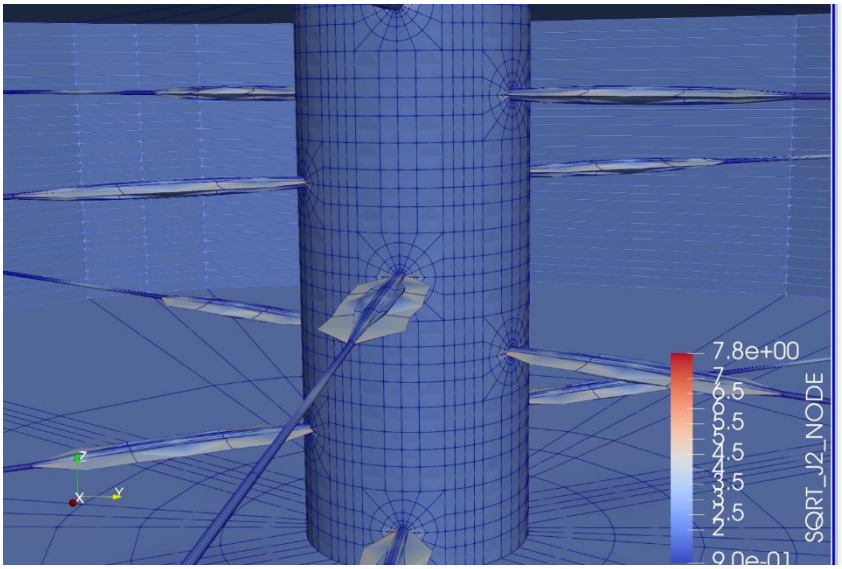

Figure 6.17 Visual result for vertical well with anisotropic condition

Well inclination 30°

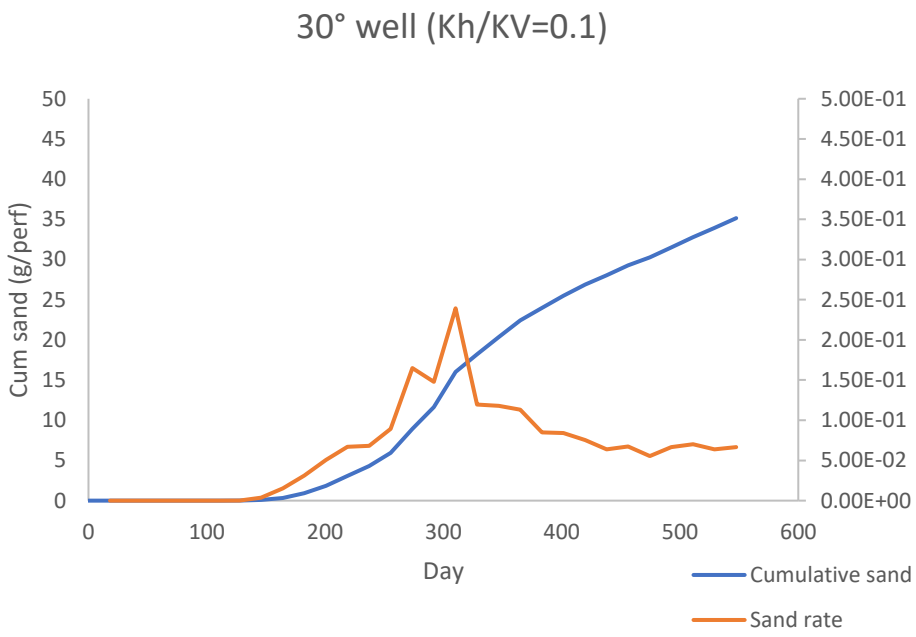

Figure 6.18 Cumulative produced sand and sand rate (simulation result for well angle=30 with anisotropic condition)

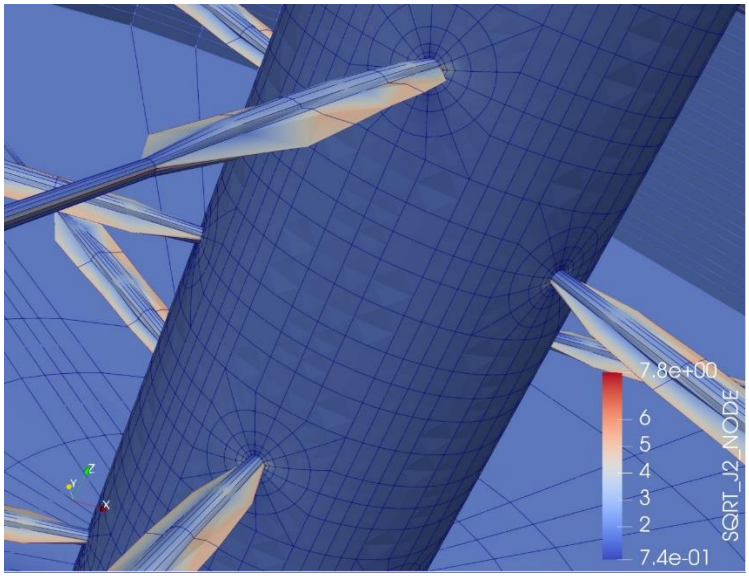

Figure 6.19 Visual result for well angle=30 under anisotropic condition

Well inclination 45°

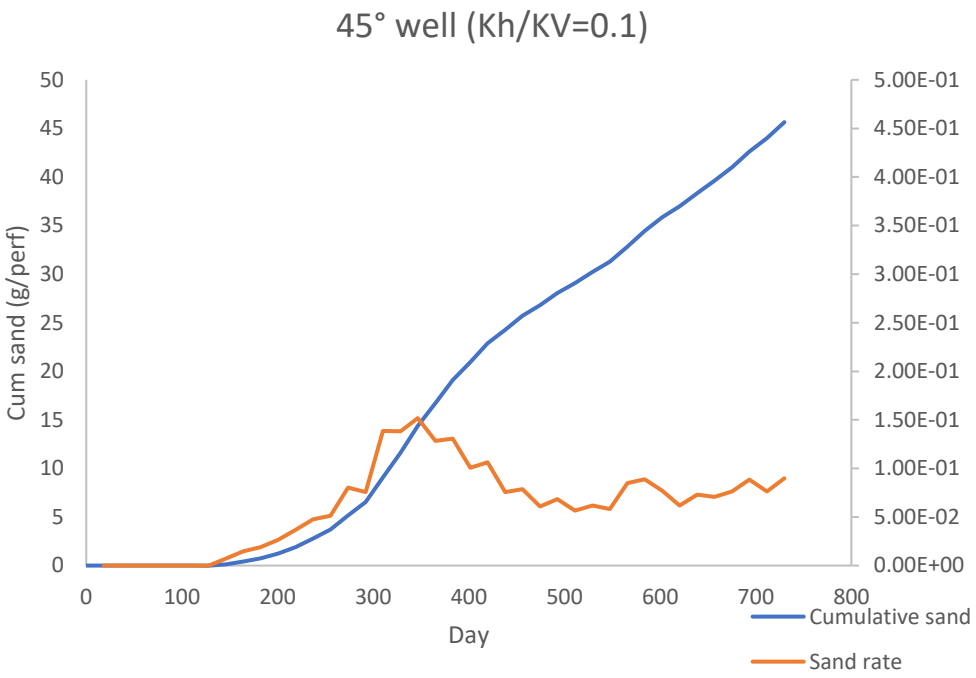

Figure 6.20 Cumulative produced sand and sand rate (simulation result for well angle=45° with anisotropic condition)

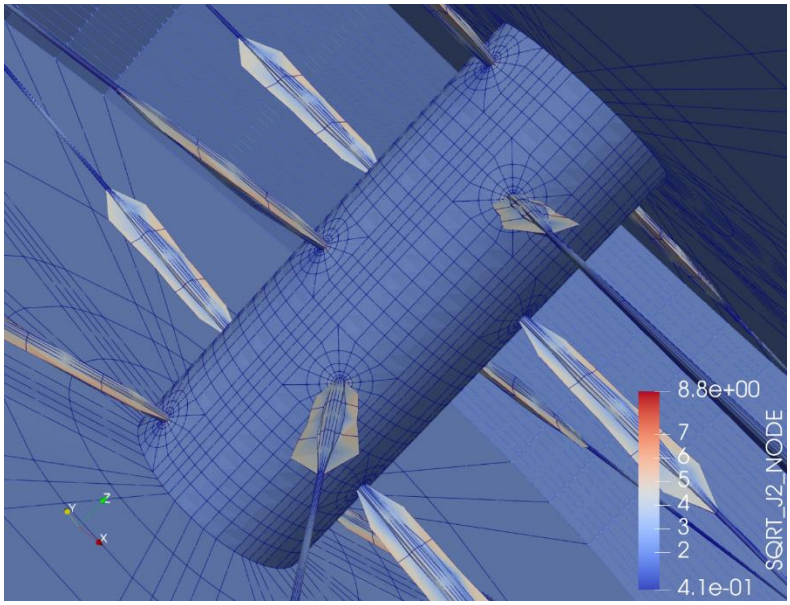

Figure 6.21 Visual result for well angle=45 with anisotropic condition

Well inclination 70°

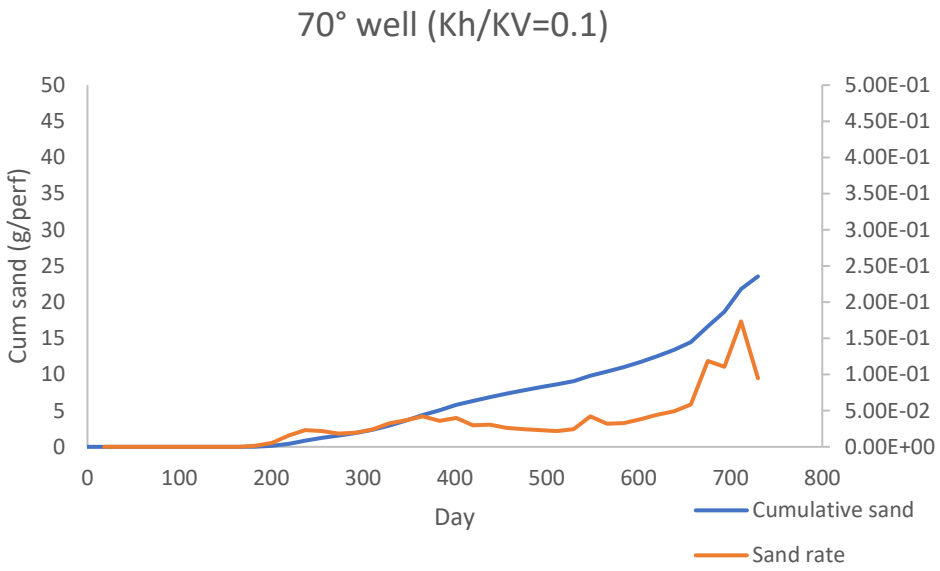

Figure 6.22 Cumulative produced sand and sand rate (simulation result for well angle=70° with anisotropic condition)

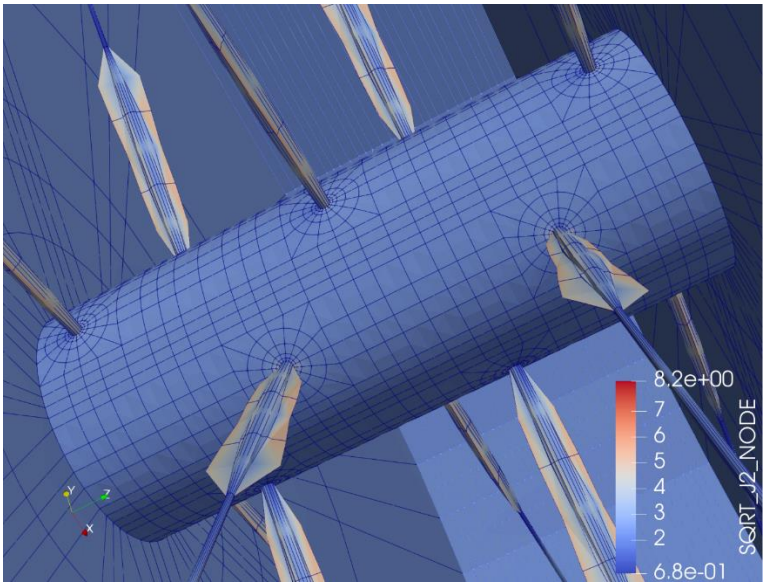

Figure 6.23 Simulation result for well angle=70 with anisotropic condition

Well inclination 90° (horizontal well)

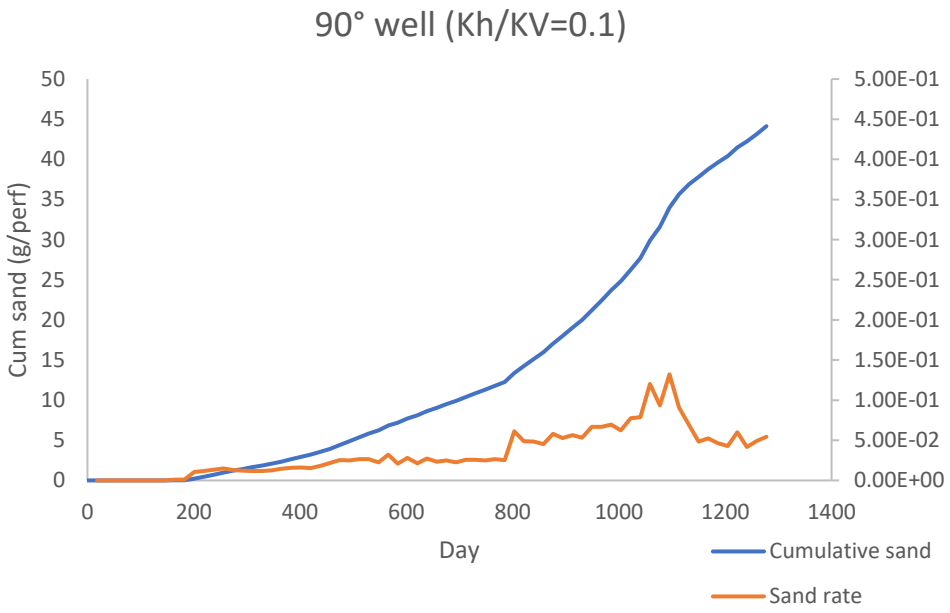

Figure 6.24 Cumulative produced sand and sand rate (simulation result for vertical well with anisotropic condition)

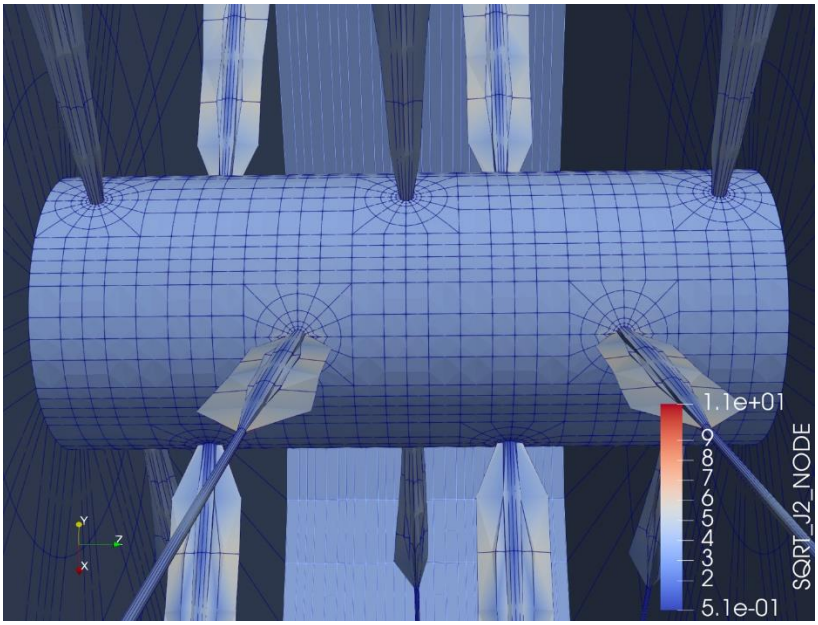

Figure 6.25 Visual result for vertical well with anisotropic condition

Because of high permeability in horizontal direction, the flow rate at the perforations on the well bottom and top is high. It causes the initiation of sand production from the top and bottom perforations, although the perforation evolution is small compared with side perforations.

APPENDIX C

Table 3.1 Calculated coefficients for constitutive relation and failure envelope

```
"** INPUT DATA  FOR COEFI PROGRAM  for Sintef(Castlegate Sandston,paraUCS= 2056
*
**---   ESTIMATEVALUES  (DEFALT DATA    OR      MANUAL  INPUT)
*
"* (A1) EAVE,POIAVE,COMPR
      0.126214D+04  0.411143D+00  0.555600D-04
"* (A2) AC(I),BETA
     -0.599768D-03 -0.599768D-03 -0.599768D-03  0.260238D+01
*       (A3)    PORO
      0.266000D+00
*       (A4)    TRESCA  -1
*       IHARD(1 FOR     KINEMATIC;2     FOR     WORK    HARDENING;3     FOR     STRAIN  HARDENING)

        3
*       SY(K):  MAX(S)-MIN(S)=SY0+INTEGRAL(EXP(B1+B2*K+...+B5*K**4))

    3  0.3202D+01  0.7095D+01 -0.1194D+04
*       (A5)    VON     MISES   -2
*       IHARD(1 FOR     KINEMATIC;2     FOR     WORK    HARDENING;3     FOR     STRAIN  HARDENING)

        3
*       SY(K):  (3.*J2)**.5=SY0+INTEGRAL(EXP(B1+B2*K+..+B5*K**4))

    3  0.3202D+01  0.7095D+01 -0.1194D+04
*       (A6)    MOHR-COULOMB    -3
*       IHARD(1 FOR     KINEMATIC;2     FOR     WORK    HARDENING;3     FOR     STRAIN  HARDENING)

        3
*       C       AND     FAI:    SH=(C0+INTEGRAL(EXP(B1+B2*K+..+B5*K**4)))-SN*TAN(FAI)

    3  0.3418D+00  0.5230D+01 -0.9451D+03
    1  0.8155D+00
*       (A7)    DRUCKER-PRAGER  -4
*       IHARD(1 FOR     KINEMATIC;2     FOR     WORK    HARDENING;3     FOR     STRAIN  HARDENING)

        3
*       SY(K)   AND     G(J1):J2**.5+G(J1)=SY0+INTEGRAL(EXP(B1+B2*K..+B5*K**4)

    3  0.0000D+00  0.5459D+01 -0.1058D+04
    3 -0.1245D+00  0.5078D+00  0.1567D-01
*       (A8)    MODIFIEDKINEMATIC       -5
*       B       AND     G(J1):  B=EXP(POLYNOMIAL)       AND     F=J2-G(J1)

    3  0.1238D+01 -0.9025D+00 -0.4438D-01
    3  0.3018D+00 -0.1245D+01 -0.3855D-01
      0.000000D+00
*       (A9)    CAP     MODEL   :       RFI     EL0     POR0    AD      FOR     DP=POR0*(DEXP(AD*J1)-1.)
        AND
*       F=R**2*J2+(J1-L)**2-(X-L)**2=0

      0.800000D+01 -0.100000D+06  0.800000D-01  0.100000D+00
      0.800000D+01 -0.100000D+06  0.800000D-01  0.100000D+00
      0.800000D+01 -0.100000D+06  0.800000D-01  0.100000D+00
      0.800000D+01 -0.100000D+06  0.800000D-01  0.100000D+00
      0.800000D+01 -0.100000D+06  0.800000D-01  0.100000D+00
*       (A10)FAILURE    ENVELOPE
*       MAXMUM  STRENGTHTHEOREM :       F=J2-G(J1)=0    FOR     COMPRESSION
    3  0.1021D-01 -0.6192D+00 -0.2407D-01
*       MAXMUM  PLASTIC STRAIN  THEOREM :       F=JE2-G(J1)=0   FOR     COMPRESSION
```

```
    1  0.3671D-02
*       MIN     STRESS  VS      MAX     STRESS
    2 -0.3792D+00 -0.1492D+00
*
**---   DATA    FOR     REFININGTHE     ESTIMATED       VALUES.
*
"**(B0) UNIT CONVERSION FOR INPUT DATA-- PRESS(TO KPSI),STRAIN(TO FRACTIO
      0.100000D+01  0.100000D+01
"* (B1) RATYP, STS AND STY
      0.300000D-01  0.100000D+00  0.800000D-01
```

B-5 Oriented perforation, perforation shot in the top and bottom direction (180° phase)

X-shape oriented perforation

Vertical well

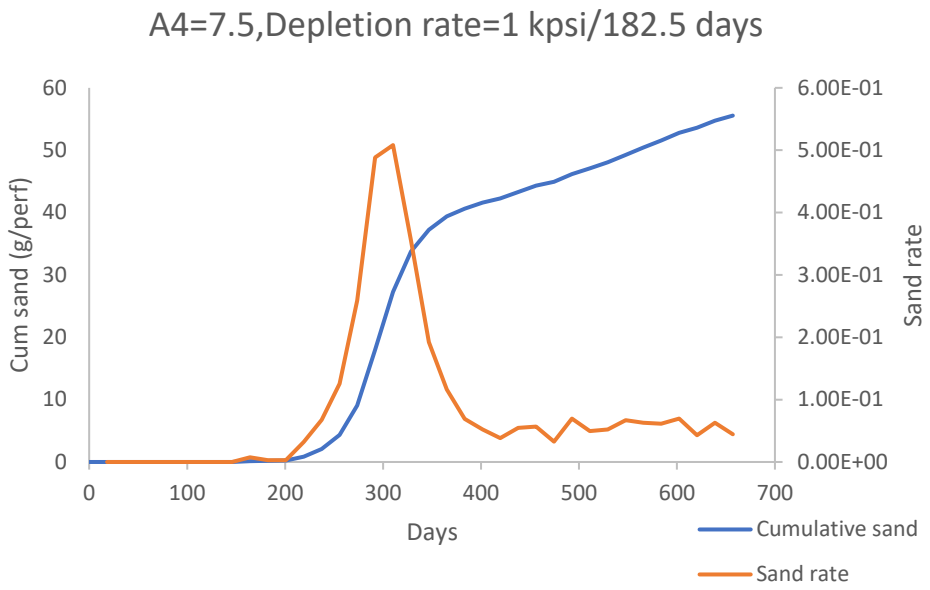

Figure 6.1 Cumulative produced sand and sand rate (simulation result for X-shape perforation under vertical well)

30°

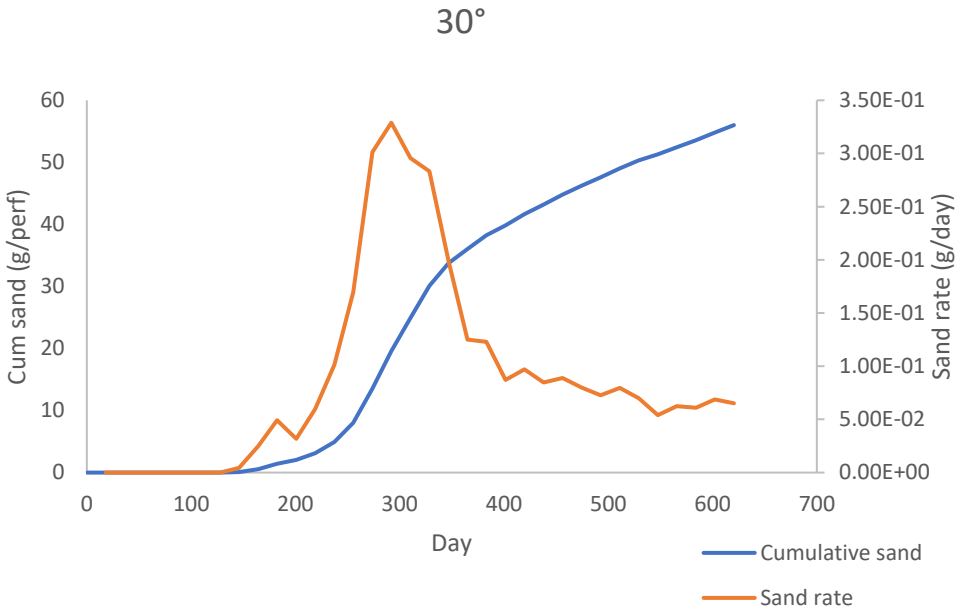

Figure 6.2 Cumulative produced sand and sand rate (simulation result for X-shape perforation under well angle=30°)

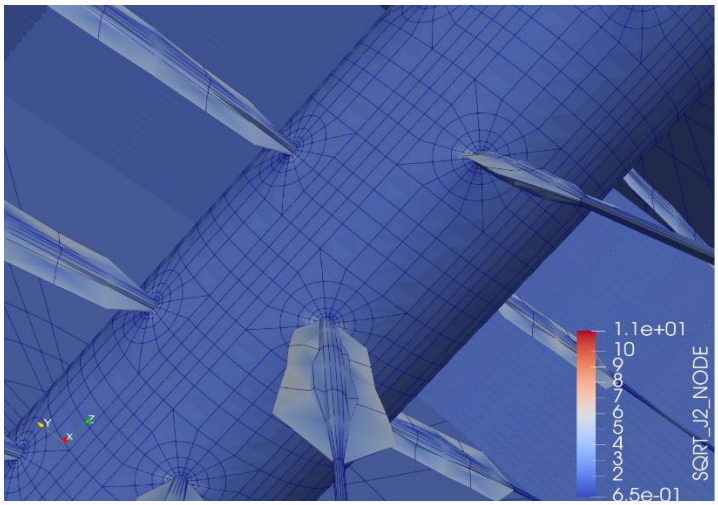

Figure 6.3 Visual result for X-shape perforation under well angle=30

45°

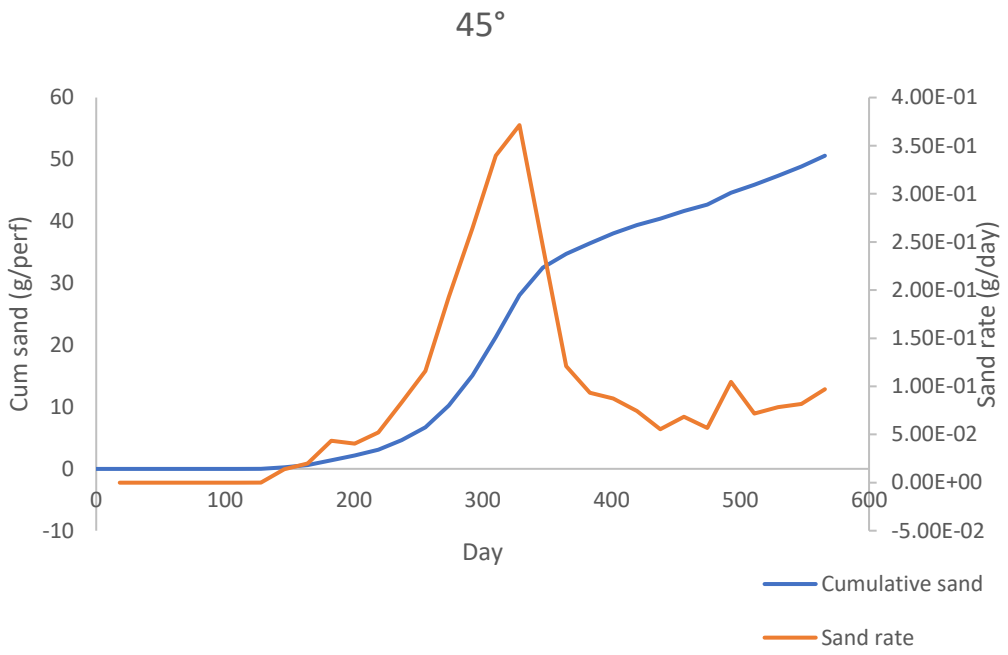

Figure 6.4 Cumulative produced sand and sand rate (simulation result for X-shape perforation under well angle=45°)

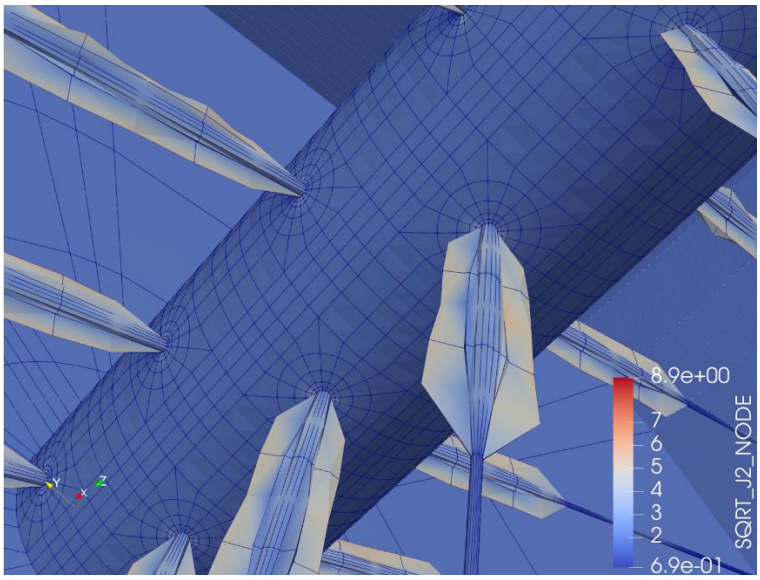

Figure 6.5 Visual result for X-shape perforation under well angle=45

70°

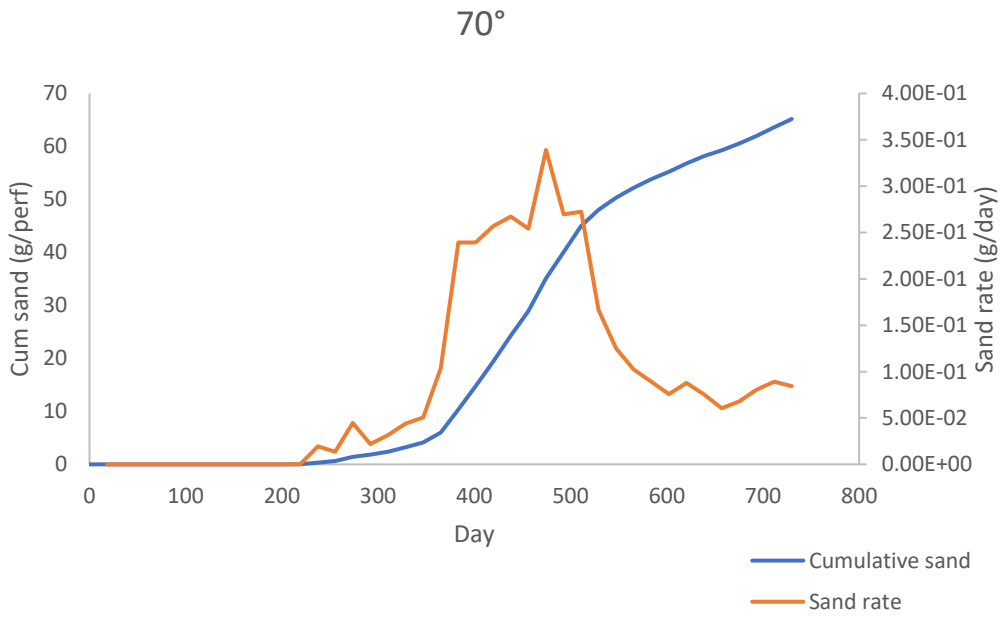

Figure 6.6 Cumulative produced sand and sand rate (simulation result for X-shape perforation under well angle=70°)

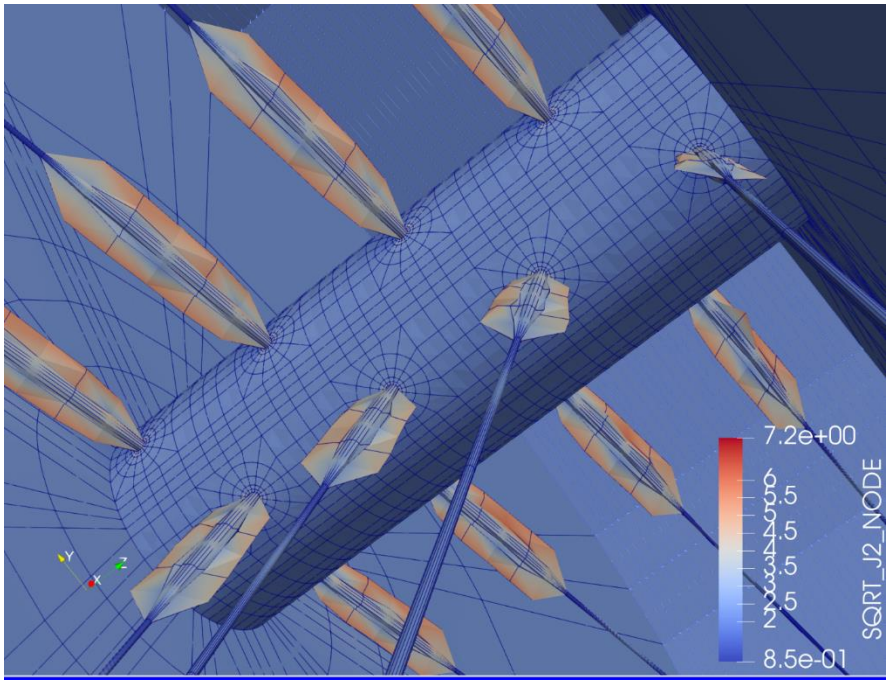

Figure 6.7 Simulation result for X-shape perforation under well angle=70

90°

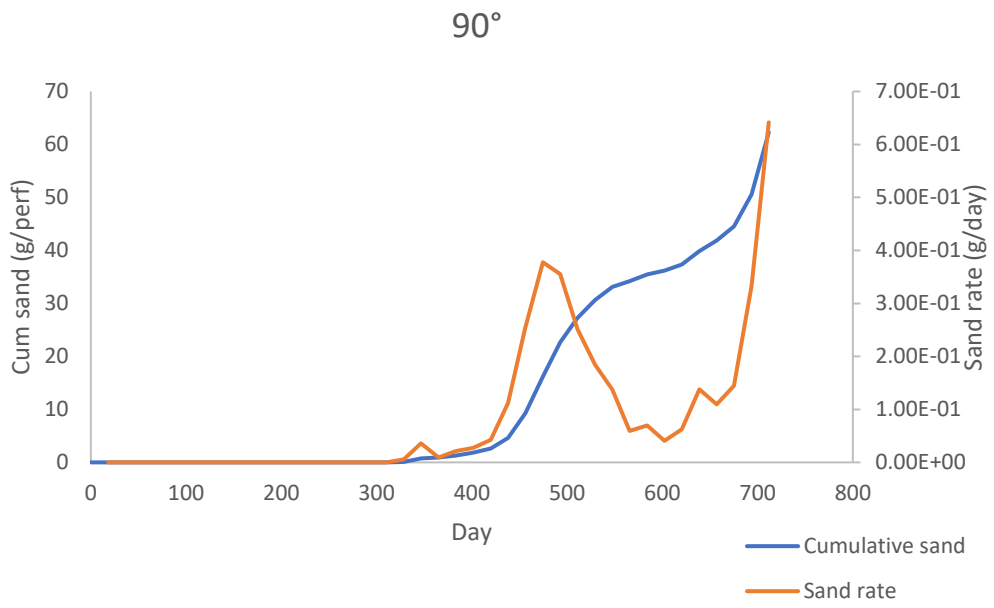

Figure 6.8 Cumulative produced sand and sand rate (simulation result for X-shape perforation under horizontal well)

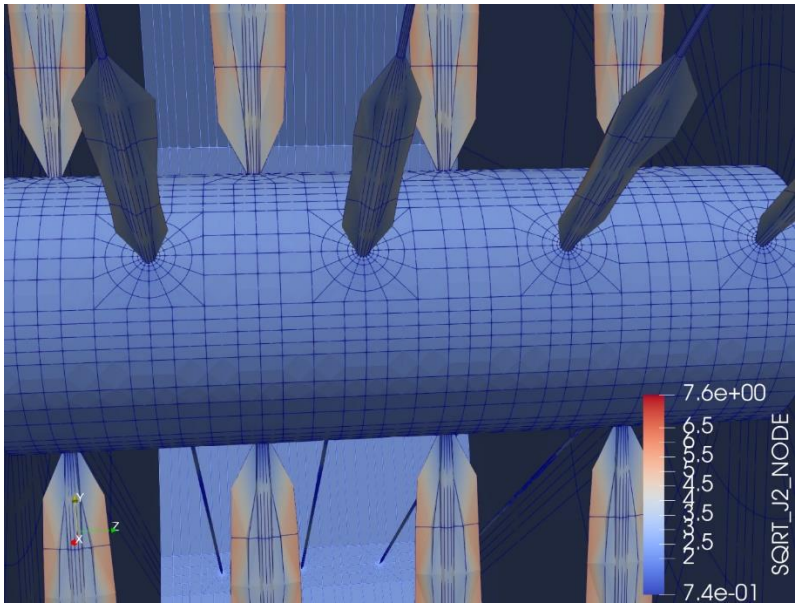

Figure 6.9 Visual Simulation result for X-shape perforation under horizontal well